Plasmonic spectroscopy of biomacromolecules with chiral metamaterial

Marion Rodier

Submitted in fulfilment of the requirements for the
Degree of Doctor of Philosophy

School of Chemistry
College of Science and Engineering
University of Glasgow

July 2019

Abstract

This thesis explores the applications of injection-moulded chiral plasmonic nanostructures for biomolecules sensing. Such nanostructures enhance the chiroptical signal generated by chiral objects with plasmonic fields. These fields can produce a greater asymmetry than circularly polarised light and are called “Superchiral” fields. They are a very efficient tool for the detection of higher order structures (tertiary, quaternary) in proteins. Subsequently plasmonic metamaterials used for sensing will be introduced. We will demonstrate that the chiral fields they generate, are sensitive to the orientation of the biomolecular material at the surface and the conformation of biomolecular complexes, and that they can sense highly symmetrical structures such as viruses. In the first results chapter it will be shown that the chiral fields are highly sensitive to the surface charges of a protein. It will be shown that the surface charges of the analyte can enhance or reduce the chiral fields depending on the handedness of the fields and the state of charge of the analyte. This new property of the chiral structures leads to several applications in biology. This effect is characterised by a new type of asymmetry in the optical rotatory dispersion (ORD) spectra, thus a new asymmetry parameter will be introduced. This offers a route to rapid determination of the isoelectric points of proteins without prior knowledge of their primary sequences. It can also help to predict protein solubility in solution, their folding and interactions with other biomolecules. The new asymmetry parameter will be shown to be sensitive to the geometry of protein-protein complexes and therefore to the specificity of an interaction between two proteins. Non-specific interaction leads to isotropic complexes and hence gives a weak chiroptical signal. It is also explained that the new asymmetry parameter, introduced in the first results chapter, is a good indicator of the order of the analyte at the metafilm surface. Furthermore, we will show that this sensitivity for surface charges allows the detection of highly symmetrical biomolecules such as plant viruses. The fingerprint in the ORD for viruses with the same geometry and same size but different isoelectric points is shown to be dissimilar. Another property of the nanostructures is the ability to display plasmonic induced transparency (PIT). The model of the PIT allows the asymmetry to be measured in the phase retardation. This parameter $\Delta\Delta\varphi$ is shown to be more sensitive to surface charges and hence allows higher accuracy in virus detection. Chiral fields are also efficient in distinguishing between virions and virus-like particles (VLP). The effect of adding a gold binding domain on the virus particles is explored, and proved efficient, even though the chemistry of the virus surface is changed. Finally, chiral fields are used to sense rod-shaped viruses. This chapter emphasizes the sensitivity of the parameters $\Delta\Delta\varphi$ and raises the problem of the sensitivity limit for bigger macromolecules. The effect on the asymmetry is shown to be dependent on the orientation of the particles. Using the chirality tensor, the detection limit of macro-biomolecules in the chiral fields will be described.

Contents

List of tables

List of figures

List of abbreviations

AFM	Atomic Force Microscopy
ATR	Attenuated Total Reflectance
APBS	Adaptative Poisson-Boltzmann Server
BSA	Bovine Serum Albumin
CaMV	Cauliflower Mosaic Virus
CCD	Charge-coupled Device
CD	Circular Dichroism
CMV	Cucumber Mosaic Virus
CPL	Circularly Polarised Light
CpMV	Cow pea Mosaic Virus
DHQase	Type II Dehydroquinase
EBL	Electron Beam Lithography
Eg-thiol	Triethylene glycol mono-11-mercaptoundecyl
EIT	Electromagnetically Induced Transparency
EM	Electron Microscopy
EtOH	Ethanol
Fab	Fragment antigen binding
Fc	Fragment crystalline
HBS	HEPES Buffered Saline
HIV	Human Immunodeficiency Virus
IgG	Immunoglobulin G
IPTG	Isopropyl β-D-1-thiogalactopyranoside
I.R	Infra-Red
ITC	isothermal titration calorimetry
IM	Injection Moulding
IPA	Iso-propyl Alcohol
LH	Left Handed
LSPR	Localised Surface Plasmon Resonance
M13	M13 filamentous bacteriophage
NTA	Nitrilotriacetic acid
OR	Optical Rotation
ORD	Optical Rotatory Dispersion
OVA	Ovalbumin
PEG	Poly ethylene glycol
PBS	Phosphate Buffer Saline
PDB	Protein Data Bank

PIT	Plasmonic Induced Transparency
PML	Perfectly Matched Layers
pI	Isoelectric Point
PMMA	Poly methylmethacrylate
PPI	Protein-protein interaction
RIU	Refractive Index Unit
RH	Right Handed
SEM	Scanning Electron Microscopy
SAM	Self-Assembled Monolayer
SHO	Single Helical Oscillator
SPP	Surface Plasmon Polariton
SP	Surface Plasmon
SPR	Surface Plasmon Resonance
TEM	Transmission Electron Microscopy
TCR	T cell receptors
TMV	Tobacco Mosaic Virus
TPS	Templated Plasmonic Substrate
TYMV	Turnirp Yellow Mosaic Virus
U.V	Ultra-Violet
VLP	Virus Like Particles

Publications

1 – Calum Jack, Affar S. Karimullah, Ryan Tullius, Larousse Khosravi Koshrashad, Marion Rodier, Brian Fitzpatrick, Laurence D. Barron, Nikolaj Gadergaard, Adrian J. Lapthorn, Vincent M. Rotello, Greame Cooke, Alexander O. Govorov and Malcolm Kadodwala, Spatial control of chemical processes on Nanostructures through Nano-localized water heating. Nature communications, 2016. 7: p 10946.

2 – Ryan Tullius, Affar S. Karimullah, Marion Rodier, Brian Fitzpatrick, Nikolaj Gadergaard, Laurence D. Barron, Vincent M. Rotello, Greame Cooke, Adrian J. Lapthorn, and Malcolm Kadodwala, “Superchiral” Spectroscopy: Detection of protein higher order hierarchical structure with chiral plasmonic nanostructures. JACS, 2015. 137 p 8381.

3 – Marion Rodier, Chantal Keijzer, Joel Milner, Affar S. Karimullah, Sharon Kelly, Adrian Lapthorn, Nikolaj Gadegaard and Malcolm Kadodwala, Biomacromolecular charge chirality detected using chiral plasmonic nanostructure. Nanoscale horiz, 2020. 5 336 – 344.

4 – Marion Rodier, Chantal Keijzer, Joel Milner, Affar S. Karimullah, Laurence D. Barron, Nikolaj Gadegaard, Adrian J. and Lapthorn Malcolm Kadodwala, Probing Specificity of Protein–Protein Interactions with Chiral Plasmonic Nanostructures. J. Phys. Chem. Lett. 2019, 10, 20, 6105-6111.

Acknowledgements

First, I would like to thank Professor Malcolm Kadodwala for giving me the opportunity to undertake my post-graduate studies under his supervision. I would like to express my gratitude for his advice and guidance during this project. I would also like to extend my sincere thanks to Dr Affar Karimullah for his continuous help and support and for sharing his experience and expertise to make this project a success. Especially with the fittings performed in this thesis. I thank Maryam Hajji and Tarun Takkar for their help and advices while writing this thesis. Furthermore, I truly appreciated the help provided by my fellow PhD students: Dr Calum Jack, Dr Ryan Tullius, Christopher Kelly, Oriol Roig Vilaseca, Katie McKay and Cameron Gilroy, with special thank to Katie McKay and Christopher Kelly for proof reading this thesis and for organising social events that initiated me to the Scottish culture. I would like to thank the project students (Erasmus and master) for their help during this project.

I would like to also express my thanks to the academic staff within the School of Chemistry. Particularly, Dr Adrian Lapthorn, who provided many of the protein samples used throughout this thesis. My thanks go to him for his advice and expertise on handling these proteins and for giving me access to his laboratory. Moreover, I would like to express my gratitude to Dr Chantal Keijzer, Dr Joel Milner from the school of Life Sciences and Dr Andy Love from the James Hutton Institute for providing the plant viruses used during this project as well as precious advice in handling them. Special thanks to Dr Chantal Keijzer for her help with the measurements and proof reading most of this thesis. I thank Dr Sharon Kelly and June Southall for their help with circular dichroism measurements. My thanks also go to all the staff at the JWNC, and members of the Gadegaard group in the School of Engineering, for access to the facilities, labs, and for assistance with the sample fabrication. I am thankful to the technical staff of the School of Chemistry for any help they provided during my experimental work. As well as to Dr Stuart MacKay and Arlene Douglas for IT support.

Finally, many thanks must go to my family, my parents and siblings and friends for their constant support and their patience during my time here despite the distance; without them I would never have finished this PhD.

Author declaration

I declare that, except where explicit reference is made to the contribution of others, that this dissertation is the result of my own work and has not been submitted for any other degree at the University of Glasgow or any other institution.

Marion Rodier

July 2019

Chapter 1: Introduction

1.1 Introduction and background:

Surface plasmon oscillations arise from the oscillation of the conduction electrons, they are induced by an electromagnetic wave[1,2] at the surface of a metal. Surface plasmons have applications in many domains such as environmental science, solar energy and medicine[2]. For example, low cost biosensors for diagnosis are required for fast genetic mapping for personalised care[3]. Plasmonics is an important area of the nanophotonic field and has attracted more and more interest in recent years thanks to improvements in fabrication techniques and spectroscopies[4]. The development of extremely efficient metamaterials has also contributed to the exponential interest in plasmonics. Metamaterials are artificially created nanostructures with the ability to confine the electromagnetic fields over structures of a size smaller than the wavelength of the light (sub-wavelength)[5], leading to optical field enhancement[6,7]. This property gives access to phenomena that cannot take place in natural materials, alloys or compounds, like negative refractive indices. The properties of metamaterials are directly linked to the shape and size of nanostructures they are made of rather than to the properties of the bulk material[8]. These nanostructures, if engineered specifically by giving them the correct diameters, shapes and pitches, allow the generation of precise plasmonic resonances. Plasmonic resonances can be obtained in several metals that contain free electrons: silver, gold and platinum. In this thesis the metamaterials used are exclusively made of gold. The thickness of the metal used was optimised previously[9]. The extreme tunability of metamaterials makes them useful in diverse fields such as sensing, photovoltaics and optics.

This thesis focuses on the sensing property of metamaterials used to look at different types of biomolecules such as proteins and viruses. Biomolecules are known for being chiral. Two objects which are mirror image to each other are called enantiomers. There are two to the power n (where n is the number of chiral centres) enantiomers for each chiral molecule. Enantiomers are distinguishable by their handedness: left and right. Being able to differentiate the two enantiomers of a molecule is of essential importance because they usually do not have the same chemical effect (for example they do not interact the same way in a reaction, or in the human body). Both enantiomers of chiral molecules exhibit the same physical properties (melting point, molecular weight…) but they rotate polarised light differently. Consequently, optical spectroscopy is a reliable technique to detect and differentiate enantiomers. Currently, the sensitivity of conventional chiroptical spectroscopies is in the order of micrograms which is extremely poor compared to other spectroscopic techniques. Furthermore, circular dichroism cannot detect chiral effects in the tertiary and quaternary structure of a protein. This potentially lack of absolute sensitivity of

chiroptical techniques is a strong limit to the study of chirality and biomolecules of several orders of structures with different types of chirality. However, metamaterials have been proven to enhance the sensitivity of the CD signal[10].

CD enhancement was first demonstrated in 2010[11]. It was shown that the electromagnetic near fields generated with plasmonic nanostructures allow the enhancement of the chiroptical effects taking place in tertiary and quaternary structures (further explanation in chapter 2) of chiral molecules[12]. Plasmonic enhanced spectroscopy enables sensing with a small volume of chiral material (micrograms)[13]. Indeed, the light is strongly confined within nanostructures of sub-wavelength size, leading to enhancement of the chiral fields around the nanostructures[14,15].

Plasmonic nanostructures can produce enhanced chiral fields called “Superchiral”. This phenomenon was first explained by Tang and Cohen[16]. They describe the interaction between the light and chiral molecules by introducing the optical chirality parameters. These fields produce a bigger asymmetry than the one generated by circularly polarised light. Lately a better understanding of the physics behind the properties of the nanostructures, with the establishment of the analogue orbital diagram model[17], has opened up new ways to increase the optical sensitivity of the metamaterial. Several studies have shown that metamaterials can exhibit plasmonic induced transparency properties[18]; this phenomenon is an analogue to the quantum one: electromagnetically induced transparency. However, the plasmonic induced transparency phenomenon, in a short spectral range, is explained with a classical model of two oscillators with a long pulse delay (chapter 2).

Although metamaterials exhibit useful physical properties and seem to be a promising asset in many fields, they are still rather expensive to produce. Currently, these metamaterials are being produced with lithography techniques: electron beams, dip-pen, and nanoimprint lithography[5]. In the case of sensing, for example, it is problematic because metamaterial can be used only once. Biological material binds the surface too strongly resulting in damage on the metamaterial after cleaning. This limits the use of metamaterials to fundamental studies and delays their availability for commercial use for diagnostic purposes. For this thesis, we chose to use injection-moulded substrates[9]. These substrates consist of nanostructures printed on polycarbonate slides using a nickel mould. This process enables the production of batches of them in a relatively short time. Thus, it is a cost-effective process, making a substrate disposable but perfectly suited for sensing. Previous studies have shown the viability of these metamaterials and their ability to produce superchiral fields[9,19,20]. It was demonstrated that the field enhancements generated by these metamaterials are sensitive to chirality in higher order structure[12] of proteins (tertiary and quaternary structure). In this thesis the properties of these nanostructures and their degree

of sensitivity are further explored. They are tested against proteins of highly similar secondary structure and thus similar chiral features. We discovered that plasmonic fields were sensitive to the surface charges of the biomolecules.

At the same time, we tested the sensitivity of these nanostructures towards bigger and more symmetrical biomolecules such as viruses and bacteriophages. Some promising results will be shown and ways to improve the sensitivity will be explored. Viruses are made of amino acids and thus display chirality. Moreover, the capsid is made of protein and exhibits surface charges. Viruses being more complex entities than proteins the surface charge is not the only variable that influences the chirality of the signal.

1.2 Thesis overview:

In the first results chapter (chapter 4) we show that the fields generated by the plasmonic nanostructures are sensitive to the surface charge distribution of biomolecules. This knowledge is of valuable importance to help understanding protein structures and reactive behaviours in the human body. Indeed, the electrostatic state of proteins govern their folding and electrostatic interactions, such as their solubility in solution and the ability to be crystallised or to interact with other proteins or receptors. We also introduce a new asymmetry parameter to characterise the change in the height of optical rotatory dispersion (ORD) spectra, induced by the surface charge distribution of proteins. The physical aspects of the change occurring in the optical signal is explained via a mathematical model. It is possible to change the overall net charge of a protein by changing the pH of the buffer it is dissolved in. We present the effect of mainly positive or negative surface charges on the chiral plasmonic fields. We show that the polycarbonate metamaterials can be used to discriminate between proteins with the same higher order structure but with slight differences in the primary sequence via the overall net charge of the molecule. These changes cannot be seen using CD. We demonstrate that the interaction of the surface charges interferes with the plasmonic fields, enhancing or diminishing the amplitude according to the handedness and the sign of the charges.

In chapter 5 we study specific and nonspecific protein-protein interaction. Specific interaction between two proteins (like antigen-antibody interaction) leads to a complex with a new biological function and an anisotropic geometry; nonspecific interaction leads to a non-functional complex and isotropic geometry. Specifically, in this chapter, we study the antigen-antibody interaction. By adding a fragment antigen binding $F(ab')_2$ monolayer to the metafilm we can show the specificity and the non-specificity of protein-protein interaction. A $(Fab')_2$ portion of an antibody was used with the corresponding antigen. Firstly, we demonstrate that the $F(ab')_2$ can form a functional monolayer at the surface. The Fab' also retains its properties and does not misfold at the surface of the substrate. Bovine serum

albumin (BSA) is loaded on a surface coated with $F(ab')_2$ fragments. The complex BSA-Fab' has a specific fingerprint in the ORD spectra characterised by the parameter introduced in chapter 4. Then, we show that ovalbumin (OVA) which can bind the same $(Fab)_2$, does not display the same fingerprint in the ORD. We explain that the geometry of the complex created is the cause of this effect, because according to the complex specificity the environment becomes isotropic. The asymmetry parameter introduced in this chapter is shown to be sensitive to the surface orientation of the protein.

In chapter 6 we show how plasmonic chiral fields interact with molecules much bigger than proteins: viruses. Viruses are more symmetric entities, so they can be harder to detect with chiroptical spectroscopy. We investigate the interaction of icosahedral plant viruses with plasmonic fields. Plasmonic spectroscopy shows promising results in virus detection. Like proteins, viruses exhibit surface charges. Thus, the way to detect the virus on the surface is down to the overall net charge of the particles. The capsid of the viruses is made of different proteins called coat proteins: each virus capsid is made of different coat proteins or an assembly of coat proteins. Consequently, even if the viruses have highly similar sizes and geometry, the interaction they have with the plasmonic fields is drastically different. In this chapter, three different viruses with diverse isoelectric points (pI), and thus disparate surface charge distributions, are shown to interact differently with the plasmonic fields. Ways to enhance the chiroptical signal by chemical binding are explored. A gold binding domain is added to the virus displaying the strongest asymmetry. Binding the virus to the metafilm surface in a specific orientation is shown to affect the asymmetry signal of the virus; it does not just enhance it; it changes the sign. We demonstrate that with the help of plasmonic fields it is possible to distinguish between virions and virus-like particles (VLP), i.e. between pathogen and non-pathogen agents.

In the last chapter, chapter 7, the limit of our technique is explored. The efficiency of the plasmonic field interaction with the analyte is shown to depend upon the orientation of the molecules on the surface and in the z direction. Rod-shaped viruses and bacteriophage are loaded on a gold surface. These two particles have similar structures, even though the bacteriophage is flexible when the virus is rigid but sit on the surface differently. Even if their interaction with the gold surface is not the same, they create the same kind of isotropic environment. Rod-shaped viruses do not bind gold easily - this can be due to their shape. Rod-shaped viruses are oriented only in two planes; thus, the chirality tensor exhibits a different behaviour. When the surface is saturated with the viruses, the environment in the z direction becomes isotropic, and the asymmetry becomes too weak. Due to the virus shapes the surface charges are not exposed to the chiral fields in the same way as with the biomolecules studied in previous chapters (4, 6). The change in the optical signal occurs in

the xy plane, and due to the shape of the chiral field and our experimental set up any change happening in this plane cannot be seen. VLP of rod-shaped viruses are studied as well and display a greater asymmetry than the virions.

1.3 References:

(1) Enoch, S.; Bonod, N. (Eds.) Plasmonics from Basics to Advanced Topics. Springer (2012).

(2) Li, Y. Plasmonic Optics : Theory and Applications. Spie (2017).

(3) Brolo, A. G. Plasmonics for Future Biosensors. Nat. Pho. (2012), 6 (11).

(4) Maier, S. A. Plasmonics : Fundamentals and Applications. Springer (2007).

(5) Smith, D. R.; Cui, T.J.; Liu, R. P. Metamaterials : Theory, Design, and Applications. Springer (2010).

(6) Hess, O.; Pendry, J. B.; Maier, S. A.; Oulton, R. F.; Hamm, J. M.; Tsakmakidis, K. L. Active Nanoplasmonic Metamaterials. Nat. Mater. (2012), 11 (7), 573–584.

(7) Anker, J. N.; Hall, W. P.; Lyandres, O.; Shah, N. C.; Zhao, J.; Van Duyne, R. P. Biosensing with Plasmonic Nanosensors. Nat. Mater. (2008), 7 (6), 442–453.

(8) Monticone, F.; Alù, A. Metamaterial, Plasmonic and Nanophotonic Devices. Rep. Prog. Phys (2017), 80 (3):036401.

(9) Karimullah, A. S.; Jack, C.; Tullius, R.; Rotello, V. M.; Cooke, G.; Gadegaard, N.; Barron, L. D.; Kadodwala, M. Disposable Plasmonics : Plastic Templated Plasmonic Metamaterials with Tunable Chirality. Adv. Mater. (2015), 27 (37), 5610–5616.

(10) Vestler, D.; Shishkin, I.; Gurvitz, E. A.; Nasir, M. E; Ben-Moshe, A.; Slobozhanyuk, A. P.; Krasavin, A. V.; Levi-Belenkova, T.; Shalin, A. S.; Ginzburg, P.; Markovich, G.; Zayats, A. V. Circular Dichroism Enhancement in Plasmonic Nanorod Metamaterials. Opt. Express (2018), 26 (14), 17841-17848.

(11) Hendry, E.; Carpy, T.; Johnston, J.; Popland, M.; Mikhaylovskiy, R. V.; Lapthorn, A. J.; Kelly, S. M.; Barron, L. D.; Gadegaard, N.; Kadodwala, M. Ultrasensitive Detection and Characterization of Biomolecules Using Superchiral Fields. Nat. Nanotechnol. (2010), 5 (11), 783–787.

(12) Tullius, R.; Karimullah, A. S.; Rodier, M.; Fitzpatrick, B.; Gadegaard, N.; Barron, L. D.; Rotello, V. M.; Cooke, G.; Lapthorn, A.; Kadodwala, M. “Superchiral” Spectroscopy : Detection of Protein Higher Order Hierarchical Structure with Chiral Plasmonic Nanostructures. J. Am. Chem. Soc. (2015), 137 (26), 8380–8383.

(13) Jack, C.; Karimullah, A. S.; Leyman, R.; Tullius, R.; Rotello, V. M.; Cooke, G.; Gadegaard, N.; Barron, L. D.; Kadodwala, M. Biomacromolecular Stereostructure Mediates Mode Hybridization in Chiral Plasmonic Nanostructures. Nano Lett. (2016), 16 (9), 5806–5814.

(14) Schäferling, M. Chiral Nanophotonics. Chiral Optical Properties of Plasmonic Systems. Springer (2017)

(16) Tang, Y.; Cohen, A. E. Optical Chirality and its Interaction with Matter. Phys. Rev. Lett. (2010), 104 (16), 1–4.

(17) Prodan, E.; Radloff, C.; Halas, N. J.; Nordlander, P. A. A Hybridization Model for the Plasmon Response of Complex Nanostructures. Science (2003), 302 (5644), 419–422.

(18) Smith, D. D.; Chang, H-R.; Fuller, K. A.; Rosenberger, A. T.; Boyd, R. W. Coupled-Resonator-Induced Transparency. Phys. Rev. A. (2003), 69 (6), 1–6.

(19) Tullius, R.; Platt, G. W.; Khorashad, L. K.; Gadegaard, N.; Lapthorn, A. J.; Rotello, V. M.; Cooke, G.; Barron, L. D.; Govorov, A. O.; Karimullah, A. S.; Kadodwala, M. Superchiral Plasmonic Phase Sensitivity for Fingerprinting of Protein Interface Structure. ACS Nano (2017), 11 (12), 12049–12056.

(20) Kelly, C.; Khorashad, L. K.; Gadegaard, N.; Barron, L. D.; Govorov, A. O.; Karimullah, A. S.; Kadodwala, M. Controlling Metamaterial Transparency with Superchiral Fields. ACS photonics (2017) 5 (2).

Chapter 2: Theory

2.1 Chirality:

The word 'Chiral' originates from the Greek "chir" meaning hand. This term was first introduced by Lord Kelvin in 1884. A chiral object cannot be superimposed onto its mirror image, exactly like two hands[1]. Objects which do not display chirality are known as achiral. Achiral objects, unlike chiral objects, possess a plane of symmetry. Two objects that are mirror images of each other are called enantiomers[1,2]. In science, and particularly in stereochemistry these terms are widely used to describe the handedness of molecules. The handedness of a molecule is defined by whether the molecule will rotate plane polarised light clockwise (right-handed) or anticlockwise (left-handed)[1]. According to group theory, chiral objects belong to the point groups: C_n, D_n, O, T or I[1]. Objects which belong to these groups do not exhibit a reflection plane, centre of inversion or rotation-reflection axes. Chirality is not limited to molecules, it appears in many objects in life such as human ears, snail shells or tornados. A tornado rotation is anti-clockwise in the northern hemisphere and clockwise in the southern hemisphere[3], as seen from space.

2.1.1 Chiral molecules:

Many molecules can display chirality[4]. In fact, most molecules from the building block of life (proteins, DNA, amino acids, sugars and peptides) are chiral. Some chiral molecules exhibit homochirality: only one of the enantiomers exists naturally. For example, amino acids and sugars are naturally levogyre (L) and dextrogyre (D) respectively[3]. In chemistry, chiral molecules are labelled dextrogyre (D) for dextro rotatory or levogyre (L) for laevo rotatory depending on the direction they rotate polarised light, clockwise or anticlockwise respectively[5]. Amino acids and sugars also exist in a synthetic form, thus it is possible to come across D-amino acids and L-sugars. An asymmetric carbon is a carbon attached to four different functional groups and it is therefore chiral. There are two enantiomeric configurations per chiral centre, consequently, the number of enantiomers for a molecule is two to the power of n. Due to their different configurations, enantiomers can have different effects and chemical properties. For instance, limonene enantiomers give two different odours. The left-handed limonene gives the odour of lemon when the right-handed one gives the odour of orange. It is illustrated in figure 2 – 1.

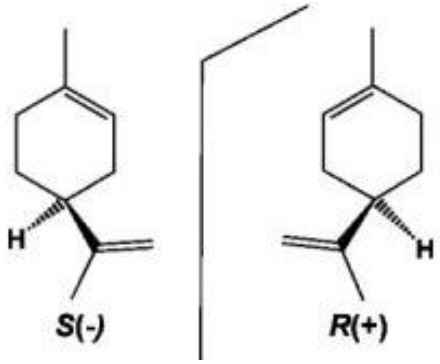

Figure 2 - 1: Illustration of chiral molecules. S(-) Limonene (left) gives a lemon odour, and R(+) limonene gives an orange odour.

The chirality of molecules can have significant repercussion on the synthesis of pharmacological compounds. Indeed, one handedness of a molecule can be a cure for a disease whereas the enantiomer has no effect or may be harmful. Thus, it is critical to be able to differentiate between the configurations of molecules. However, chiral molecules have the same physical properties (mass, boiling point, solubility, etc) making it difficult to distinguish them from each other[2]. Nonetheless, enantiomers have different optical properties and therefore can influence circularly polarised light differently. When left- and right-handed circularly polarised lights pass through a chiral medium with different velocities due to different refractive index[5], the phenomenon occurring is called optical rotatory dispersion (ORD). Depending on its handedness a molecule will absorb more of one handedness of light and less of the other, this phenomenon is called dichroism[5]. The effect of chiral molecules on polarised light can be related to their configuration. In fact, Cahn Ingold and Prelog defined a nomenclature for these molecules. They labelled the asymmetric centre rectus (R) or sinister (S)[1]. Each functional group next to the chiral centre is given a number according to its atomic number. The atom with the biggest atomic number will be numbered 1, the second biggest 2 etc in a decreasing manner. Following the numbers from 1 to 4 give the sense of rotation, clockwise R or anticlockwise S. They added the letter P (plus) or M (minus) to characterise the direction of the optical rotation[1]. This type of nomenclature is still currently used. The signs "+" and "-" are associated with the notation dextro rotatory and laevo rotatory. Indeed, in a coordinate system the negative numbers are placed on the left and the positive ones on the right, thus laevo rotatory is labelled "+" and dextro rotatory is labelled "-". This notation is used in the case of two non-equivalent chiral centres and along with D and L.

2.1.2 Chirality models:

To describe the chirality in a medium or a system (like chiral structures) simple chiral models were established. Charges in a medium can move when excited by an electromagnetic wave, the charge movements give rise to induced electric and magnetic dipoles. Thus,

optical rotation and circular dichroism arise from higher order interactions especially electric dipole-magnetic dipole interaction and electric dipole-electric quadrupole interaction[1,6]. However, in an isotropic media of chiral molecules the quadrupole contribution to optical rotation averages to zero; therefore in this section we focus on electric dipole-magnetic dipole contribution to optical activity[7] (section 2.2). The rotatory power R is the property of a medium to rotate the plane of polarisation of linearly polarised light that is transmitted through it[8]. The magnitude of ORD and CD effects are related to the rotatory power R[4]:

$$R = \mu.m, \quad (1)$$

where μ is the electric dipole transition moment and m is the magnetic dipole transition moment. As this is a scalar dot product, it follows that μ and m cannot be perpendicular, otherwise the scalar dot product is equal to 0, which would be the case if the molecule was achiral. Hence, for optical activity to arise μ and m must have parallel components[8].

This condition is fulfilled for two simple models: the coupled oscillator (known as the Born-Kuhn model) and the helical oscillator (known as the Kauzman model) models (figure 2 – 2)[7,9].

Kuhn designed the coupled oscillator model with two dipolar oscillators to describe chiral molecules[10,11]. This model consists of two separate oscillators inclined at an angle of θ and separated by a distance h[12] (figure 2 – 2). An oscillating dipole is induced in the upper oscillator by an incident wave[10,11] and is confined along the long axis. The upper oscillator is coupled with the lower one hence induces an oscillation of charges. An electric field can be associated with both upper and lower oscillators, the resultant electric field of system as the whole follows a helical path. The electric component of the first oscillator is parallel to the magnetic component of the second oscillator. Hence, the components of the rotatory power μ and m are parallel and optical activity arise[2].

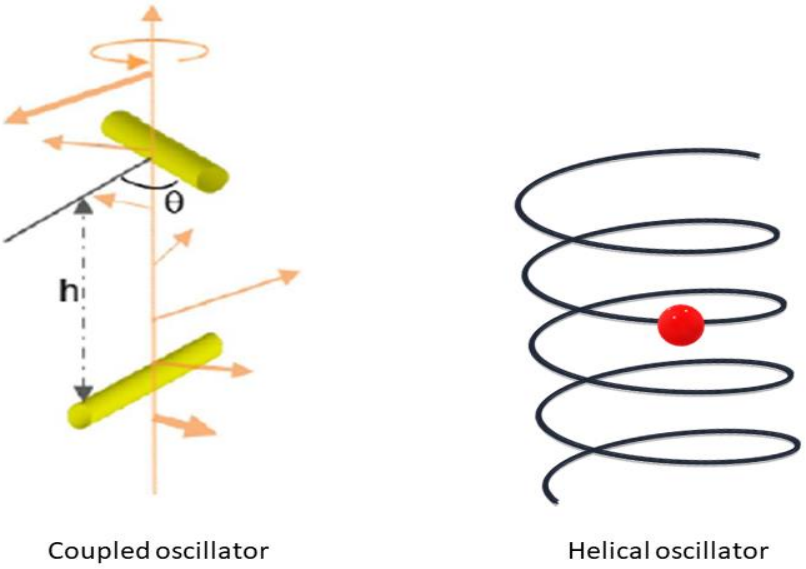

Figure 2 - 2: Figure adapted from refence[11]. Representation of the two oscillator models for chirality. In the coupled oscillator representation h is the distance between the two oscillators and θ is the rotation angle between the two oscillators.

The second model is called the helical oscillator or single helical oscillator (SHO)[8,13]. This model consists of an electron moving up and down a helix pattern[14](figure 2 – 2). This electron is bound to equilibrium via a spring. The vertical motion of the electron through its vertically helical path gives rise to the dipole moment and the rotatory motion induces the magnetic dipole moment. The helical path can be right or left (parallel or anti-parallel), so m is either positive or negative; therefore R changes signs as well. This results in the inversion seen between LH and RH spectra in CD and ORD.

These two types of chirality models quantify the level of chirality in a chiral system[9]. The helical oscillator model characterises systems with strong optical activity, while systems with weaker optical activity are characterised by the coupled oscillator model. The nanostructures used in this thesis exhibit a strong optical activity therefore the model applying to them is the helical oscillator model. We can reduce the optical activity of the structures, and thus be in the configuration of the coupled oscillator, by simply reducing the thickness of the gold metafilm coating them[9].

2.2 Optical activity:

Refractive index can be defined as the ratio of the speed of light in a medium to the speed of light in a vacuum. In a medium, the speed of light is slower and given by[2]:

$$v = \frac{c}{n}, \tag{2}$$

where n is the refractive index and c is the speed of the light in the vacuum. The refractive index characterises the behaviour of a light wave within a material. When light is incident

on a material, the atoms of the material interact with the electric field and the magnetic field of the light, causing interferences with the incident wave. Light matter interactions give rise to numerous phenomena: refraction, reflection and rotation of light[1]. These depend on the type of light and the properties of the material involved in the interaction. Any interaction involving polarisation dependence between the light and a material is known as optical activity. A material able to change the angle of optical rotation of right- or left-handed polarised light, is said to be optically active. Optical activity occurs in chiral media and can be described as the addition of two effects: optical rotation and optical rotatory dispersion[2]. Electronic optical activity enables the measurements of the circular dichroism and vibrational optical activity. This thesis investigates the optical activity occurring in the visible range of light, known as natural optical activity[1].

2.2.1 Polarisation:

The electric field of light oscillates perpendicularly to the direction of propagation[1]. For unpolarised light this direction is random and fluctuates. However, polarised light has an established direction of oscillation for its electric field. Polarised light can be circular, linear, or elliptic depending on the electric field direction of oscillation[1,2]. In this thesis we mainly use linearly polarised light. Linearly polarised light is defined as P or S according to the way it is reflected from a surface. The polarisation is said to be S-polarised if the electric field of the light is perpendicular to the incident plane. The magnetic field is thus parallel to the incident plane. The polarisation is said to be P-polarised when the electric field is parallel to the incident plane, the magnetic field being perpendicular (figure 2 - 3).

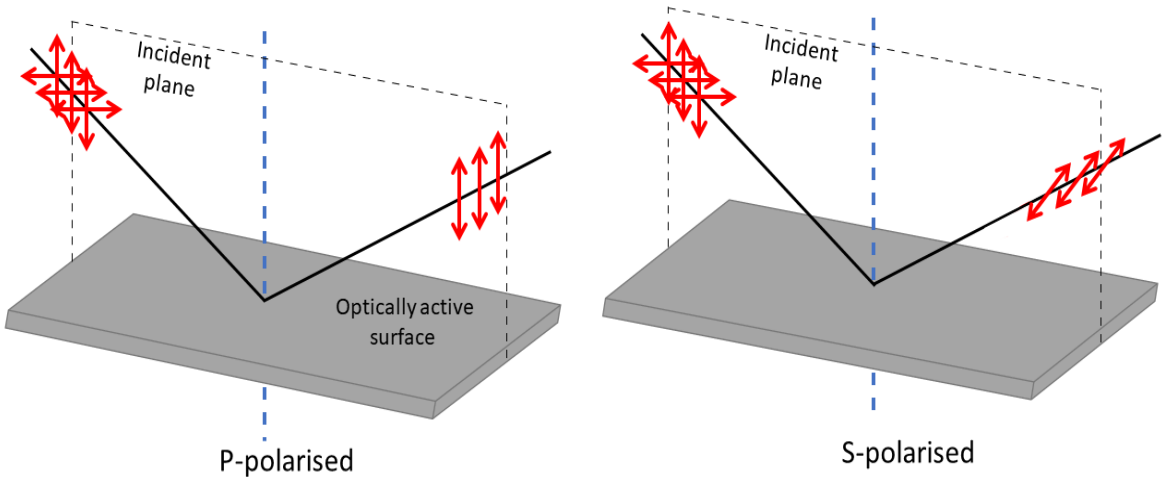

Figure 2 - 3: Representation of P- (left) and S-polarised (right) light reflecting on a surface.

2.2.2 Optical rotation:

Light is an electromagnetic wave and thus can be described through its electric field vector and its magnetic field vector[5]. Circularly polarised light can be left- or right-handed. The electric field vector movement defines the handedness of the light. For circularly polarised light, the time dependent electric field vector $\vec{e}$ onto a plane perpendicular to the direction of propagation z describes a helix. The direction of rotation of $\vec{e}$ describes the handedness of the light: clockwise is right-handed polarised light, anti-clockwise is left-handed polarised light (see figure 2 – 4)[1].

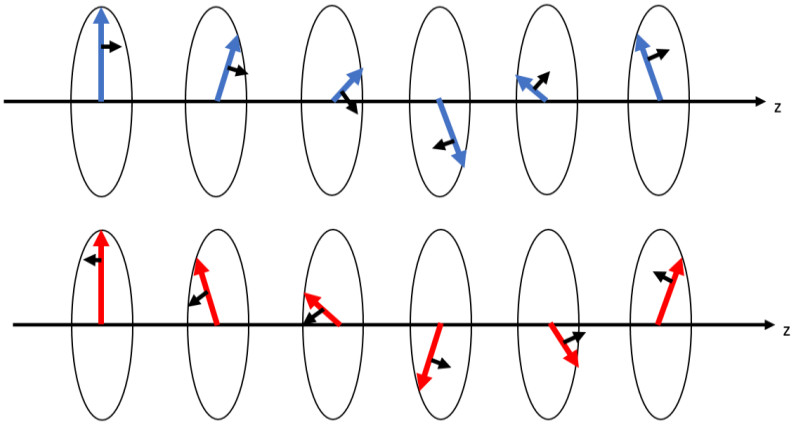

Figure 2 - 4: Scheme of the direction of propagation of the electric field vector along z. Top figure schematises the rotation of the electric field vector for RCPL and the bottom figure schematises the rotation of the electric field vector for LCPL. (Figure adapted from reference[1]).

Optical rotation occurs when there is a rotation of the plane of polarisation of a linearly polarised light beam going through a chiral material. Plane polarised light is couponed of equal amplitudes of right circularly polarised light (RCPL) and left circularly polarised light (LCPL)[1,5]. RCPL and LCPL propagate through a chiral material with unequal velocities resulting in a difference in the phase between RCPL and LCPL.

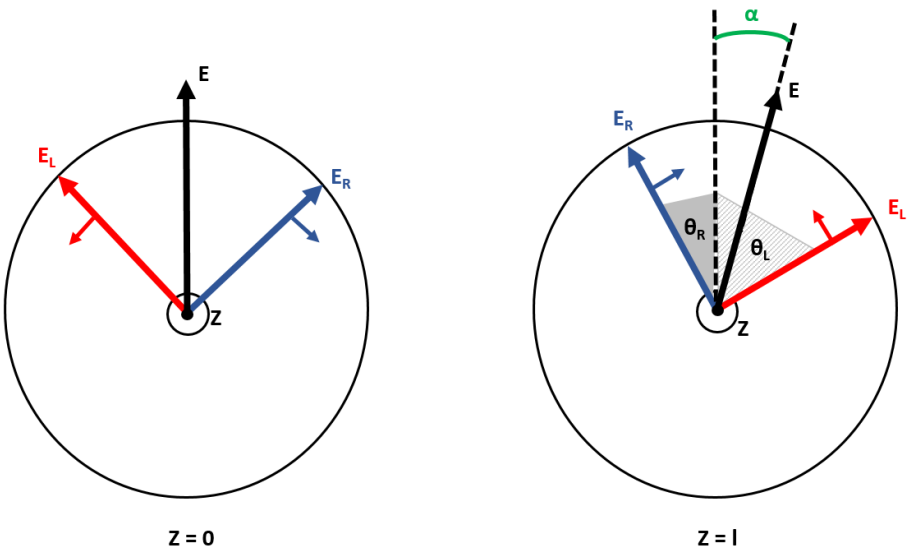

Figure 2 - 5: Scheme of the electric field vector of linearly polarised light, separated into right and left circularly polarised lights. The direction of propagation is along the Z axis which is out of the paper plane. The left figure shows the position of the electric field vector when the light has not propagated through the material. The right figure shows the position of the electric field vector at a further point along Z. (figure adapted from reference[1]).

When RCPL and LCPL recombine, the orientation of the plane of the polarised light is changed, resulting in the phenomenon of optical rotation. This change in the orientation of the plane polarisation can be characterised by the angle: α[1] (figure 2 – 5).

If a linearly polarised light beam with a frequency of ω = $^{2\pi c}/_{\lambda}$ propagates through an optically active material, at z (direction of propagation) = 0, and the electric field vectors of the RCPL and the LCPL are parallel at the same moment, at the point z = l the electric field vectors of RCPL and LCPL are rotated by an angle θ, relative to the original electric field vector. Respectively the angles for the right and left components are[1]:

$$\Theta^{R} = \frac{-2\pi cl}{v_r} \tag{3}$$

$$\Theta^{L} = \frac{2\pi cl,}{v_l} \tag{4}$$

with, v_l and v_r being the velocity of LCPL and RCPL in the material. RCPL and LCPL are then out of phase and this is expressed by the following equation:

$$\alpha = \frac{1}{2}(\Theta^{R} + \Theta^{L}) = \frac{\pi cl}{\lambda}\left(\frac{1}{v_l} + \frac{1}{v_r}\right), \tag{5}$$

where α is the angle of rotation in radian. From equation 5 we can simplify by c (equation 2) and introduce the refractive index in the equation[5]:

$$\alpha = \frac{\pi l}{\lambda}(n_l - n_r), \quad (6)$$

here n_l and n_r are the refractive indexes of LCPL and RCPL respectively.

2.2.3 Optical rotatory dispersion and circular dichroism:

The interaction of a natural light beam with a material is characterised by two coefficients: the refractive index as described above and the extinction coefficient[5]. The extinction coefficient Ɛ describes the damping of the oscillation amplitude of the wave i.e., how much incident light is absorbed as it passes through the material. RCPL and LCPL are absorbed differentially in an optically active medium. Since plane polarised light is a combination of RCPL and LCPL, linearly polarised light becomes elliptically polarised after absorption by an optically active medium[1]. Indeed, elliptically polarised light is the sum of right and left circularly polarised lights which now have different amplitudes due to differential absorption in the chiral medium. The ellipticity is given by[5]:

$$\text{Tan } \psi = \frac{(E_R - E_L)}{(E_R + E_L)}, \quad (7)$$

This is the ratio of minor and major axes of the ellipse: the difference and sum of the amplitudes of the circular components in perpendicular directions. Here E_R and E_L are the electric field vectors of the light. If at non-aborbing frequencies, the refractive index of a chiral medium is different for E_L and E_R then at absorbing frequencies the absorption of E_L and E_R will be different[1]. This is known as circular dichroism.

The refractive index n and the extinction coefficient x depend on the wavelength λ[5], these dependencies are shown in figure 2 - 6.

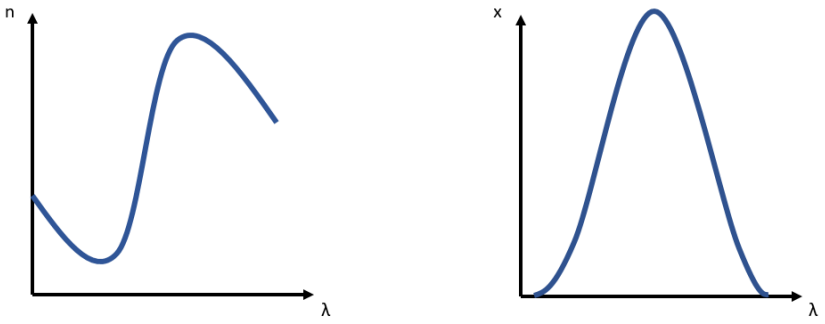

Figure 2 - 6: Variation of the refractive index (left) and the extinction coefficient (right) with the wavelength.

The refractive index and absorption coefficients also depend on the handedness of the light. Therefore, the interaction of light with a material can be characterised by four coefficients: n_L, n_R, x_L and x_R. Depending on the material, the rotatory power can have a minimum or a

maximum[5]. If $n_L < n_R$ when $\lambda < \lambda_{max}$ the substance is dextrogyre and the other way around would be levogyre[5].

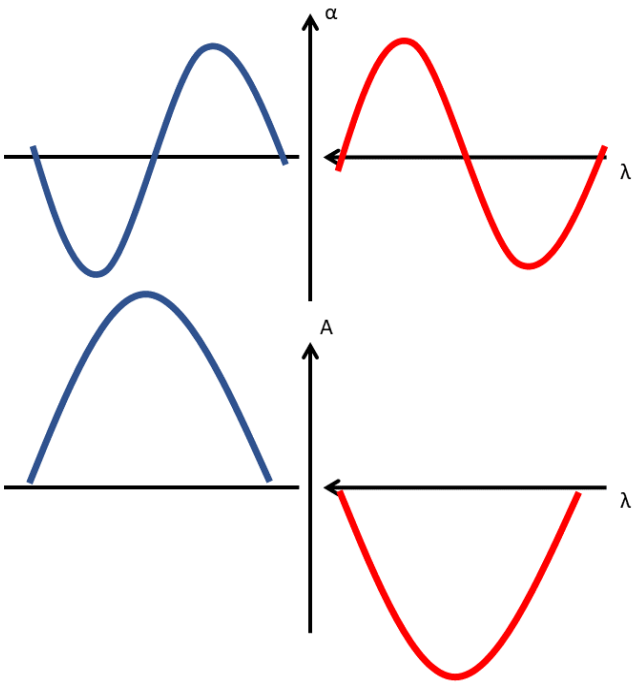

Figure 2 - 7: Scheme of ORD and CD absorption spectra from a dextrogyre (left picture) and a levogyre (right picture) chromophore. α is the rotatory power and A is the dichroic absorption.

Optical rotatory dispersion is the measurement of optical rotation as a function of wavelength and can be simply described as an unequal rotation of the plane of polarisation of light at different wavelengths. ORD and CD are closely related (figure 2 – 7) in the absorption region through a phenomenon known as the Cotton effect. The ORD displays a bisignate line shape with an inflection point at the ellipticity maximum whilst the ORD maxima and minima are at the CD minima (figure 2 - 8)[1]. The ORD and CD are further related by the complex dielectric function; ORD is characterised by the real part of the function and CD by the imaginary part.

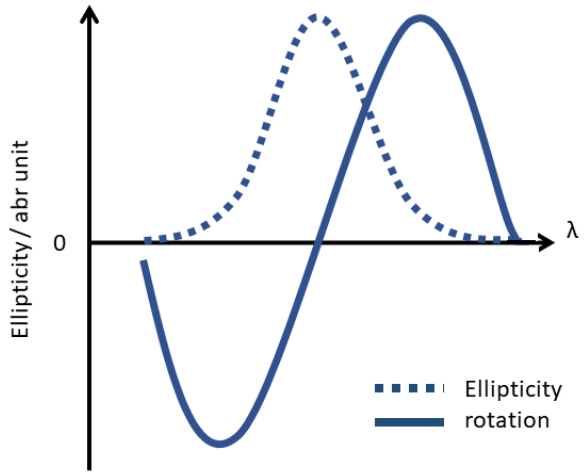

Figure 2 - 8: Scheme of an ellipticity versus an optical rotatory dispersion.

When a molecule interacts with light, the electrons within can be excited. This excited state is not stable, thus a molecule eventually relaxes back to its fundamental state and releases energy to the system, resulting in an effect that alters the velocity of light during light matter interactions. When the wavelength of the light matches the molecules frequency the electrons are promoted to a higher energy state for a length of time which is long enough for the energy of the system to dissipate into another process, this is called the loss[5]. The loss causes the intensity of the light beam to be reduced as it passes through the medium, leading to an absorption band on an optical spectrum. This also shows that there is a relation between absorption and diffusion. Kramers and Kronig have shown that given the absorption band, as a function of wavelength, the dispersion curve can be found. As the relationship is linear, this theorem allows the conversion between CD and ORD signals. The expression used is the following[1,5]:

$$[\varphi_k(\lambda)] = \frac{2}{\pi}\int_0^\infty [\theta_k(\lambda)]\frac{\lambda'}{\lambda^2-\lambda^2{}'}\,d\lambda' \tag{8}$$

$$[\theta_k(\lambda)] = -\frac{2}{\pi\lambda}\int_0^\infty [\phi_k(\lambda)]\frac{\lambda'}{\lambda^2-\lambda^2{}'}\,d\lambda', \tag{9}$$

respectively for the absorptive and the reflective modes. λ is the wavelength, φ_k is the real Kerr angle and θ_k is the complex Kerr angle.

2.2.4 Tensor of optical activity:

Optical activity can be described by the relation between an electric quadrupole and magnetic dipole[20–22]. These terms can describe the rotation of the polarisation plane of a linearly polarised propagating wave via the chirality tensor, detailed below. Electric oscillations that follow Drude's model must be the solutions to Maxwell equations.

Maxwell's equations are very important to the understanding of electromagnetic waves[17,18]:

$$\nabla \cdot D = \rho_{ext} \quad (10)$$

$$\nabla \cdot B = 0 \quad (11)$$

$$\nabla \times E = -\frac{\delta B}{\delta t} \quad (12)$$

$$\nabla \times H = J_{ext} + \frac{\partial D}{\partial t} \quad (13)$$

These equations connect the macroscopic fields (D the dielectric displacement, E the electric field, H the magnetic field and B the magnetic induction) with an external charge density ρ_{ext} and the current density J_{ext}. Nevertheless, these equations do not account for other phenomena happening in media, and how these phenomena (diffraction, refraction and scattering) affect the behaviour of electromagnetic waves[19]. Consequently, in order to supplement Maxwell equations, the so-called constitutive equations have been created[19]. The mathematical reason why further equations are needed is that there are a total of twelve scalars unknown for the four field vectors D, B, E, and H if all interactions between the electromagnetic wave and a media are accounted for. Equations 10 and 11 can be derived from equations 12 and 13 and thus are not independent. Six unknown scalars are given by equations 12 and 13. There are six more unknown scalars left, those are given by the constitutive equations[19]. We only display the constitutive equations relevant for this thesis. We can therefore express D and B as a function of E and H. For reasons of relativistic consideration[19], these relations are linear. For isotropic non-magnetic media the constitutive equations are[17,19]:

$$D = \varepsilon_0 \varepsilon_r E, \quad (14)$$

$$B = \mu_0 \mu_r H, \quad (15)$$

where ε_0 and μ_0 are respectively the electric permittivity and the magnetic permittivity of vacuum.

In this thesis we limit ourselves to linear nonmagnetic medium, but we need to account for the chirality of the medium. We adapted the constitutive equations in order to characterise the vector field of the system[21,23]. The simulation for a chiral dielectric (further explanation in 2.4.3) was realised using these equations for a chiral dielectric medium[24,25]:

$$D = \varepsilon_0 \varepsilon_r E + i\xi^T B, \quad (16)$$

$$H = \frac{B}{\mu_0 \mu_r} + i\xi^T E, \quad (17)$$

where ε_0 is the permittivity of free space, ε_r is the relative permittivity, μ_0 is the permeability of free space, μ_r is the relative permeability, E is the complex electric field, B is the complex magnetic flux density. H is the magnetic field; D is the electric displacement field. The chiral

property of the layer is described by the second rank tensor ξ, which is zero for an achiral medium, ξ^T is the transpose of ξ. ξ is a local parameter describing the chirality of a chiral dielectric[16] and is given by[22]:

$$\xi = \beta_c \left(\frac{1}{\hbar\omega + \hbar\omega_0 + i\Gamma_{12}} + \frac{1}{\hbar\omega - \hbar\omega_0 + i\Gamma_{12}}\right), \quad (18)$$

here β_c is an intrinsic coefficient that determines the magnitude of chiral properties. $\hbar\omega 0$ (where ħ is the reduced Planck's constant, h/2π, and ω0 is the absorption frequency) and Γ are the energy and intrinsic width of the resonant chiral excitation of the dielectric. ξ_{ij} (i,j = x, y and z) sign defines the handedness of the chiral dielectric, its value is wavelength dependent. It is the handedness of the chiral dielectric which sets the sign of the tensor elements[22,23].

The chirality tensor that describes the optical activity of an isotropic medium is:

$$\xi^{iso} = \begin{vmatrix} \xi_{xx}^{iso} & 0 & 0 \\ 0 & \xi_{yy}^{iso} & 0 \\ 0 & 0 & \xi_{zz}^{iso} \end{vmatrix}, \quad (19)$$

where $\xi^{iso}_{xx} = \xi^{iso}_{yy} = \xi^{iso}_{zz}$.

In order to model a layer of adsorbed biomolecules which are rotationally isotropic (the layer has a symmetry C_∞) and with a well-defined orientation, with respect to the surface, we need to simulate the effect of an anisotropic chiral dielectric layer. A layer is called isotropic when molecules have no specific orientation in respect to the surface. A layer is called anisotropic when molecules have a well defined orientation on the surface. There are significant differences between the chiral properties of anisotropic media and those of isotropic media affecting the chirality tensor ξ. For an anisotropic chiral medium with a C_∞ symmetry, Theron and Cloete[20] proposed the following chirality tensor ξ_{aniso} :

$$\xi^{aniso} = \begin{vmatrix} \xi_{xx}^{aniso} & \xi_{xy}^{aniso} & 0 \\ -\xi_{yx}^{aniso} & \xi_{yy}^{aniso} & 0 \\ 0 & 0 & \xi_{zz}^{aniso} \end{vmatrix} \quad (20)$$

The electric dipole-magnetic dipole contribution to the optical activity is accounted for by the diagonal elements. The diagonal elements are no longer equal with each other[22]: $\xi_{xx}^{aniso} = \xi_{yy}^{aniso} \ll \xi_{zz}^{aniso}$, explaining the signal in the z direction and the averaging out of the signal in the xy plane. The term ξ_{xy}^{aniso} account for the electric dipole-magnetic dipole contribution to optical activity which is not zero for anisotropic media. It is possible to relate the diagonal elements for the isotropic and anisotropic tensors by[22]:

$$\xi_{xx}^{iso} = \xi_{yy}^{iso} = \xi_{zz}^{iso} = \frac{1}{3}\left[2\xi_{xx}^{aniso} + \xi_{zz}^{aniso}\right] \quad (21)$$

Numerical simulation (chapter 4) of the constitutive equation supplementing Maxwell's equation were performed using COMSOL v4.4 Multiphysics software with the Wave Optics Module. Normally incident electromagnetic waves were applied to a port on the top surface and reflections were measured from there as well. Polarisation was defined in the port conditions for circularly polarised light and linear polarisations. Periodic boundary conditions were used on all four vertical boundaries to account for the periodicity of the nanostructures with perfectly matched layers behind the input and output ports, (top and bottom). Values of Au permittivity and refractive index of polycarbonate were taken from the literature[15,16].

2.2.5 Superchirality:

Chiral light matter interactions are relatively weak: for example, circular dichroism is a very small effect, typically amounting to a difference of only about 1 part in 10^3 or 10^4 between the extinction coefficients for light with left- or right-circular polarisation[26,27]. This can be explained by the mismatch between the helical pitch of circularly polarised light and the size of chiral molecules like proteins[17]. The helicity of circularly polarised waves depends upon the wavelength of the light, so that the circularly polarised fields rotate 360° over one wavelength, typically hundreds of nanometres in the visible region[28]. This length scale is much larger than the tens of nanometres over which molecular chirality is manifested, consequently the circularly polarised fields undergo a barely perceptible twist over the distance of molecular dimension.

Recently it was thought that enhanced dissymmetry could take place if the field lines were reoriented over a distance shorter than the wavelength, ideally very close to the molecule size. Electromagnetic fields that are far more contorted than circularly polarised light can be generated because of the development of near fields optic technologies: photonics, plasmonics, metamaterial[29]. The nanostructures have sub-wavelength cavities that allow the scale of molecular chirality and the scale of electromagnetic wave to match[30]. It is why interest in superchiral electromagnetic fields from surface plasmon has arisen from the observation of large chiral optical response of biomolecule in the presence of chiral metallic nanostructures. Studies have shown that the largest evanescent fields (defined in section 2.3.2) from localised surface plasmons (section 2.3.4) resonance can create superchiral fields from two- and three-dimensional chiral metallic nanostructures[27,29]. The chiral fields are a consequence of the evanescent nature of the localised surface plasmon resonances. Nearfields created by light scattering from chiral nanostructures can locally have a chiral asymmetry greater than circularly polarised light. In contrast to circularly polarised light, these local chiral fields do not undergo normal temporal rotation of the electric and magnetic vectors but oscillate out of phase[28].

Tang and Cohen[6,31] introduced a parameter called optical chirality in order to guide the design of superchiral fields. To describe the chirality of electromagnetic fields, a time-even pseudo scalar was introduced. Optical chirality is defined as the degree to which the electric vector and the magnetic vector (E and B) wrap around a helical axis as they propagate through space[32]. The equation which characterises the optical chirality C, of the electromagnetic field is[27,31]:

$$C \equiv \frac{\varepsilon_0}{2} E \cdot \nabla \times E + \frac{1}{2\mu_0} B \cdot \nabla \times B, \quad (22)$$

where ε_0 is the permittivity of the free space, μ_0 is the permeability of the free space, and E and B are respectively the electric and the magnetic fields. The first part of the equation describes the twist in the electric field and the second part describes the twist in the magnetic field. The twist is greater than CD. Values of C are normalised to circularly polarised light where C=+1 corresponds to LH circularly polarised light and C=−1 is RH circularly polarised light[6]. For monochromatic polarised light, in CD standard theory, the dissymmetry (which characterises the enantioselectivity of the light) factor is[33]:

$$g_{CPL} \equiv \frac{2(A^+ - A^-)}{(A^+ + A^-)}, \quad (23)$$

where $A^{\pm}$ is the absorption of the left CPL (A^+) and right CPL (A^-). g is also proportional to the ratio C/U_e (where $U_e = \frac{\epsilon_0}{4}|E|^2$ is the time-average electric energy density) for RH and LH CPL because the polarised lights only differ by the sign of their optical activity. Tang and Cohen generalised the CD theory to include a pair of arbitrary mirror image fields, and showed that the dissymmetry factor becomes[33]:

$$g = g_{CPL}\left(\frac{cC}{2\omega U_e}\right), \quad (24)$$

with g_{CPL} the dissymmetry factor of the circularly polarised light, c the speed of the light, U_e the local energy density, ω the angular frequency. Equation 24 shows that the magnitude of g depends on the optical chirality of the incident light and not only on the chirality properties of the matter, unlike in standard theory of CD. The electromagnetic fields that have a value of C>1, relative to CPL are called superchiral[30]. Indeed, in CPL the field vectors undergo a complete revolution at a constant rate once per wavelength. Therefore, the quantity ($cC / 2\omega U_e$) equals to 1. In order to increase the dissymmetry factor, the optical chirality C must increase and the value of $cC / 2\omega U_e$ will be greater than 1 in some regions of space. Thus, these fields have a greater helicity than CPL.

Tang and Cohen managed to generate these fields with a standing wave. They showed the presence of superchiral fields at the nodes of the standing wave. Using essentially chiral

plasmonic nanostructures with electromagnetic waves is a simpler way to get superchiral fields with higher level of chirality[11] in the near field region of the nanostructures. Indeed, superchiral fields arise from the coupling between the incident light and the evanescent fields of the surface plasmons[27] (section 2.3.2). Plasmonic nanostructures produce an enhancement of the optical activity. The differences in the effective refractive indices of chiral samples exposed to left- and right-handed superchiral fields are found to be up to 10^6 times greater than that those observed in optical polarimetry measurements, thus allowing picogram quantities of adsorbed molecules to be characterised[27].

2.3 Fundamental of plasmonics:

2.3.1 Plasmon oscillations:

Plasmon oscillations occur in metallic thin films. In a metal, at equilibrium, there is the same amount of positive charges (ions) and negative charges (electrons) at all points of the metal, thus the total charge in the metal is zero. The electrons in the metal can be moved by electromagnetic fields resulting in an oscillation by going back to their equilibrium[34]. The electrons which oscillate are the free electrons of the metal, which can be considered as a gas of electrons, called plasma of electrons[17,18]. When an electromagnetic field is applied to a metal the free electron gas is displaced, from the equilibrium, by a distance x (figure 2 – 9)[18]. This displacement creates an excess of positive charges on one side and an excess of negative charges on the other side, producing a charge density. In response to this, the positive ionic core induces a force that is pulling the electrons back to their original position. The electrons have acquired momentum and will keep moving to the other direction. Hence the electrons are oscillating between the two sides.

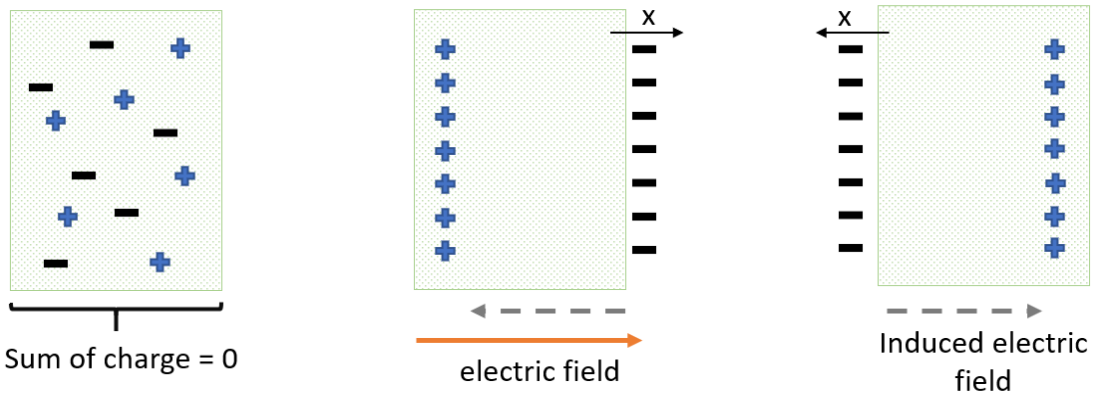

Figure 2 - 9: Picture of the movement of the charge in a metal under electromagnetic excitation.

Due to the acquired momentum of the electrons the phenomenon keeps repeating in varying directions, creating oscillations. The frequency of the oscillation can be modified by changing the metal (silver, gold, platinum), the thickness of the metal, or by introducing defects or structures in the metal. The electric field along x is given by[35]:

$$E = \frac{nex}{\epsilon_0}, \tag{25}$$

where n is the electron density, e the electronic charge, x the electron displacement, and ε_0 the permittivity of the metal.

According to equation (25), the force F experienced by the electrons is[36]:

$$ma = F = -eE = -e\frac{enx}{\epsilon_0}, \tag{26}$$

a being the acceleration of the electron and using Newtons law (F = ma). Thus, the electron displacement satisfies the differential equation[36]:

$$\frac{d^2x}{dt^2} = a = -\frac{e^2nx}{m\epsilon_0} \tag{27}$$

The oscillation of electron gas is known as plasma oscillation with the corresponding plasma frequency of ω_p.

$$\frac{d^2x}{dt^2} = -\omega_p^2 x \tag{28}$$

Therefore:

$$\omega_p = \sqrt{\frac{ne^2}{\epsilon_0 m}}, \tag{29}$$

where m is the mass of an electron. This equation applies only for plasmon generated in bulk metal.

2.3.2 Surface plasmon polariton:

It is possible to generate plasmonic excitation at the interface of a metal thin film, excited by an electromagnetic wave. This excitation gives rise to a surface plasmon polariton (SPP)[37]. A surface plasmon polariton is an electromagnetic excitation that propagates along a metal-dielectric interface[27]. It is a strong coupling between an electromagnetic wave and an electrically polarised wave. This phenomenon is similar to the one occurring in bulk metal[38]. The light propagates at the surface of the metal, excites the free electrons, which induces an electric field[17] (figure 2 – 10). The amplitude of the wave decreases as they propagate away from the surface. Thus, this field is called “evanescent” because the amplitude of the field exponentially decays perpendicularly to the surface[39] (figure 2 – 10). The high sensitivity of SPPs to surface conditions is due to their confinement to the interface

creating electromagnetic field enhancement[40]. This enhancement of the electromagnetic field leads to optical phenomenon enhancements such as Raman scattering and second harmonic generation.

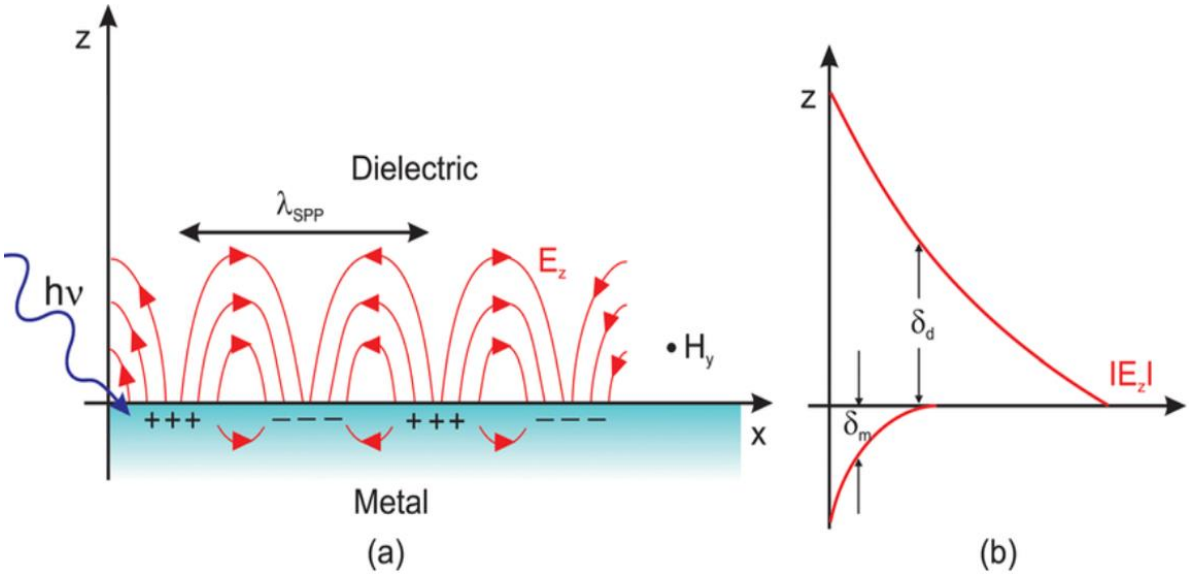

Figure 2 - 10: Figure taken from reference[41]. (a) shows the effect on charges between a metal and a dielectric when excited by an electromagnetic wave. (b) shows the decay of the electric field as it propagates away from the surface.

The solutions of Maxwell's equations in each medium (metal and dielectric), associated with the boundary conditions, characterise the electromagnetic field of a surface plasmon polariton. The continuity of the electric field and the magnetic field across the surface, along with the reduction of these fields in the z direction, are expressed by the boundary conditions[42]. According to these boundary conditions, at z = 0, the tangential components of E and H are continuous, meaning: $E_{xd} = E_{xm}$ and $H_{xd} = H_{xm}$., with E being the electric field and H the magnetic field strength. The dispersion relation connecting the wavenumber k to the dielectric function of the metal and the dielectric for p-polarised wave is[41]:

$$\frac{k_{zd}}{k_{zm}} = \frac{\varepsilon_d}{\varepsilon_m}, \tag{30}$$

where k_{zd} and k_{zm} are the z-components of wave vectors of the dielectric and the metal respectively and, ε_d and ε_m the dielectric functions of the dielectric and the metal. To generate an electromagnetic wave between a dielectric and a metal surface k_d and k_m must be real and positive. Additionally, ε_m must be in the opposite sign for the surface wave to exist and to satisfy Maxell's equation boundary conditions. This equation illustrates the excitation of the electronic cloud by a photon[40,43].

We also know that:

$$k^2_{zd} = k^2_x - \varepsilon_d k_0^2 \quad (31)$$

$$k^2_{zm} = k^2_x - \varepsilon_m k_0^2, \quad (32)$$

with k_0 being the wave vector of the photon in free space.

From equation 32 we get the SPP dispersion relation:

$$k_{SPP} = k_0 \sqrt{\frac{\varepsilon_d \varepsilon_m}{\varepsilon_d + \varepsilon_m}} \quad (33)$$

For the plasmonic excitation to occur, ε_m must be large and negative and ε_d small and positive. These conditions are met in the visible frequency range. Indeed, at these frequencies, for metal-air and metal-liquid ε_m is large and negative (the imaginary part of the constant is dominant in visible wavelength, thus ε_m is negative).

At the same frequency, the momentum of the SPP is larger than that of the incident light (figure 2 – 11). This leads to a mismatch of momentum between the SPP and the light. This means that the SPP cannot be directly excited by light. However, the SPP can be excited by a momentum transfer[38].

The bulk plasmon frequency in the metal can be related to the SPP by the following equation[17]:

$$\omega_{SPP} = \frac{\omega_p}{\sqrt{2}} \quad (34)$$

This means that SPP can be excited at a shorter wavelength (visible) than in the bulk plasmon.

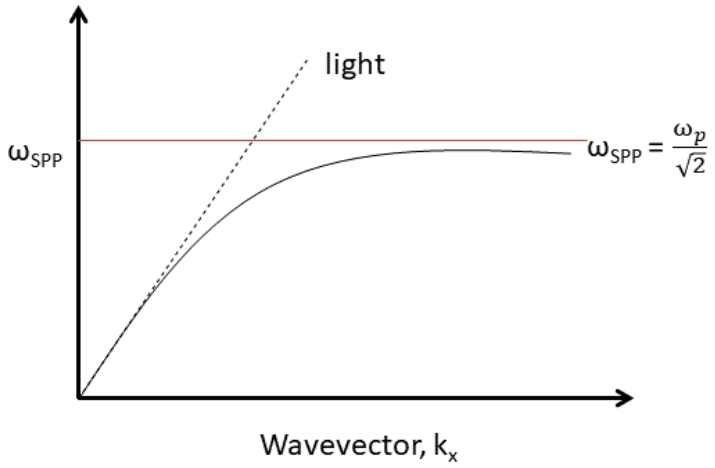

Figure 2 - 11: Graph of the SPP dispersion curve compared to the one of the light in vacuum. At any given frequency the wavevector of SPP is higher than the light one.

2.3.3 Plasmon excitations:

In order to excite SPPs we must fulfil both energy and momentum conservation. Plasmons can be excited on a planar metal surface through a dielectric medium if the frequency of the p-polarised incident light is equal to the frequency of the SPP. Another requirement is that the direction of the propagation of the light must be parallel to the surface[17]. However, we can see from figure 2 – 11 that the SPP wavenumber is larger than the one of the light in the dielectric medium adjacent to the metal. Because of this momentum mismatch, the incident light cannot couple to the SPP. Experimental set up was created in order to reduce the momentum of the incident light and thus allow frequency matched coupling to take place. Two methods involving prisms are widely commented in literature[44,45]. The first one is called the Kretschmann configuration[46], it involves attenuated total reflection (ATR). The second method is named the Otto configuration and comprises diffraction effects[40] (figure 2 – 12). In the Kretschamnn configuration, a prism with a refractive index higher than that of the dielectric is used atop a thin metal film. The incident light will be reflected in a denser environment, leading to an increase in the wavenumber. Under the resonance conditions (wave vector of the light and SPP have a matching frequency), the SPP and the light coupled efficiency are almost 100%[18]. Unfortunately, this configuration cannot be used with thick or bulk metal. The layer of metal must be extremely thin to allow the propagation of the light. For thicker metal, SPP can be excited using the Otto configuration. The resonance conditions are similar than the one in the Kretschamnn configuration. In both cases evanescent fields are generated[17,18].

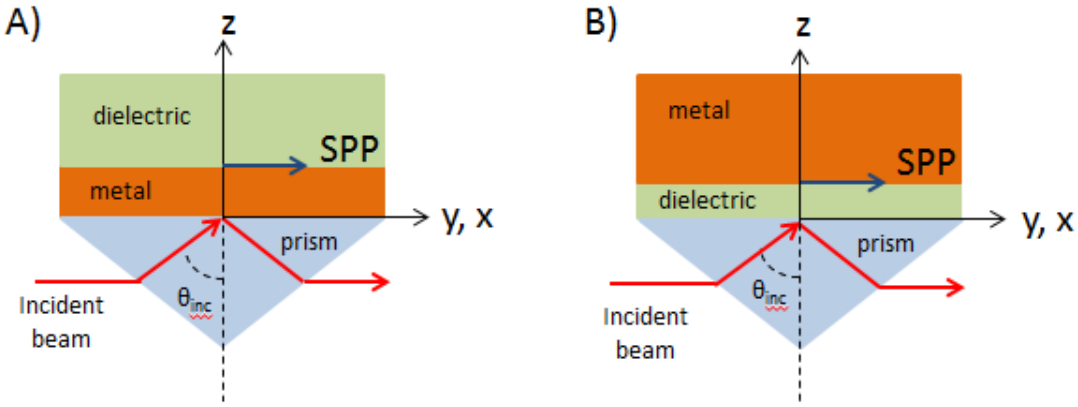

Figure 2 – 12: Scheme of the set up used to excite SPP. A) is the Kretschmann configuration and B) is the Otto configuration.

SPP excitation can also be achieved by patterning the surface of the metal with holes of a constant lattice. This method is known as the "grating excitation"[41] and is used in this thesis to generate plasmon excitations. The creation of a grating on the surface by the structures can induce light scattering that leads to a decrease in the SPP momentum. Consequently,

there is no more mismatch between the light and the SPP frequency and coupling can take place.

For this thesis we generated the surface plasmon with plasmonic nanostructures. In nanostructures the local electromagnetic fields are confined in a sub-wavelength volume[47]. Because the fields cannot propagate anymore there is no need for the momentum to match[48]. The excitation and the field enhancement are obtained with light reflection. These nanostructures work in a similar way to antennas.

The optical resonance generated by the excitation of nanostructures by an electromagnetic wave, can be tuned by changing the periodicity and the symmetry of the nanostructures. The incident light is scattered by the nanostructures producing evanescent waves which interfere and propagate away from the surface. This phenomenon, called plasmonic induced transparency, makes the light to slow down and is discussed further in this chapter (section 2.4.2). The overlapping of the two surface plasmon modes is possible if the metal film is thin enough, because the two modes become then resonant[35].

2.3.4 Localised surface plasmon resonance:

In contrast to SPP, which propagate waves between a dielectric and a metal, localised surface plasmon resonances (LSPR) are non-propagating waves[47,49]. Indeed, the plasma is contained at the surface of nanostructures[50]. In fact, these properties solve the matching momentum condition issue, as the surface plasmon (SP) no longer propagates[18]. Moreover, this phenomenon consists of the excitation of the conduction electrons of the metal by an electromagnetic field. The excitation of the surface plasmon occurs in the same way as for the bulk metal. An EM field is applied to the nanostructure, moving the free electrons within the structure in one direction. When returning to their equilibrium position, the electrons oscillate, creating the plasma oscillation (figure 2 – 13). LSPR is often observed in silver and gold nanoparticles with a size of 10 nm to 200 nm[51]. It results in an enhancement of fields around the surface of the nanoparticles where field intensity can be between 10-10,000 times greater than the intensity of the incident field. LSPR gives resonance in the visible and near infrared regions. Spherical structures are widely studied because they give simple optical spectra; more complex structures can exhibit complex spectra with several resonances. By varying the shapes and sizes of nanostructures, “hot spots” (localised spots with enhanced electromagnetic fields) can be created, the surrounding fields of these “hot spots” allow us to control resonance[42].

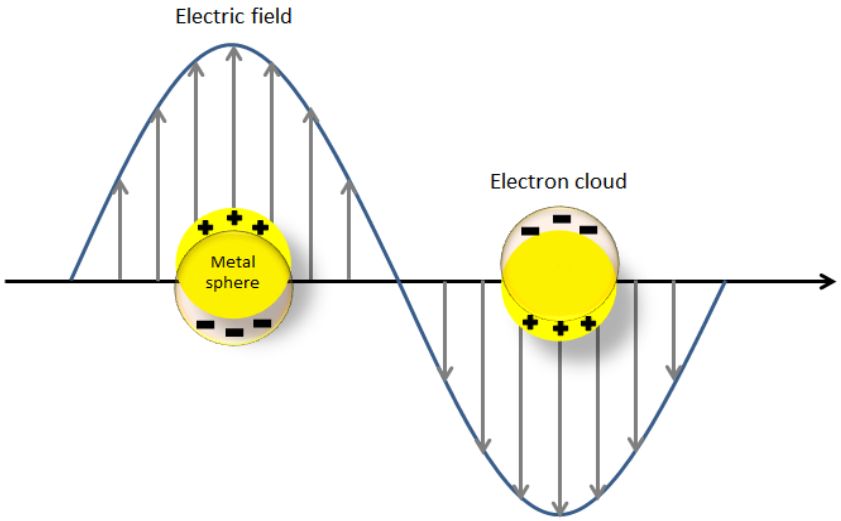

Figure 2 – 13: Effect of localised surface plasmon resonance on gold nano-particles.

2.3.5 Refractive index dependence and field decay:

We recall here that for SPP to occur, ε_m and ε_d must be of opposite signs. Because LSPR is a similar process we must apply a similar condition. When ε_m is approximately equal to $-2\varepsilon_d$ the electromagnetic field is enhanced, relative to the incidence field[52]. This condition is satisfied in the visible region of an optical spectrum. The position of the LSPR excitation depends on the dielectric constant of the metal and thus the refractive index (ε_m depends on the refractive index as $\varepsilon = n^2$)[53]. The change of the surrounding environment, including that of the analyte, will cause a shift in position of LSPR (shift in the wavelength λ_{max} towards the infra-red). This shift is characterised by the following equation[27,52]:

$$\lambda_{max} = m\Delta n \left[1 - e^{\frac{-2d}{l_d}}\right], \qquad (35)$$

Where m is the refractive index of the bulk metal, Δn is the change in the refractive index caused by the analyte, d is the thickness of the analyte and l_d is the EM field decay length (the decay in the field is assumed to be perpendicular to the surface)[54]. However, this equation is oversimplified, and although it explains the behaviour of the EM field, it cannot characterise the effect of shape and size of the particles on λ_{max}. Equation 35 shows the refractive index sensing is better with LSPR than with SPP. Indeed, the decay length of the evanescent field is longer for SPP than for LSPR (200nm and 0.1nm respectively, for gold metal[17]), meaning that SPP is strongly depending on the refractive index of the analyte bulk solution. In the case of LSPR, because the decay length is much smaller, the dependence of the refractive index is more affected by molecules that adhere directly onto the surface. The decay in the fields is measured in refractive index unit (RIU)[55] and depends on the metal, the metal thickness and on the wavelength at which it is measured[56].

2.3.6 Plasmonic hybridisation:

From the interface between metal and dielectric rise specific optical modes known as "plasmonic" modes[17,18]. Plasmonic modes are a combination of surface plasmons with a SPP (photon field)[36]. They arise from the coupling between charge oscillations and the electromagnetic fields at the metal surface. The resonance of these optical modes depends on the nature of the interface[57]. Metamaterials consist of periodic arrays of nanostructure indentations[24]. If the inter-particle separation is small enough (typically, the size of the decay of the electric field) to allow significant overlap of plasmonic modes, the strong near-field interaction leads to hybridisation of individual particle plasmon modes to form a new set of coupled modes delocalised over the entire structure. This coupling drastically alters the optical properties of the metamaterial. Consequently, the optical properties of metamaterials can be tuned by changing the size, the geometry and the depth of the nanostructures[9] (this alters the LSPR) or the type of metal used ((gold, silver, etc…) this alters the SPP).

Three types of plasmonics coupling are widely discussed in the literature: solid-solid, inverse-inverse and solid-inverse[58]. It has been shown that the interactions taking place in all three systems can be intuitively understood in terms of strong coupling between dipole (or quadrupole) plasmonic modes[59]. The coupling in plasmonic nanostructures can be explained with an analogy to an orbital molecular diagram[57]. Park applied the analogy to a coupled-dipole nanoantenna system composed of two nanorods aligned end-to-end and separated by a small gap[60]. In this plasmonic dimer system the single particle plasmon modes couple with each other via Coulomb interactions. In this system, the oscillating entity is the free electron charge in the metal[60]. When the charge density in the two particles oscillates in phase along the axis of the dimer, it generates a symmetric mode with strong electric field in the gap. When the two oscillations are 180° out of phase, it generates an anti-symmetric mode whose small electric field can be almost negligible (figure 2 – 14).

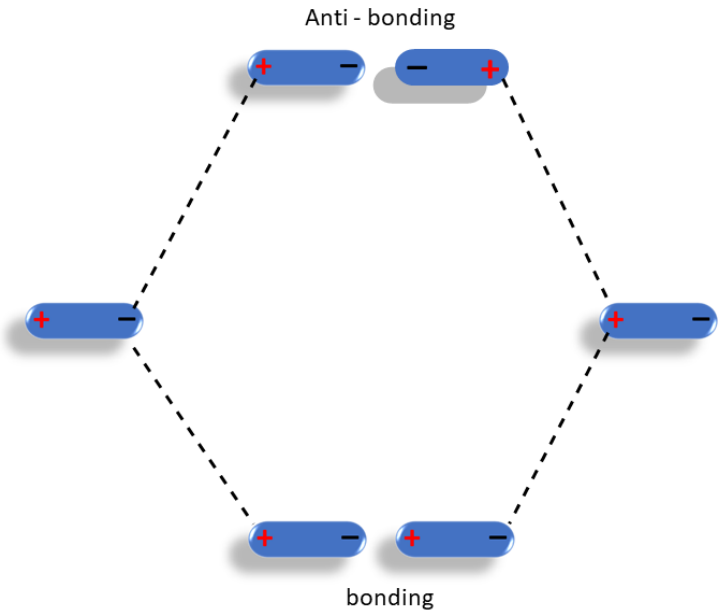

Figure 2 - 14: Hybridisation scheme adapted from reference[60] representing coupling between dipoles of two nanorods aligned end-to-end and separated by a small gap. Bottom level has the lower energy and is the "symmetric" mode. Top level is the higher in energy and is the "anti-symmetric" mode.

Considering the molecular analogy, the symmetric mode corresponds to the bonding orbital (of low energy) whereas the anti-symmetric mode is the anti-bonding orbital (of high energy)[60]. There are two hybrid plasmons generated: the symmetric (in phase) hybrid plasmon which possesses a large dipole moment and interacts strongly with light; the anti-symmetric (out of phase) hybrid plasmon (excited at higher energy) with a small net dipole moment caused by the nanodimers being aligned anti-parallel. Therefore, this mode does not interact with light and is often "invisible" in experiments and simulations, but it can interact with the symmetric mode to produce Fano resonances as described later[60]. For these reasons, the symmetric mode is often referred to as the bright mode and the anti-symmetric mode as the dark mode.

This hybridisation model allows the explanation of resonances in complex nanostructures and is applied to our own system in the next paragraph.

2.3.7 Hybrid plasmonic nanostructures:

The nanostructures used in this study are known as "hybrid" plasmonic nanostructure[9,17,60] (or solid-inverse structures) and are displayed in figure 2 - 15. The metamaterial structures we designed consist of a solid shuriken shaped nanostructure and a cavity of identical shape above it. The shuriken has 6 arms and a circle shaped core[9]. Further technical details about the nanostructures (diameter, depth, etc…) are given in chapter 3. Solid and inverse structures are respectively associated with an electric (bright) and magnetic (dark) mode[60].

We applied the molecular analogy detailed in paragraph 2.3.6 to our system and thus can say that the bright mode is generated from the solid structure because it has a large dipole moment and interacts strongly with light (symmetric mode)[60,57]. Additionally, the dark mode arises from the cavity inside the shuriken structures. It is referred to as the dark because it has a small dipole moment and cannot be excited directly by incident light (anti-symmetric mode)[9,60]. Since these modes overlap, it is possible for them to couple via a coulomb interaction. In the literature it was showed that depending on the polarisation of light a shift toward the infra-red is proof of strong plasmonic coupling between the nanostructures and the nanostructure cavity and a blue shift is proof of a weaker coupling[56,60].

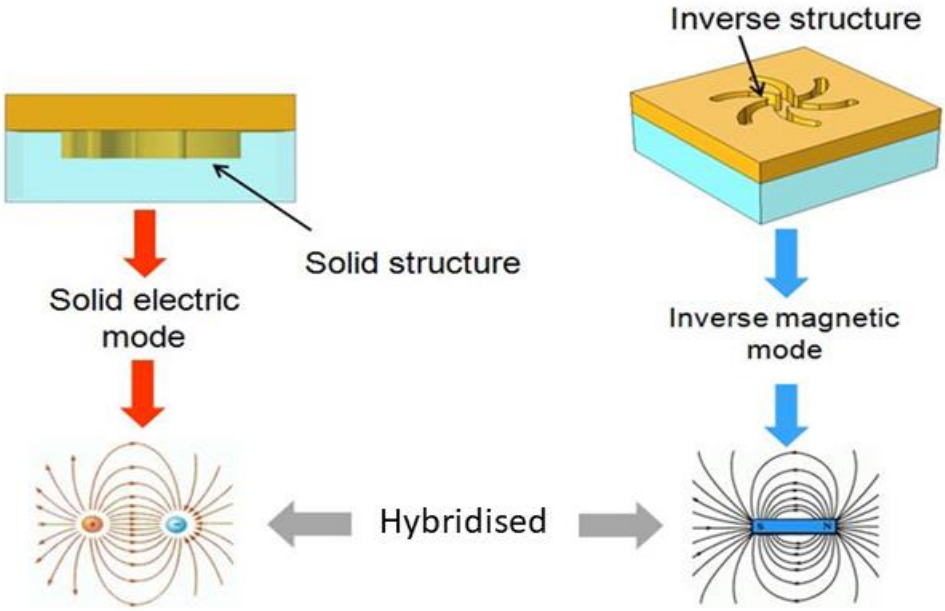

Figure 2 - 15: Scheme of a shuriken nanostructure. On the left is a representation of the solid structure associated with the solid electric mode (bright mode). On the right is a representation of the shuriken cavity, the inverse structure associated with the inverse magnetic mode (dark mode).

The shurikens used in this thesis are chiral, so they can only belong to C_n, D_n, O, T or I[1,9]. As a shuriken has 6 arms and a circle shaped core thus it belongs to the C_6 group (symmetry elements being the rotation around the z axis, figure 2 – 16)[9]. The irreducible representations associated with these modes are A, B, E_1, E_2. According to the C_6 character table, A and E_1 are the bright modes (they have dipolar functions), but A exists only in the z direction and accordingly cannot exist for our experimental set up because we have a normal incidence[9] (polarisation in the xy plane). The quadratic mode characterises the dark mode and thus is E_2.

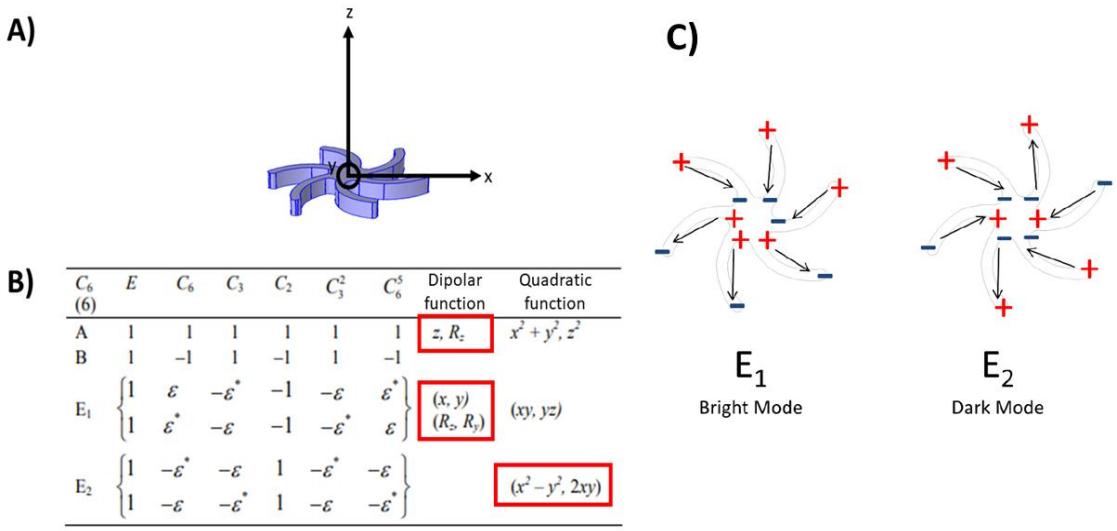

C_6 (6)	E	C_6	C_3	C_2	C_3^2	C_6^5	Dipolar function	Quadratic function
A	1	1	1	1	1	1	z, R_z	x^2+y^2, z^2
B	1	−1	1	−1	1	−1		
E_1	$\begin{Bmatrix}1 & \varepsilon & -\varepsilon^* & -1 & -\varepsilon & \varepsilon^* \\ 1 & \varepsilon^* & -\varepsilon & -1 & -\varepsilon^* & \varepsilon\end{Bmatrix}$						(x, y) (R_x, R_y)	(xy, yz)
E_2	$\begin{Bmatrix}1 & -\varepsilon^* & -\varepsilon & 1 & -\varepsilon^* & -\varepsilon \\ 1 & -\varepsilon & -\varepsilon^* & 1 & -\varepsilon & -\varepsilon^*\end{Bmatrix}$							$(x^2-y^2, 2xy)$

Figure 2 – 16: A) Representation of the shape of the shuriken nanostructure with the symmetry axis. B) C_6 character table. C) Representation of the bright and dark modes.

With this information we are able to produce the diagram in figure 2 – 17. The coupling between electric and magnetic modes is also influenced by any medium on the surface. The shape of a molecule, its space orientation and even its surface charges, can influence the coupling and affect the optical response of the nanostructures.

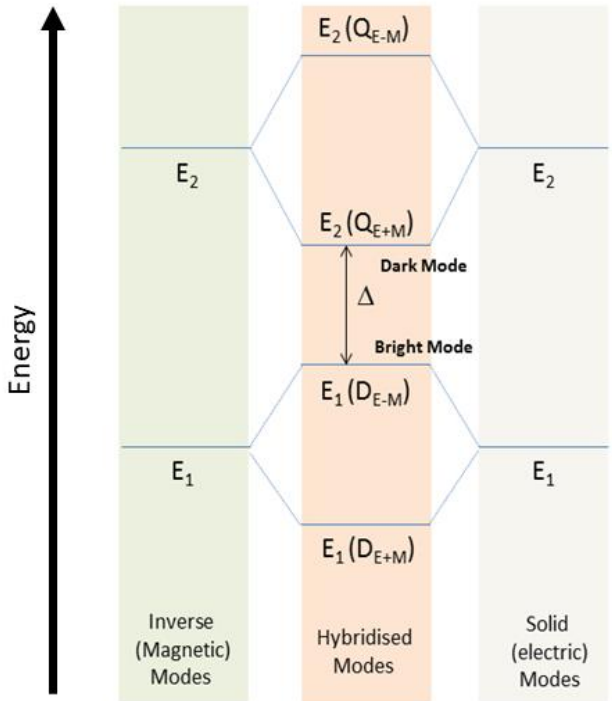

Figure 2 - 17: Analogy of an orbital molecular diagram describing the coupling between bright and dark modes in the hybrid plasmonic nanostructure. Δ Is the separation in energy between the two modes.

Our nanostructures are called “hybrid” because of the coupling between the solid and inverse modes which gives rise to hybrid modes: in and out of phase modes[57,60] (i.e, symmetric and anti-symmetric modes, paragraph 2.3.6); the mode with the lowest energy being the one in phase, and the mode with the highest energy being the one out of phase. In figure 2 – 17 the modes associated with the electric dipole are labelled D_{E+M} and D_{E-M}, and the modes associated with the quadrupole are Q_{E+M} and Q_{E-M}.

We can control the coupling between the bright and dark modes by changing the energy gap Δ, which can be changed by varying the thickness of the gold layer of our substrates[9]. This gives tuneable nanostructures, for example a strong coupling creates the plasmonic analogue of electron induced transparency (EIT). The control we manage to obtain over the coupling between dark and bright modes can be illustrated with electromagnetic modelling of the electric and magnetic fields[9] (figure 2 – 18). Figure 2 – 18 shows the distribution of electric and magnetic fields for substrates of two different thicknesses: 30 nm and 100 nm. For the substrate coated with 30 nm gold (thinner layer than normally used) we see different spatial distributions of electric and magnetic fields on the solid (bottom surface) and cavity (top surface) structures. Overlap between electric and magnetic fields of the top and bottom surfaces are not maximised, thus the coupling between the bright and dark modes is not optimal.

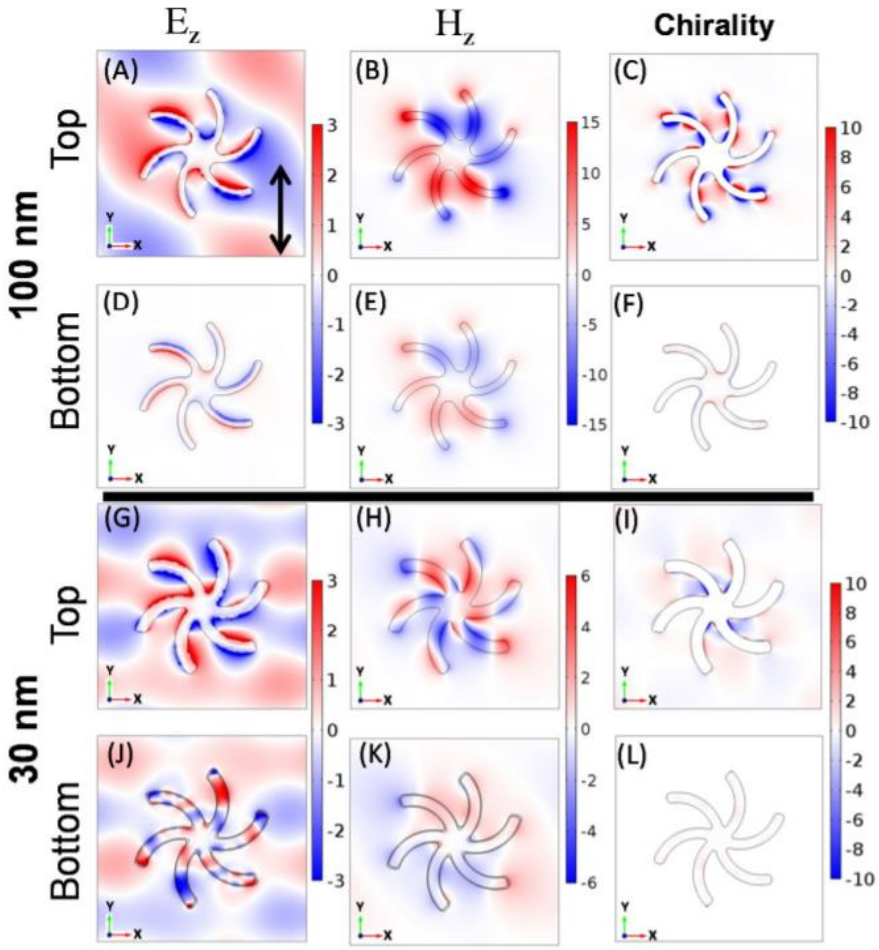

Figure 2 – 18: figure taken from reference[9]. The first two columns show plots for the z-components of the E (in MV/m) and H (1x10-4 A/m) fields and the third column shows the chirality, normalised to values of circularly polarised light. 100 nm plots are at a wavelength of 694 nm which is the first peak in ORD for the simulations, and for the 30 nm they are at a wavelength of 680 nm which is at the peak in the ORD for the 30 nm simulation. First two rows show plots for the 100 nm gold-coated substrate, (A-C) Top surface of the inverse structure (D-E) bottom surface (that is the surface of the solid structure). Bottom two rows show the plots for the 30 nm gold-coated substrate (G-I) top surface and (J-L) the bottom surface. The colour range is limited to create comparable scales for all the plots. The black arrowed line in (A) shows the polarisation of incident light.

In the case of a substrate coated with 100 nm gold (thickness used in all experiments) we see that the electric fields associated with top and bottom surfaces have matching spatial distributions, but are out of phase; while magnetic fields have identical distributions and are in phase indicative of optimal coupling. It is this latest configuration which gives rise to

interference phenomena such as plasmonic induced transparency or Fano resonances (detailed in 2.4).

2.4 Interferences:

Interferences in plasmonic systems are the results of the coupling between the bright and dark modes[60]. Depending on the strength of this coupling we can observe two interference phenomena: Fano resonances and plasmon-induced transparency. These interference effects are often explained by using an analogy involving two weakly coupled harmonic oscillators driven by an external force[61] (figure 2 – 19).

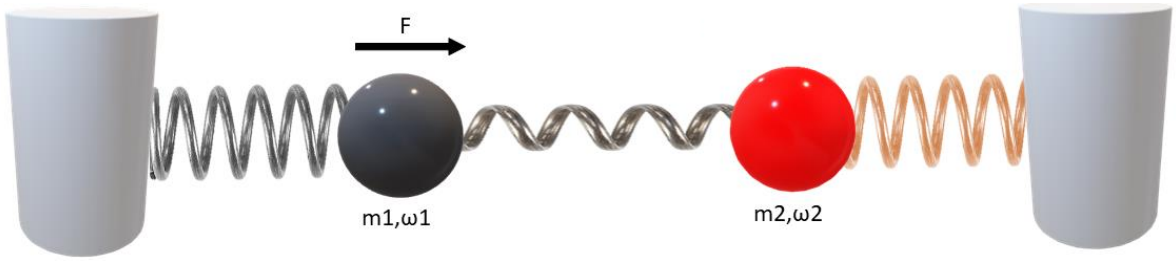

Figure 2 - 19: Representation of a couple oscillator. The black oscillator (m_1) generates the bright mode and the red oscillator (m_2) generates the dark mode.

An external force is applied on this harmonic oscillator system (this would correspond, in plasmonic spectroscopy, to the dipole excitation with an electromagnetic wave)[62]. This external force F is applied to one of the oscillators which has a mass m_1 and thus begins to oscillate at the frequency ω_1. The oscillator m_1 moves at a given frequency and causes the second oscillator to oscillate through the spring. When the first and the second oscillators resonate at the same frequency (or when the frequencies overlap), the oscillations of m_1 couple with the second oscillator of mass m_2 and induce an oscillation frequency of ω_2. The second oscillator is not driven by the external force but only by the oscillation of m_1. In this analogy, m_1 generates the “in phase” mode and m_2 the “out of phase” mode, which correspond in plasmonic spectroscopy, as explained in section 2.3.6, to the bright and dark modes respectively[62]. Due to the strength of the second oscillation of m_2 at its frequency ω_2, two driving forces are then applied onto the first resonator. The two forces are out of phase and interfere destructively and thus cancel each other out[62]. It is these interference effects that take place in plasmonic systems.

2.4.1 Fano resonance:

The most common interference phenomenon taking place within plasmonic nanostructures is the Fano resonance. The Fano resonance was first described by Ugo Fano, in a quantum system, as a coupling between a discrete mode and a continuous mode[63]. This phenomenon can be described by a threefold effect. For frequencies far from the resonant frequency the background scattering process (continuum) dominates. As the system

approaches the resonant frequency, the background scattering amplitude varies slowly with energy while the resonant scattering amplitude displays important changes in both phase and amplitude. At the resonant frequency, this phase change results in destructive and constructive interference phenomena between the discrete and continuum states over an extremely narrow spectral range. It materialises by an optical signal having an asymmetric line shape instead of a Lorentzian displayed in figure 2 - 20. In plasmonic spectroscopy, the continuous mode rises from the background (surface wave) and the discrete mode comes from the hotspot (localised mode), or in other words, a strong bright mode and a weak dark mode[62,64,65](localised). For interferences to occur these modes must be of overlapping frequency spectra[66], conditions satisfied in plasmonic material as broad and narrow resonances occur for all eigenmodes of structures and spectrally overlap[67].The bright mode is excited by the incident electromagnetic wave unlike the dark mode that cannot be directly excited. However, this dark mode can be indirectly excited by the near field arising from the bright mode[61]. The field generated by the dark mode will interfere with the bright mode field. This interference can either enhance or diminish the signal, this is controlled by the phase of each field[68].

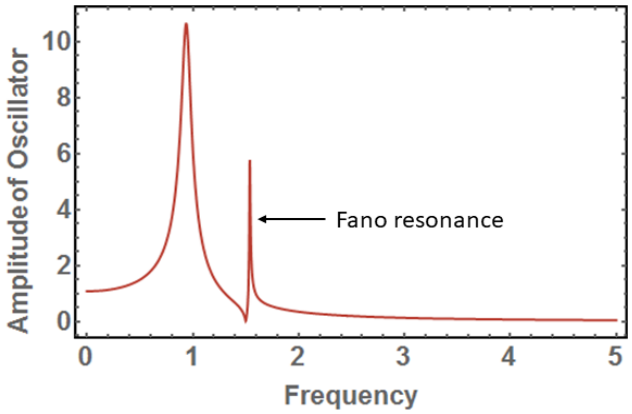

Figure 2 - 20: Graph of a Fano resonance line shape from the interferences of the two optic modes.

2.4.2 Plasmonic induced transparency:

A phenomenon similar to the Fano resonance is plasmonic induced transparency[69]. This phenomenon is a plasmonic analogue to electromagnetically induced transparency (EIT) and is called plasmonic induced transparency (PIT)[70,71].

A) Electromagnetically induced transparency :

Electromagnetically induced transparency is a quantum phenomenon occurring in atomic systems and is the result of a destructive interference between two excitation pathways, which controls the optical response, in the electronic level[72]. The characteristic of EIT is to

produce a narrow transparency window within an absorption peak (figure 2 – 21) because both absorption and reflection phenomena are eliminated at the resonant frequency of a transition, creating the "transparency"[73,74]. The EIT phenomenon can be explained with a three-level system[72] (figure 2 – 21). In this system, for EIT to occur two dipole transitions must be allowed and the other one forbidden. The system is irradiated with a probe and couple beams with frequencies of ω_p and ω_c respectively. If the system is irradiated only by the probe beam it results a typical absorption spectrum around the probe beam frequency due to the electronic transition from state $|1\rangle \rightarrow |3\rangle$. But if the system is irradiated by a couple beam as well, a transparency window arises. Because of the simultaneous irradiations, two excitation pathways become then available: from $|1\rangle \rightarrow |3\rangle$ and from $|2\rangle \rightarrow |3\rangle$[71]. The two pathways interfere with each other in a destructive manner. According to quantum mechanics, in the case of two possible pathways, interference between their probability amplitudes will occur. The two terms are proportional to the probability amplitude of the ground state and state two (but of opposite phases). Thus, over a narrow range of the spectrum, due to the opposite phases the probability amplitudes cancel out.

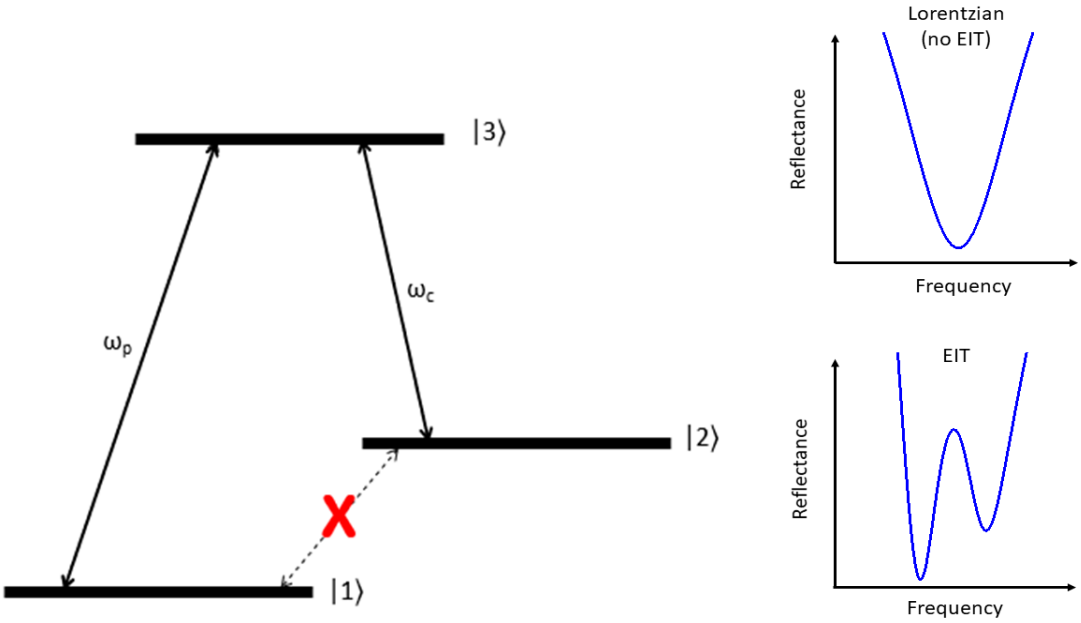

Figure 2 - 21: Energy level diagram for EIT in a three-level atomic diagram.

B) Plasmonic electromagnetically induced transparency :

The plasmonic analogue of EIT is called plasmonic induced transparency (PIT)[71]. PIT involves coupling between two distinct resonators in a unit cell of a metamaterial, the coupling between two states is not happening with a pump beam but is the result of destructive interferences between two resonators[70]. One resonator is highly radiative possessing a broader resonance feature and is called bright resonator, whereas the other

resonator is a sub-radiant dark resonator since it has a much sharper resonance linewidth[75]. For PIT to occur there must be a coherent coupling between the bright and dark mode resonators with similar resonant amplitude. The dark mode of a plasmonic system is analogous to the metastable level |2⟩ in the atomic system. Excitation of the dark mode only occurs through a near-field interaction between adjacent structures[21]. The two different pathways (to make the analogy with EIT in atomic system) are a direct excitation of the bright mode (|1⟩→|3⟩) and the excitation of the dark mode through the bright mode coupling back to the bright mode (|1⟩→|3⟩ |2⟩→|3⟩)[71]. Therefore, when the bright and dark modes couple, destructive interferences occur and lead to a transparency window in the absorption spectra. The strength of the PIT depends on the strength of the coupling of the bright and dark modes and their spatial overlap[75]. Consequently, the PIT spectra can be modified and tuned by varying the coupling strength of the bright and dark modes. This can be accomplished by altering the design of plasmonic nanostructures.

2.4.3 Modelling of PIT for plasmonic nanostructures:

In this thesis we will be modelling the PIT effect occurring in the nanostructure using a mathematical model. We considered that all nanostructures of the substrate (chapter 3) are getting excited by the incident light. The coupled oscillator model for plasmon induced transparency first proposed by Zhang et al[75] and subsequently used in work by Tassin et al[75] provides the basis of the model. The system is described by the following equations[9,21]:

$$\omega_{\mathrm{r}}^{-2}\ddot{p}(\mathrm{t}) + \gamma_{\mathrm{r}}\omega_{\mathrm{r}}^{-1}\dot{p}(\mathrm{t}) + \mathrm{p}(\mathrm{t}) = \mathrm{gf}(\mathrm{t}) + \tilde{\kappa}\mathrm{q}(\mathrm{t}) \tag{36}$$

$$\omega_{\mathrm{d}}^{-2}\ddot{q}(\mathrm{t}) + \gamma_{\mathrm{d}}\omega_{\mathrm{d}}^{-1}\dot{q}(\mathrm{t}) + \mathrm{q}(\mathrm{t}) = -\tilde{\kappa}p(t) \tag{37}$$

Here the radiative (bright) resonator is described by the excitation *p(t)* with a resonance frequency ω_{r} and damping factor γ_{r}. Similarly, the dark mode excitation is described by *q(t)* with a resonance frequency ω_{d} and damping factor γ_{d}. The two resonators are coupled via a complex coupling constant $\tilde{\kappa}$. The bright mode is driven by an external force f(t) and g is a constant indicating the coupling strength between the oscillator and the external force. Two terms are introduced in the solutions, $e^{-i\theta}$ and $e^{-i\phi}$, these terms account for any retardation phase shifts that occur in the bright and dark mode excitations, θ and ϕ respectively.

The equations 36 and 37 are solved by assuming the following to be the solutions[9]:

$$p(t) = e^{-i\theta}P(\omega)\mathrm{e}^{-\mathrm{i}(\omega\mathrm{t})} \tag{38}$$

$$q(t) = e^{-i\varphi}Q(\omega)\mathrm{e}^{-\mathrm{i}(\omega\mathrm{t})} \tag{39}$$

where P is the displacement of the bright mode in the frequency domain and Q is the dark mode displacement in the frequency domain. Since the coupling depends on the phase difference between the two oscillators, we consider that $\tilde{\kappa} = \kappa e^{-i(\theta-\phi)}$. Inserting solutions 38 and 39 in 36 and 37 gives the following relations:

$$P(\omega)e^{-i\theta} = \frac{gF(\omega)-\tilde{\kappa}Q(\omega)e^{-i\phi}}{D_r} \tag{40}$$

$$Q(\omega)e^{-i\theta} = \frac{-\tilde{\kappa}P(\omega)e^{-i\phi}}{D_d} \tag{41}$$

Where $D_d = 1 - \left(\frac{\omega}{\omega_d}\right)^2 - i\gamma_d \frac{\omega}{\omega_d}$ and $D_r = 1 - \left(\frac{\omega}{\omega_r}\right)^2 - i\gamma_r \frac{\omega}{\omega_r}$.

Using equation 40 in equation 41 gives:

$$P(\omega) = \frac{g\,\mathrm{D_d}(\omega)F(\omega)}{e^{-i\theta}\left(D_r(\omega)D_d(\omega)-\kappa^2 e^{-2i(\theta-\phi)}\right)} \tag{42}$$

Equation 42 can provide the gold susceptibility using the relationship:

$$\chi(\omega) = \frac{P(\omega)}{E(\omega)} \tag{43}$$

Where $E(\omega) = F(\omega)$.

Hence

$$\chi(\omega) = \frac{gD_d(\omega)}{e^{-i\theta}\left(D_r(\omega)D_d(\omega)-\kappa^2 e^{-2i(\theta-\phi)}\right)} \tag{44}$$

Since our plasmonic system is based on a metallic thin film and not a transparent substrate[9], we need to cater for this through an effective medium approach and take an average of the susceptibility from the gold film and the plasmonic system.

$$\chi_{Avg}(\omega) = \frac{\chi(\omega)+\chi_{Au}}{2}, \tag{45}$$

Here χ_{Au} is the susceptibility of gold (Au). As the refractive index is the square root of the permittivity, the refractive index can then be found using:

$$n_{EIT} = \sqrt{\chi_{Avg}(\omega)+1}\,, \tag{46}$$

Reflectivity is given by:

$$Reflectivity = \left|\left(\frac{n_{Sol}-n_{EIT}}{n_{Sol}+n_{EIT}}\right)^2\right| \tag{47}$$

Here n_{Sol} is the refractive index of the solution.

In order to apply the mathematical model to our experimental data, a script was written in MatLab (Matworks R2016b). This model enables the generation of a theoretical reflectance spectrum. An experimental reflectivity spectrum was imported in MatLab and plotted on top of the model generated by the script. Table 2 - 1 shows the definitions of the parameters used in the MATLAB implementation of the model. The parameters were set up in a way that allows us to change them. The parameters were changed so that the model would match the experimental data[21].

parameters	units	Definition	Initial
ω_r	nm	Bright (radiative) mode resonance frequency	731.3 ± 0.2
ω_d	nm	Dark mode resonance frequency	724.4 ± 0.2
κ	No unit	Coupling coefficient	0.0282 ± 0.0002
Υ_r	No unit	Bright (radiative) mode damping	0.0379 ± 0.0002
Υ_d	No unit	Dark mode damping	0.0192 ± 0.0002
θ	Degree / °	Bright (radiative) mode phase	- 8.0 ± 0.1
ϕ	Degree / °	Dark mode phase	- 8.0 ± 0.1
n_e	No unit	Refractive index of solution	1.33 ± 0.01
g	No unit	Incident light coupling coefficient	0.061 ± 0.003
c_{gold}	No unit	Multiplier for gold contribution to susceptibility	0.316 ± 0.003

Table 2 - 1: Table of parameters and their descriptions, used to implement the plasmon induced transparency model. The third column of the table shows the initial values used in Figure 2 - 22 which shows effects of varying individual parameters.

We develop an understanding of the model parameters by making small variations and evaluating the changes in reflectance. This allows for an intuitive approach to understanding the changes seen in experimental results and improving our matching. Figure 2 - 22 shows the resulting effect on the calculated reflectance by varying individual parameters, varied by an amount like those seen in our experimental results, from their initial values (Table 2 - 1) in the plasmon induced transparency model. Changes in ω_r show a shift for the entire envelope of the reflectance whereas changes in ω_d move the increased reflectance peak in the middle. Both these changes also vary the heights of the peaks as the resonance positions of the bright and dark modes change relative to one another. Changes in κ affects the overall strength of the PIT effects, it also increases the splitting of the two dips in reflectance. Increasing bright mode damping Υ_r causes the overall plasmon extinction to decrease and increasing the dark mode damping Υ_d reduces the effect of the plasmon induced transparency, reducing the middle reflectance peak and height of the dips on either

side. Changes in θ and Φ cause the ratio of the height in the side dips to vary without any significant resonance shifts. Increasing g has an almost similar effect to increasing Υ_r but in the opposite direction. By increasing the plasmonic extinction and making the overall envelope deeper, we represent increased coupling and strength of the plasmonic excitation to the incident light. Increasing c_g increases the reflectance due to plain gold thereby shifting the entire reflectance, including the background, higher without any significant change in the shape of the resonance features. The refractive index of the surrounding environment (n_e) has no significant changes over the kind of expected experimental values.

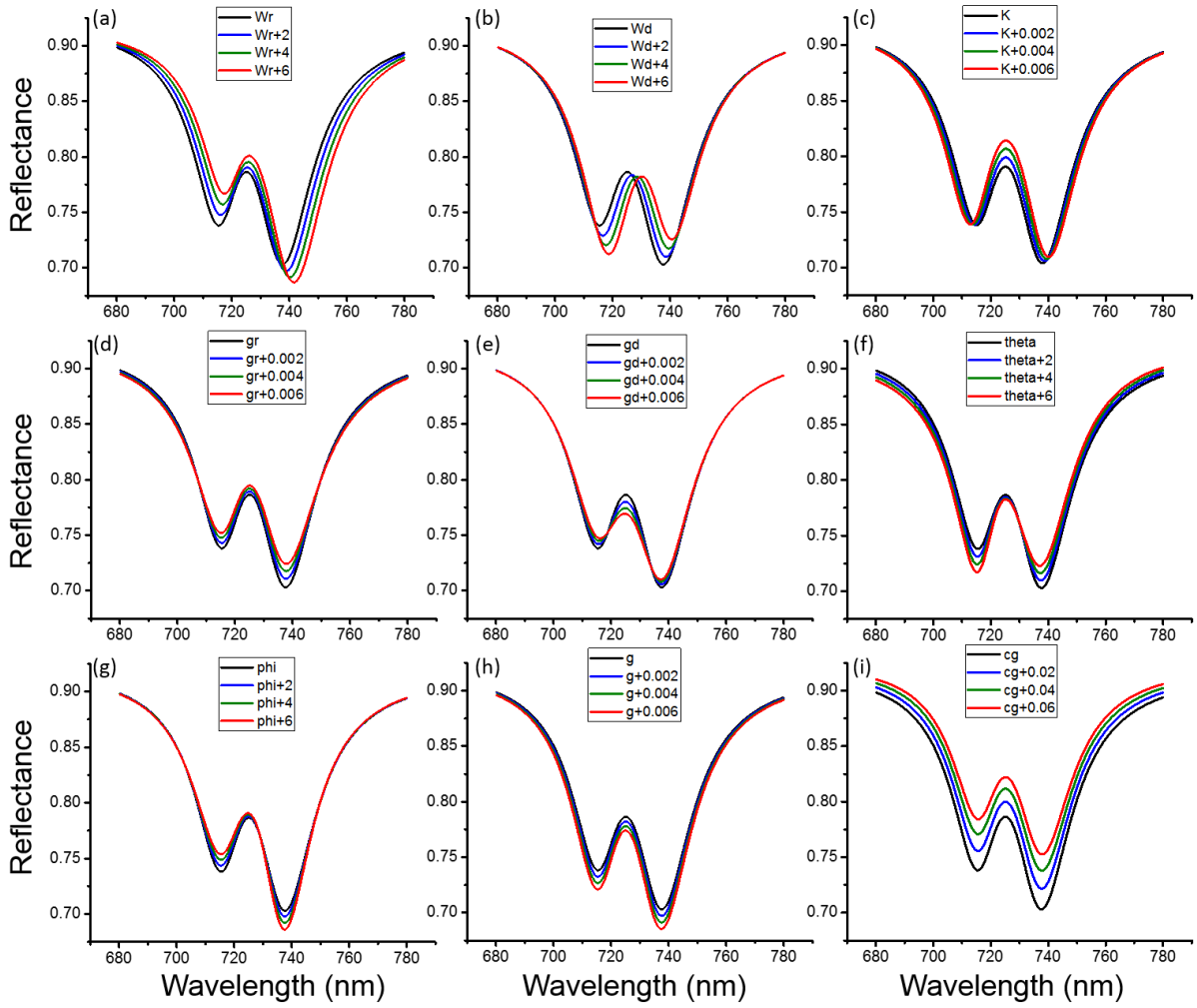

Figure 2 - 22: Reflectance spectra obtained by systematically changing individual parameters. Reflectance plots shown for (a) ω_r, (b) ω_d, (c) κ, (d) Υ_r, (e) Υ_d, (f) θ, (g) Φ, (h) g and (i) c_g.

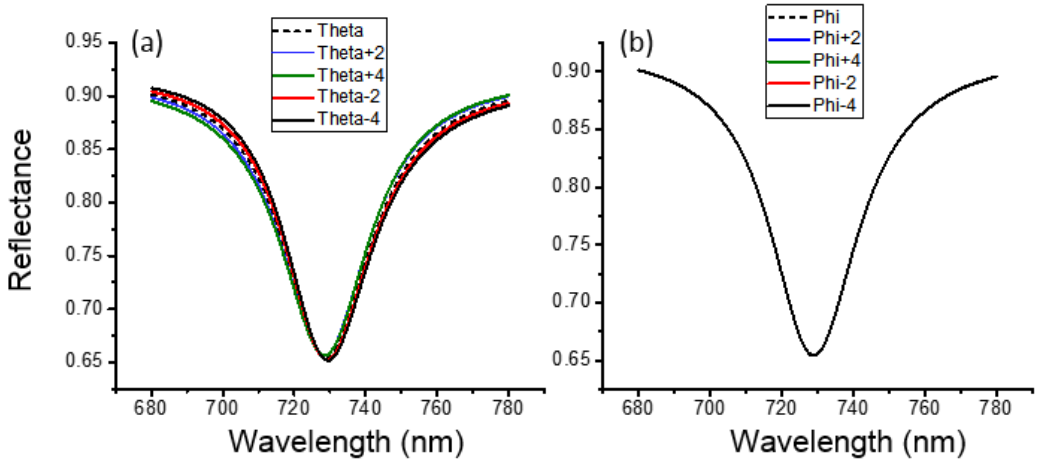

Figure 2 - 23: Reflectivity plot with κ=0 for varying (a) Theta and (b) Phi.

PIT is critical to the measurement, since it allows phase changes to be determined[21]. Consequently, in a system which does not display PIT (i.e. with κ=0), for instance one which exhibits a Fano like resonance, the ϕ term has no meaning and the θ parameter cannot be unambiguously determined. Without the presence of coupling (κ=0) between the bright and dark modes, the model shows no characteristics of an asymmetric line shape. Figure 2 - 23 shows a single peak representing the bright mode only. θ which is the phase difference between the bright mode and the excitation changes the shape of the reflectivity. Figure 2 – 23 (a) shows changes that within experimental error can be considered as a shift in ω_r, which equates to a change in the refractive index. Due to the absence of coupling the φ value has no effect on the reflectivity, Figure 2 – 23 (b). Hence without any coupling, the measurements of the phase differences as achieved by a coupled oscillator mechanism would not be possible.

2.5 Biosensing:

This thesis focuses on the biosensing technique used with our structures. In this section we give a brief review of biosensing and explain where the chirality of the building block of life comes from. Most of the molecules from the building block of life are naturally homochiral[76] (only one of the enantiomers exists) as is the case for amino acids (naturally L) or sugars (naturally D). A biosensor is a device (chip, nanoparticles, metamaterial) which can detect physico-chemical changes[77]. When light or an electromagnetic wave interacts with a periodic pattern of nanostructures, and when certain conditions are satisfied, interferences are created at specific wavelengths. These interferences can be constructive or destructive and affect the signals in absorption and transmission.

Proteins are made of amino acids connected with peptide bonds. Proteins are defined by their amino acid sequences and their structures. Four structure levels exist for proteins,

each one of them exhibits different types of chirality. These structures are called: primary, secondary, tertiary, and quaternary (in this thesis tertiary and quaternary are often referred to as “higher order structures”).

The primary structure is the sequence of amino acids that compose the protein, with peptide bonding. The peptide bond is the bond between the carboxyl acid and the amino group of two amino acids. There is a known nomenclature for naming the sequence of amino acids: beginning with the first amine, called N-term, and ending with the last carboxylic acid, called C-term.

The secondary structure describes the protein folding. A protein can exhibit alpha helices, beta sheets, beta turns and omega loops (figure 2 – 24). These structures are formed due to hydrogen bonds between amino acids. An α-helix is a helical structure; these are chiral because they are orientated clockwise and are therefore dextrogyre. This kind of fold gives more energetic stability to the protein.

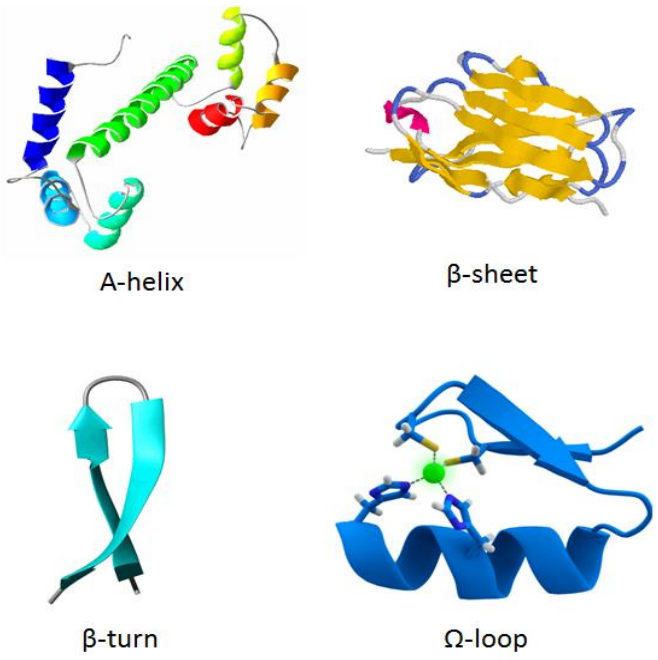

Figure 2 - 24: Cartoons of the different types of fold a protein can exhibit in its secondary structure.

Another secondary structure is the β-sheet. These are periodic structures. They are not flat as they fold alternatively on the top and on the bottom of the sheet. This also occurs due to hydrogen bonding, but unlike the α-helixes the hydrogen bonds are in between amino acids which are further away from each other. These sheets can be parallel or anti-parallel. If two strands have the same orientation, then they are parallel; if one strand is flipped around, then the two strands have opposite orientations and they are anti-parallel. The chirality here arises from the twist in the β-sheets.

The β-turn is a fold that occurs most of the time between two other secondary structures (α-helix and β-sheets). The Ω-loop is quite similar and could be a specific kind of β-turn involving more amino acids and with an omega shape. The chirality for the shape rises from the direction of the rotation of the loop.

Because all these elements give quite strong chirality, they can affect polarised light. Therefore, the secondary structure of a protein can be detected with CD. Indeed, the α-helix and the β-sheet give specific spectra displayed in figure 2 – 25.

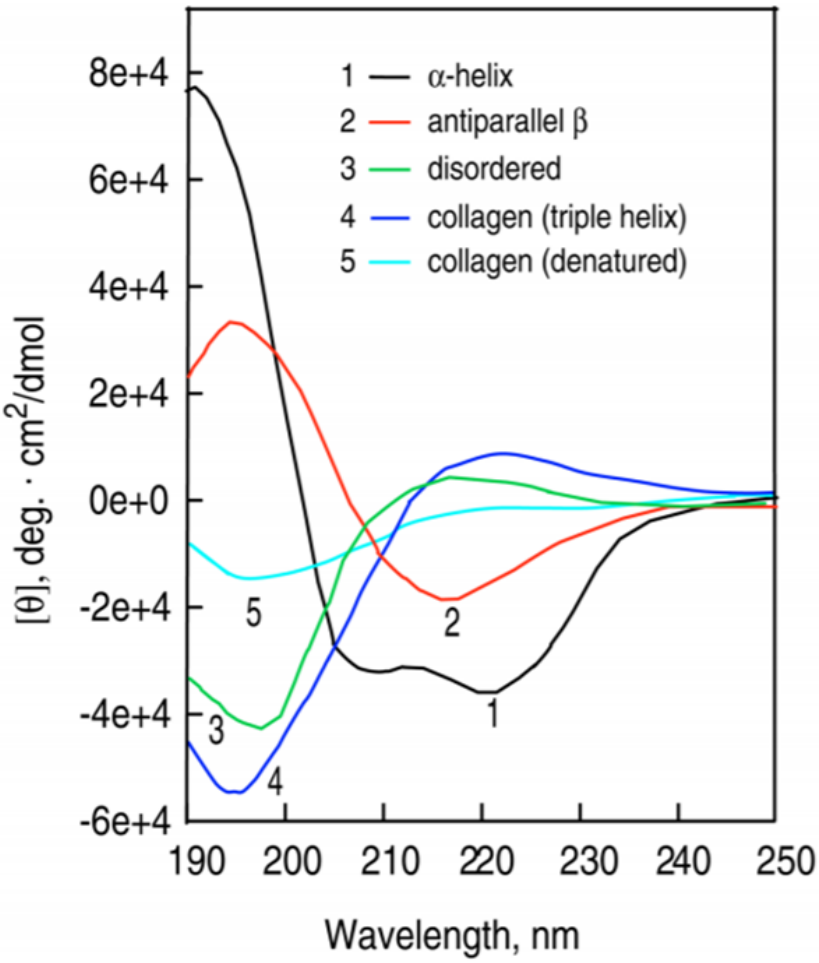

Figure 2 - 25: CD spectra of protein, figure taken from reference[78].

The tertiary structure of the protein is the one that defines the function of the protein. If this conformation is changed, then the protein loses its function. It is the folding of the polypeptide chain that creates the tertiary structure. It consists of a 3D arrangement of the secondary structure, all the β-sheet and α-helix structures can form blocks in space. This kind of folding happens due to four types of bonding: covalent bound (S – S), hydrogen and ionic bonds, electrostatic interaction (Van der Waals), The solvent used can influence the ternary structure as well.

The quaternary structure can be seen as an arrangement between the different monomers of the protein. For example, the protein can form a trimer, or it can be two blocks of monomers assembled by ligands.

CD does not give any information about quaternary structures[79,80]. It is possible to look at all the structures with more complex spectroscopic methods such as: X-ray diffraction, X-ray crystallography or NMR. CD can detect changes in the secondary and tertiary structures. In the case of tertiary structures however the CD signal is sensitive to only certain aspects of the structures in the near UV (250-350nm): the aromatic amino acids and the disulphide bonds. These changes can be seen in the near and far UV. We also showed that our spectroscopic technique can detect this change in the ternary and quaternary structures.

2.6 References:

(1) Barron, L. D. Molecular Light Scattering and Optical Activity. 2nd Edition. Cambridge University Press, (2004).

(2) Djerassi, C. Optical Rotatory Dispersion: Applications to Organic Chemistry. McGraw-Hill (1960).

(3) Meierhenrich, U. Amino Acids and the Asymmetry of Life. Springer-Verlag Berlin Heidelberg. (2008)

(4) Hicks, J. M. The Physical Chemistry of Chirality. ACS Symposium Series (2002), 810, 2-16.

(5) Velluz, L.; Le Grand, M.; Grosjean, M. Optical Circular Dichroism: Principles, Measurements, and Applications. Weinheim, Verlag chemie, N.-Y., Academic Press (1965).

(6) Tang, Y; Cohen, A. E. Enhanced Enantioselectivity in Excitation of Chiral Molecules by Superchiral Light. Science (2011), 332 (6027), 333–337.

(7) Yin, X.; Schäferling, M.; Metzger, B.; Giessen, H. Interpreting Chiral Nanophotonic Spectra: The Plasmonic Born-Kuhn Model. Nano Lett. (2013), 13 (12), 6238–6243.

(8) Condon, E. U. Theories of Optical Rotatory Power. Rev. Mod. Phys. (1937), 9 (4), 432–457.

(9) Karimullah, A. S.; Jack, C.; Tullius, R.; Rotello, V. M.; Cooke, G.; Gadegaard, N.; Barron, L. D.; Kadodwala, M. Disposable Plasmonics: Plastic Templated Plasmonic Metamaterials with Tunable Chirality. Adv. Mater. (2015), 27 (37), 5610–5616.

(10) Kuhn, W. The Physical Significance of Optical Rotatory Power. Trans. Faraday Soc. (1930), 26, 293–308.

(11) Tang, Y.; Sun, L.; Cohen, A. E. Chiroptical Hot Spots in Twisted Nanowire Plasmonic Oscillators. Appl. Phys. Lett. 2013, 102 (4).

(12) Wang, X.-O.; Gong, L.-J.; Li, C.-F. Application of Classical Models of Chirality to Optical Rectification. J. Chem. Phys. (2008), 129 (7).

(13) Condon, E. U.; Altar, W.; Eyring, H. One-Electron Rotatory Power. In Barut, A. O.; Odabasi, H.; Van der Merwe A. (Eds.) Selected Scientific Papers of E. U. Condon, Springer, N.-Y. (1991), 349-384.

(14) Yamamoto, T.; Sano, M. Theoretical Model of Chirality-Induced Helical Self-Propulsion. Phys. Rev. E (2018), 97 (1), 1–11.

(15) Johnson, P. B.; Christy, R. W. Optical Constants of Noble Metals. Physical Review B. (1972), 6 (12), 4370–4379.

(16) Sultanova, N.; Kasarova, S.; Nikolov, I. Dispersion Properties of Optical Polymers. Acta Phys. Pol. A (2009), 116 (4), 585–587.

(17) Maier, S. A. Plasmonics: Fundamentals and Applications; Springer, (2007).

(18) Enoch, S.; Bonod N. (Eds.) Plasmonics: From Basics to Advanced Topics. Springer (2012).

(19) Kong, J. A. Electromagnetic Wave Theory, Wiley-Interscience (1975).

(20) Theron, I. P.; Cloete, J. H. The Electric Quadrupole Contribution to the Circular Birefringence of Nonmagnetic Anisotropie Chiral Media: A Circular Waveguide Experiment. IEEE Trans. Microw. Theory Tech. (1996), 44 (8), 1451–1459.

(21) Kelly, C.; Khorashad, L. K.; Gadegaard, N.; Barron, L. D.; Govorov, A. O.; Karimullah, A. S.; Kadodwala, M. Controlling Metamaterial Transparency with Superchiral Fields. ACS Photonics (2018), 5 (2), 535–543.

(22) Kelly, C.; Tullius, R.; Lapthorn, A. J.; Gadegaard, N.; Cooke, G.; Barron, L. D.; Karimullah, A. S.; Rotello, V. M.; Kadodwala, M. Chiral Plasmonic Fields Probe Structural Order of Biointerfaces. JACS (2018), 140 (27), 8509–8517.

(23) Govorov, A. O.; Fan, Z. Theory of Chiral Plasmonic Nanostructures Comprising Metal Nanocrystals and Chiral Molecular Media. ChemPhysChem (2012), 13 (10), 2551–2560.

(24) Monticone, F.; Alù, A. Metamaterial, Plasmonic and Nanophotonic Devices. Reports Prog. Phys. (2017), 80 (3), 036401.

(25) Pelet, P.; Engheta, N. Coupled-Mode Theory for Chirowaveguides. J. Appl. Phys. (1990), 67 (6), 2742–2745.

(26) Parson, W. W. Modern Optical Spectroscopy, Second Edition; Springer-Verlag Berlin Heidelberg, (2015).

(27) Hendry, E.; Carpy, T.; Johnston, J.; Popland, M.; Mikhaylovskiy, R. V.; Lapthorn, A. J.; Kelly, S. M.; Barron, L. D.; Gadegaard, N.; Kadodwala, M. Ultrasensitive Detection and Characterization of Biomolecules Using Superchiral Fields. Nat. Nanotechnol. (2010), 5 (11), 783–787.

(28) Davis, T. J.; Hendry, E. Superchiral Electromagnetic Fields Created by Surface Plasmons in Nonchiral Metallic Nanostructures. Phys. Rev. B - Condens. Matter (2013), 87 (8), 1–5.

(29) Hendry, E.; Mikhaylovskiy, R. V; Barron, L. D.; Kadodwala, M.; Davis, T. J. Chiral Electromagnetic Fields Generated by Arrays of Nanoslits. Nano Lett. (2012), 12 (7), 3640-3644.

(30) Tullius, R.; Karimullah, A. S.; Rodier, M.; Fitzpatrick, B.; Gadegaard, N.; Barron, L. D.; Rotello, V. M.; Cooke, G.; Lapthorn, A.; Kadodwala, M. “Superchiral” Spectroscopy: Detection of Protein Higher Order Hierarchical Structure with Chiral Plasmonic Nanostructures. J. Am. Chem. Soc. (2015), 137 (26), 8380–8383.

(31) Tang, Y.; Cohen, A. E. Optical Chirality and Its Interaction with Matter. Phys. Rev. Lett. (2010), 104 (16), 1–4.

(32) Yang, N.; Tang, Y.; Cohen, A. E. Spectroscopy in Sculpted Fields. Nanotoday (2009), 4 (3), 269-279.

(33) Schäferling, M.; Dregely, D.; Hentschel, M.; Giessen, H. Tailoring Enhanced Optical Chirality : Design Principles for Chiral Plasmonic Nanostructures. Phys. Rev. X (2012) 2 (3), 1–9.

(34) Trügler, A. Optical Properties of Metallic Nanoparticles: Basic Principles and Simulation; Springer-Verlag Berlin Heidelberg, (2016).

(35) Barnes, W. L.; Dereux, A.; Ebbesen, T. W. Surface Plasmon Subwavelength Optics. Nature (2003), 424 (6950), 824–830.

(36) Shahbazyan, T. V; Stockman, M. I. (Eds.) Plasmonics : Theory and Applications; Springer (2013).

(37) Anker, J. N.; Hall, W. P.; Lyandres, O.; Shah, N. C.; Zhao, J.; Van Duyne, R. P. Biosensing with Plasmonic Nanosensors. Nat. Mater. (2008), 7 (6), 442–453.

(38) Li, L. Manipulation of Near Field Propagation and Far Field Radiation of Surface Plasmon Polariton; Springer, 2017.

(39) Bertolotti, M.; Sibilia, C.; Guzmán, A. M. Evanescent Waves in Optics: An Introduction to Plasmonics. Springer Series in Optical Sciences (2017) Vol. 140. 0342-4111.

(40) Barnes, W. L. Surface Plasmon-Polariton Length Scales: A Route to Sub-Wavelength Optics. J. Opt. A Pure Appl. Opt. (2006), 8 (4).

(41) Zhang, J.; Zhang, L.; Xu, W. Surface Plasmon Polaritons : Physics and Applications. J. Phys-D-appl phys (2012), 45 (11).

(42) Das, G.; Coluccio, M. L.; Alrasheed, S.; Giugni, A. Plasmonic Nanostructures for the Ultrasensitive Detection of Biomolecules. Riv. del nuevo Cim. (2016), 39 (11), 547-588.

(43) Jain, P. K.; El-Sayed, M. A. Plasmonic Coupling in Noble Metal Nanostructures. Chem. Phys. Lett. (2010), 487 (4–6), 153–164.

(44) Polo, J. A.; Mackay, T. G.; Lakhtakia, A. Electromagnetic Surface Waves; Elsevier Insight, (2013).

(45) Hayashi,S.; Okamoto, T. Plasmonics : Visit the Past to Know the Future. J. Phys-D-appl phys (2012), 45 (43).

(46) Hutter, E.; Fendler, J. H. Exploitation of Localized Surface Plasmon Resonance. Adv. Mater. (2004), 16 (19), 1685–1706.

(47) Lis, D.; Cecchet, F. Localized Surface Plasmon Resonances in Nanostructures to Enhance Nonlinear Vibrational Spectroscopies: Towards an Astonishing Molecular Sensitivity. Beilstein J. Nanotechnol. (2014), 5, 2275–2292.

(48) Maurer, T.; Adam, P.-M.; Lévêque, G. Coupling between Plasmonic Films and Nanostructures: From Basics to Applications. Nanophotonics. (2015), 4 (3), 363–382.

(49) Kelly, K. L.; Coronado, E.; Zhao, L. L.; Schatz, G. C. The Optical Properties of Metal Nanoparticles: The Influence of Size, Shape, and Dielectric Environment. J. Phys. Chem. B (2003), 107 (3), 668–677.

(50) Salomon, A.; Prior, Y.; Fedoruk, M.; Feldmann, J.; Kolkowski, R.; Zyss, J. Plasmonic Coupling between Metallic Nanocavities. J. Opt. (2014), 16 (11), 114012.

(51) Mazzotta, F.; Johnson, T. W.; Dahlin, A. B.; Shaver, J.; Oh, S.-H; Höök, F. Influence of the Evanescent Field Decay Length on the Sensitivity of Plasmonic Nanodisks and Nanoholes. ACS photonics (2015), 2 (2), 256-262.

(52) Haes, A. J.; Haynes, C. L.; Mc Farland, A. D.; Schatz, G. C.; Van Duyne, R. P.; Zou, S. Plasmonic Materials for Surface-Enhanced Sensing and Spectroscopy. MRS Bull. (2005), 30 (5), 368-375.

(53) Svedendahl, M.; Chen, S.; Dmitriev, A.; Käll, M. Refractometric Sensing Using Propagating versus Localized Surface Plasmons: A Direct Comparison. Nano Lett. (2009), 9 (12), 4428–4433.

(54) Willets, K. A.; Van Duyne, R. P. Localized Surface Plasmon Resonance Spectroscopy and Sensing. Annu Rev Phys Chem (2007), 58, 267–297.

(55) Kaminska, I.; Maurer, T.; Nicolas, R.; Renault, M.; Lerond, T.; Salas-Montiel, R.; Herro, Z.; Kazan, M.; Niedziolka-Jönsson, J.; Plain, J.; Adam, P.-M.; Boukherroub, R.; Szunerits, S. Near-Field and Far-Field Sensitivities of LSPR Sensors. J. Phys. Chem. C (2015), 119 (17), 9470–9476.

(56) Ong, B. H.; Yuan, X.; Tjin, S. C.; Zhang, J.; Ng, H. M. Optimised Film Thickness for Maximum Evanescent Field Enhancement of a Bimetallic Film Surface Plasmon Resonance Biosensor. Sensors Actuators B Chem. (2006), 114 (2), 1028–1034.

(57) Prodan, E.; Radloff, C.; Halas, N. J.; Nordlander, P. A Hybridization Model for the Plasmon Response of Complex Nanostructures. Science (2003), 302 (5644), 419–422.

(58) Hentschel, M.; Weiss, T.; Bagheri, S.; Giessen, H. Babinet to the Half: Coupling of Solid and Inverse Plasmonic Structures. Nano Lett. (2013), 13 (9), 4428–4433.

(59) Schäferling, M. Chirality in Nature and Science, (2017) in Chiral Nanophototonics, Springer Series in Optical Sciences, Vol. 205, 5-42. Springer, Cham.

(60) Park, W. Optical Interactions in Plasmonic Nanostructures. Nano Converg. (2014), 1 (2), 1–27.

(61) Luk'yanchuk, B.; Zheludev, N. I.; Maier, S. A.; Halas, N. J.; Nordlander, P.; Giessen, H.; Chong, C. T. The Fano Resonance in Plasmonic Nanostructures and Metamaterials. Nat. Mater. (2010), 9 (9), 707–715.

(62) Miroshnichenko, A. E.; Flach, S.; Kivshar, Y. S. Fano Resonance in Nanoscale Structures. Rev. Mod. Phys. (2010), 82 (3), 2257–2298.

(63) Fano, U. Interaction between Configurations with Several Open Shells. Phys. Rev. (1965), 140 (1A).

(64) Rahmani, M.; Luk'yanchuk, B.; Hong, M. Fano Resonance in Novel Plasmonic Nanostructures. (2013), Laser & Photonics Review, 7 (3), 329–349.

(65) Gallinet, B.; Martin, O. J. F. Analytical Description of Fano Resonances in Plasmonic Nanostructures. (2011), AIP Conference Proceedings 1398, 73.

(66) Limonov, M. F.; Rybin, M. V; Poddubny, A. N.; Kivshar, Y. S. Fano Resonances in Photonics. Nature Photonics (2017), 11 (9), 543–554.

(67) Verellen, N.; Sonnefraud, Y.; Sobhani, H.; Hao, F.; Moshchalkov, V. V.; Van Dorpe, P.; Nordlander, P.; Maier, S. A. Fano Resonances in Individual Coherent Plasmonic Nanocavities. Nano Lett. (2009), 9 (4), 1663–1667.

(68) Giannini, V.; Francescato, Y.; Amrania, H.; Phillips, C. C.; Maier, S. A. Fano Resonances in Nanoscale Plasmonic Systems: A Parameter-Free Modeling Approach. Nano Lett. (2011), 11 (7), 2835–2840.

(69) Kamenetskii, E.; Sadreev, A.; Miroshnichenko, A.(Eds.) Fano Resonances in Optics and Microwaves; Springer, (2018).

(70) Cao, W.; Singh, R.; Zhang, C.; Han, J.; Tonouchi, M.; Zhang, W. Plasmon-Induced Transparency in Metamaterials: Active near Field Coupling between Bright Superconducting and Dark Metallic Mode Resonators. Appl. Phys. Lett. (2013), 103 (10).

(71) Zhang, S.; Genov, D. A.; Wang, Y.; Liu, M.; Zhang, X. Plasmon-Induced Transparency in Metamaterials. Phys. Rev. Lett. (2008), 101 (4), 1–4.

(72) Smith, D. D.; Chang, H.; Fuller, K. A.; Rosenberger, A. T.; Boyd, R. W. Coupled-Resonator-Induced Transparency. Phys. Rev. A (2003), 69 (6), 1–6.

(73) Fleischhauer, M.; Imamoglu, A.; Marangos, J. P. Electromagnetically Induced Transparency: Optics in Coherent Media. (2005), Rev. Mod. Phys. 77 (2), 633-673.

(74) Liu, N.; Langguth, L.; Weiss, T.; Kästel, J.; Fleischhauer, M.; Pfau, T.; Giessen, H. Plasmonic Analogue of Electromagnetically Induced Transparency at the Drude Damping Limit. Nat. Mater. (2009), 8 (9), 758–762.

(75) Tassin, P.; Zhang, L.; Zhao, R.; Jain, A.; Koschny, T.; Soukoulis, C. M. Electromagnetically Induced Transparency and Absorption in Metamaterials: The Radiating Two-Oscillator Model and Its Experimental Confirmation. Phys. Rev. Lett. (2012), 109 (18), 1–5.

(76) Barron, L. D. Chirality and Life. Space Sci. Rev. (2008), 135, 187–201.

(77) Brolo, A. G. Plasmonics for Future Biosensors. Nature Photonics. (2012), 6 (11), 709–713.

(78) Greenfield, N. J. Using Circular Dichroism Collected as a Function of Temperature to Determine the Thermodynamics of Protein Unfolding and Binding Interactions. Nat. Protoc. (2006), 1 (6), 2527–2535.

(79) Kelly, S. M.; Price, N. C. The Use of Circular Dichroism in the Investigation of Protein Structure and Function. Curr. Protein Pept. Sci. (2001), 1 (4), 349–384.

(80) Kelly, S. M.; Jess, T. J.; Price, N. C. How to Study Proteins by Circular Dichroism. Biochim. Biophys. Acta - Proteins and Proteomics (2005), 1751 (2).

Chapter 3: Experimental

3.1 Introduction:

For this project we used special custom-made polycarbonate slides as substrates. We called them injection-moulded substrates. In this chapter we will explain the fabrication process. We will also describe the experimental material, and give the protocols used to perform biosensing measurements. Nanofabrication and metal coating were done in the James Watt Nanofabrication centre at the School of Engineering (University of Glasgow), and biosensing measurements were performed at the School of Chemistry.

3.2 Fabrication of the nanostructures:

As said above, the metamaterials used for the project were custom–made. Our metamaterials consisted of nano indented polycarbonate slides, which were coated with metal. We called these templates plasmonic substrates (TPS)[1]. To produce these substrates, we used a technique called high-throughput injection-moulding.

3.2.1 Fabrication of the mould:

High-throughput injection-moulding is a technique used in industry which allows mass production. The process is detailed in the next paragraph. As stated in the name, a mould is required. This mould consists of a nano indented metal template. This template was created once and reused several times when more polycarbonate substrates were needed. The metal template can be re-used if it is cleaned properly, with ethanol and iso-propyl alcohol (IPA), dried with nitrogen gas, and then plasma cleaned with oxygen plasma. The mould was cleaned before and after use and stored in a cleanroom environment[1].

The mould, or master, is fabricated by electron beam lithography (EBL). The process goes as follows[2] (figure 3 – 1). A silicon wafer is cleaned with several solvents: acetone, methanol and IPA. The wafer is then sonicated and dried under Nitrogen gas. The wafer is spin coated to a 100 nm thickness with a poly methyl methacrylate resist (PMMA MW = 2010). This last step defines the depth of the nanostructure printed by the master with injection-moulding. After being spin coated, the wafer is baked in the oven at 180ºC for 5 min to allow the solvent to evaporate. The desired nano-pattern is then printed on the resist with an electron beam writer (vistec VB6). IPA and methyl Isobutyl Ketone 2.5:1 ratio at 25º C for a minute are used to develop the resist (figure 3 - 1). A layer of 1 mm Nickel is then put on the substrate. Acetone is used to get rid of any remaining PMMA which then allows the separation of the Nickel (Ni), now patterned with nanostructures (shim), from the wafer. Ni was chosen for its high thermo-conductivity, which helps when it comes to cool down the polymer on the mould.

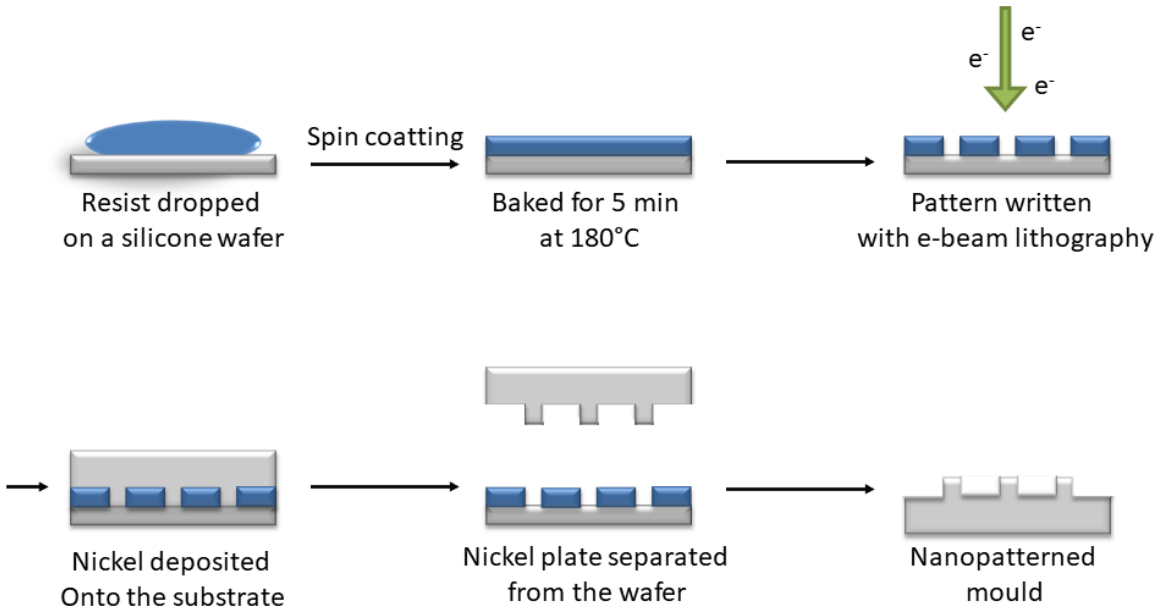

Figure 3 - 1: Scheme of the fabrication of the nanopatterned nickel mould.

3.2.2 Injection-moulding:

The mould created can then be used for injection-moulding. For this process an Engel Victory 28 hydraulic injection-moulder was used (figure 3 - 2). Polycarbonate was used to fabricate the slide because it is a polymer which is easily available and it is the best polymer for nanostructure fabrication, indeed it can replicate nanofeatures very well. The master is put on the back plate itself fixed to a moving plate.

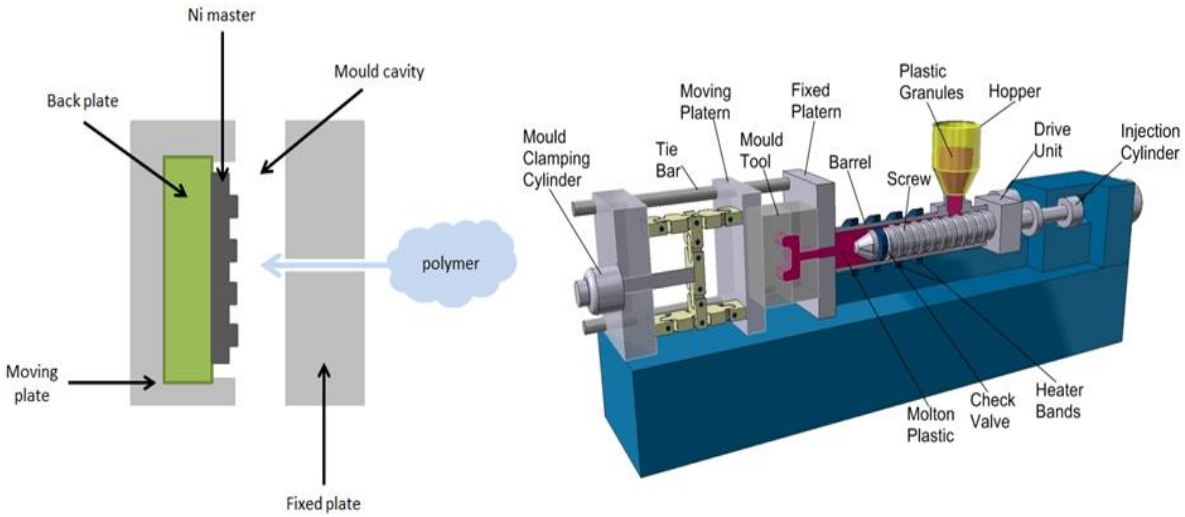

Figure 3 - 2: Scheme of the injection-moulder machine. The picture on the left show the mould chamber. The picture on the right is an overall view of the machine parts.

Beads of polycarbonate are heated to 280º C (to melt the polycarbonate) via the hopper (figure 3 – 2 right). A certain amount of polymer is then injected into the moulding cavity and

the mould pressed on the polycarbonate in order to print the nanostructure (figure 3 - 3). This process happens at a constant rate. The temperature and pressure of the process are set up on the machine. The temperature in the mould chamber is 140 ºC because it is the vitreous temperature of polycarbonate. Then, the polycarbonate is left to cool down, the mould chamber opened, and the polycarbonate substrate is released. The whole process starts again after that and is used to produce about 300 substrates. It takes about half a day.

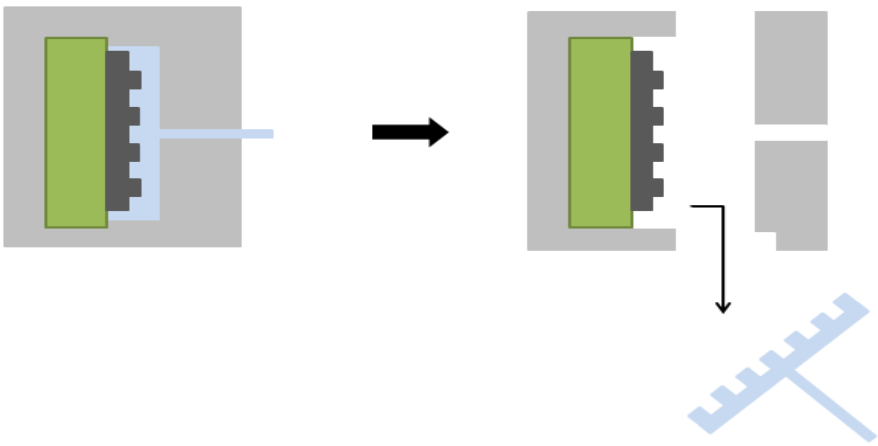

Figure 3 - 3: Graph of the moulding process. View of the slide production in the mould chamber.

3.2.3 Metal evaporation:

The slides obtained after injection-moulding, are only polycarbonate (figure 3 – 4 A)). In order to get a plasmon from them, or to get any optic signal at all, they need to be coated with metal. In this thesis we used mainly slides coated with 100 nm gold (figure 3 – 4 B). We made the metal deposition the following way.

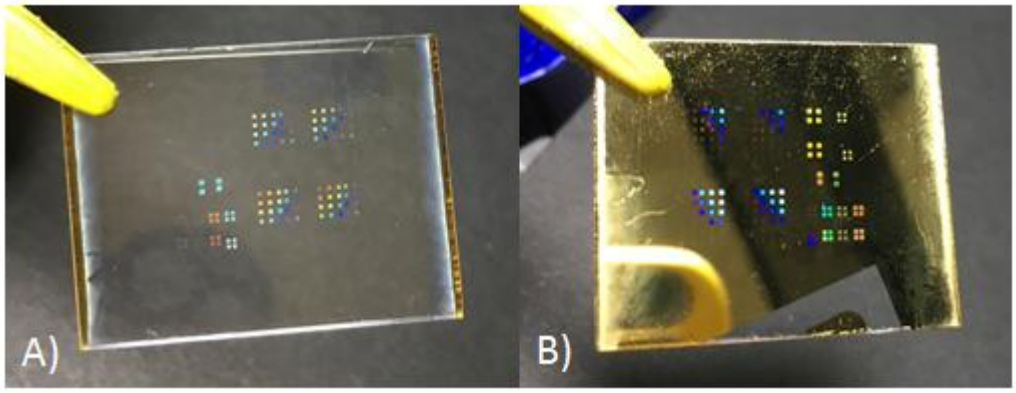

Figure: 3 - 4: Picture of the TPS. A) is a polycarbonate slide. B) Gold coated polycarbonate slide.

A plastic slide was first cleaned with methanol and IPA and dried under N_2 gas. The slides were loaded in an electron beam evaporator called plassys MEB – 400. Here 100 nm ± 1.5 nm gold is evaporated at the substrate surface at the rate of 0.3 $nm.s^{-1}$ ± 0.02 $nm.s^{-1}$. This gives us the slides used for the experiment. Before carrying out any experiment, the gold slides were washed with ethanol unless being previously coated with a self-assemble monolayer (SAM).

3.2.4 Metamaterial features:

The substrate consists of different types of nanostructures, as shown in figure 3 - 5. In this thesis we used only one shape, so we will describe only this type. But the injection-moulding method allows us to create nanostructures of different sizes and shapes. The structures used in this thesis are called shurikens. On the figure 3 - 4 we can see iridescent squares. These squares are 3 µm wide and consist of a pattern of surikens (figure 3 - 5). The shurikens are structures with six curved arms oriented clockwise (right-handed) or anti-clockwise (left-handed).

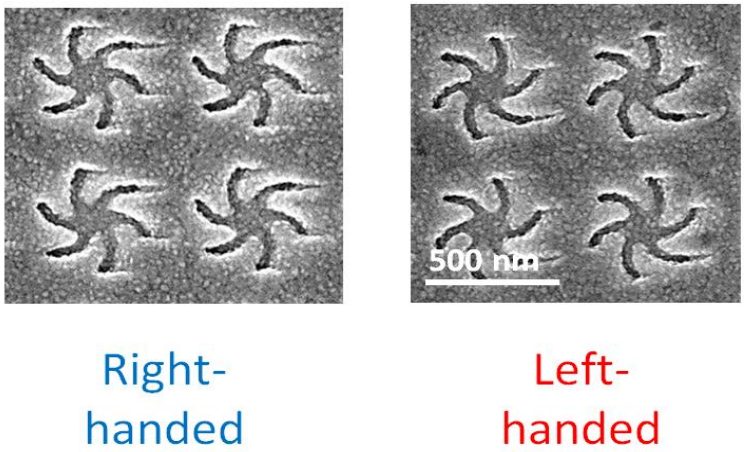

Figure 3 - 5: Scanning electron microscopy image of left- and right-handed shuriken structures.

The core of the structure is a circle. The diameter of a single structure (from one arm to another) is 500 nm. Two structures are spaced by 200 nm. This gives a total pitch (distance from the arm of one structure to the arm of the structure next to it) of 700 nm, and explains the position of the resonance in the spectra (710 nm). The depth of each structure is 80 nm into the polymer, and the thickness of the arm is 30 nm. The squares mentioned above contain 430 shurikens along each side, which gives a total of 184 900 nanostructures per square. When coated with 100 nm Au, we get a continuous thin film of nanostructures.

3.3 Spectroscopy:

3.3.1 Polarisation microscope:

The experiments for this thesis were all carried out with the same microscope. It is a custom-built device that can record ORD and reflectivity spectra (figure 3 – 6 and figure 3 - 7). We used this microscope to record changes in linearly polarised light. The light comes out a 50 W tungsten halogen light source (Thorlab), then goes through a lens and a nanoparticle polariser (Thorlab). The now linearly polarised light is sent to a beam splitter (Thorlab 50:50 700 nm-1000 nm CCM-1BSO14/M). The beam is diverted and the polarisation of the light changes by 90º. It goes through the objective (10x lens with 0.3 numerical aperture Olympus UPlanFLN 10x). The light reflected from the sample surface is sent back to the beam splitter and then through another calcite polariser. The angles of this polariser are set at 0º, 45º,90º and 135º (Stokes angles) to record the intensity of the light. The four Stokes angles are enough to describe the whole state of polarisation (unpolarised, partially polarised and fully polarised) of an electromagnetic wave. The LabVIEW program would then calculate the ORD with the following formula:

$$\text{ORD} = \frac{1}{2}\tan^{-1}\frac{(I_{45}-I_{135})}{(I_0-I_{90})} \quad (1)$$

Where I is the intensity of light. For the recording of reflectivity, the spectrometer is set at 0º.

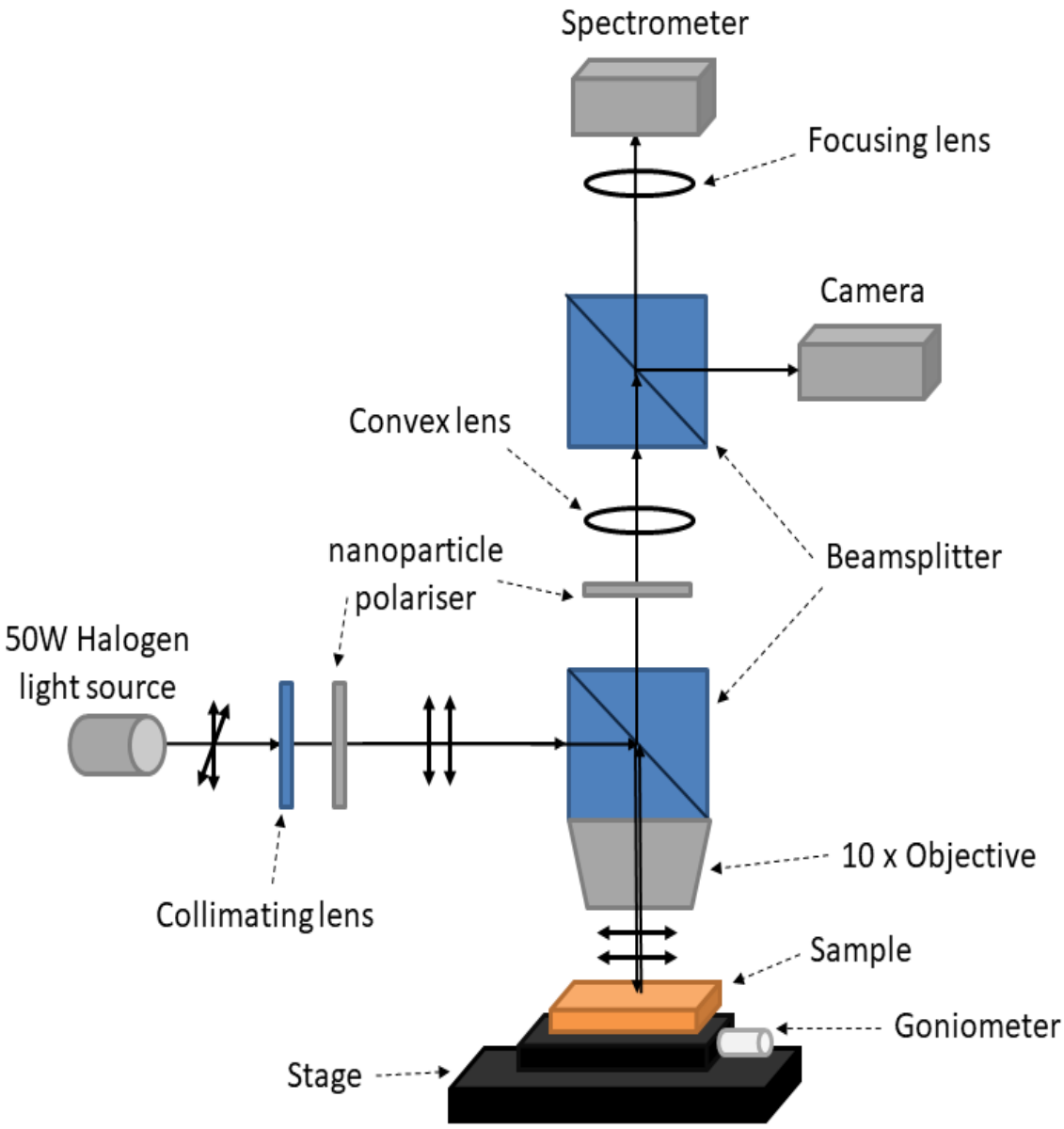

Figure 3 - 6: Scheme of the polarisation microscope.

The polarised light goes through a second beam splitter to a camera (Thorlab CMOS camera DCC1645C) and the spectrometer (Ocean Optic USB 4000) via a focusing lens. The spectrometer is plugged into a computer. The spectra are recorded with LabVIEW 2014. The camera is a guide used for the alignment of the microscope. It is operated by the computer thanks to the Thorlab camera software.

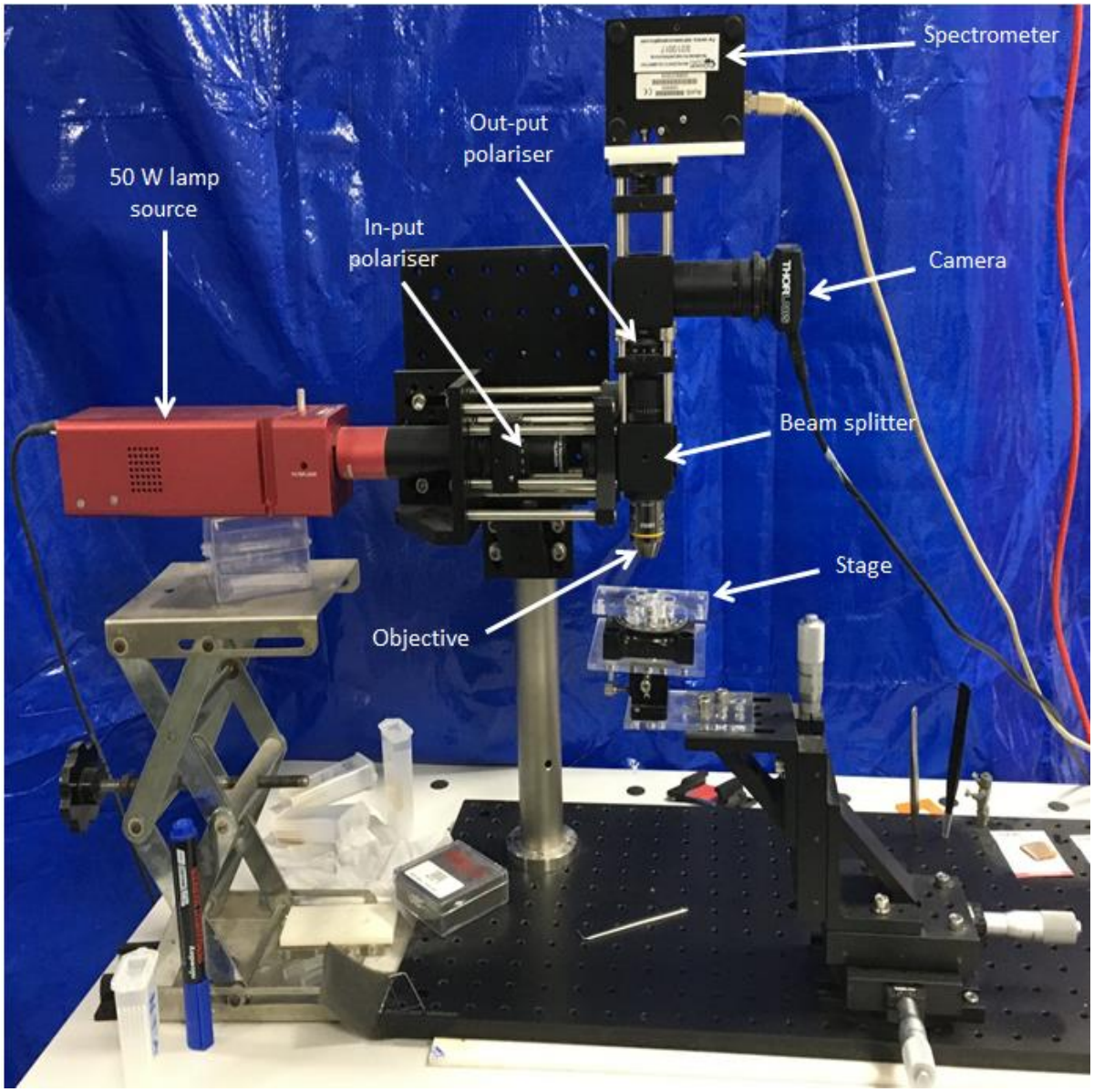

Figure 3 - 7: Picture of the polarisation microscope used for all the optical measurement.

Thanks to the camera we can adjust the focus of the microscope. It is also vital to keep measuring the signal of the square, made of nanostructures, at the same position. Indeed, it is possible to set up reference recorded on the camera to make sure we reproduce the measurement at the exact same position. Figure 3 – 8 shows the image we get from the camera. The red colour is due to the beam splitter discriminating light outside of the range of 700 nm to 1000nm. The data processing and analysis (creation of graphs) was done with Origin pro 9.

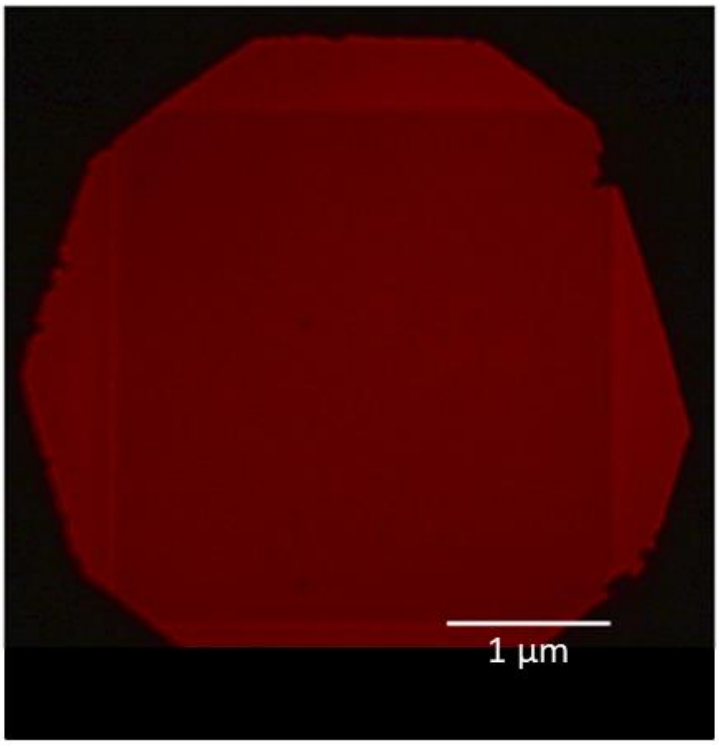

Figure 3 - 8: Picture of the RH square taken with Thorlab camera.

3.3.2 Microfluidic cell:

The polarisation microscope was used with the custom-made metamaterial in order to do biosensing measurements. The position of the plasmonic resonances depends on the refractive index of the material on top of the surface. Measuring an ORD signal from the substrate with air (no material on top of the slide) gives a signal around 600 nm. The beam splitter lets the light through at the wavelength range of 700 nm to 1000 nm (because our resonance is around 718 nm and higher, a broader beam splitter would be less accurate). No air measurement could be taken with the microscope (if needed, another microscope was available with a broader range of wavelength). Thus, optic measurements must be done with liquid on top of the surface. Indeed, high refractive index shifts the wavelength toward the red. Measurements can take time, up to an hour, thus we needed a way to keep the liquid on top of the substrate for a certain amount of time. We created a cell, with a 3D printer, that contained the analyte and the substrate (figure 3 - 9). The substrate was put on the 3D printed sample holder. On top of it was a piece of solid silicone with a hole in the middle, it contained the liquid on top of the shuriken squares. Hypodermic needles were placed through the silicon and the sample holder (which had needle sized holes on both sides) to empty and refill the cell with different protein solutions. In order to keep the liquid inside and close the cell, a cut glass microscope slide was placed on top of the piece of silicone. To maintain all of this from moving and to fill the void a 3D printed holder; a piece of plastic with a hole in the middle was added (orange piece figure 3 - 9). Buffer was first

injected into the cell, in order to align the microscope and take blank measurement. The liquid analyte was injected through the needle and left on top of the slide for an hour. Then the slide was rinsed with buffer and measurement taken. As proteins can bind metal nanostructures, rinsing the cell would not wash the proteins away, and it would get rid of any “floating” molecules. This rinse reduces averaging of the signal and thus enhances the asymmetry.

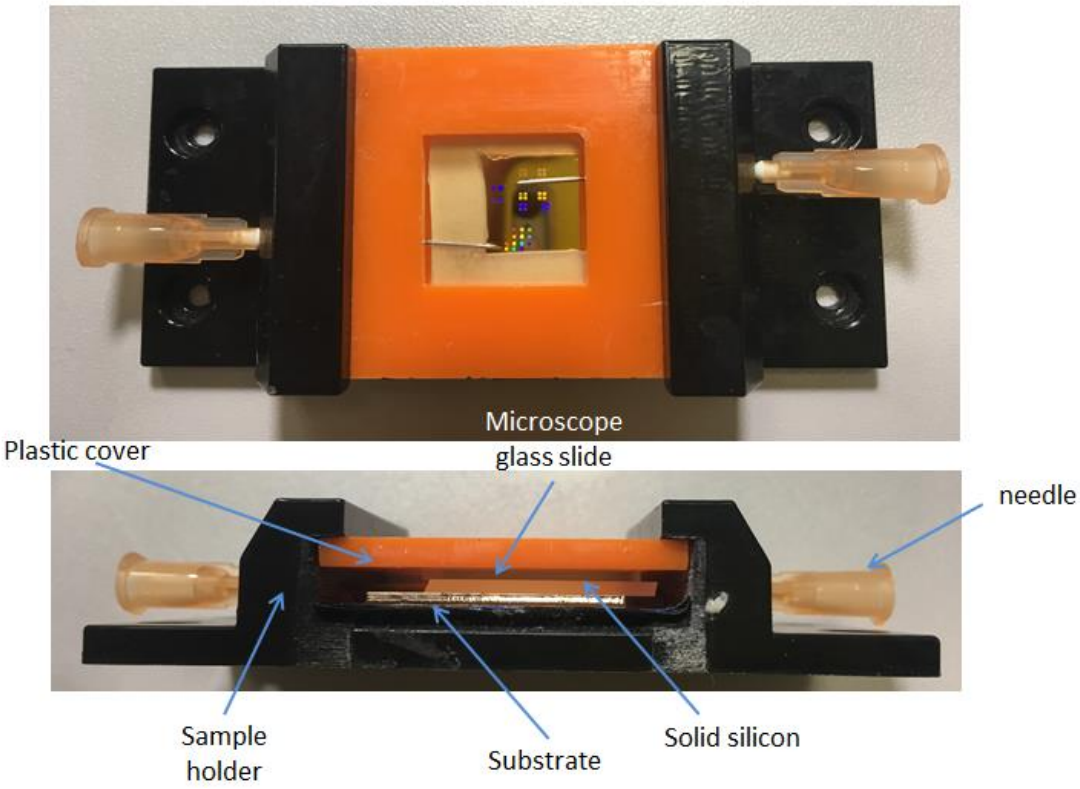

Figure 3 - 9: Picture of the microfluidic cell containing the gold substrate.

This kind of cell contains 300 µL of liquid. The cell was positioned on the stage for the light to shine perpendicularly to it.

3.3.3 Spectroscopy:

A) Optical rotatory dispersion:

The definition of an ORD was already given in chapter 2. We can measure this signal from both right – and left – handed structures. Both ORDs must be equal and opposite when plotted together. In fact, that is how we know that the microscope is aligned correctly. If the ORD spectra are not equal and opposite, it means that the nanostructures do not reflect light in the same way. This can be due to the position of the substrate on the stage or to the input light coming at an angle (this is corrected by changing the tilt of the stage). The ORD

signal was calculated by LabVIEW program. The signal was recorded several times in the structure in order to reduce the noise. The ORD from the flat gold was recorded as well, several times, then subtracted from the nanostructures ORD signal to get rid of background effect. Indeed, due to the way the substrate is coated with gold, the thin film contains defect, moreover the polycarbonate surface is not completely smooth, thus the flat gold signal is not a perfect flat line on the spectrum as it should be. Subtracting the flat gold signal from the ORD signal gives a smoother graph and removes the small but broad peak induced by the gold thin film (usually around 600nm). The ORDs we get are of a bisignate shape shown in figure 3 - 10. The ORDs arise due to plasmonic excitation, but the position of the peak (wavelength) is controlled by the refractive index of the surrounding medium. That is why we get a shift when we put a material on the surface. Several parameters can be extracted from these spectra. These parameters quantify the asymmetry (the unequal way to reflect light, change in refractive index etc…). A blank measurement was first performed (buffer) and every analyte measurement was compared to the blank data. Four spectra were recorded and averaged for each handiness. We introduced an asymmetry parameter arising from the peak-to-peak height difference in the ORD between the LH (red on figure 3 - 10) and the RH structure (blue on figure 3 - 10). We called it h.

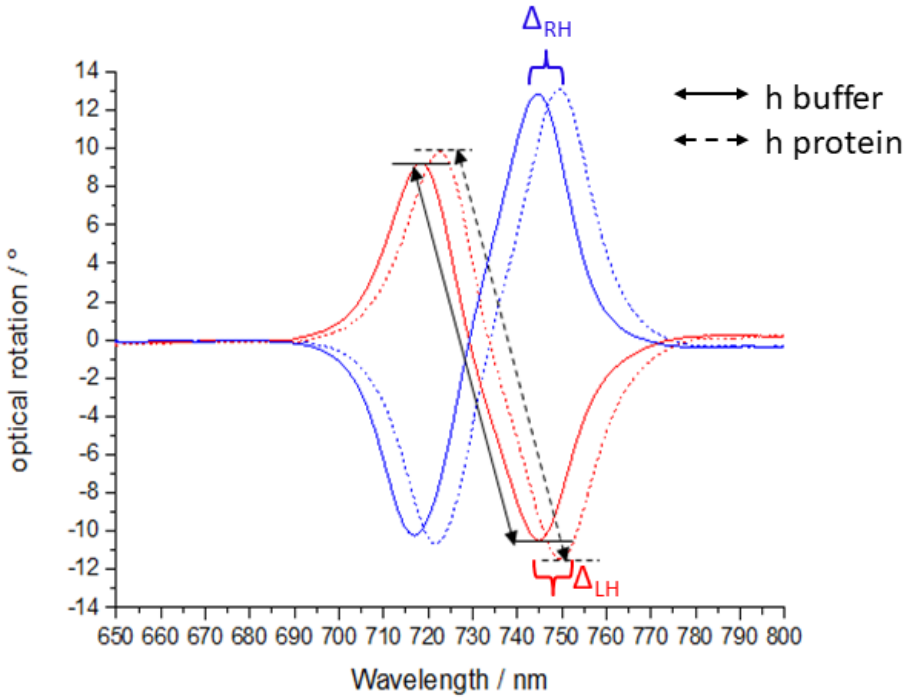

Figure 3 - 10: ORD graph from LH and RH nanostructures. The black arrow shows the distance we measured to calculate the peak to peak height. The solid arrow shows the distance from peak one to peak two in buffer and the dash one the same distance but with protein measurement.

To calculate this parameter, we measured the distance between the two peaks of the bisignate signal. The distance between peak one and peak two was measured for both blank and proteins. The ratio, protein versus buffer, for the two handedness was calculated (with LabVIEW) using:

$$h_{LH/RH} = \frac{peak\ to\ peak\ analyte}{peak\ to\ peak\ buffer} \quad (2)$$

From there we extracted the asymmetry parameter which is the ratio of h in RH divided by h in LH.

$$A = \frac{h_{RH}}{h_{LH}} \quad (3)$$

If the result is one then there is no asymmetry (achiral media). If the ratio is below one then the peak to peak height in LH signal is higher than the one in RH, and If the ratio is above one then the peak to peak height in RH signal is higher than the one in LH.

We defined another parameter, the average shift, which describes the protein quantity at the surface of the slide. It is calculated by measuring the average shift between left and right hand (figure 3 - 10):

$$\text{Average shift} = (\Delta_{LH} + \Delta_{RH}) / 2 \quad (4)$$

In this thesis all the comparisons between different proteins were done using this parameter, we compared proteins with similar average shift rather than similar concentration. Looking at the shift for the LH and RH ORD we can quantify an asymmetry in the refractive index. Indeed, due to its presence on the surface and its handedness, a protein will change the refractive index surrounding the structure, and cause an asymmetry in the wavelength position. This asymmetry is calculated in the second peak of the ORD the following way:

$$\Delta\lambda_{RH/LH} = \lambda^{RH/LH}_{(analyte)} - \lambda^{RH/LH}_{(buffer)} \quad (5)$$

Equation 5 gives the shift due to the refractive index in each handiness. To find the difference between the size of the shift and thus the asymmetry, we just have to subtract $\Delta\lambda_{RH}$ from $\Delta\lambda_{LH}$ (we do this by convention):

$$\Delta\Delta\lambda = \Delta\lambda_{RH} - \Delta\lambda_{LH} \quad (6)$$

If the analyte is achiral then $\Delta\Delta\lambda = 0$. Indeed, an achiral material has the same contribution on the field of both LH and RH structures. The shift for the LH and RH will thus be equal giving a $\Delta\Delta\lambda = 0$. If $\Delta\Delta\lambda$ is not zero, then the analyte is chiral. This happens with proteins (chiral molecules), due to its chirality the protein will interact with one field better than with

the other one. This interaction induces a bigger change in the refractive index of one handedness, leading to ΔΔλ ≠ 0. All these parameters will be used later in this thesis.

B) Reflectance:

Another type of measurement was carried out; the reflectivity coming from LH and RH. To perform this measurement, the output polariser was set to zero. We measured the absorbance of the structure in comparison to the one of plain metal. These were taken at the same time as the ORDs. Reflectance was recorded on the structure, then on flat gold. The former was divided by the later, by the software:

$$\text{Reflectance} = \frac{I_{nanostructure}}{I_{background}} \quad (7)$$

Several of these spectra were recorded in order to reduce the noise. Like ORD measurements, reflectance spectra were first taken in buffer and then with protein solution. As for the ORD measurements, buffer was used as reference. Unlike the ORD spectra, the reflectance between LH and RH are not equal and opposite. They are rather similar and are supposed to be because they quantify the reflectance of the structure which must be the same. Differences between the two spectra arise due to the surrounding chiral medium. We introduce here a new asymmetry parameters ΔΔS (figure 3 - 11). This is the difference in the separation between the two peaks in the reflectance.

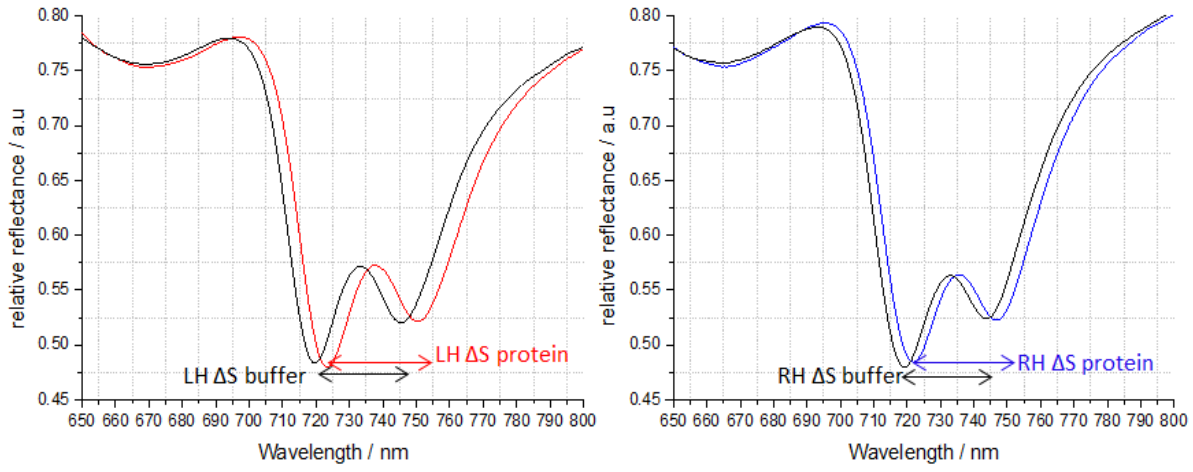

Figure 3 - 11: Asymmetry parameter in reflectivity spectra. The graph on the left shows the reflectance from the LH structure. The graph on the right shows the reflectance of the RH structure.

The dip we see in LH and RH reflectance is due to plasmonic induced transparency; it can be explained by the strong coupling between dark and bright modes (see chapter 2). In the

figure 3 - 11 it is shown how we extract the parameters ΔS_{LH} and ΔS_{RH}, from there we get $\Delta\Delta S$.

$$\Delta S_{RH/LH} = {}^{RH/LH}\Delta_{Sanalyte} - {}^{RH/LH}\Delta S_{buffer} \quad (8)$$

$$\Delta\Delta S = \Delta S_{LH} - \Delta S_{RH} \quad (9)$$

When an achiral material is put on top of the surface the spacing does not change and $\Delta\Delta S = 0$. If the spacing in the reflectance changes, it means that the chiral materiel changes the properties of the structure, enough to lead to a change in the way the structure reflects the incident light.

3.3.4 Circular dichroism:

Several CD measurements were performed using the spectrometer Jasco J-810 Spectropolarimeter (163-900 nm). Protein solutions were given to Dr Sharon Kelly who ran the CD spectrometer and she gave us the data to plot the graph and do the analysis. This technique was used to get the CD spectra of type 2 dehydroquinase (DHQ) 15 and DHQ 38 in buffer with different pHs. Measurements were taken in the far UV (190 nm – 260 nm) and near UV (250 nm – 320 nm). CD spectra of the protein solutions were taken for each pH. Then the same spectra were recorded for buffer solution for the 3 pHs. The absorbance of the pH was also measured every time to be sure that the detector was not saturated. The CD spectra of buffer was subtracted from the protein one.

3.4 Surface functionalisation:

Functionalisation of the gold surface has several advantages; it increases the binding of the protein on the surface and orders the analyte. Ordering the protein at the surface of the slide means that all molecules will bind the gold in the same position (via the same gold binding domain). This reduces averaging caused by the random orientation of the protein in space and increases the asymmetry of the optical signal. This thesis will focus on two different types of surface functionalisation: one being a self-assembled monolayer (SAM), and the other being fraction antibody bind onto the gold (known as Fabs).

3.4.1 Nitrilotriaceticacid:

Functionalised surfaces with NTA were used to do biosensing with His-tag proteins. The self-assembled monolayer (SAM) used belongs to the family of the Alkanethiol[3–7], $SH(CH_2)_nX$, X being a functional group chosen according to the analyte we wished to bind. For us, the functional group is Nitrilotriaceticacid (NTA). This functional group can react with nickel which then creates an anchor for proteins. The SAMs have the properties to bind on metal via a gold sulphur bond. Theses organic molecules self-assemble on a substrate with a certain order and form a monolayer. In our case, we used two types of thiol, the one with the functional group and another one to space the first thiol in order to avoid saturation of

the surface. The protein can bind non specifically to gold. Hence another thiol was used without a protein binding group at the end of the carbon chain, to saturate the surface at one end and space the protein at the surface. This second thiol is called a spacer. The sample was coated with the SAM as follows. The thiols used for our surface functionalisation are: nitrilotriacetic acid (NTA-SAM) chelating agent bind Ni(II)(Prochimia Surface) and a spacer triethylene glycol mono-11-mercaptoundecyl (EG-thiol) (Sigma Aldrich, CAS: 130727-41-2). The gold substrate was first put into a solution of 95% ethanol to clean it. 1 mM of NTA and 0.9 mM EG-thiol were dissolved in a solution of 95% ethanol. The substrates were then put into this solution and left there overnight (16h – 20h). The next day the samples were taken out of the solution and rinsed with 95% ethanol solution. After being rinsed, they were incubated in a 1 mM solution of NaOH for 5 min, to remove the acidity on the surface. The substrates were taken out to be rinsed with water and set to incubate for 1 hour in a solution of 40 mM $NiSO_4^{2-}$, this will then be the receptor of the protein. To finish, a final rinse of the substrate was performed with 1 mL of HBS buffer (Hepes buffered saline = 10 mM HEPES and 150 mM NaCl in water at pH 7.2), and 5 mL of water. The samples were then dried under a steam of nitrogen and kept in the fridge (they can be kept there up to two weeks). Figure 3 -12 summarises the way SAM formed onto the gold and bound His-tag protein.

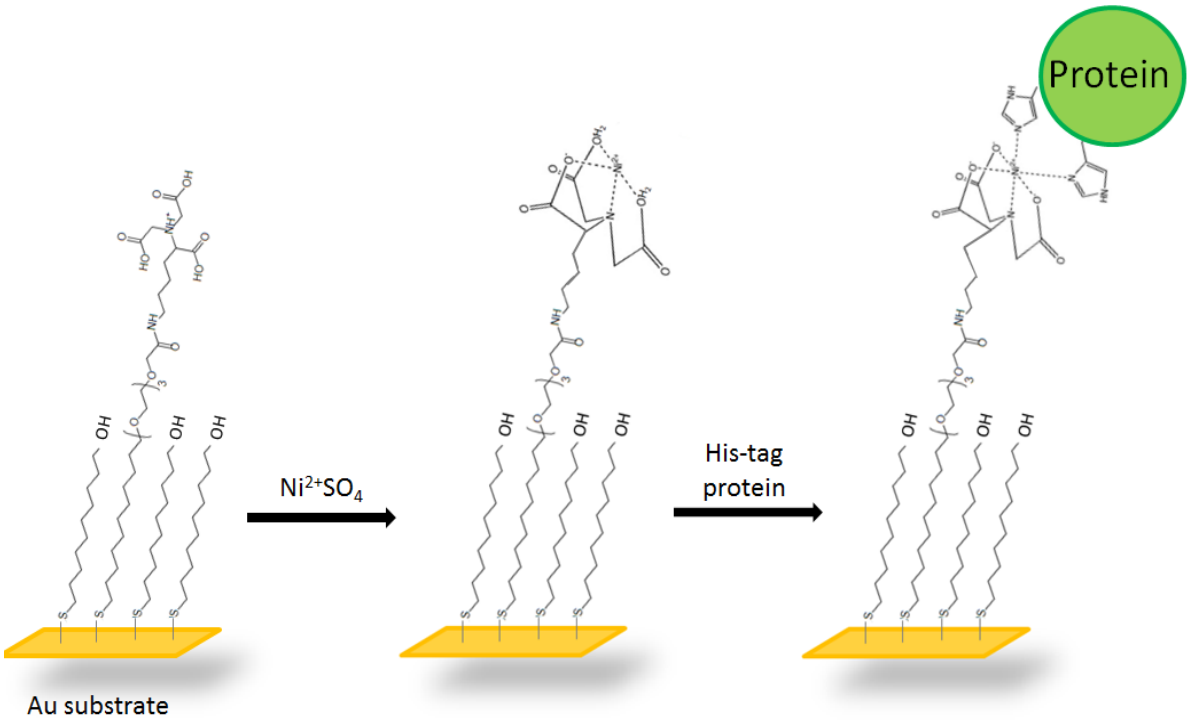

Figure 3 - 12: Scheme of His-tag protein immobilisation with NTA-SAM coated slide. Figure adapted from reference[3].

The His-tag protein will bind to the Ni, therefore we need to form a complex between the NTA and the nickel.

3.4.2 Fragment antigen binding:

Another way to bind a protein or a virus at a specific position is to use an antibody. Indeed, antibodies have receptors that can recognise proteins or viruses and bound to them. It was explained in chapter 2 that in the z direction, the field at the surface is evanescent, exponentially decaying from the surface. Because of this, the molecules put on top of the surface cannot be too big (more than 50 nm would be problematic). An antibody itself would still be detected, but a complex antibody-protein is likely to be too far away from the surface. The antibody can be fragmented to keep only the part with the protein receptor. This portion of antibody is called fragment antigen binding (Fab), and can bind to the gold surface[8], thanks to the sulphur at the end of the fragmented chain (figure 3 - 13). The Fab' fragments were provided by Dr. Chantal Keijzer using Thermo Fisher scientific Pierce $F(ab')_2$ Kit.

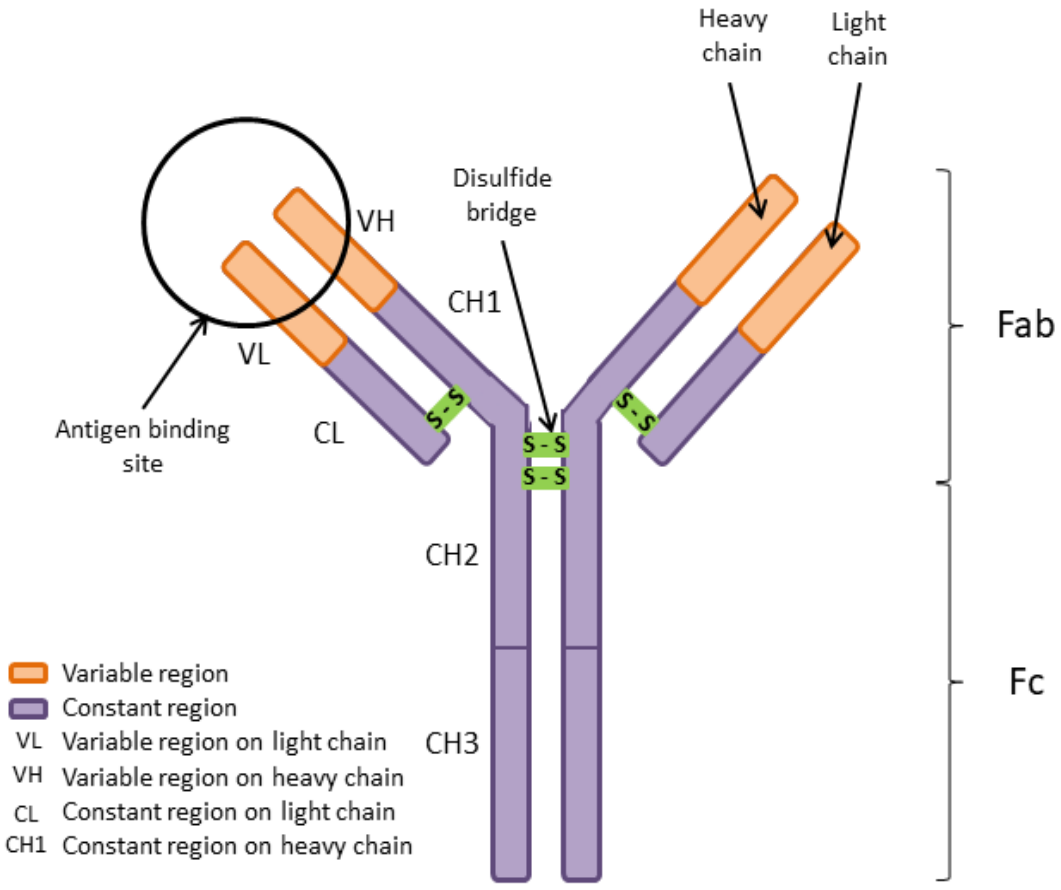

Figure 3 - 13: Scheme of an antibody fragment. The bottom part of the antibody called fragment crystallisable (Fc), interacts with the cell surface. The Fab fragment is on top of the Fc.

The Fab' solution preparation with spacer was done in our lab at the School of Chemistry. We established the method to functionalise the surface, further explanation will be given in chapter 5.

The Fab' fragments were obtained from rabbit IgG (150 kDa). An endopeptidase (an enzyme that breaks peptide bond) was used to fragment the $F(ab')_2$ from the Fc. After this treatment the Fc was broken into pieces (peptide fragments) and it was so degraded that it could be separated from the Fab' fragments. After dialysis we obtained $F(ab')_2$ fragments. First a solution of immobilised pepsin (Acid-type protease, MW 35,000) was prepared using digestive buffer (120mL, 20mM sodium acetate, pH 4.4; 0.05% sodium azide). With pepsin there is a chance of auto-digestion, hence here a resin was added, so the pepsin was immobilised. The enzyme needed to be activated with 10 mM cysteine; gel filtration was used to remove the excess of cysteine (this step is important to prevent overdigestion). Second, the rabbit IgGs were purified and digested by pepsin. After digestion the Fc fragment was broken into pieces; they were removed by dialysis. Fab' fragments were reduced to sulfhydrul-containing univalent Fab' fragments. Fab' purification was done with a Protein A plus column, with PBS and IgG elution buffer (pH 2.8) at room temperature. Coating the surface of a slide with the Fab is straightforward. A microfluidic cell was built; ORD and reflectivity were recorded with the cell filled up with digestive buffer. The Fab' fragments in digestive buffer and spacer were then injected in the cell and left on the surface for over an hour to stick on the gold. Then the cell was washed with the buffer in which the protein was dissolved. Measurements were taken to check the Fab stuck on the surface. If there was a shift toward the red in the spectra, we knew it had worked.

3.5 Analyte preparation:

3.5.1 Preparation of virus solutions:

All viruses used in this thesis were plant viruses. They were provided by Dr. Chantal Keijzer and Dr. Andy Love. Virus solutions for biosensing were prepared in our laboratory at the School of Chemistry, as well as all buffer exchange procedures. Plants were grown over 6 weeks. They were infected by the virus around week 4. The preparations details of virus solutions are given below[9].

A) Cauliflower mosaic virus:

In the case of the Cauliflower mosaic virus (CaMV) the virus preparation was done over 3 days in a cold room (4ºC). Leaves were collected from the infected plants then put into a blender and ground up with 2 mg/L and potassium phosphate buffer (0.5 M KPO4 buffer, pH 7.2 containing 0.75% Sodium sulphite). The liquid was transferred to a beaker, 1 M of

Urea and triton X – 100 was added to the mixture. The beaker was left overnight covered with foil under a gentle stirring. The following day, the extract was transferred into tubes and spun in a centrifuge for 10 min. The supernatant was filtered and put into tubes in the centrifuge at 45 Krpm for an hour at 4ºC. The pellets were re-suspended in 2mL of water. The tubes were put on a shaker in the cold room for an hour. The solution was spun to clear for 15 min at 4°C at 4.5 Krpm. The supernatant was transferred into 4 mL tubes and mixed with phosphate sulphite buffer, then centrifuged for 1h at 4ºC at 45 Krpm. The supernatant was then discarded, and the pellets re-suspended in 1 mL buffer. The solution was left to dissolve overnight. Finally, a density gradient centrifugation was performed. Several solutions were prepared.1.25ml of: 40%-35%-30%-25%-20%-15%-10% sucrose solutions in appropriate buffer were poured in tubes and set for centrifugation at 35 Krpm for 3h at 4°C. The clear band (the virus containing one) was then collected. This was centrifuged at 45 Krpm for 1h at 4°C, and the pellets left to dissolve overnight in the appropriate buffer at 4°C.

B) Cucumber mosaic virus:

Similarly to the CaMV, the plants were infected after 4 weeks of growth with N. benthamiana. The plants were infected when their leaves reached the size of 3 cm – 4 cm. The infection with cucumber mosaic virus (CMV) was done in the following way. The infected leaves were ground up using a mortar with 1 – 2 mL of water. The sap was collected in an Eppendorf and cellite was added to the preparation. 10 µL of sap was taken to infect the plants by rubbing their leaves with it. The plants were put in a chamber to carry on growing. Symptoms were visible after 5 to 10 days. The next step was the virus preparation. The infected leaves were harvested. Manipulation for this preparation must be done in a fumehood. The leaves were placed in a blender 1 mL of ice-cold buffer A (0.1 sodium citrate, pH 7.0, 20 mM EDTA ,0.1% sodium diethyldithiocarbamate (DIECA) (w/v), 0.1% (v/v) 2-mercaptoethanol) was added for 1 g of infected tissue. The mixture was blended first at low speed and then, when all the tissue had passed through the blend, at high speed. After that, it was transferred to a 1 L bottle and ice-cold chloroform 1:1 was added. After being mixed, the solution was transferred into tubes to be centrifuged for 10 min at 4ºC at 10 Krpm. The aqueous phase was removed and passed through a miracloth filter. After that, it was transferred into centrifuge tubes and mixed with 5 mL of buffer A + 10% sucrose. This was spun for 1h30 min at 4ºC at 35 Krpm. The supernatant was discarded, and the pellets re-suspended in 3 – 5 mL of buffer B (10 mM Tris, pH 7.0, 0.5 mM EDTA, 2% Triton X-100). The pellets were then left overnight to dissolve. The next day, the pellets were briefly vortexed and then stirred at 4ºC for 2h. Then the solution was centrifuged at 4.5 Krpm for

15 min at 4ºC. The supernatant was discarded and 5 mL of a solution of buffer C + 10% sucrose was added (buffer C = 10 mM Tris, pH 7.0, 0.5 mM EDTA). Then the tubes were centrifuged for 1h 30 min at 35 Krpm. The supernatant was discarded and 2mL – 5mL of cold buffer C was added to the pellet. The pellets were left to dissolve overnight at 4ºC. The following day, the OD260 was measured and compared to the extinction coefficient, in order to obtain the virus concentration. This virus can be stored at 20ºC if mixed with 50% sterile glycerol. Otherwise it is stored at 4ºC.

C) Cow pea mosaic virus:

The preparation of cow pea mosaic virus (CpMV) was done according to the following process. Leaves were harvested and then blended with 0.1 M phosphate buffer pH 7 (3 mL for 1g tissue). The mixture was squeezed between two muslin cloths. Then it was centrifuged at 10 krpm at 4ºC for 20 min. PEG 6000 was added to the supernatant to a concentration of 4%, as well as 0.2 M NaCl. The solution was stirred for 1h to dissolve the PEG and get the virus particles to precipitate. Then the solution was centrifuged at 4ºC at 10 Krpm for 20 min. The pellets were re-suspended in 10 mM sodium phosphate buffer pH 7.0 (0.5 mL/ g of tissue). The dissolved pellets were centrifuged for 20 min at 15 Krpm at 4ºC. The supernatant was centrifuged again at 35 Krpm for 2h30 min at 4ºC. The pellets were re-suspended in sodium phosphate buffer (small amount ≈ 500 µL). The liquid was collected and centrifuged with an Eppendorf centrifuge at 10,000 xg for 15 min (this removed eventual plant contamination, pieces of leaves). The supernatant contained both RNA-containing and empty particles. The concentration of the empty particles can be determined by UV-spectroscopy. The concentration of virions was determined with bicinchoninic acid assay (BCA). The particles were purified using a sucrose gradient, the method is detailed in CAMV protocol.

3.5.2 Microscopy:

In this thesis we will show virus images taken by Dr Andrew Love with a transmission microscope (TEM). We describe here the process of this high-resolution microscope. This microscope works in a similar way to a light microscope except that it uses electrons instead of light, the source of which being an electron gun. An electron beam is sharply focused, via electromagnetic lenses (because electrons are negatively charged) and is transmitted through a thin sample under vacuum. The transmitted electrons are collected on a charge coupled device (CCD) camera. An image is collected from the electron transmitted through the surface. This image is enlarged by passing down through several lenses. The dark spot of a TEM imaging is an area of low electron transmission, and the bright spots are the area of high electron transmission. TEM images provide information about the material

composition compared to a scanning electron macroscope (SEM) which focuses only on the surface of a material.

The samples used in TEM must be less than 100 nm thick, otherwise the electrons cannot pass through. The samples put under TEM in this thesis were stained with dye. This enhances the absorption and reduces the quasi-transparency of the biological samples.

The TEM used in this thesis is the high contract 120 kV Jeol JEM-1400. The Gatan orius CCD camera has a resolution of 4008 x 2672 pixels.

3.5.3 Preparation of protein solutions:

We grew the proteins in Dr Lapthorn laboratory, a biology laboratory where the conditions were optimal for protein growth and purification. First, the cells were grown overnight in Luria broth (LB media) and 10 µL of ampicillin at 37ºC under gentle shaking. One litre of media was dispatched between 4 flasks, into which the cells (grown in the overnight tube) were added. The flasks were put in the incubator (37ºC) for 2h30. The optical density (OD) of the solution was measured at 600 nm. If the OD was around 0.6 then Isopropyl β-D-thiogalactopyranoside (IPTG) was added into the flasks, otherwise the flasks were incubated a bit longer. The mixture was then ice-shocked by putting the flasks in ice for 2 min to 3 min. Next, the flasks were put in the incubator at 16ºC overnight. Then the protein cells were harvested. The liquid in the flasks was put in two plastic bottles into the centrifuge at 4°C at 5 Krpm for 15 min. The pellets were then re-suspended in 50 mM tris pH 7.4. The pellets were collected and sonicated for 15 min. Finally, the solution was centrifuged for 20 min at 5 Krpm. The following day the protein solutions were purified. The frozen pellets of cells were thawed and fully mixed before the cells were broken open. The tubes of cells were put in a beaker of slushy ice to maintain the temperature of the solution at 4°C. The solution was sonicated for 20 min with 30 seconds of sonication followed by 30 seconds of rest (frequency 10 A), to break the cells and stop the sample from overheating and denaturing the protein. After sonification, the liquid was centrifuged at 24 Krpm for 30 minutes to separate the cell debris and insoluble material from the soluble cell contents. Then the liquid was put through a Ni-affinity column. This kind of column, immobilised metal affinity chromatography (IMAC), is commonly used for His – Tag proteins because there is a specific covalent bond between amino acid and metal particularly for Histidine. The cell lysate was passed through a nickel resin column that had been equilibrated with a 20 mM Tris buffer pH 7.9. Three samples were collected: the flow through, the wash and the elute using wash buffer (20 mM Tris 0.5 M NaCl 20 mM imidazole pH 7.9) and elute buffer (20 mM tris HCl 0.5 M NaCl 0.3 mM imidazole). The proteins were eluted with buffer. The protein concentration was determined by UV absorption. This was done with the nanodrop 1000

(Thermos Fisher Scientific). This method is based on the fact that some amino acids (tryptophan and tyrosine) exhibit a peak at 280 nm due to their aromatic group. From the literature, we can get the protein molecular extinction coefficient and calculate the concentration in mg/mL.

3.5.4 Protein crystallisation:

The protein we wished to crystallise was first re-concentrated by centrifuging it, to reach the concentration of 15 mg/mL. Then crystallisation trays were used to test several buffer conditions. In order to obtain these crystals, we used precipitation agents in the buffer tested for crystallisation. These agents are different salts and polymers mixed in different concentration. 1µL of the protein solution was added into a well on the crystallization plate and mixed with 10 µL of buffer. The proteins were left to crystallise for two days. The solutions were then checked under a microscope to spot protein crystals or precipitate. If one of the two was found, another crystallisation plate was set up with conditions close to the one that gave promising result. Several types of crystal were observed during the process: needles or three dimensions crystals.

3.5.5 Protein dialysis:

The type II dehydroquinase protein (DHQ) samples we made contained EDTA due to the purification process used only with DHQ protein. To remove it, we performed a dialysis. This technique is used to exchange buffers the protein is in. The technique is very straightforward, the protein in its buffer is put into a membrane and the membrane is then immersed into 2L of a non EDTA containing buffer. The buffer can go through the membrane, but the protein cannot. After a certain time, the protein in the membrane is dissolved in the non EDTA containing buffer. Here is how we proceeded. 100 mL of 1 molar tris buffer pH 8 was dissolved in 1.9 L water. 4 mL of the protein solution was poured in a cellulose membrane (Sigma-Aldrich: dialysis cellulose membrane flat width 25 mm retain most protein of molecular weight 12,000 Da or greater). The cellulose membrane was kept in a sodium chloride solution, and before use it was washed with tap water (inside and out). Two clamps were used to maintain the protein solution inside the membrane. The cellulose membrane was then immersed in the 2 L solution of tris buffer. This was left under gentle stirring for a day in a cold room (4°C). The protein was then pipetted out of the membrane, the diluted buffer was collected. The protein concentration was checked again by UV absorption using a nanodrop spectrometer.

3.6 Data modelling:

3.6.1 Phase asymmetry

In this thesis the asymmetry will be characterised by the phase parameter given by the matching equation[10,11] (chapter 2). Any alteration in the reflectance spectra is subtle so the data were matched, and the asymmetry parameter was used to display the asymmetry. Here, we focused on the change in the phase between LH and RH reflectance and this was calculated as follows:

$$\Delta\varphi_{RH/LH} = \varphi^{RH/LH}_{(analyte)} - \varphi^{RH/LH}_{(buffer)} \quad (10)$$

$$\Delta\Delta\varphi = \Delta\varphi_{RH} - \Delta\varphi_{LH} \quad (11)$$

The $\Delta\Delta\varphi$ value was used to quantify the phase change of the signal between the LH and RH reflectivity spectra.

3.6.2 Electrostatic maps:

Electrostatic maps of the DHQ protein, will be produced later in this thesis (in chapter 4). These maps show the electrostatic charges on the protein surface. They were generated after following several steps. Indeed, information about the protein structure was first needed. Dr Adrian Lapthorn was given the crystal of DHQ, we had previously made by finding the right buffer conditions, to perform X-ray diffraction on them. From there we generated pdb files; these files contain information about the protein structure such as nucleic acid atom coordinates (in Angströms), the occupancy and the temperature factor. For DHQ 15 and 38 these files were loaded in a server (PDB2PQR server version 2.0.0), to generate the protein structure at 3 different pHs conditions. This server generated a pqr file that contained information about the amino acid atoms coordinates and their charges. This last step is not needed to get the electrostatic maps if we do not change the pH. The pqr or the pdb file was then opened in PyMOL (version 1.40). PyMOL software by Schrödinger is a software of molecular visualisation, developed in Python. A plugin of this software Adaptative Poisson-Boltzmann solver (APBS) which applied the Poisson-Boltzmann equation to the protein was used to generate the electrostatic maps. We recall here that the Poisson-Boltzmann equation is used to calculate the electrostatic potential of an electric charge in solution, incorporating the ionic strength of the solution and the thermic effect on the particles in solution.

The plugin set a grid on the protein and from there ran the calculation. It then generated a map displaying the overall net charges of the protein (figure 3 - 14).

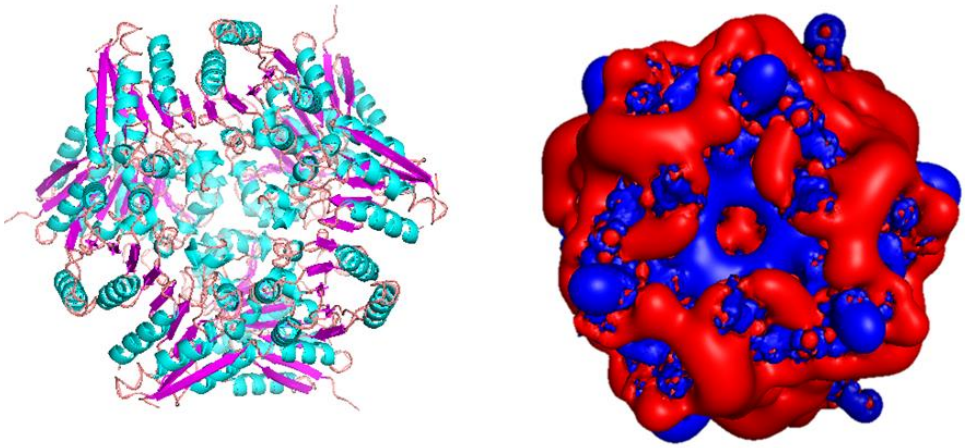

Figure 3 - 14: PyMOL generated electrostatic map. The figure on the left shows the structure of DHQ 12, the figure on the right is the electrostatic map for the same protein, generated using APBS plugging.

3.7 References:

(1) Karimullah, A. S.; Jack, C.; Tullius, R.; Rotello, V. M.; Cooke, G.; Gadegaard, N.; Barron, L. D.; Kadodwala, M. Disposable Plasmonics: Plastic Templated Plasmonic Metamaterials with Tunable Chirality. Adv. Mater. (2015), 27 (37), 5610–5616.

(2) Gadegaard, N.; Mosler, S.; Larsen, N. B. Biomimetic Polymer Nanostructures by Injection Molding. Macromol. Mater. Eng. (2003), 288 (1), 76–83.

(3) Bain, C. D.; Biebuyck, H. A.; Whitesides, G. M. Comparison of Self -Assembled Monolayers on Gold: Coadsorption of Thiols and Disulfides. Langmuir (1989), N° 5, 723–727.

(4) Prime, K. L.; Whitesides, G. M. Adsorption of Proteins onto Surfaces Containing End-Attached Oligo (Ethylene Oxide): A Model System Using Self-Assembled Monolayers. J. Am. Chem. Soc. (1993), 115 (23), 10714–10721.

(5) Sigal, G. B.; Bamdad, C.; Barberis, A.; Strominger, J.; Whitesides, G. M. A Self-Assembled Monolayer for the Binding and Study of Histidine-Tagged Proteins by Surface Plasmon Resonance. Anal. Chem. (1996), 68 (3), 490–497.

(6) Ostuni, E.; Yan, L.; Whitesides, G. M. The Interaction of Proteins and Cells with Self-Assembled Monolayers of Alkanethiolates on Gold and Silver. Colloids Surf B Biointerfaces (1999), 15 (1), 3–30.

(7) Prime, K. L.; Whitesides, G. M. Self-Assembled Organic Monolayers : Model Systems for Studying Adsorption of Proteins at Surfaces. Science (1991), 252 (5009), 1164–1167.

(8) Crivianu-Gaita, V.; Thompson, M. Immobilization of Fab' Fragments onto Substrate Surfaces: A Survey of Methods and Applications. Biosens. Bioelectron. (2015), 70, 167–180.

(9) Foster, G. D.; Taylor, S. C. (Eds.) Plant Virology Protocols. From Virus Isolation to Transgenic Resistance. MIMB vol.81 (1998).

(10) Tassin, P.; Zhang, L.; Zhao, R.; Jain, A.; Koschny, T.; Soukoulis, C. M. Electromagnetically Induced Transparency and Absorption in Metamaterials: The Radiating Two-Oscillator Model and Its Experimental Confirmation. Phys. Rev. Lett. (2012), 109 (18), 1–5.

(11) Gu, J.; Singh, R.; Liu, X.; Zhang, X.; Ma, Y.; Zhang, S.; Maier, S. A.; Tian, Z.; Azad, A. K.; Chen, H- T.; et al. Active Control of Electromagnetically Induced Transparency Analogue in Terahertz Metamaterials. Nat. Commun. (2012), 3, 1151–1156.

Chapter 4: Protein surface charges chirality sensed using chiral plasmonic nanostructures

The surface charge distributions of complex biomolecules such as proteins is a unique fingerprint. The charges affect proteins characteristics and functions such as folding and electrostatic interactions. Therefore, it is a key concept in understanding chemical processes in biology. Proteins can exhibit different states of surface charges depending on the environment. Currently, it is possible to predict the distribution of charges only for proteins that have well known sequences and structures. In this chapter, we show that this essential property currently “invisible” to optical spectroscopy, can be detected by monitoring asymmetries in the chiroptical response of protein-plasmonic nanostructures complexes.

4.1 Introduction:

Proteins are made up of smaller building blocks called amino acids that are attached to one another by peptide bonds, forming a polypeptide chain. These amino acids can be polar or non-polar and contribute to the overall charge of a protein. The ionisable amino acid residue at protein surfaces results in a stereo-specific charge distribution that directs how proteins interact with the surrounding environment. Since surface charges play a role in electrostatic interaction between molecules, they can influence the folding of proteins and thus their function[1–3]. This fundamental physical property can influence the solubility, the aggregation and the crystallisation of the protein. The surface charges depend on the local environment of the protein, more specifically the pH of the solution the protein is resuspended in[3]. Nowadays, available experimental information is limited but it is possible to model the distribution of charges of proteins that have well-defined primary sequences and structures[4,5]. Most of the established spectroscopy techniques such as circular dichroism (CD), UV – visible absorbance and X – Ray are insensitive to the surface charge distributions[4], except for techniques such as isoelectric focusing. Electrophoresis, which can be a gel or a capillary[6], is a separation method in which biomolecules are separated according to their isoelectric points, zero net charges, within a continuous pH gradient[7,8,9]. With conventional spectroscopy the surface charge distribution does not give rise to a definitive spectral fingerprint. Indeed, the intensity of spectroscopy to electrostatic properties arises because chromophores / electronic transitions of the amino acids are not significantly perturbed by the ionisation state of the side chains. Currently there is no known spectroscopic phenomenon that allows rapid characterisation of chiral surface charge distributions.

Here we will be using structurally homologous series of enzymes type II dehydroquinase (DHQase), derived from different organisms. DHQase enzymes are involved in the Shikimate pathway[10] and have been widely studied and thus have well characterised sequences, allowing the surface charge distributions on these proteins to be mapped. These proteins have a similar higher order structure (secondary and tertiary), however, the different primary structures (linear sequence) will cause them to have slightly different surface charge distributions[11] but they are indistinguishable with conventional structurally sensitive spectroscopy (i.e. circular dichroism). In general, DHQases are stable with the pH scale ranging from acidic to basic. Hence, by varying solution pH, surface charge distributions can be manipulated in a systematic and controllable manner without distorting the structure. Moreover sequence-diverse over-expression clones of DHQase were available to us. First, we focused on two forms of type II DHQase to verify that chiral plasmonic fields could be used to detect protein surface charges. In more detail, two recombinant His-tagged DHQase proteins were used: *Propionibacterium acnes (*DHQ 15) and *Zymomonas mobilis* (DHQ 38) overexpressed in tris buffer. The His-tagged DHQ 15 and DHQ 38 were immobilised on a metal surface in a similar orientation by means of a self-assembled monolayer[12]. The PyMOL software with Adaptative Poisson-Boltzmann Solver (APBS) plug-ing was used to produce electrostatic maps of DHQase, depending on the pH[5]. Here, we hypothesised that chiroptical properties of chiral plasmonic structures are altered by the chiral charge distributions of adsorbed biomacromolecules. The changes induced for left- and right-handed plasmonic nanostructures are asymmetric and reflect the chirality and sign of the biomolecular charge distribution, as shown in the ORD by a change in the amplitude of the signal and a phase change in the reflectivity. The theory developed here is as follows: the protein induced a mirror image of its charges onto the gold surface and a change in the gold charge distribution and subsequently enhanced or diminished the fields produced by the nanostructures, depending on the nanostructure handedness. This theory was then tested on more DHQases with different sequences.

Chiral plasmonic systems have already been demonstrated to provide ultrasensitive: enantiomeric detection[13,14], secondary structure characterisation[15,16], and detecting levels of structural order in biolayers[17]. These observations have been rationalised in terms of the interaction of chiral near fields with adsorbed biomaterials. The chiral near fields have a greater chiral asymmetry than equivalent circularly polarised light, a property referred to as superchirality (chapter 2). In this chapter, we describe a new chiral plasmonic phenomenon, the perturbation of chiral plasmonic properties by static chiral charge distributions. We have applied an asymmetry parameter to detect the surface charge density of the protein. Being able to predict the distribution of surface charge of a protein will help to better understand

electrostatic interaction and thus other processes in which proteins are involved. Moreover, it allows for the prediction of the physical behaviour of the protein without prior knowledge of the structure.

4.2 Theory:

4.2.1 Biophysical meaning of surface charges:

The surface distribution of charges in proteins in general has a direct impact on many biochemical processes including ligand-protein interactions, protein folding, aggregation of protein, crystallisation, electron exchange, the mobility in solutions and the stability of a protein at different pH values[3]. The surface charge distribution of a protein strongly depends on the local environment and will change according to the pH[3]. This change in the charge distribution leads to changes in biochemical processes listed above. For example, if a protein is in a solution with a pH at a distant value from its isoelectric point (pI), it creates an excess of charges at the surface (negative or positive) allowing the protein to unfold, which can be verified by a change in the pKa value. Proteins have specific pKa values at physiologic pH, however, these values will change when the proteins folds change. Proteins protonation or deprotonation occurs via functional groups C- and N- terminal and some amino acids being charged at physiological pH. Table 4 – 1 lists the amino acid known to display charges at physiological pH.

amino acid	charge
aspartic acid	-
glutamic acid	-
Lysine	+
Arginine	+
Histidine	+

Table 4 - 1: Amino acid with charges at physiological pH.

There is a unique parameter for each protein which is an indicator of the protein surface charge according to the pH. This parameter is called the pI and is the pH value at which the density of surface charge of the protein is even. At the pI the protein is a zwitterion (no overall net charge), and usually aggregates[18,19] and precipitates in protein solution. When the pH is higher or lower than the pI, the protein will have an excess of negative or positive charges at the surface, respectively (figure 4 – 1). This parameter can be applied to bacteria and viruses as well and can be determined by isoelectric focusing[20].

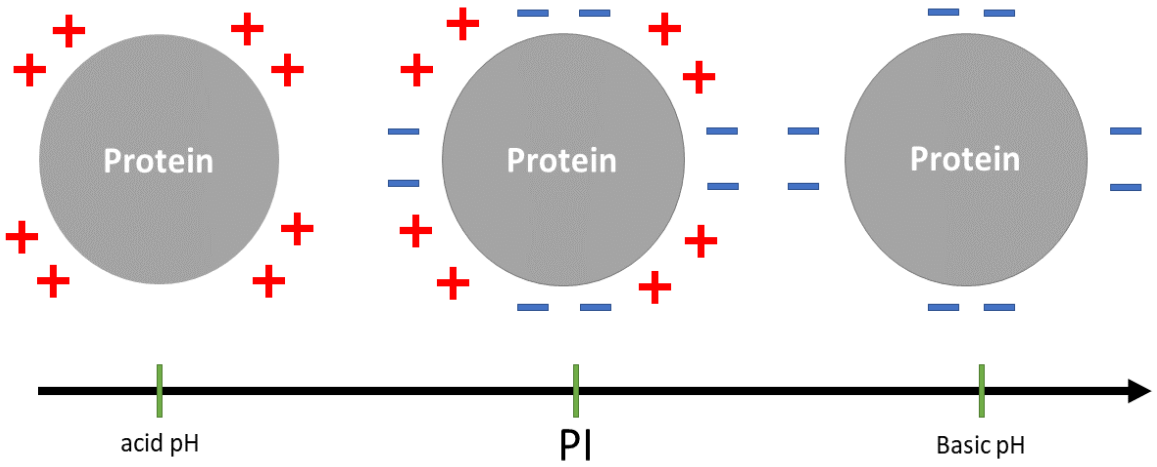

Figure 4 - 1: Surface charges behaviour of the protein around its pI

4.2.2 Type II dehydroquinase (DHQase):

DHQases are proteins involved in the third step of the Shikimate pathway catalysing the 3-dehydroquinate in 3-dehydroshikimate[10]. The Shikimate pathway is a chain of biosynthetic reactions that generate aromatic amino acids (tyrosine, tryptophan and phenylamine). These reactions take place in plants, fungi and bacteria and do not exist in mammals. DHQases are made up of an ensemble of 12 monomers that have a molecular weight of about 16,000 Da. DHQases enzymes are typically 150 amino acids in length, easily produced, have high stability both thermally (up to 87°C) and to extreme pH[11,21,22]. DHQases have a dodecamer quaternary structure (diameter ~ 10 nm), point group T which can be described as a tetramer of trimers. This limits significantly the orientations the molecules can adopt on the surface, linked via the N-terminal histidine tag (figure 4 - 2). This reduces asymmetries in the chiroptical response of the protein-chiral plasmonic nanostructure complex due to orientation effects.

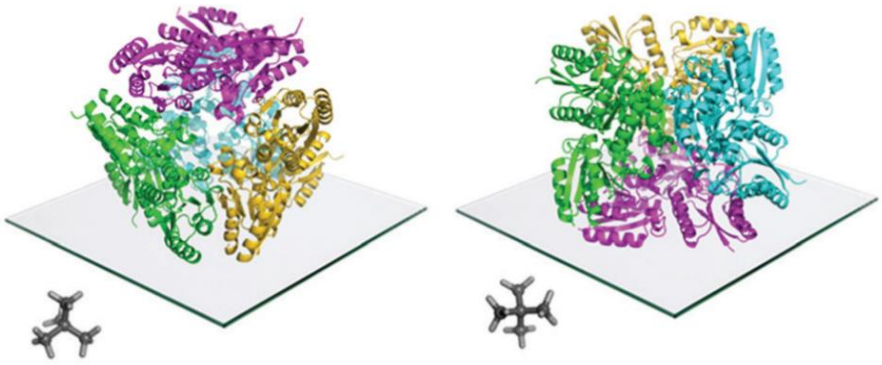

Figure 4 – 2: Illustration of the two orientations that the DHQase proteins can adopt on the surface of the metafilm. The trimers of molecules are coloured the same to highlight the tetramer of trimers. A neopentane ball and stick molecule is shown as an insert to highlight more easily how the symmetry is related to the surface.

These structures are given numbers to differentiate them such as DHQ 3, DHQ 5 or DHQ 8. The primary structure of DHQase is strongly conserved with 47 % of invariant structure. Since the structures and sequences of DHQ molecules are known, we used this information to map their charge distribution and check that the prediction from our experimental data matched the theoretical one.

4.3 Results and discussion:

4.3.1: Influence of the pH on plasmonic nanostructures:

First, we confirmed that the substrate we used could be exposed at pH scale ranges from acidic to basic without causing damage. The substrate was coated with a self-assembled monolayer (SAM) that was made of nitrilotriacetic acid (NTA) and a spacer triethylene glycol mono-11-mercaptoundecyl (EG-thiol)[23]. The His-tagged DHQs bind to the NTA head groups and the EG-thiol prevent non-specific interactions with the surrounding surface[17]. This strategy both immobilises DHQ in a well-defined orientation and minimises potential distortions of the higher order structure. The spacer is hydrophilic and thus attracts ions H^+ and it is slightly protonated and therefore induces a small error in the pH value[24]. Thus, the pH at the surface of the metafilm is slightly lower than the pH of the buffer that we used, however, this small error did not affect the protein measurements. Moreover, the metafilm being insensitive to the pH change (figure 4 - 3), any effect observed after taking the measurements had to be protein induced.

As there is no change in the shape of the signal, we have demonstrated that the nanostructures are not damaged at any of the pH values tested. There was also no change in the height of the ORD signal, hence a change of pH on its own did not affect the chiral fields induced by the nanostructures. We have also excluded any damage to the SAM as shown by the absence of a blue shift in the ORD and this was confirmed by the reflectance data (figure 4 – 3). The data showed that charges alone did not interfere with the chiral field. Moreover, we can add that the use of a SAM minimised the possibility of structural desorption of the proteins when immobilised on the surface.

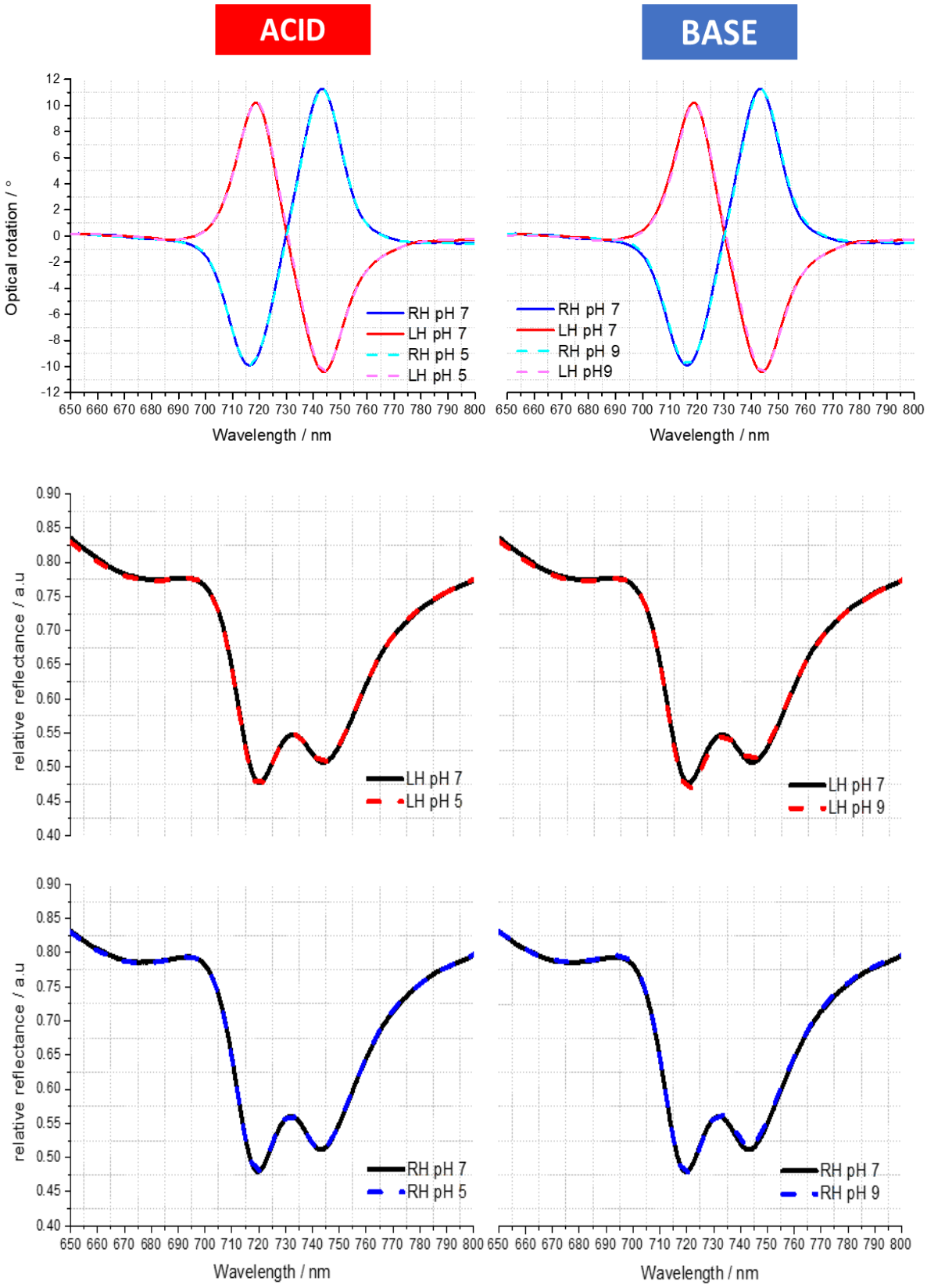

Figure 4 - 3: ORD and reflectance spectra of LH and RH nanostructures from NTA coated substrate at pH 5, pH 7 and pH 9.

4.3.2 Influence of the surface charge distribution on the asymmetry:

The surface charges of a protein can be altered by changing the pH of the solution the protein is resuspended in. The DHQase from *Propionibacterium acnes* (DHQ 15) and *Zymomonas mobilis* (DHQ 38) with a pI of 6.24 and 7.26, respectively, were exposed at different pH from acidic, pH 5, to basic pH 9 via neutral pH 7.5, to assess their effect on chiral fields. DHQ 15 and DHQ 38 have a 43% identical amino acid sequence over 145 acid residues with essentially the same secondary, tertiary and quaternary structure. This was confirmed by determining the X-ray structures of the two proteins (Appendix – figure 4 – 17). The structures have a root-mean deviation over 110 residues of 1.3 Å with the largest difference in the flexible 10 residue lid domain that is seen in all DHQases (figure 4 – 4)[11]. A Bis-Tris propane buffer was used because it has a broad pH range (pH 2.5 to pH 9.5) that will allow DHQ molecules to stay in solution without precipitating. Given the pI of the DHQase this range of the pH should generate both positively and negatively charged forms of the protein. For CD measurements at pH 5, an acetate buffer was used (citric acid, mixed with the Bis-Tris propane to produce the desired buffer pH, is not transparent in the UV). At pH 7.5 and pH 9 Tris buffer was used.

4.3.2.1 DHQ38 and DHQ15 surface charges with pH:

First, we carried out a simulation of the distribution of charge at the protein surface using the PyMOL software. The crystal structures of DHQ 15 and DHQ 38 were used to investigate the effect of changing pH by calculating the protonation and atomic charges for all atoms of both DHQ 15 and DHQ 38 dodecamers at the three pH values studied. The 20 amino acid N-terminal histidine tag was omitted from the model and calculations as this was shown not to adopt an ordered structure in most structures. The overall net charge of the proteins was calculated with the plug-ing APBS in PyMOL by using the Poisson-Boltzmann equation that is often used to characterise the electrostatic state of the surface[25,26]. This equation takes into account the solvent and salt effects, with the input of a local dielectric constant. As mentioned previously, this equation can be applied to proteins with known structures. An electrostatic map was drawn from each protein tested at the different pH values and is displayed in figure 4 - 4. The proteins behaved as expected; the positive charges and negative charges dominated at an acidic pH or basic pH, respectively. The chiral electrostatic potential of the proteins changes significantly from positive to negative as the pH is switched from below to above the isoelectric points of the proteins. In figure 4 - 4, both proteins are displayed in the same orientation for both the structure and the electrostatic maps.

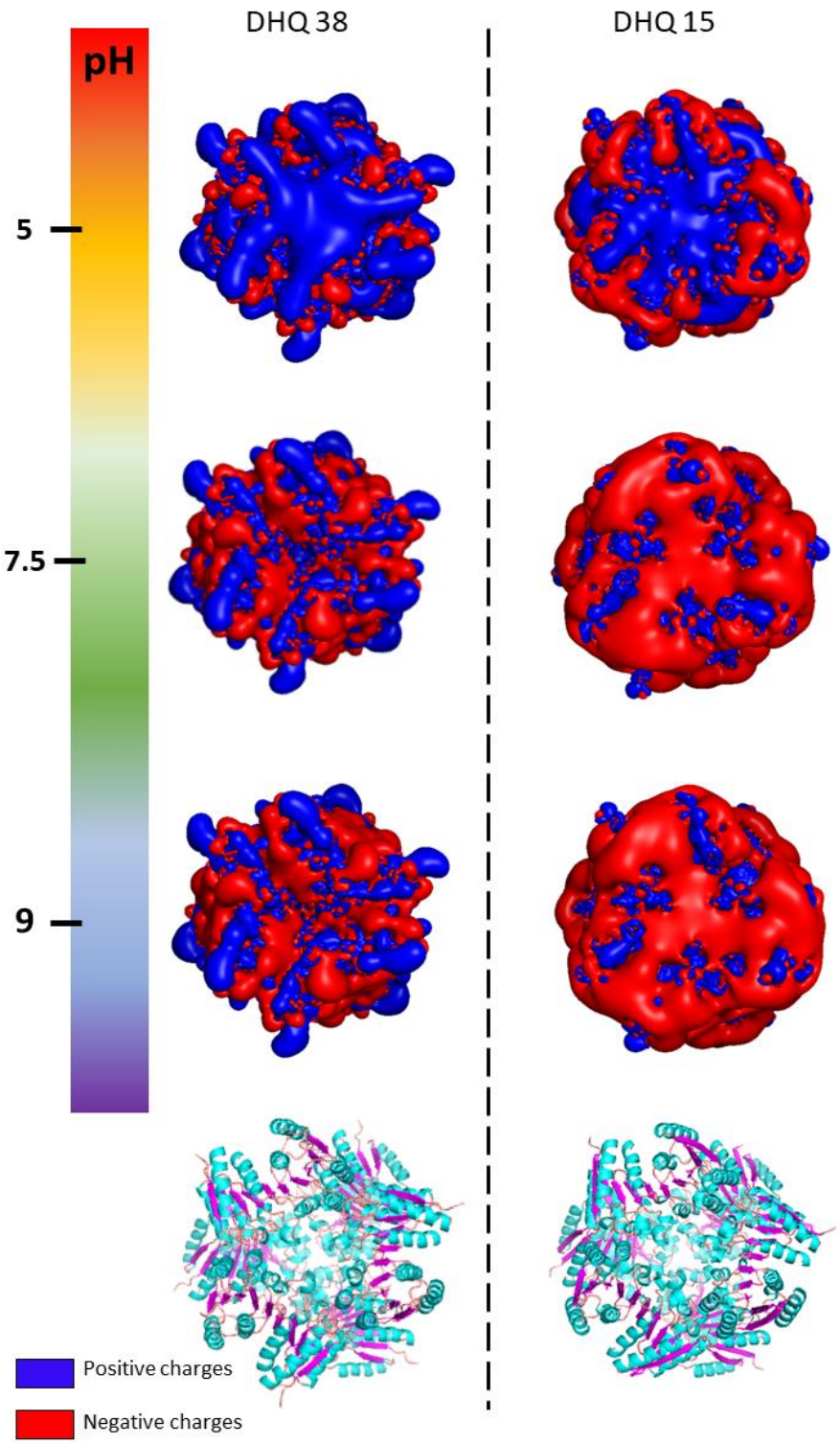

Figure 4 - 4: PyMOL generated electrostatic potential map of DHQ 38 (PDB code 6SMF) and DHQ 15 (PDB code 6SME). The figure shows the changes in the overall net charges as the pH increases going from 5 (top) to 9 (bottom) with the ribbon representation of the two dodecamers shown below for comparison (α helix and β sheet coloured cyan and magenta respectively). The charge densities at all the pHs have an intrinsic anticlockwise (i.e., left-handed) sense of twist.

Figure 4 - 4 shows that the DHQases behaved slightly differently as a function of pH. For example, at pH 7.5 DHQ 38 has a more even distribution of charges than DHQ 15. This is due to the difference in the pI. DHQ 38 almost reaches its pI value at pH 7.5. Because the pI of DHQ 15 is lower, it will display a majority of negative net charges at a lower pH, and thus the distribution of surface charges at pH 7.5 cannot be even.

4.3.2.2 Influence of surface charges on the chiral plasmonic fields:

The stability of DHQ 15 and DHQ 38 in solution over a pH range of 5 – 9 was confirmed using CD. The CD spectra for both DHQ 15 and DHQ 38 are shown in figure 4 - 5. The proteins could be resuspended in buffer at different pH values without leading to denaturation (misfold) using CD. A misfolded protein leads to a loss of the quaternary, tertiary and secondary structures, and displays an unfolded state. CD can be used to detect a change in the secondary structure (β-sheets, α-helix)[27] and thus is a reliable method to confirm the stability of a protein. We were able to detect the characteristic signal of α-helix that these proteins usually exhibit at this UV range. The far-UV region CD spectra display no significant changes, which is consistent with the secondary structures remaining intact (i.e they do not denature). Near-UV CD spectrum which is sensitive to the higher order structure (tertiary) does not display dramatic changes that would be consistent with significant change in high order structure. Any slight variations with the pH, seen in the far UV spectra, can be assigned to changes in the aggregation state since the pI of the DHQ is very close to pH 7. Consequently, the CD data provide strong evidence that over the pH range used, there is no change in the higher order structure of the DHQ which could affect the reflectance and ORD measurements.

The difference in the intensity, between DHQ 15 and DHQ 38 CD spectra, was due to the number of proteins in solution: DHQ 38 solution had a lower concentration than DHQ 15. We take the opportunity here to show that the proteins give the same signal with CD, therefore it is not possible to distinguish them from one another.

In order to monitor asymmetries induced by the immobilised proteins in reflectance and ORD spectra collected from LH and RH structures, we exposed the proteins to plasmonic fields. The proteins are symmetric and either have a spherical (DHQ 15) or cubic (DHQ 38) geometry and do not produce an asymmetry in the shift of the signal (ΔΔλ). The shift in LH and RH signal is equal.

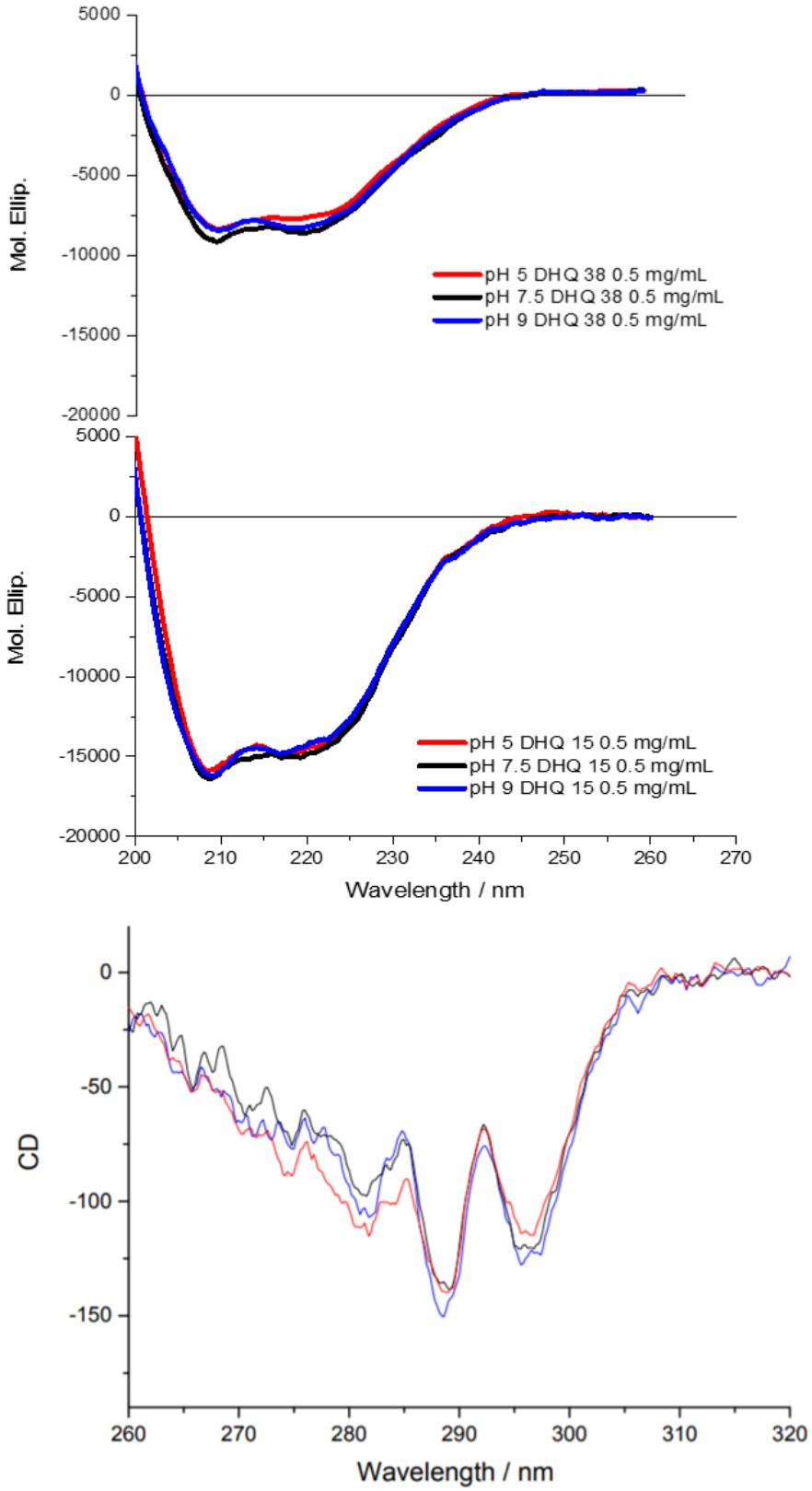

Figure 4 - 5: CD spectra of DHQ 38 (top) and DHQ 15 (bottom) taken in the far UV at three different pH values: pH 5, pH 7.5 and pH 9. The red line represents pH 5 (acidic), the black line shows the neutral pH 7.5 and the blue line the highest pH 9 (basic).

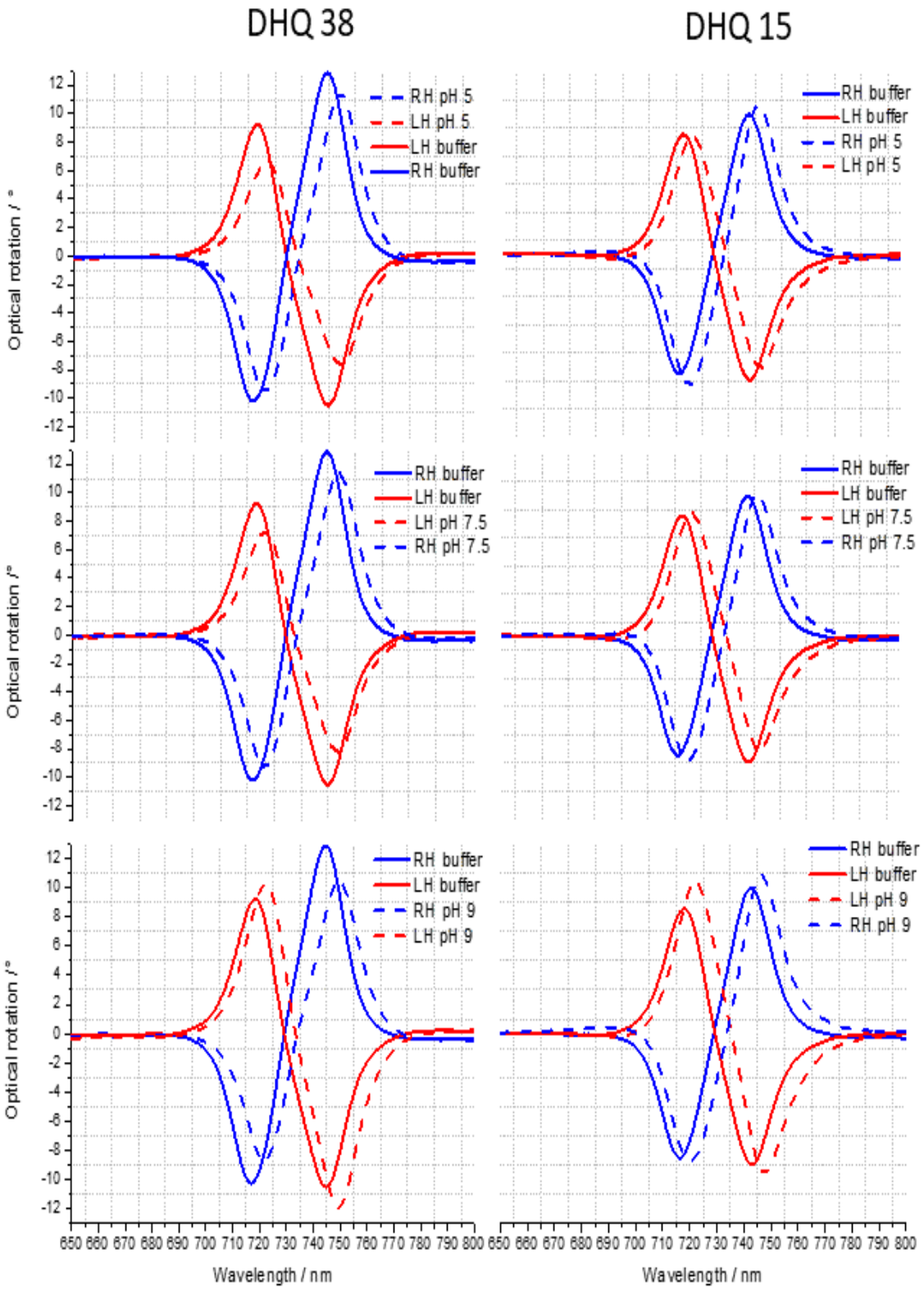

Figure 4 - 6: ORD spectra of DHQ 38 and DHQ 15 at pH 5, pH 7.5 or pH 9. The measurement called buffer (straight line) were taken at pH 7.5. The dots line is the measurement of the proteins in the buffer solution with pH 5, 7.5 and 9.

We obtained similar results with both proteins in the ORD signal (figure 4 - 6). The data clearly show an asymmetric change in the optical properties of LH and RH structures. The asymmetries in the ORD are parameterised using a factor A (chapter 3) derived from the relative changes in the peak to peak height of the bisignate line shape (table 4 - 2). No asymmetric changes occur when the pH is changed by the buffer in the absence of immobilised DHQases (section 4.3.1), however the asymmetry parameters are dependent on both the DHQase and the pH. We noticed that the RH signal differed between the two DHQ molecules, but the LH signal showed the same change.

Moreover, when the pH increased, the LH ORD became higher, while the RH ORD became higher or lower for DHQ 15 or DHQ 38, respectively. When DHQ 38 was loaded onto the surface at pH 7.5 which is close to the pI of DHQ 38, we observed that the height of both the RH and LH ORD decreased. Whereas, DHQ 15 at pH 7.5 had a similar height in the ORD as the buffer signal.

	DHQ 15			DHQ 38		
pH	5	7.5	9	5	7.5	9
charges	18	-64	-69	74	-4	-9
Optical parameters						
A	1.15 ± 0.02	1.07 ± 0.02	0.93 ± 0.02	1.25 ± 0.02	1.13 ± 0.02	0.75 ± 0.02
matching parameters						
ΔΔφ	-1.50 ± 0.20	-0.40 ± 0.20	3.40 ± 0.20	0.15 ± 0.20	-2.30 ± 0.20	-3.60 ± 0.20

Table 4 - 2: A (RH/LH ratio), matching parameters and net charges for DHQ 15 and DHQ 38 with pH 5, pH 7.5 or pH 9.

The A value showed the same trend for DHQ 15 and DHQ 38, with the asymmetry in DHQ 38 being larger: A decreases with increasing pH from > 1 at pH 5 to < 1 at pH 9. We notice that the absolute value of A differs between the two proteins.

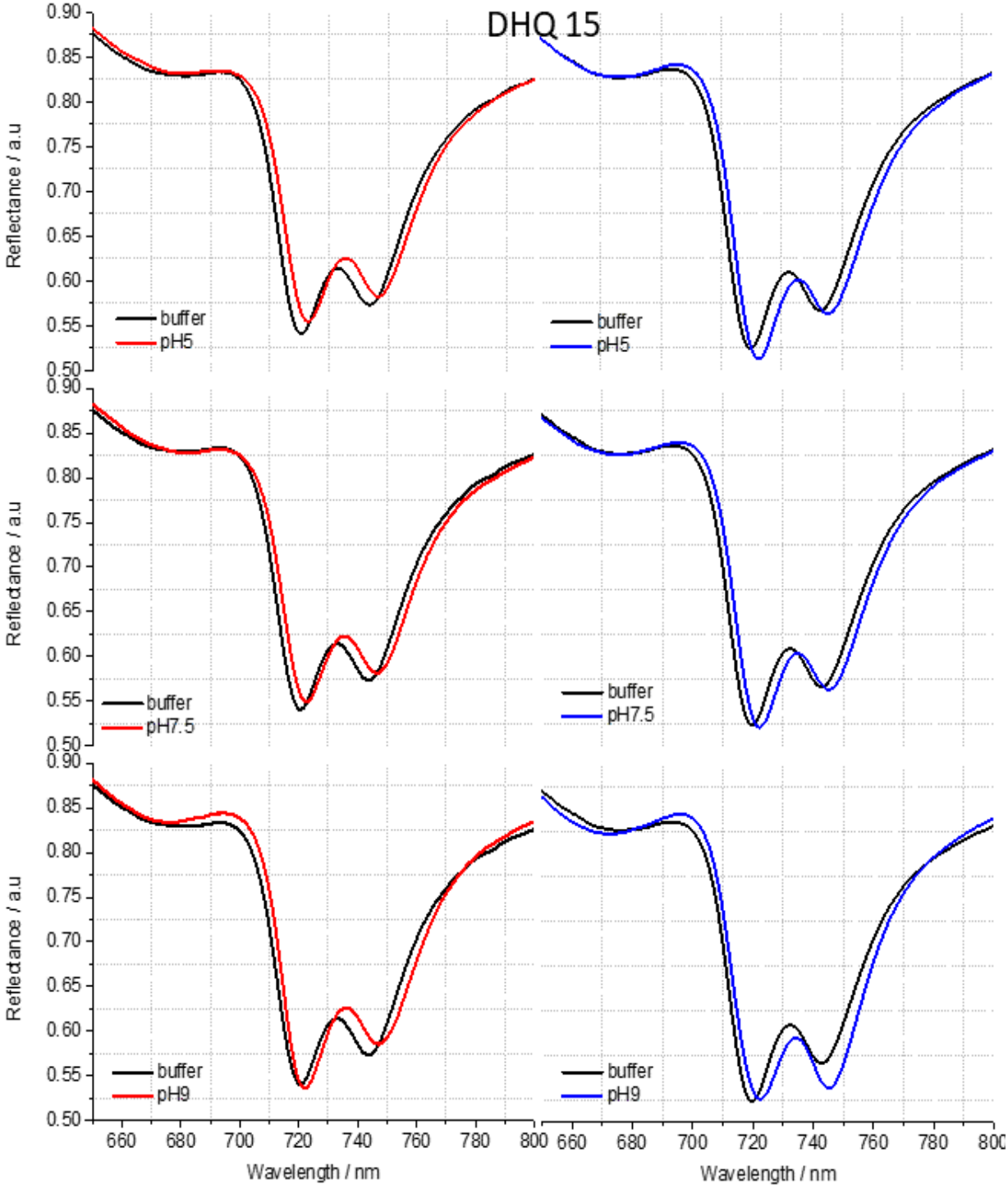

Figure 4 - 7: DHQ 15 LH (red) and RH (blue) reflectance at pH 5, 7.5 and 9, from top to bottom.

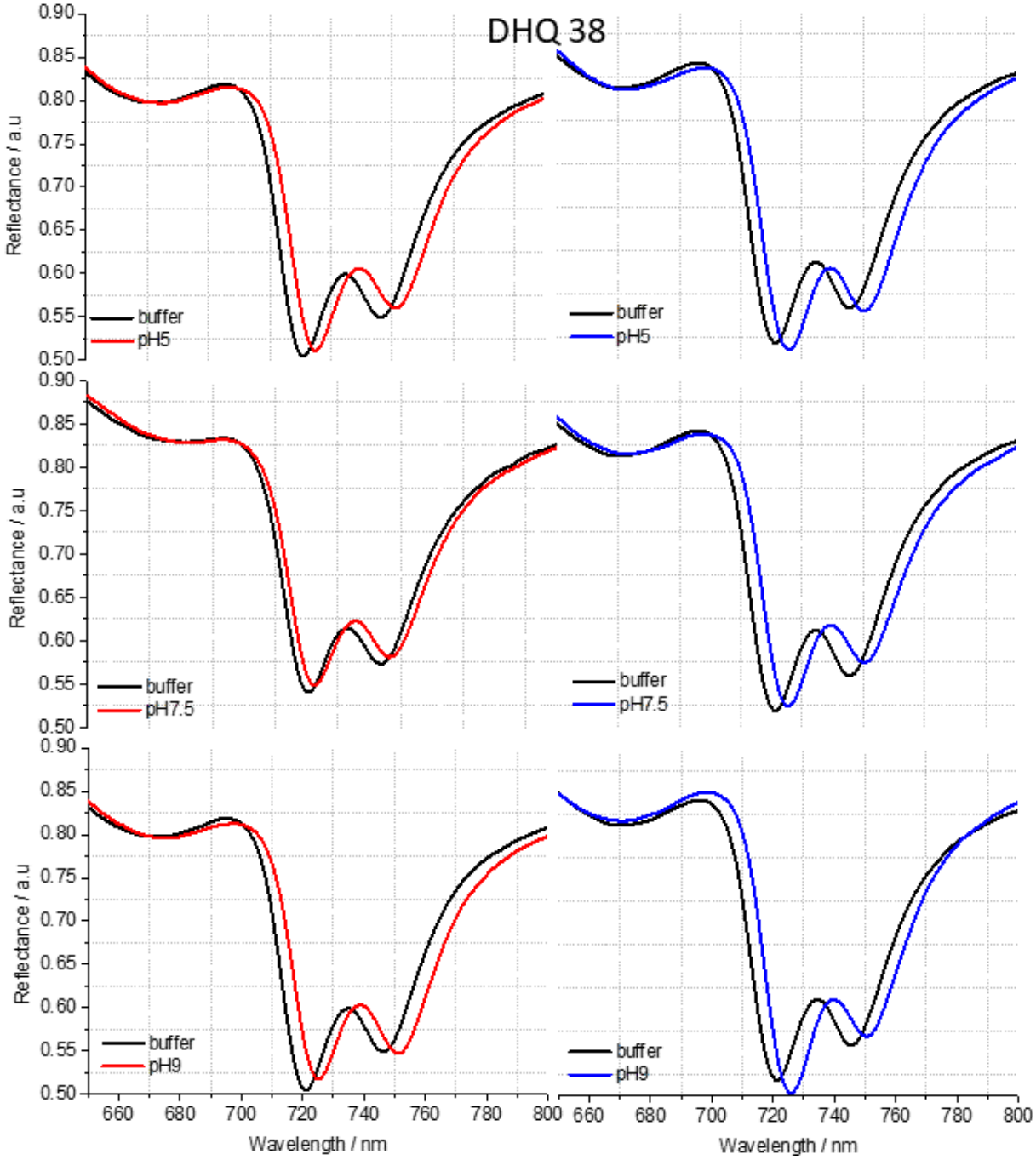

Figure 4 - 8: DHQ 38 RH (blue) and LH (red) reflectance at pH 5, 7.5 and 9, from top to bottom.

The reflectance data were collected at the same time as the ORD. The spectra are displayed in figure 4 - 7 and 4 - 8 in the appendix with the graphs in figure 4 – 14 and 4 - 15. Changes in the reflectance spectra are parameterised by a factor ΔΔφ (the phase of the dark mode, table 4 - 2) which is derived from matching the plasmonic induced reflectivity line shape, that is characteristic of the shuriken structure (chapter 2 and 3). As explained in

chapter 2, PIT and Fano resonances arise from an interference phenomenon that takes place between the bright and dark modes of plasmonic nanostructures.

A is above 1.00 at pH 5, when according to their pI the protein is positively charged, and the ratio is below 1.00 when the protein is negatively charged. Figure 4 – 9 shows how the values of A change with different pHs, and how they qualify the surface charges of the proteins. If A is higher than 1.00, it means that the LH signal amplitude is very small compared to the RH signal amplitude and thus the protein is positively charged. If A is lower than 1.00, the LH signal is higher than the RH signal and the protein is negatively charged. This shows that depending on the surface charges the LH chiral fields can be enhanced or decreased. In figure 4 – 4 it illustrates the fact that the charge distribution displays an inherent left-handed sense, and it can explain why the LH optical signal shows a stronger response to pH changes.

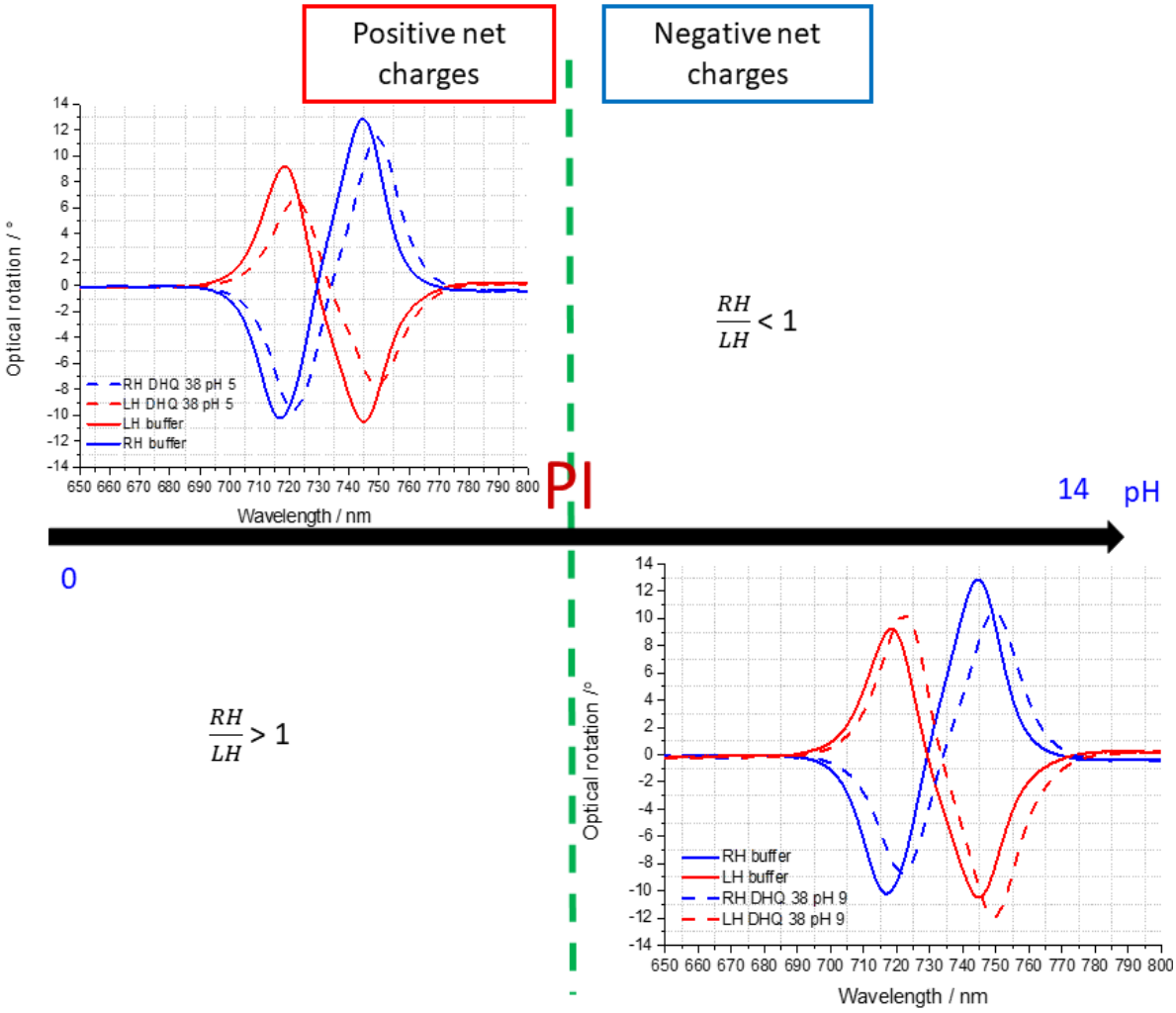

Figure 4 - 9: ORD of DHQ 38 at different pH values: pH 5, pH 7.5 and pH 9. The data show how the asymmetry in A changes with the charge density of DHQ 38.

The effect of incrementally changing the pH on A was also studied. The pH was first decreased from 7.5 to 4.5 and then increased from this to 9, it allowed us to generate a pH titration curve (figure 4 - 10). The graph shows that A strongly depended on the pH, hence can be used to indicate the state of the charge density of the protein. The data shows a reversible and incremental change in A. We also noticed that the pI value was slightly different than estimated. Indeed, the charges flipped at pH conditions higher than the pI value. This indicates a small error in the pH at the surface due to the monolayer. Substrates used for these experiments were coated with a self-assembled monolayer, which is hydrophilic and thus attracts H^+ ions. Therefore, we assumed that the surface of the gold must be more acidic than the solution that was injected into the microfluidic cell.

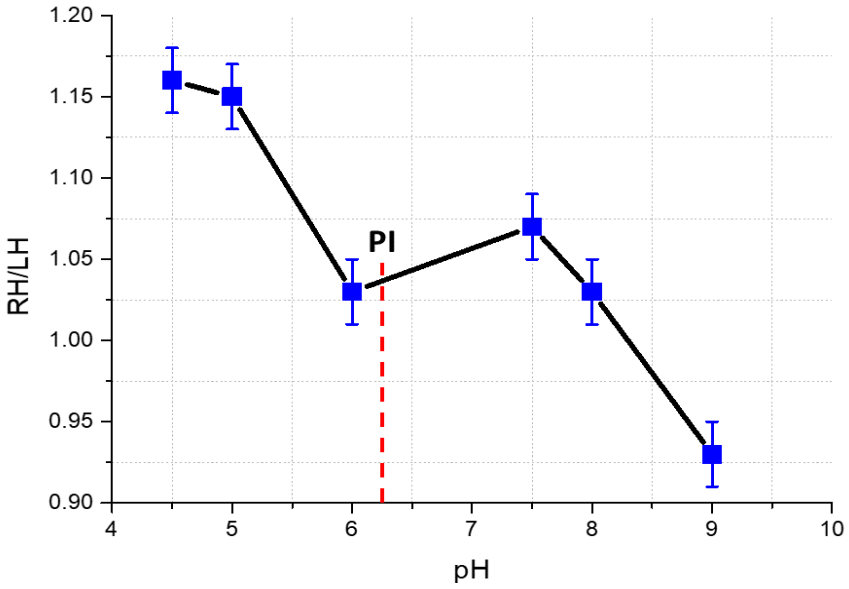

Figure 4 - 10: pH titration of DHQ 15

These observed pH induced asymmetries cannot be reconciled with previously proposed models[24] of how chiral molecular layers can influence the chiroptical response of chiral plasmonic structures[28]. Electronic simulations which replicated previous reported phenomena are based on the constitutive equations (chapter 2 – 2.2.5). One component of these equations is the chiral asymmetry parameter ξ^T, second rank tensor describing the chiral property of a medium which is zero for achiral materials. Details on the parameters are given in chapter 2,but we recall its form here:

$$\xi = \beta_c \left(\frac{1}{\hbar\omega + \hbar\omega_0 + i\Gamma_{12}} + \frac{1}{\hbar\omega - \hbar\omega_0 + i\Gamma_{12}}\right), \quad (1)$$

In chapter 2 it was showed that the value of ξ at a particular wavelength is dependent on the chiroptical properties of the chiral material. Typical magnitudes of ξ for biomolecules are in the range 10^{-5} to 10^{-4} [29]. Thus the model implies that any change in the optical properties

of the chiral plasmonic structure can only arise from a change in the CD response of the molecule. However, it was showed that the CD spectra of DHQ 15 and DHQ 38 show no significant changes with pH. This means that neither the structure nor ξ values are changed. Consequently, pH induced changes in chiroptical properties of the plasmonic structure occur even though the chiral molecular response of the protein remains unchanged. Hence, a parameter, not considered in previous numerical modelling, must be accounted for to rationalise the current observations.

The change in the chiral fields is due to the interaction of the gold with a charged material that is loaded on the surface[30]. An electrostatic interaction between the LH charge distribution on the DHQase and the conduction electrons of the metal generates a RH chiral image charge distribution. This image charge interacts with the plasmonic field and changes the level of optical activity. The gold charges will move to compensate the net charge of the protein at the surface. Hence the distribution of charges in the nanostructures is drastically changed and alters the plasmonic fields arising from the movement of these charges. Moreover, if the material at the surface of the gold is negatively charged, the surface will induce a positive charge and if the material at the surface of the gold is positively charged, the surface will induce a negative charge.

The surface charge distribution of the protein is controlled by the stereostructure of the proteins which acts as a scaffold on which the charges are distributed. The generation of the image charge distribution will cause either a net enhancement or a depletion of the electron density in the near surface region depending on whether the protein has a net negative or positive charge. It is assumed that a depletion of electron density reduces the intensity of the plasmonic resonance. On the other hand, an enhancement of electron density will increase the plasmonic resonance. Both the chiral properties of the image charge distribution and the level of electron charge enhancement/depletion will be perturbed through the interaction with the chiral fields that exist within the skin depth of the metal. Thus, the level of influence of the induced image charge on the chiroptical response of the nanostructure will arise from a convolution of these effects. The effect on the chiral fields is opposite; when the LH signal is enhanced, the RH signal will decrease and when the RH signal is enhanced, the LH signal will decrease, this results in a significant difference in A.

To summarise, negatively charged gold (electrons) disturbed the chiral fields, while positively charged gold enhanced the signal. The gold is negatively charged when the analyte is positively charged and positively charged when the analyte is negatively charged.

4.3.3 Sensitivity to the structure:

Here, we tested whether our spectroscopic method is sensitive enough to react surface charges and can be applied to detect proteins with different primary structures. This would allow us to differentiate proteins that have the same geometry (quaternary structure) but that differ in primary sequence. Several DHQ molecules were tested with plasmonic spectroscopy under physiological conditions and we were able to detect a difference in amplitude in the ORD signal. This amplitude difference was stronger in the left-handed signal. The parameter A followed the same trend as explained in figure 4 - 9. Table 4 – 3 contains the structural and matching parameters for all the DHQs tested here.

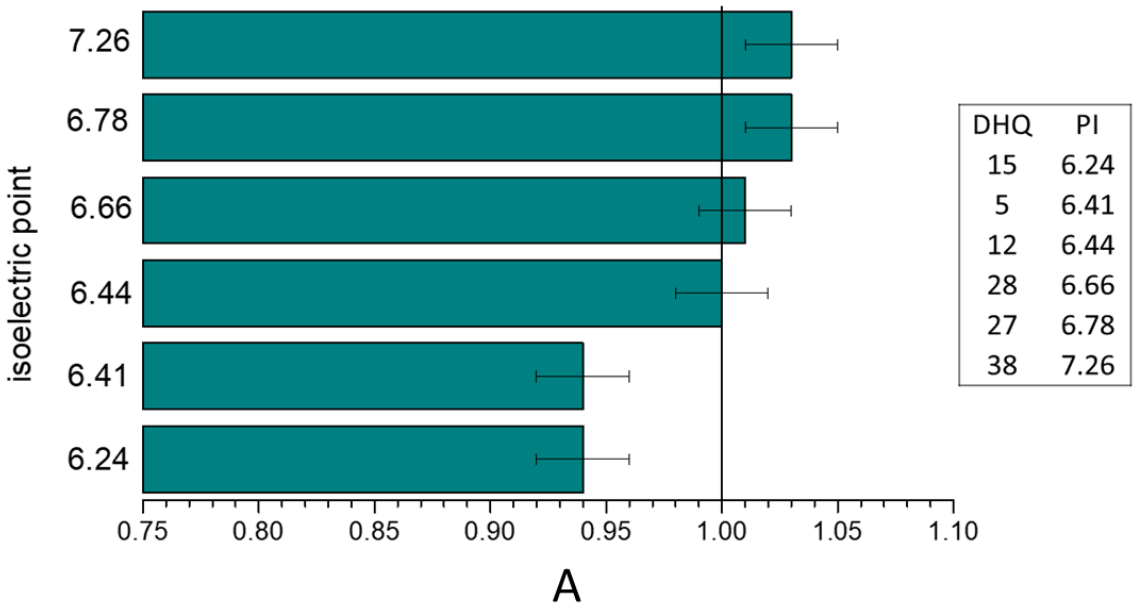

Figure 4 - 11: Isoelectric point of DHQ function of A for DHQ 15, DHQ 5, DHQ 12, DHQ 28, DHQ 27, and DHQ 38 at pH 7.8.

Table 4 - 3 shows the association of the structure of DHQs with their pI.

DHQ	Molecular weight of the tagged monomer	Sequence length without the tag	pI	Secondary structure (H:helix, S:strand, O: other)	Quaternary structure	ΔΔϕ	A
5	18683.1	150	6.41		12	-0.6	0.94
12	18448.6	155	6.44	H:46.3, S:15.4, O:38.3	12	-1.1	1
15	17939.2	143	6.24	H:47,6, S:18,9, O:33.6	12	-0.4	0.94
27	18279.8	148	6.78		12	0	1.03
28	18976.7	150	6.66		12	-1.9	1.01
33	17633.7	144	6.36	H:45;6, S:18.1, O:36.3	12	0.9	1.07
36	18624.1	150	6.75	H:45.2, S:18.5, O:36,3	12	2.3	0.91
38	17988.5	146	7.26	H:45.1, S:18.1, O:36.8	12	-2.2	1.03

Table 4 - 3: Structural and matching parameters for all the DHQase proteins characterised in 50mM Tris pH 7.5

The parameter A decreases when DHQ molecules have a pI that is closer to the acidic value of the pH range tested, whereas, A increases for DHQ molecules that have a more physiological pH, see figure 4 - 11. The difference in the pI values is approximately 1 between the lowest and the highest values but is large enough to enable to distinguish three groups of proteins with a similar A value. All the experiments were performed at pH 7.8, therefore most of the DHQ molecules were negatively charged except for DHQ 38 and DHQ 27, which had a higher pI. In addition, DHQ 28 and DHQ 12 were in their zwitterion form, confirming the surface was slightly acidic.

The asymmetry parameter ΔΔφ extracted from the matching graphs showed an interesting correlation with the pI values of the proteins (figure 4 - 12). We would expect ΔΔφ to be 0 at the pI. However, the parameter decreased at lower pI values of the different proteins with increasing negative charge, except for DHQ 27 where the ΔΔφ is 0.

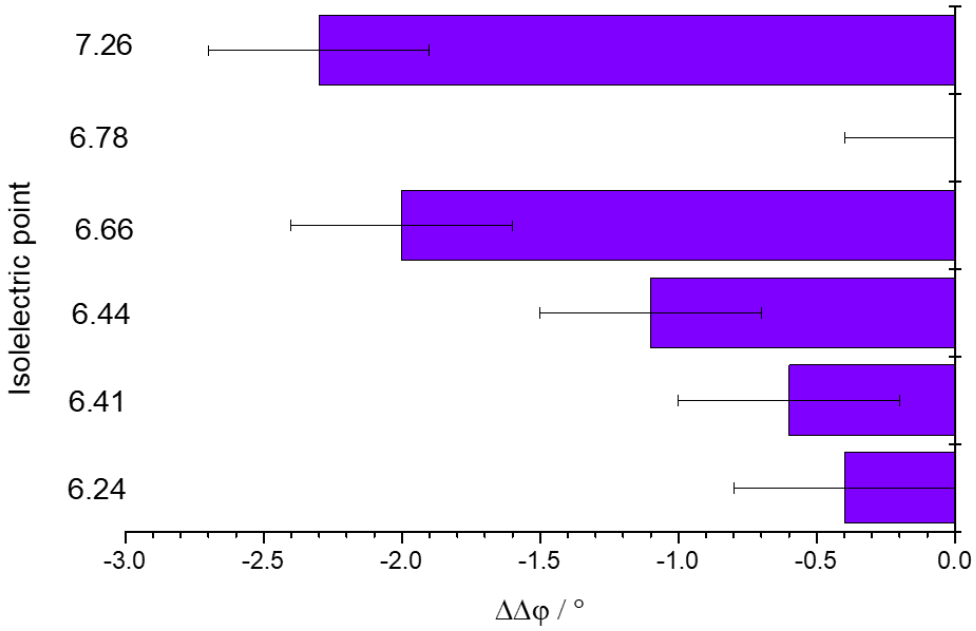

Figure 4 - 12: Isoelectric point of DHQase function of ΔΔφ for DHQ 15, DHQ 5, DHQ 12, DHQ 28, DHQ 27, DHQ 38 at pH 7.4.

It means that negative charges of the gold surface have a stronger effect on the chiral fields. It coincided with the data shown in table 4 - 2, where ΔΔφ was rather low for proteins with an overall negative charge. These DHQ molecules induced positive charges on gold. In gold, the negative charges are derived from moving electrons, while the positive charges are holes created by missing electrons. It means that the electrons have a stronger influence on the field than the holes. However, DHQ 27 did not follow this trend. This could be due to the surface charge of the protein at this pH being even, thus DHQ 27 is a zwitterion.

To support the phenomenological description a numerical model was used (figure 4 – 13). The theory of the model is explained in chapter 2. This numerical model is used to determine how a chiral perturbation of the near surface region of the gold affects the chiroptical response. We modelled a chiral perturbation of the near gold surface and saw that the results we obtained for A could be replicated with a 10nm thick layer ($\xi = 3x10^{-3} + 3x10^{-5}$). This result is an order magnitude which is too large for proteins but is still in a realistic range.

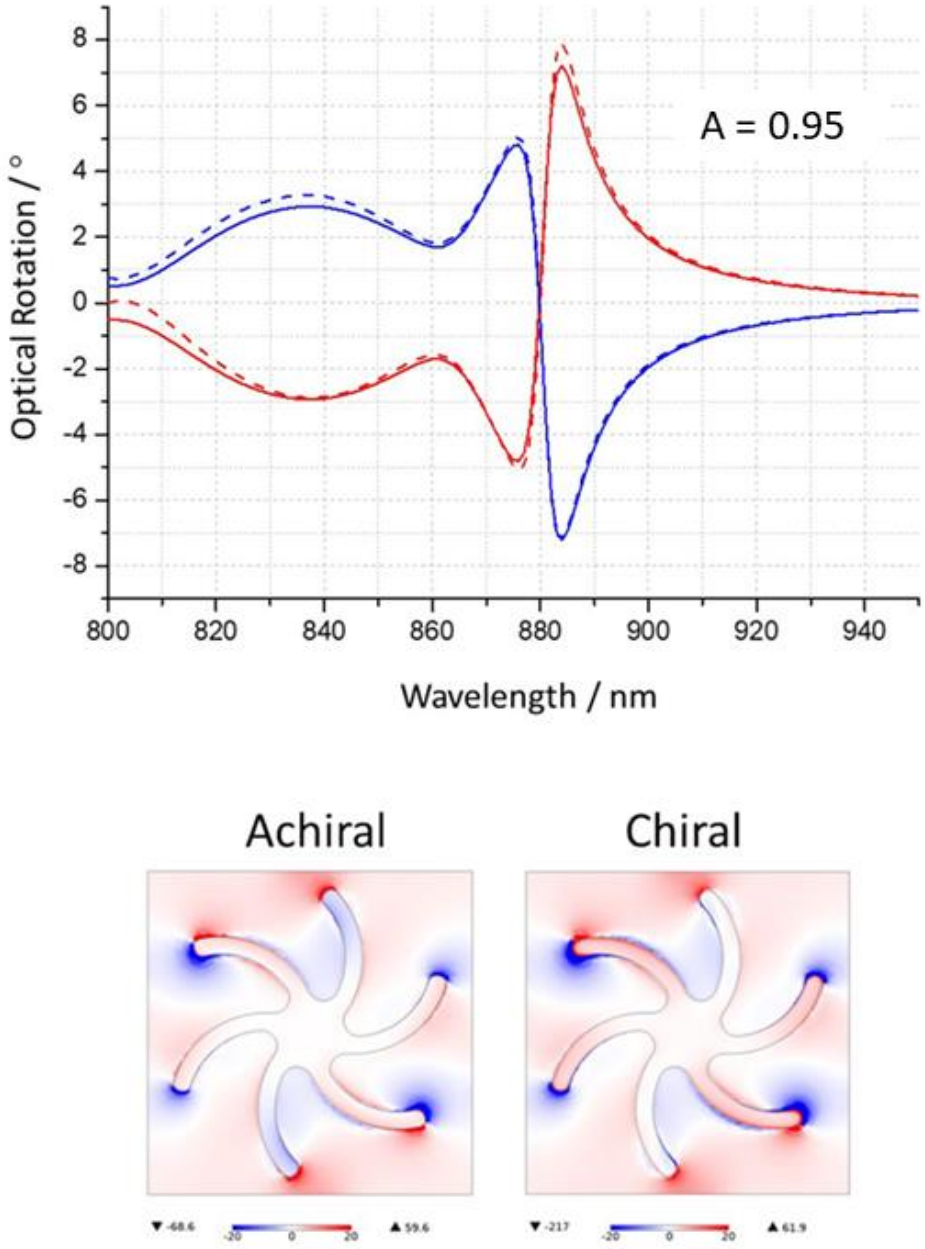

Figure 4 – 13: Numerical simulation of ORD spectra from the shuriken with a value of ξ = 0 + 0i (solid line) and ξ = $3x10^{-3}$ + $3x10^{-3}$i (dashed line). Blue in the RH data and red is the LH data. Below the optical chiral map for the LH structure. The chiral layer increases the net LH chiral asymmetry of the near field.

Thus, the numerical simulations support the plausibility that an image charged induced chirally perturbed gold layer can produce the experimentally observed effects.

4.4 Conclusion:

In this chapter, we presented experimental data which clearly demonstrate that different chiroptical responses can be observed for our model proteins which have essentially the same secondary, tertiary and quaternary structures. These responses do not map simply to primary amino acid sequence which is a measure of the structural similarity of the proteins, but rather to the surface charge distribution of the biomolecule and how this is complexed to the chiral plasmonic structure. A phenomenological model, based on the induction of a chiral mirror image charge distribution within the skin depth of the metal, was used to rationalise the sensitivity of the chiral plasmonic structure to the biomolecular charge distribution. Controlling the surface charges of a protein is possible by changing the pH of the solution it is resuspended in. Type II DHQases in solution with a pH ranging from acidic to basic were studied with chiral fields. Here, we showed that the amplitude of the optical signal increased or decreased according to the DHQase density of charge and the handedness of the plasmonic field. This perturbation in the plasmonic field can be explained by the fact that the DHQase induced a movement of charges on the gold surface. Indeed the proteins create a “chiral gold” layer that perturbs the optical activity of the intrinsically chiral plasmonic structure. The new distribution of charges on the gold can then subsequently interfere with the local chiral field and either enhance or reduce the signal. Depending on the chirality of the field, when a handedness of field is enhanced the other one is reduced and vice versa. This phenomenon occurs even with a chemical self-assembled monolayer at the gold surface. Moreover, it permits to detect the changes in the surface charge distributions, which are invisible to routine spectroscopic techniques. It allows the discrimination of structurally homologous molecules that differ in their surface charge distributions.

This ability of the chiral plasmonic field to respond to surface charge density was proven useful to distinguish between proteins with different sequences, but very similar higher order structures. Indeed, several DHQases with rather similar pI values were loaded onto plasmonic fields and we showed that A value extracted from the ORD of the signal was directly linked to the surface charge distribution. We were able to show that at acidic pH with overall positive charges A was larger than 1 while at basic pH with overall negative charges A was less than 1. Because the sequences of the DHQases consist of different amino acids, the charge distributions will not be identical. Thus, all the DHQ molecules should have different fingerprints in the chiral fields. Finally, numerical simulation confirmed that the effect seen on the plasmonic fields is due to the combination of the surface charge of the protein and its chirality. A change in the CD signal is not the only cause of this effect.

In conclusion, we showed that chiral plasmonic fields are a valid method to determine surface charge density of proteins with unknown structures. This is a valuable property to be able to detect modifications spectroscopically: for example modifications to proteins within the cell such as phosphorisation[31], glycolisation[32] and methylation[33] to name a few of them. All of them can result in significant modifications to the surface charges of the molecules. These chemical modifications are related to various biological processes in both normal and disease states[34]. The phenomenon described here provides a new fundamental way to probe the electrostatic properties of molecules whilst retaining the benefits of the sensitivity and speed of using a plasmonic platform.

4.5 References:

(1) Strickler, S. S.; Gribenko, A. V.; Gribenko, A. V.; Keiffer, T. R.; Tomlinson, J.; Reihle, T.; Loladze, V. V.; Makhatadze, G. I. Protein Stability and Surface Electrostatics: A Charged Relationship †. Biochemistry (2006), 45 (9), 2761–2766.

(2) Linse, S.; Brodin, P.; Johansson, C.; Thulin, E.; Grundström, T.; Forsén, S. The Role of Protein Surface Charges in Ion Binding. Nature (1988), 335, 651–652.

(3) Gitlin, I.; Carbeck, J. D.; Whitesides, G. M. Why Are Proteins Charged ? Networks of Charge – Charge Interactions in Proteins Measured by Charge Ladders and Capillary Electrophoresis. Angew. Chem. Int. (2006), 45 (19), 3022–3060.

(4) Leung, C.; Kinns, H.; Hoogenboom, B. W.; Howorka, S.; Mesquida, P. Imaging Surface Charges of Individual Biomolecules. Nano Lett. (2009), 9 (7), 2769–2773.

(5) Felder, C. E.; Prilusky, J.; Silman, I.; Sussman, J. L. A Server and Database for Dipole Moments of Proteins. Nucleic Acids Res. (2007), 35 (suppl.2), 512–521.

(6) Lecoeur, M.; Gareil, P.; Varenne, A. Separation and Quantitation of Milk Whey Proteins of Close Isoelectric Points by On-Line Capillary Isoelectric Focusing-Electrospray Ionization Mass Spectrometry in Glycerol-Water Media. J. Chromatogr. A (2010), 1217 (46), 7293–7301.

(7) Haddad, P. R. Encyclopedia of Separation Science. TrAC Trends Anal. Chem. (2000), 23 (9), III–IV.

(8) Cargile, B. J.; Bundy, J. L.; Freeman, T. W.; Stephenson, J. L. Gel Based Isoelectric Focusing of Peptides and the Utility of Isoelectric Point in Protein Identification. J. Proteome Res. (2004), 3 (1), 112–119.

(9) Righetti, P. G. Determination of the Isoelectric Point of Proteins by Capillary Isoelectric Focusing. J. Chromatogr. A (2004), 1037, 491–499.

(10) Mir, R.; Jallu, S.; Singh, T. P. The Shikimate Pathway: Review of Amino Acid Sequence, Function and Three-Dimensional Structures of the Enzymes. Crit. Rev. Microbiol. (2015), 41 (2), 172–189.

(11) Roszak, A. W.; Robinson, D. A.; Krell, T.; Hunter, I. S.; Fredrickson, M.; Abell, C.; Coggins, J. R.; Lapthorn, A. J. The Structure and Mechanism of the Type II Dehydroquinase from Streptomyces Coelicolor. Structure (2002), 10 (4), 493–503.

(12) Sigal, G. B.; Bamdad, C.; Barberis, A.; Strominger, J.; Whitesides, G. M. A Self-Assembled Monolayer for the Binding and Study of Histidine-Tagged Proteins by Surface Plasmon Resonance. Anal. Chem. (1996), 68 (3), 490–497.

(13) Zhao, Y.; Askarpour, A. N.; Sun, L.; Shi, J.; Li, X.; Alù, A. Chirality Detection of Enantiomers Using Twisted Optical Metamaterials. Nat. Commun. (2017), 8, 6–13.

(14) García-Guirado, J.; Svedendahl, M.; Puigdollers, J.; Quidant, R. Enantiomer-Selective Molecular Sensing Using Racemic Nanoplasmonic Arrays. Nano Lett. (2018), 18 (10), 6279–6285.

(15) Hendry, E.; Carpy, T.; Johnston, J.; Popland, M.; Mikhaylovskiy, R. V.; Lapthorn, A. J.; Kelly, S. M.; Barron, L. D.; Gadegaard, N.; Kadodwala, M. Ultrasensitive Detection and Characterization of Biomolecules Using Superchiral Fields. Nat. Nanotechnol. (2010), 5 (11), 783–787.

(16) Tullius, R.; Platt, G. W.; Khosravi Khorashad, L.; Gadegaard, N.; Lapthorn, A. J.; Rotello, V. M.; Cooke, G.; Barron, L. D.; Govorov, A. O.; Karimullah, A. S.; Kadodwala, M. Superchiral Plasmonic Phase Sensitivity for Fingerprinting of Protein Interface Structure. ACS Nano (2017), 11 (12), 12049–12056.

(17) Kelly, C.; Tullius, R.; Lapthorn, A. J.; Gadegaard, N.; Cooke, G.; Barron, L. D.; Karimullah, A. S.; Rotello, V. M.; Kadodwala, M. Chiral Plasmonic Fields Probe Structural Order of Biointerfaces. JACS (2018), 140 (27), 8509–8517.

(18) Pihlasalo, S.; Auranen, L.; Hänninen, P.; Härmä, H. Method for Estimation of Protein Isoelectric Point. Anal. Chem. (2012), 84 (19), 8253–8258.

(19) Sillero, A.; Ribeiro, J. M. Isoelectric Points of Proteins: Theoretical Determination. Anal. Biochem. (1989), 179 (2), 319–325.

(20) Michen, B.; Graule, T. Isoelectric Points of Viruses. J. Appl. Microbiol. (2010), 109 (2), 388–397.

(21) Reiling, S.; Kelleher, A.; Matsumoto, M. M.; Robinson, G.; Asojo, O. A. Structure of Type II Dehydroquinase from Pseudomonas Aeruginosa. Acta Crystallogr. Sect. F Struct. Biol. Commun. (2014), 70, (PT11) 1485–1491.

(22) Liu, C.; Liu, Y-M.; Sun, Q-L.; Jiang, C-Y.; Liu, S-J. Unraveling the Kinetic Diversity of Microbial 3-Dehydroquinate Dehydratases of Shikimate Pathway. AMB Express (2015), 5 (1) 7.

(23) Ostuni, E.; Yan, L.; Whitesides, G. M. The Interaction of Proteins and Cells with Self-Assembled Monolayers of Alkanethiolates on Gold and Silver. Colloids Surf B Biointerfaces (1999), 15 (1), 3–30.

(24) Prime, K. L.; Whitesides, G. M. Self-Assembled Organic Monolayers : Model Systems for Studying Adsorption of Proteins at Surfaces. Science (1991), 252 (5009), 1164–1167.

(25) Nicholls, A.; Honig, B. A Rapid Finite Difference Algorithm, Utilizing Successive Over-relaxation to Solve the Poisson–Boltzmann Equation. J. Comput. Chem. (1991), 12 (4), 435–445.

(26) Fogolari, F.; Brigo, A.; Molinari, H. The Poisson-Boltzmann Equation for Biomolecular Electrostatics: A Tool for Structural Biology. Journal of Molecular Recognition. (2002), 15 (6) 377–392.

(27) Krell, T.; Horsburgh, M. J.; Cooper, A.; Kelly, S. M.; Coggins, J. R. Localization of the Active Site of Type II Dehydroquinases. Identification of a Common Arginine-Containing Motif in the Two Classes of Dehydroquinases. J. Biol. Chem. (1996), 271 (40), 24492–24497.

(28) Govorov, A. O.; Fan, Z. Theory of Chiral Plasmonic Nanostructures Comprising Metal Nanocrystals and Chiral Molecular Media. ChemPhysChem (2012), 13 (10) 2551–2560.

(29) Kelly, C.; Khosravi Khorashad, L.; Gadegaard, N.; Barron, L. D.; Govorov, A. O.; Karimullah, A. S.; Kadodwala, M. Controlling Metamaterial Transparency with Superchiral Fields. ACS Photonics (2018), 5 (2), 535–543.

(30) Goldsmith, M-R.; George, C. B.; Zuber, G.; Naaman, R.; Waldeck, D. H.; Wipf, P.; Beratan, D. N. The Chiroptical Signature of Achiral Metal Clusters Induced by Dissymmetric Adsorbates. Phys. Chem. Chem. Phys. (2006), 8 (1), 63–67.

(31) Pawson, T.; Scott, J. D. Protein Phosphorylation in Signaling – 50 Years and Counting. Trends Biochem. Sci. (2005), 30 (6), 286–290.

(32) Ohtsubo, K.; Marth, J. D. Glycosylation in Cellular Mechanisms of Health and Disease. Cell (2006), 126 (5), 855–867.

(33) Murn, J.; Shi, Y. The Winding Path of Protein Methylation Research: Milestones and New Frontiers. Nat. Rev. Mol. Cell Biol. (2017), 18 (8), 517–527.

(34) Karve, T. M.; Cheema, A. K. Small Changes Huge Impact: The Role of Protein Posttranslational Modifications in Cellular Homeostasis and Disease. J. Amino Acids (2011), 2011, 1–13.

4.6 Appendix:

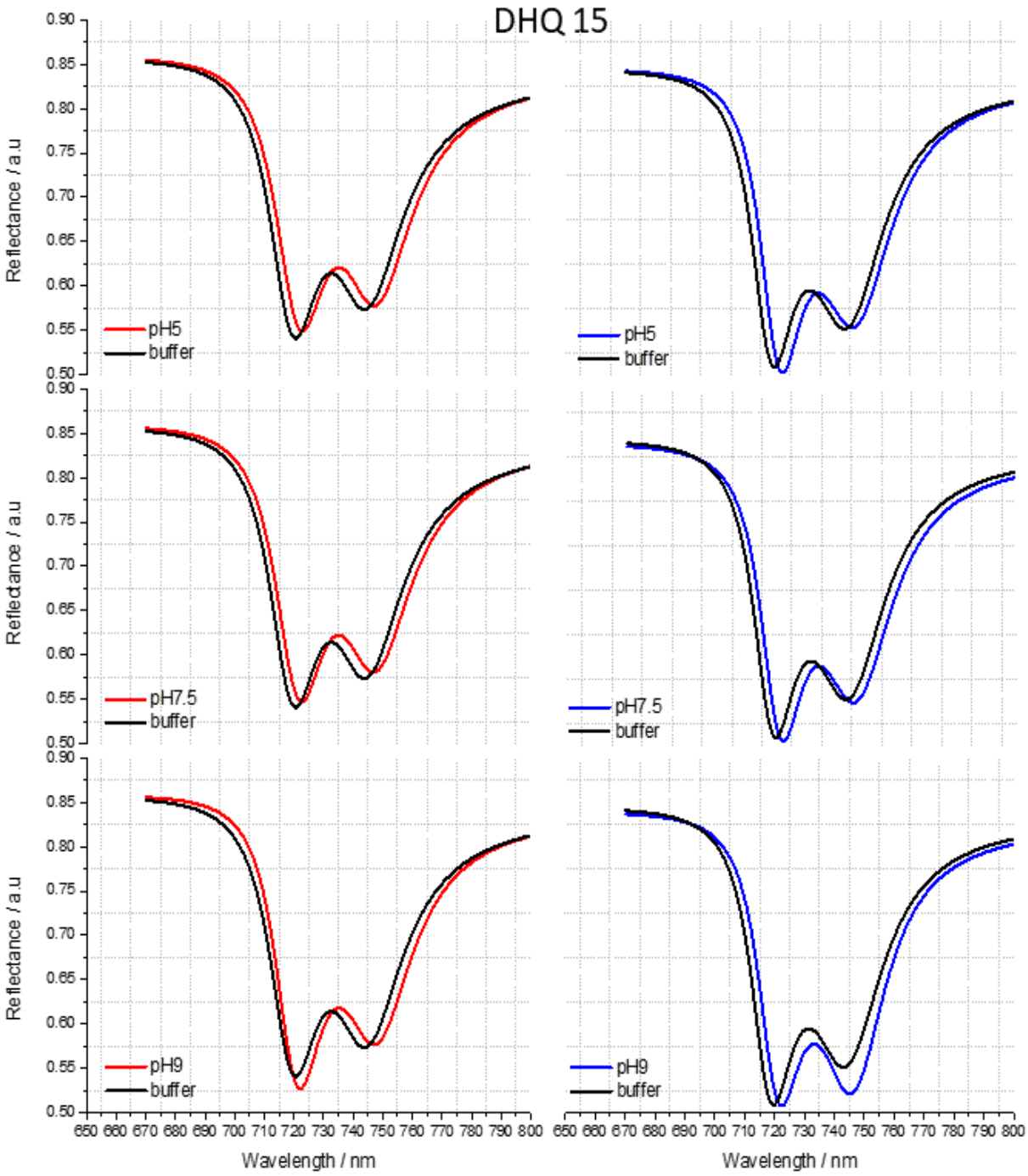

Figure 4 - 14: Matched graphs from the experimental reflectance data for DHQ 15. The spectra were matched for all pH values tested. The pH is going from acidic to basic from the top to the bottom of the figure.

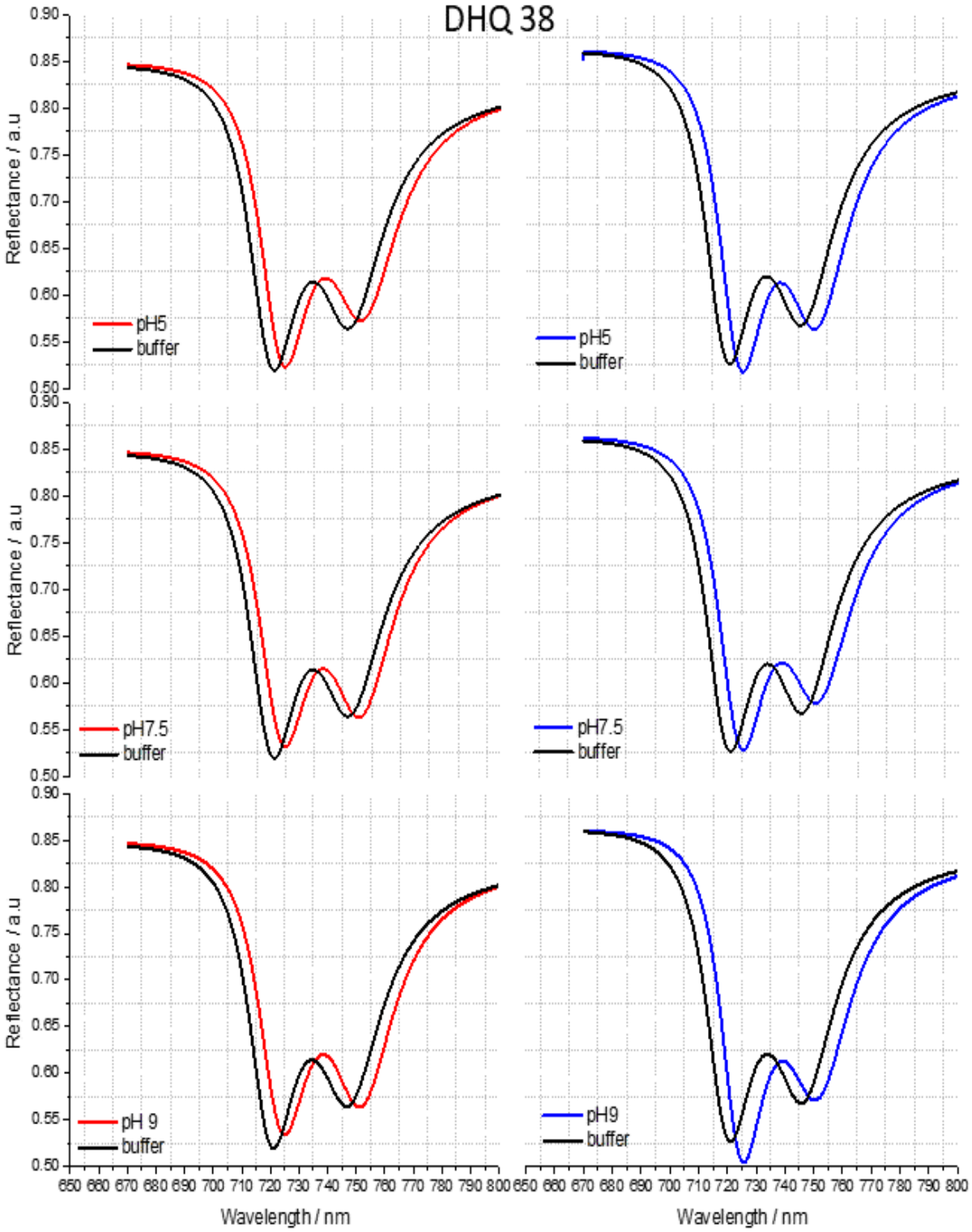

Figure 4 - 15: Matched graphs from experimental reflectance data for DHQ 38. The spectra were matched for all pH values tested. The pH is going from acidic to basic from the top to the bottom of the figure.

Buffer Titration

The following table can be used to determine the appropriate mix of 1.0 M Citric acid and 1.0 M BIS-TRIS propane to produce the desired buffer pH. The recommended volumes produce a 0.1 M buffer in a final volume of 1,000 microliters. pH measurements performed at 25° Celsius.

CBTP Buffer Titration Table

pH	1.0 M Citric acid (µl)	1.0 M BIS-TRIS propane (µl)	Water / Other (µl)
2.5	90	10	900
2.7	85	15	900
2.9	80	20	900
3.2	75	25	900
3.4	70	30	900
3.8	65	35	900
4.1	60	40	900
4.5	55	45	900
5.0	50	50	900
5.5	45	55	900
6.4	40	60	900
7.1	35	65	900
7.6	30	70	900
8.2	25	75	900
8.8	20	80	900
9.1	15	85	900
9.5	10	90	900

Figure 4 - 16: Buffer table for Bis-tris propane at different pH. Figure taken from https://hamptonresearch.com/uploads/support_materials/HR2-831_833_CBTP_Buffer_Table.pdf

Primary sequence DHQase:

DHQ15

MGSSHHHHHHSSGLVPRGSHMSKQILVLNGPNLGRLGRREPQIYGTTTHDDLAARLIEY
GRELGLDVEVRQTDSEERMMGWIHQAADDRTPVVINPAAWSHYNIAIADALVQLVAPCIE
VHISNIAAREEFRHHSVVSAHVTGTIAGLGLKGYELALSWLATD

DHQ 38

MGSSHHHHHHSSGLVPRGSHMAKKPTIFILNGPNLNLLGLREPTIYGHQTLEDIANKLKL
QAEKLDVTVEIRQSNHEGALIDWLQEAQAVKAKAVILNAAAYTHTSVAIYDAIRAITVPVIE
VHLSNPHAREAFRHKSYVGEAALGTISGFGAESYSLALDAAAKL

```
Length of alignment = 145
Sequence 3015Propionibacterium_ac/1-143 (Sequence length = 143)
Sequence    3038Zymomonas_mobilis/2-146 (Sequence length = 146)

3015Propionibacterium_ac/1-143 MSKQ-ILVLNGPNLGRLGRREPQIYGTTTHDDLAARLIEYG
                                 |  |..||||||  || ||| |||  | .|.| .|   .
   3038Zymomonas_mobilis/2-146 AKKPTIFILNGPNLNLLGLREPTIYGHQTLEDIANKLKLQA

3015Propionibacterium_ac/1-143 RELGLDVEVRQTDSEERMMGWIHQA-ADDRTPVVINPAAWS
                                 |.. ||.||.. |  ...|...| |    .|..|.|| .
   3038Zymomonas_mobilis/2-146 EKLDVTVEIRQSNHEGALIDWLQEAQAVKAKAVILNAAAYT

3015Propionibacterium_ac/1-143 HYNIAIADALVQLVAPCIEVHISNIAAREEFRHHSVVSAHV
                               | ..|| ||.  .  | ||||.||  ||| ||| | |.
   3038Zymomonas_mobilis/2-146 HTSVAIYDAIRAITVPVIEVHLSNPHAREAFRHKSYVGEAA

3015Propionibacterium_ac/1-143 TGTIAGLGLKGYELALSWLATD
                                |||.|.|  .| |||   |
   3038Zymomonas_mobilis/2-146 LGTISGFGAESYSLALDAAAKL

Percentage ID = 43.45
```

Figure 4 – 17: Pairwise Sequence alignment between DHQ15 and DHQ38.

matching parameters (ΔΔ)						
DHQ	15			38		
pH	5	7.5	9	5	7.5	9
ω_r	0.00 ± 0.20	0.00 ± 0.20	-0.20 ± 0.20	0.55 ± 0.20	1.05 ± 0.20	0.80 ± 0.20
ω_d	0.00 ± 0.20	0.00 ± 0.20	-0.20 ± 0.20	0.50 ± 0.20	1.00± 0.20	0.80 ± 0.20
κ	-11.5 ± $2.00.10^{-04}$	-14.00 ± $2.00.10^{-04}$	-38.5 ± $2.00.10^{-04}$	-3.00 ± $2.00.10^{-04}$	12.00 ± $2.00.10^{-04}$	4.5 ± $2.00.10^{-04}$
γ_r	-5.00 ± $3.00.10^{-04}$	0.00 ± $3.00.10^{-04}$	0.00 ± $3.00.10^{-04}$	-20.00 ± $3.00.10^{-04}$	0.00 ± $3.00.10^{-04}$	-20.00 ± $3.00.10^{-04}$
γ_d	-6.00 ± $2.00.10^{-04}$	-6.00 ± $2.00.10^{-04}$	-21.00 ± $2.00.10^{-04}$	1.00 ± $2.00.10^{-04}$	15.00 ± $2.00.10^{-04}$	12.00 ± $2.00.10^{-04}$
θ	0.00 ± 0.20	0.00 ± 0.20	0.00 ± 0.20	0.00 ± 0.20	0.00 ± 0.20	0.00 ± 0.20
φ	-1.50 ± 0.20	-0.40 ± 0.20	3.40 ± 0.20	0.15 ± 0.20	-2.30 ± 0.20	-3.60 ± 0.20

Table 4 - 4: Matching parameters extracted from the reflectance data for DHQ15 and DHQ38 at pH 5,7.5 and 9.

matching parameters (ΔΔx)								
DHQ	5	12	15	27	28	33	36	38
ω_r	-0.50 ± 0.20	0.00 ± 0.20	-0.70 ± 0.20	2.20 ± 0.20	0.20 ± 0.20	0.00 ± 0.20	-1.90 ± 0.20	-0.20 ± 0.20
ω_d	-0.50 ± 0.20	0.00 ± 0.20	-1.00 ± 0.20	2.20 ± 0.20	0.20 ± 0.20	0.00 ± 0.20	-0.90 ± 0.20	-0.20 ± 0.20
κ	3.00 ± $2.00.10^{-04}$	-1.00 ± $2.00.10^{-04}$	-2.00 ± $2.00.10^{-04}$	5.00 ± $2.00.10^{-04}$	10.00 ± $2.00.10^{-04}$	-5.00 ± $2.00.10^{-04}$	-4.00 ± $2.00.10^{-04}$	2.00 ± $2.00.10^{-04}$
γ_r	0.00 ± $3.00.10^{-04}$	0.00 ± $3.00.10^{-04}$	4.00 ± $3.00.10^{-04}$	0.00 ± $3.00.10^{-04}$	-10.00 ± $3.00.10^{-04}$	0.00 ± $3.00.10^{-04}$	-1.50 ± $3.00.10^{-04}$	0.00 ± $3.00.10^{-04}$
γ_d	9.00 ± $2.00.10^{-04}$	5.00 ± $2.00.10^{-04}$	-5.00 ± $2.00.10^{-04}$	3.00 ± $2.00.10^{-04}$	10.00 ± $2.00.10^{-04}$	-4.00 ± $2.00.10^{-04}$	6.00 ± $2.00.10^{-04}$	6.00 ± $2.00.10^{-04}$
θ	0.00 ± 0.20	0.00 ± 0.20	0.00 ± 0.20	0.00 ± 0.20	0.00 ± 0.20	0.00 ± 0.20	0.00 ± 0.20	0.00 ± 0.20
φ	-0.60 ± 0.20	-1.10 ± 0.20	-2.90 ± 0.20	0.00E+00 ± 0.20	-2.00 ± 0.20	0.90 ± 0.20	2.30 ± 0.20	-2.30 ± 0.20

Table 4 - 5: Matching parameters extracted from the reflectance data for the representative DHQase proteins.

Chapter 5: Probing specific and non-specific protein-protein interactions with chiral fields

Protein-protein interactions (PPIs) play a pivotal role in many biological processes. Discriminating functionally important well-defined protein−protein complexes formed by specific interactions from random aggregates produced by nonspecific interactions is therefore a critical capability. In this chapter, we show that chiral plasmonic fields probe the structural order and hence the level of PPI specificity in a model antibody-antigen system. Using surface-immobilised Fab′ fragments of polyclonal rabbit IgG antibodies with high specificity for bovine serum albumin (BSA), we show that chiral plasmonic fields can discriminate between a structurally anisotropic ensemble of BSA-Fab′ complexes and random ovalbumin (OVA) -Fab' aggregates, demonstrating their potential as the basis of a useful proteomic technology for the initial rapid high-throughput screening of PPIs.

5.1 Introduction:

Protein-protein interactions (PPIs) are ubiquitous players in biological processes. These interactions can take many forms such as the interactions between antigens and antibodies, hormones and receptors or in DNA replication (transcription and translation[1]). A range of interactions mediate the formation of a protein-protein bond including electrostatic interactions, hydrogen and disulphide bonds, van der Waals forces and hydrophobic/hydrophilic effects[1]. Functionally important PPIs involve specific interactions between two or more proteins resulting in a structurally well-defined complex. Nonspecific PPIs produce random aggregates which have no biological function[2]. Detecting and characterising PPIs and discriminating between functionally relevant specific and nonspecific interactions is a fundamental problem in proteomics and has broader implications in areas such as immunology, medical diagnostics, and biosensing[1,2]. The prerequisite signature of a specific PPI is the formation of a well-defined complex. The specificity of these complexes can be probed by crystallography[3] and NMR, but these approaches are time-consuming and complex. Unfortunately, rapid low-resolution spectroscopic techniques such as circular dichroism (CD) are ineffective[4] at characterising the higher order structure of a protein-protein complex.

In this chapter we focus on the antigen-antibody interaction. An antigen is any substance, which is recognised by the adaptive immune system including antibodies. The variable domain of an antibody is composed of amino acid sequences that define each type of antibody and its binding affinity to an antigen. A specific interaction can be defined by an antibody capable of binding with high affinity to an antigen via recognition of a specific

epitope (antibody-binding site) of an antigen by the paratope (antigen-binding site) of the antibody i.e., an immunocomplex is formed[2]. A non-specific interaction occurs when an antibody is capable of binding to other sites than the epitope of an antigen. These interactions can be studied with a range of analytical techniques such as enzyme-linked immunosorbent assay (ELISA), radioimmunoassay (RIA), surface plasmon resonance, or isothermal titration calorimetry (ITC)[5]. These techniques for rapid routine assaying of PPIs, rely on using the strength (i.e., selectivity) of the binding in a protein-protein complex to parametrize the nature of the PPI[3]. Binding affinity strength is a more qualitative method of parametrizing the specificity of a PPI compared to direct structural characterisation of protein-protein complexes[6].

Antigen-antibody interactions have been widely studied[7] and are applied in many different fields including immunology, for diagnostic purposes and even biosensing due to their ability to recognise and immobilise a protein on a biosensor. An antibody consists of several regions. The fragment antigen-binding (Fab) is the portion of the antibody that recognises and binds antigens and can be used to immobilise antigens on the surface. Here, we used the protease pepsin to generate $F(ab')_2$ fragments, which have the advantage of being significantly smaller than the intact antibody; an interesting property because our spectroscopic technique is size-dependent in the z direction (see – chapter 2). The $F(ab')_2$ fragment was attached to the surface in the same way as a chemical self-assembled monolayer (SAM)[8]. Surface functionalisation is often used in biosensing as it enhances the chiroptical signal[9]. For example, if a protein has a variety of orientations on the surface, in the same way that it can have several orientations in solution, the optical signal is a collection of data that represent these different orientations[10,11]. Since what we see on an optical spectrum is an average of all these different protein orientations, the overall chiroptical signal will be weaker. Antibodies can be used to create a monolayer to immobilise proteins on the surface[12]. Previous work proved that this method was efficient[11,13]. Metal surfaces can be functionalised with thiols, disulphides, amines, nitriles and phosphines[14]. With SAM, the protein or virus that is used must contain a His-tag[15]. Even if the protein binding is more specific, when a protein contains a His-tag at several positions on the amino acid chain, this will introduce several space orientations, which can affect the optical signal.

In this chapter a fundamentally new spectroscopic method for studying the nature of protein-protein complexes is presented. Chiral near fields created by the optical excitation of chiral plasmonic structures are used to detect the level of structural order within a protein-protein complex. In this chapter we studied the complexes based on a Fab' fragment of the polyclonal rabbit IgG antibody (more details in 5.2.2) with high specificity for bovine serum

albumin (BSA) and little or no cross-reactivity to other serum proteins. We showed that $F(ab')_2$ fragments can be used to functionalise the gold surface by binding to the gold surface via an S-H bond[16]. We will show that $F(ab')_2$ fragments, the antigen-binding parts of an antibody, can be generated and that they retain the properties and the specificity of intact antibodies[7]. However, structural distortion in the Fab' fragment induced by immobilisation on the gold surface results in a loss of selectivity. Consequently, the Fab' fragment can now form complexes with either BSA or ovalbumin (OVA). OVA binds the Fab' in a less specific manner than BSA. We showed that the changes induced by the complexes are asymmetric between left- and right-handed structures. The magnitude of the asymmetry is dependent on the structural order of the chiral medium, with structurally anisotropic i.e., order media producing a larger asymmetry than the equivalent isotropic one. Thus, the level of structural order of a protein-protein complex can be used to discriminate between specific and non-specific PPIs.

5.2 Antibodies and proteins:

5.2.1 Specific and non-specific protein-protein interactions:

As mentioned above, there are specific and non-specific protein-protein interactions. It is possible to tell the difference between the two, by looking at the geometry of the new complexes formed after the interaction between two proteins. For example, an antibody can recognise and bind an antigen in a specific or non-specific manner and form an anisotropic complex or isotropic complex, respectively. Specific interactions result in a structurally well-defined complex, while non-specific interactions lead to random aggregates with no biological function.

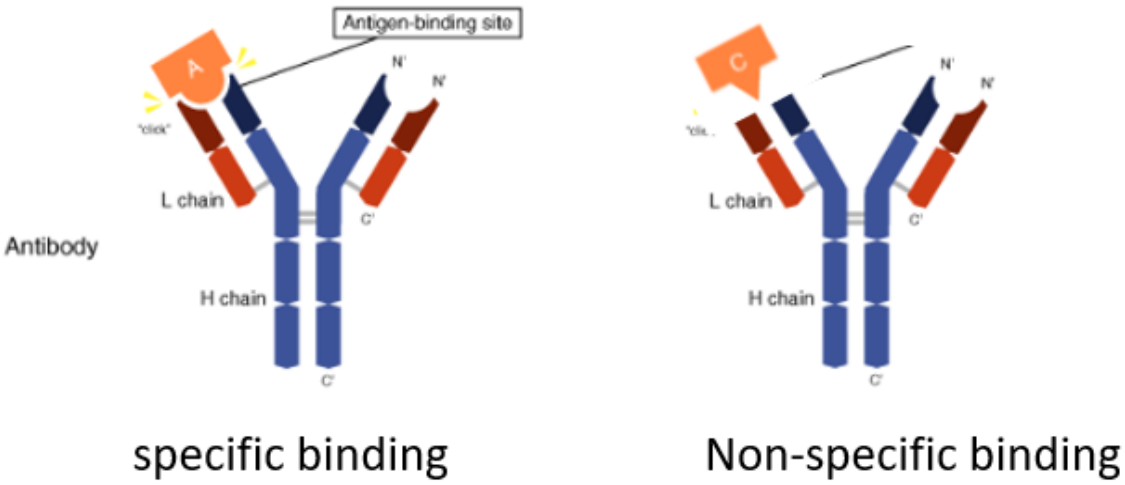

Figure 5 - 1: Illustration of specific and non-specific protein-protein interactions. Figure adapted from: https://www.mblintl.com/products/what-are-antibodies-mbli/

An example of a non-specific interaction would be a protein binding to a non-specific receptor, because a non-specific antigen can bind a receptor if it has some characteristics of the specific antigen (figure 5 - 1).

5.2.2 Antibodies and Fab:

In vivo, B cells can present antigenic peptides on their cell surface via major histocompatibility complex class II (MHC_{II}) molecules to naive $CD4^+$T cells. When a $CD4^+$T cell expresses a T cell receptor (TCR) which specifically recognises the antigen//MHC_{II} complex, it will activate the B cell, which subsequently differentiates into an antibody secreting plasma cell.

Antibodies can be polyclonal or monoclonal; a monoclonal antibody can only recognise a single antigen epitope, whereas a polyclonal antibody is a collection of immunoglobulin molecules which can recognise and bind to many different epitopes of a single antigen[17] (figure 5 - 2). Polyclonal antibodies are produced, in the body, by different B cell clones. Monoclonal antibodies are generated in identical B cells, themselves being clones of a single parent cell. To summarize, an antigen can bind to a polyclonal antibody in various ways depending on antibody specificity and result in several space orientations, while with a monoclonal antibody the antigen can only bind in one specific manner. Although monoclonal antibodies specifically recognise a single antigen epitope and therefore might enhance specific orientation, they are expensive to produce because they are grown *in vitro* with specifically selected cells, therefore, BSA-specific $F(ab')_2$, fragments derived from polyclonal rabbit IgG were used instead.

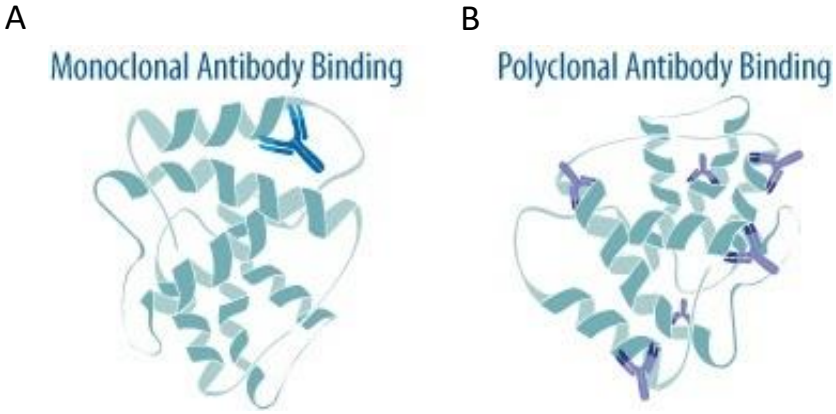

Figure 5 - 2: Example of the difference in the protein-antibody binding between a monoclonal (A) and a polyclonal antibody (B). figure taken from https://www.rndsystems.com/resources/protocols/primary-antibody-selection-optimization.

Antibodies also called immunoglobulins are divided into five categories according to their activity and constant region: IgA, IgD, IgE, IgG, and IgM. IgG is the most abundant type of

antibody and can be found in blood, tissues and fluids. Antibodies consist of a pair of heavy and light chains linked together by a disulphide bond. The heavy chain weighs 50,000 Da and the light chain 25,000 Da[18]. The light chain is divided in a variable (VL) and constant region (CL), (figure 5 - 3). The specificity of an antibody is determined by the variable region on both the heavy and light chains. The antigen binding sites are formed by the pairing of one variable region on the light chain (VL) and one variable region on the heavy chain (VH), (figure 5 - 3) domains from the two different polypeptides chains. Antibody behaviour on gold surface has been investigated previously, especially for IgG.

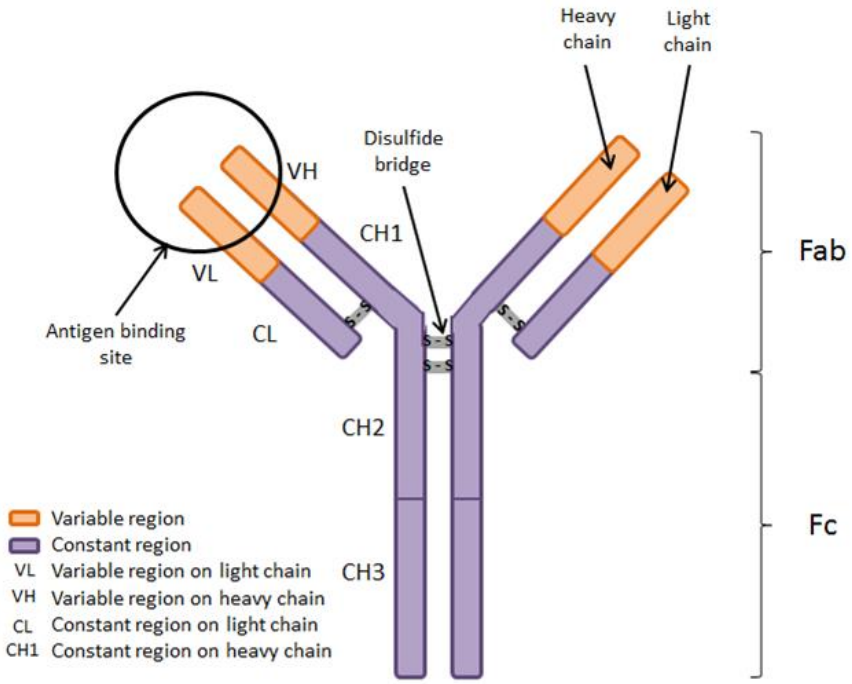

Figure 5 - 3: Representation of an antibody. The antigen binding sites are indicated in orange. The heavy and light chains are linked by a disulphide bridge.

Previous work[19] established that IgG can adopt at least four adsorption geometries on gold surfaces. The possible orientations are as follows (figure 5 - 4): on the side (fragment crystalline (Fc) domain and antigen on the surface), straight (IgG vertical fc on the surface), flat (all the fragments attached to the surface), upside down (both antigen domains attached to the surface).

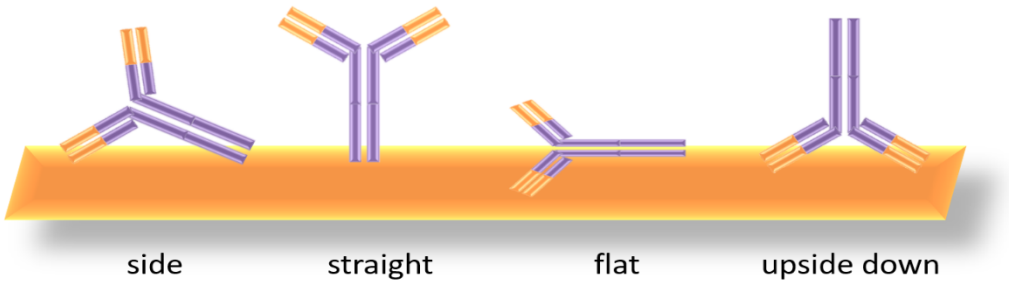

Figure 5 - 4: Schematic description of the four-possible orientations of antibodies on gold surface.

Studies have also shown that immobilising IgG onto a gold surface significantly degrades its effectiveness[19]. This degradation of performance is attributed to a combination of structural heterogeneity and the large size of IgG facilitating denaturation on adsorption. The lack of control over antibody orientations and the possibility of antibodies to denaturise at the surface[20] make IgG poorly effective for surface functionalisation. To minimize the loss of functionality an approach based on immobilising functional active fragments of IgG has been used. IgG can be cleaved into fragments called $F(ab')_2$[21]. The size of intact IgG is ~15-12nm, while the size of $F(ab')_2$, the antigen domain minus the Fc fragment is only around 4nm[22,23]. Compared to the whole antibody, immobilised $F(ab')_2$ fragments adopt more homogeneous adsorption structures and are less susceptible to denaturing[24,25]. $F(ab')_2$ fragments are suitable for surface functionalisation because they are relatively small and can be oriented at the surface via S-H bonds. Unlike intact IgG, the antigen-$F(ab')_2$ complex will be entirely exposed to the evanescent field (BSA = 8nm, thus $F(ab')_2$ + BSA = 12 nm)[26]. On a gold surface it is possible that $F(ab')_2$ get structurally distorted resulting in a complex with ovalbumin (OVA) even though the Fab' used are BSA-specific.

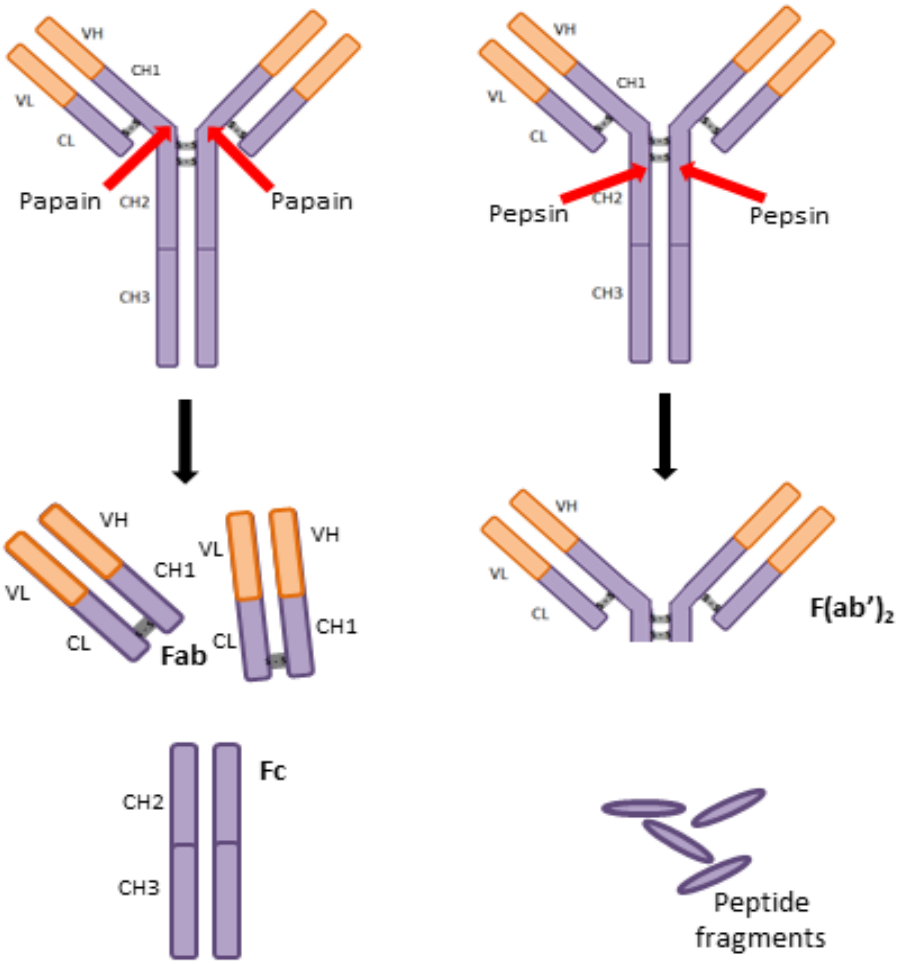

Figure 5 - 5: Representation of the effects of the cleavage by the enzyme papain and pepsin. The left side represents the generation of Fab with papain and shows the fragment obtained after cleavage. The right side represents the generation of F(ab')$_2$ and shows the product after cleavage with pepsin.

Depending on the enzyme used during the fragmentation two types of antigen fragments can be obtained namely Fab or F(ab')$_2$[25]. These types of fragments are often used in research, in industry or even in hospital to treat overdoses. The mechanism of fragmentation is explained in figure 5 - 5 and more details are given in chapter 3. The IgG can be treated with specific protease papain to release a smaller 50 KDa antigen-binding fragment (Fab') and produces a Fc region (fragment crystalline region). The enzyme pepsin cleaves the heavy chain below the disulphide bond leaving the two Fab fragments linked together forming F(ab')$_2$ fragments. The latter was used in our experiments. No intact Fc region is produced during pepsin fragmentation because Fc fragments are extensively degraded resulting in peptides with no biological function. Degraded Fc fragments can be separated from F(ab')$_2$ by dialysis or gel filtration. The IgG protein can be broken down into its constituent F(ab')$_2$ fragments which have free sulfhydryls for attachment to gold surfaces.

Previously, it was shown that sulphur can create a strong bond with gold nanoparticles[16]. In our case we used gold thin film, but the $F(ab')_2$ fragments were still expected to bind to the surface (figure 5 - 6). These free sulfhydryls produce a consistent attachment point for the poly anti-BSA Fab' fragments so it should significantly limit the effects due to the binding orientation.

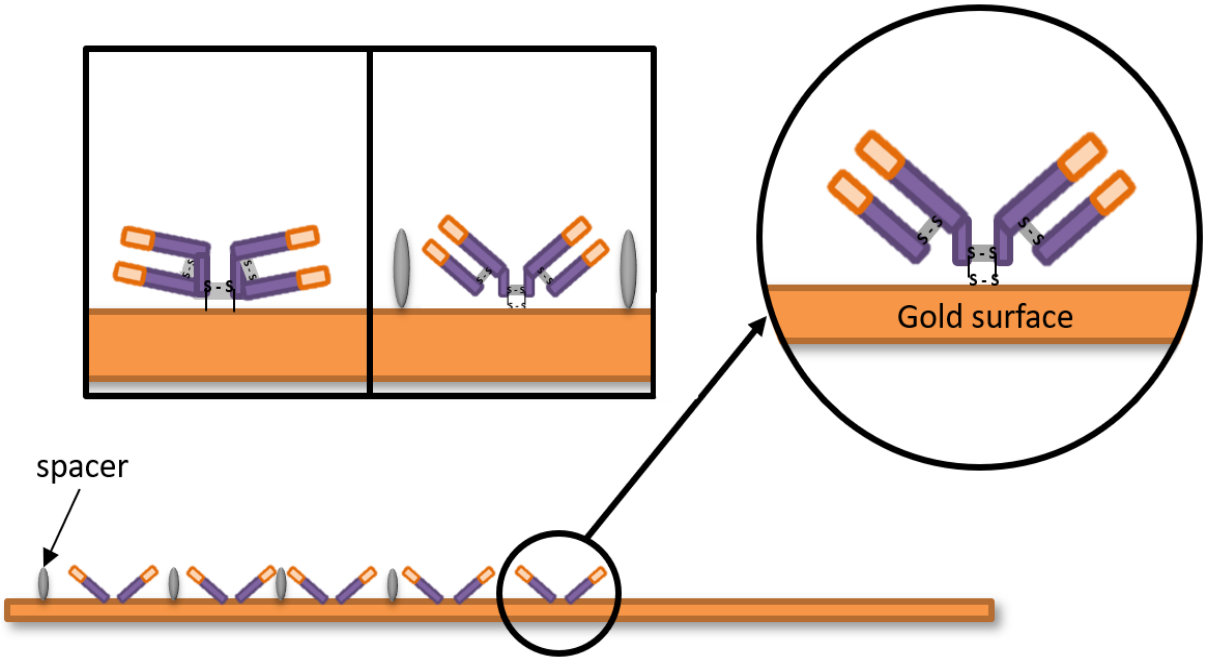

Figure 5 - 6: Representation of $F(ab')_2$ fragments on the gold surface. This figure shows the effect of adding EG-thiols as spacers.

We assumed that the reaction of thiols with gold would be similar as seen in the case of a self-assembled monolayer (SAM) through a cleavage of the S-H bond[27]. To minimize the degree to which the Fab' fragments were denaturised, they were adsorbed with thiols (triethylene glycol mono-11-mercaptoundecyl: EG-thiol) as spacers[24,28]. A spacer is a molecule with a thiol terminal which inhibits the interaction between proteins and the surface, therefore preventing denaturation of the proteins. Because proteins have a hydrophilic surface and the functional group of the spacer is hydrophilic[29,30] due to the functional group being an alcohol, there is no possible interaction between the two. The EG-thiol was selected because it is non-toxic to proteins and will not affect their activity (it will not denaturise proteins). The EG-thiol is a neutral spacer molecule; therefore, any interactions between Fab' molecules and a surface will be minimised[31]. Furthermore, the EG-thiol cannot elicit an immune response, or react with an antigen[32]. Since the EG-thiol is achiral it can be added to a chiral molecule without having any impact on the asymmetry of the signal.

5.3 Theory and modelling:

The proposition that A and ΔΔφ can be used to parametrize structural order (anisotropy) can be validated using electromagnetic numerical simulations. The influence of a chiral molecular (dielectric) medium on the chiroptical properties of a plasmonic nanostructure is derived from Maxwell's constitutive equation described in chapter 2.

We recall that for structurally isotropic chiral medium the diagonal element of the chirality tensor ξ are:

$$\xi^{iso}_{xx} = \xi^{iso}_{yy} = \xi^{iso}_{zz} \quad (1)$$

While for structurally anisotropic medium:

$$\xi^{aniso}_{xx} = \xi^{aniso}_{yy} \ll \xi^{aniso}_{zz} \quad (2)$$

The diagonal elements for isotropic and anisotropic tensors are related by:

$$\xi^{iso}_{xx} = \frac{1}{3}\left[2\xi^{aniso}_{xx} + \xi^{aniso}_{zz}\right] \quad (3)$$

The differences in the chiral response of isotropic and anisotropic expressed in equations 1,2 and 3 are responsible for the enhanced CD from proteins orientated in membrane (lipid) layer[33]. It was estimated in previous studies[33] that for proteins with CD resonances in the UV, $\frac{\xi^{aniso}_{zz}}{\xi^{aniso}_{xx}}$ > 10. Consequently it was assigned that $\xi^{iso}_{xx} = 1.7 \times 10^{-4}$ for isotropic and $\xi^{aniso}_{xx} = 1 \times 10^{-5}$ and $\xi^{aniso}_{zz} = 5 \times 10^{-4}$ for anisotropic chiral media. With these parameters, the effect of 20 nm thick anisotropic and isotropic protein layers was simulated with a refractive index of 1.5. The simulated ORD and reflectance spectra are shown on figure 5 - 7.

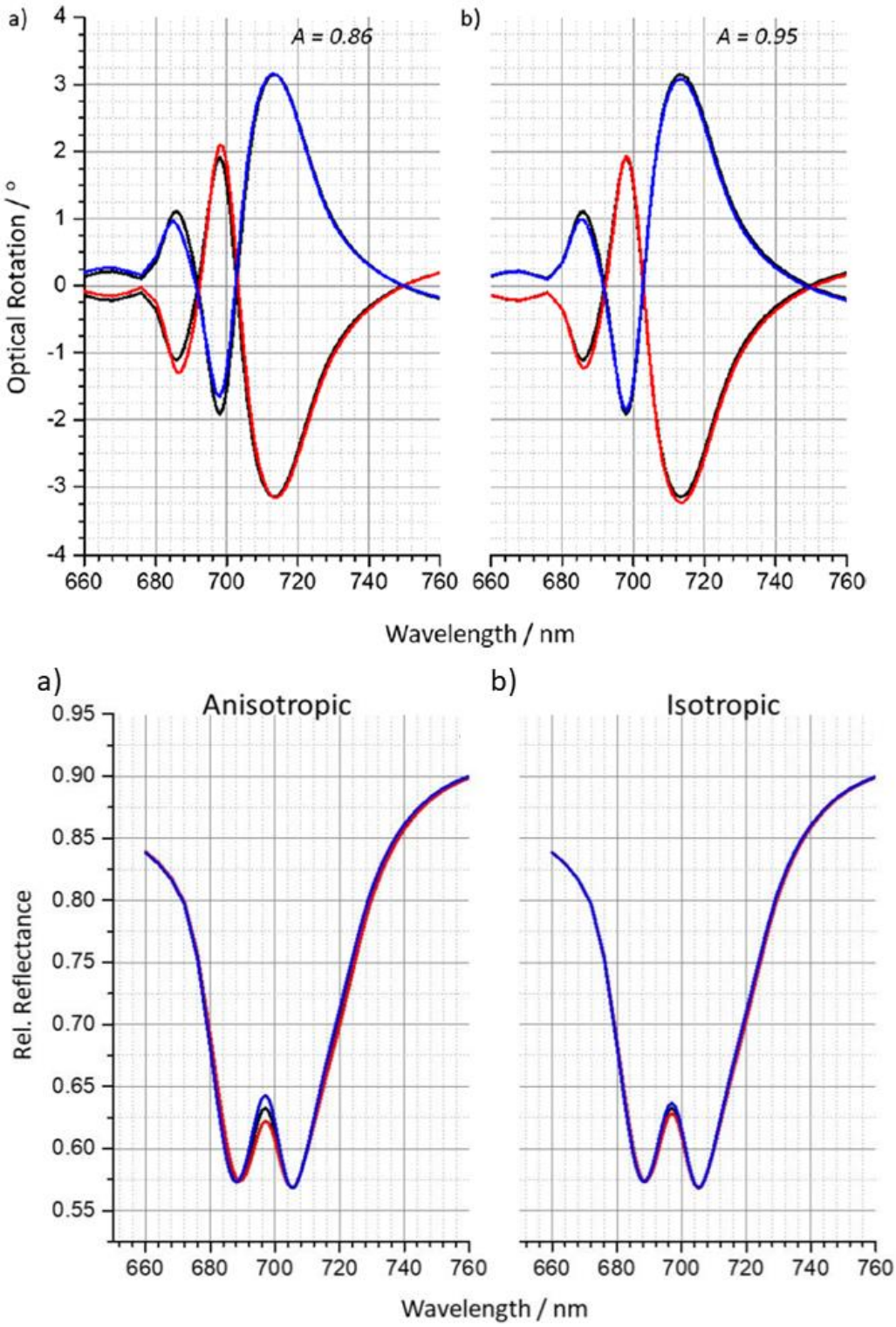

Figure 5 - 7: Simulated ORD and reflectance spectra for (a) anisotropic and (b)isotropic chiral layers. Red and blue spectra are for left- and right-handed structures, respectively. The black spectra are provided for comparison and are for achiral dielectric layers.

The deviation from a pure bisignate line shape is attributed to the modelling underestimating the coupling of the bright and dark modes of the nanostructures (chapter 3). The simulation

demonstrated that anisotropic chiral media induced significantly larger asymmetries in ORD and reflectance (A = 0.86) compared to the isotropic one (A = 0.95).

5.4 Results and discussion:

The experiment can be divided into three steps. First, the surface was functionalised with $F(ab')_2$ using two different concentrations. The effect of the surface coverage on the optical signal was checked, first for $F(ab')_2$ fragments on its own, and then mixed with a thiol spacer. Second, a control with BSA loaded on a non-functionalised surface (plain gold) was carried out for reference measurement. Third, protein measurements were taken with a functionalised surface. $F(ab')_2$ fragments were used with BSA tested at two different concentrations. Then, a negative control experiment was carried out using OVA protein, which was not expected to bind BSA-specific $F(ab')_2$. The substrates are the ones described in the experimental chapter (chapter 3).

5.4.1 Surface coverage with $F(ab')_2$ fragments:

The aim was to create an even and functional mono-layer of $F(ab')_2$ at the substrate surface, with the antigen orientated in such a way that the antigen domain was facing away from the surface. For comparison, $F(ab')_2$ layers without EG-thiol spacers, formed from buffer solution with concentrations of 10 µg/mL and 100 µg/mL, were also studied[15,34]. The mixed-Fab' layers were deposited by incubating freshly prepared plasma-cleaned substrates in buffered solution of 10 µg / ml F(ab')2 and 0.9 mM EG-thiol. They were left for one hour within a microfluidic environment. Subsequently, the functionalised substrates were rinsed with a flow of buffer for several minutes. A shift in the signal (toward the red, 800 nm) indicates an increase in the refractive index, and thus is proof that the $F(ab')_2$ fragments are coating the gold thin film and were not washed off the surface when the substrate was rinsed with buffer. The $F(ab')_2$ at 10 µg/mL with 0.9 mM EG-thiol, were left overnight on the surface, to see if more fragments were binding the surface, however, it did not give a better binding or surface coverage (The average shift and asymmetry parameter were identical to those taken after 1 hour of incubation). Figure 5 - 8 displays the ORD spectra of the surface coated with $F(ab')_2$ and figure 5 – 9 the reflectance associated with the ORD. Three different $F(ab')_2$ solutions were loaded at the surface: 10µg/mL $F(ab')_2$, 100µg/mL $F(ab')_2$ and 10µg/mL $F(ab')_2$ + 0.9mM EG-thiol. The parameters extracted from these graphs are displayed in table 5 - 1.

Looking at the data for $F(ab')_2$ at 10µg/mL, $F(ab')_2$ at 100µg/mL the graphs show that the intensity of the ORD increased in left- and right-handedness.

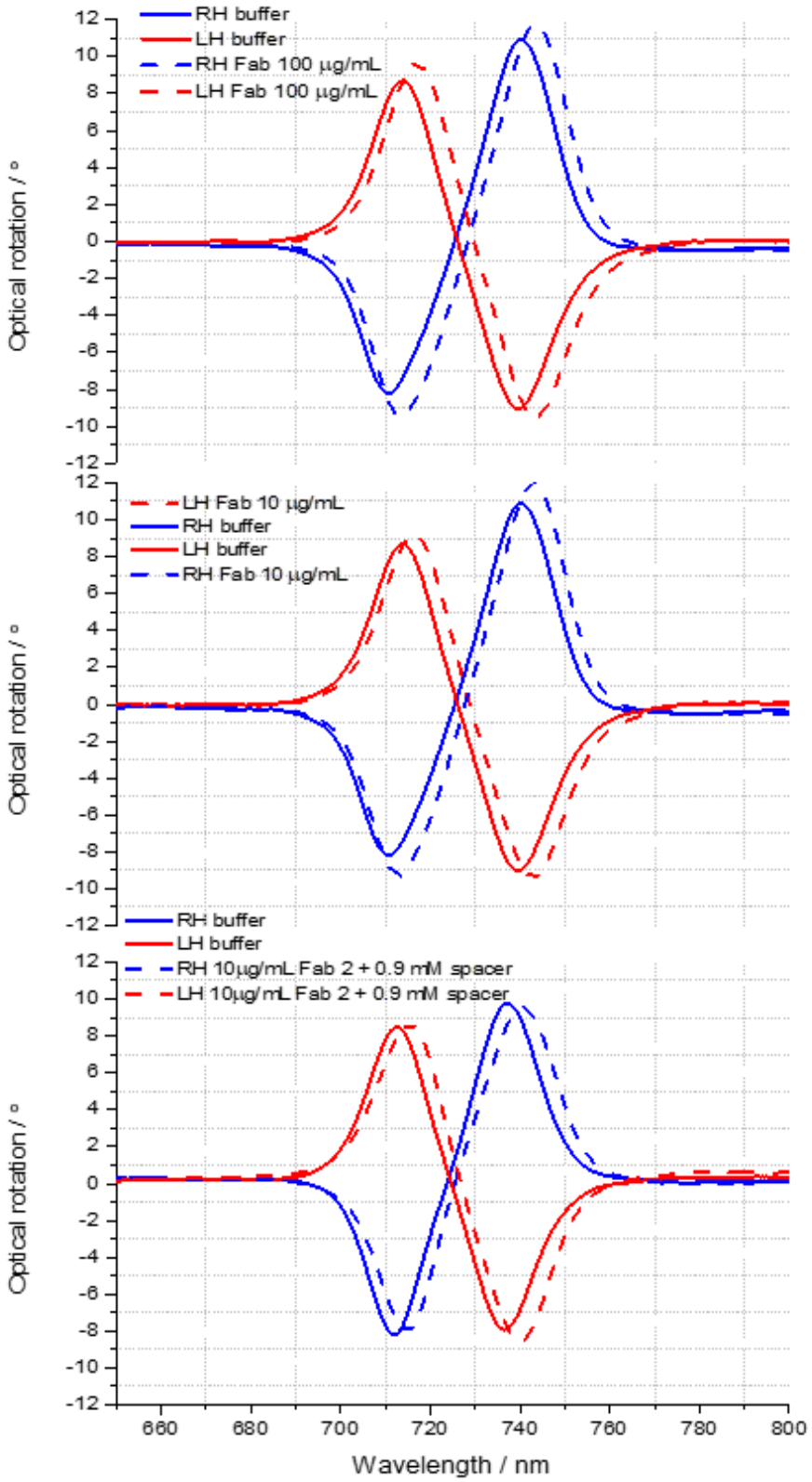

Figure 5 - 8: Represents ORD spectra of a functionalised slide with different concentrations of F(ab')$_2$. The first, second and third spectra show the ORD of a 100µg/mL, 10µg/mL and 10µg/mL plus 0.9mM spacer solution, respectively. The continuous lines are measurements taken in digestive buffer and the dash lines are measurements taken from slides coated with F(ab')$_2$ fragments.

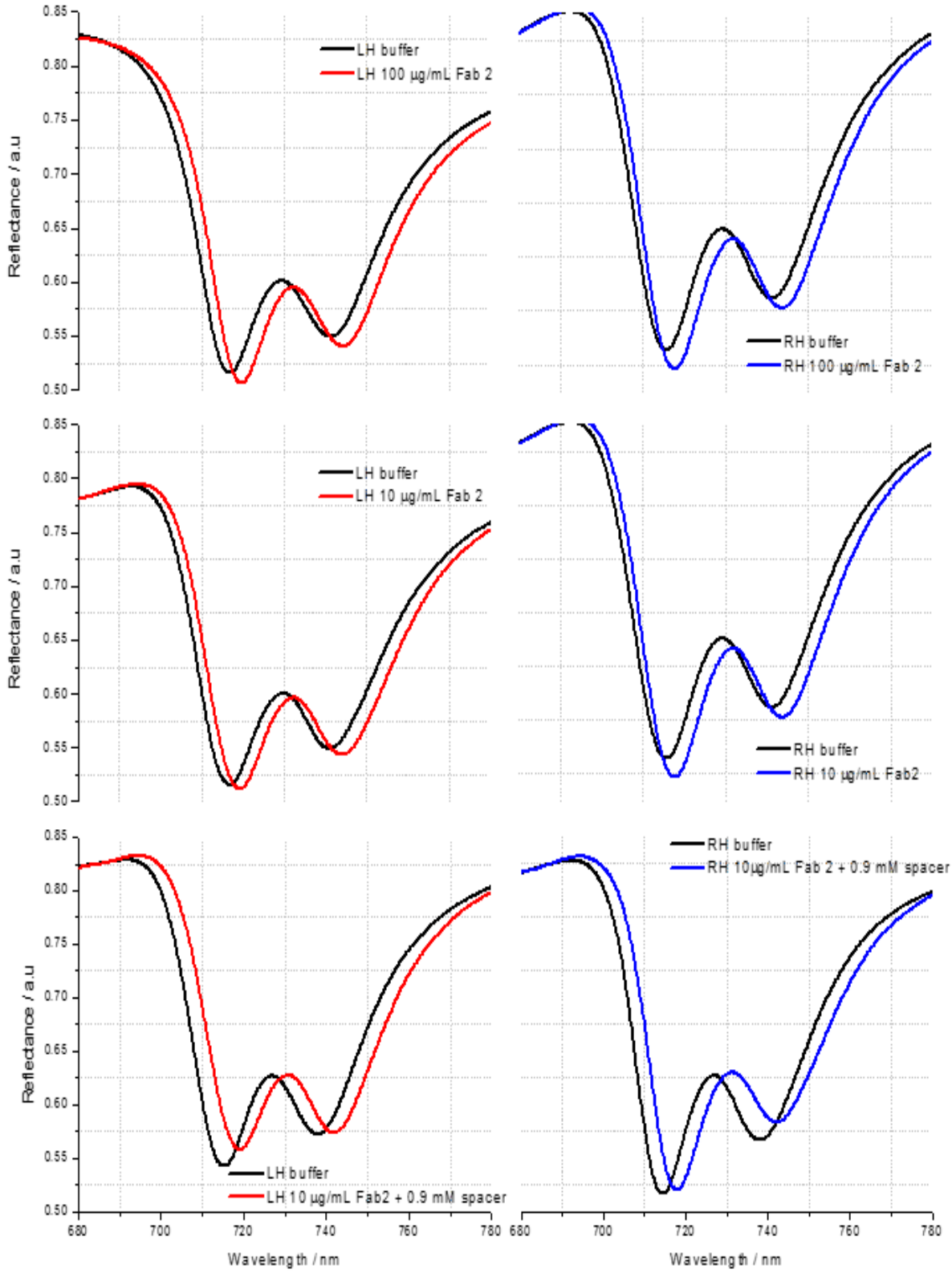

Figure 5 - 9: Represents the reflectivity spectra of functionalised slides with different concentrations of F(ab')$_2$. The first, second and third spectra show the reflectivity of a 100µg/mL,10µg/mL and 10µg/mL plus 0.9mM EG-thiol solution. The black lines are blank measurements (buffer) and the coloured lines are LH (red) and RH (blue) F(ab')$_2$ measurements.

A similar optical change in both LH and RH handedness correlates with less asymmetry. Thus, we might have $F(ab')_2$ bound to the gold in different orientations. The asymmetry parameters between the two concentrations are the same with an error.

	$F(ab')_2$ 10 µg/mL	$F(ab')_2$ 100 µg/mL	$F(ab')_2$ 10 µg/mL + 0.9mM EG-thiol
Optical parameters			
Average shift	3.00 ± 0.20	3.30 ± 0.20	3.50 ± 0.20
A	1.05 ± 0.02	1.03 ± 0.02	0.92 ± 0.02
matching parameters			
$\Delta\Delta\gamma_d$	$- 2.00 \pm 2.00.10^{-4}$	$4.00 \pm 2.00.10^{-4}$	$12.00 \pm 2.00.10^{-4}$
$\Delta\Delta\varphi$	-0.70 ± 0.20	-0.60 ± 0.20	- 3.00 ± 0.20

Table 5 - 1: Represents the asymmetry and average shift value taken from the ORD for different concentrations of $F(ab')_2$ and for a solution of $F(ab')_2$ and EG-thiol. The second part of the table is the asymmetry in $\Delta\Delta\varphi$ and $\Delta\Delta\gamma_d$ for the reflectivity signal of slides coated with $F(ab')_2$. Buffer alone is used as a reference.

The principal conclusions from these data are that there was no significant difference in the amount of $F(ab')_2$ adsorbed from the two solutions and that the observed levels of asymmetry (parametrized by A and $\Delta\Delta\varphi$) were lower in the absence of the spacer. This result is consistent with the expected behaviour, specifically that the presence of the EG-thiol reduces the level of structural perturbation on the adsorbed $F(ab')_2$. EG-thiol improves the orientation of $F(ab')_2$ at the surface because the fragments have less space to expand on the surface, furthermore, the thiol spacer also prevents interaction between $F(ab')_2$ fragments. This spacer prevents the denaturation of the fragments on the surface, even though the fragments are slightly denatured, without the spacer it would have been very likely to be worse. EG-thiol prevents BSA from binding in between $F(ab')_2$ fragments. We can see on the graph that when the EG-thiol is added only the left ORD increases its intensity. Hence the phase change happens mainly in the LH leading to a larger asymmetry. In addition, these findings are validated by the reflectivity data (figure 5 - 9), $\Delta\Delta\varphi$ being about three times higher for the $F(ab')_2$ mixed with the spacer.

The second part of table 5 - 1 displays the matching parameters extracted from the experimental data. The LH parameters were subtracted from the RH parameters in the same way we quantified the asymmetry in the experimental data ($LH/RH_{protein}$-LH/RH_{buffer} and RH – LH). Only the parameters showing a significant change in the $\Delta\Delta$ values are shown table 5 - 1. Additional details with all the parameters can be found in the appendix.

The matching parameters quantify the change in the optical signal and allow us to calculate the asymmetry. The biggest asymmetry is seen in ΔΔφ. The data help us to understand how the addition of EG-thiol prevents the denaturation of $F(ab')_2$ fragments and any interaction between the fragments. The asymmetry seen in the φ can be attributed to retardation effects in the phase; a similar phenomenon was seen with proteins[35]. φ is the phase associated with the dark mode[36]. γ_d shows a change because this parameter is linked to the dark mode (chapter 2).

5.4.2 Bovine serum albumins (BSA):

5.4.2.1 BSA on unfunctionalized surface and BSA-$F(ab')_2$ complex:

BSA is a protein widely used in biology research. It is stable and has a well-characterised structure[37], with an isoelectric point of 4.7. Here, we used the same experimental conditions as explained in literature[11] (the experimental methodology is given in details in chapter 3). BSA has 583 amino acids and displays an Albumin fold which is predominantly an α-helix and is a monomer in solution.

Here, we show the graphs extracted from measurements taken with BSA on a functionalised surface and on plain gold (figure 5 – 10). Both the ORD and reflectance show significant differences. The ORD from BSA-$F(ab')_2$ complex and $F(ab')_2$ displays a change in the peak-to-peak height of the signal. This change in the ORD height happens in both the LH and RH signals but is much more intense in the LH. The ORD of BSA shows a small asymmetry in the ΔΔλ, with the shift in LH being slightly bigger. This phenomenon cannot be seen in the ORD of the BSA-$F(ab')_2$ complex, however the change in peak heights makes the asymmetry more difficult to detect. The reflectance confirms these observations, the LH reflectivity for BSA is slightly more shifted and both LH and RH reflectance display an increase in the signal height for the BSA-$F(ab')_2$ complex.

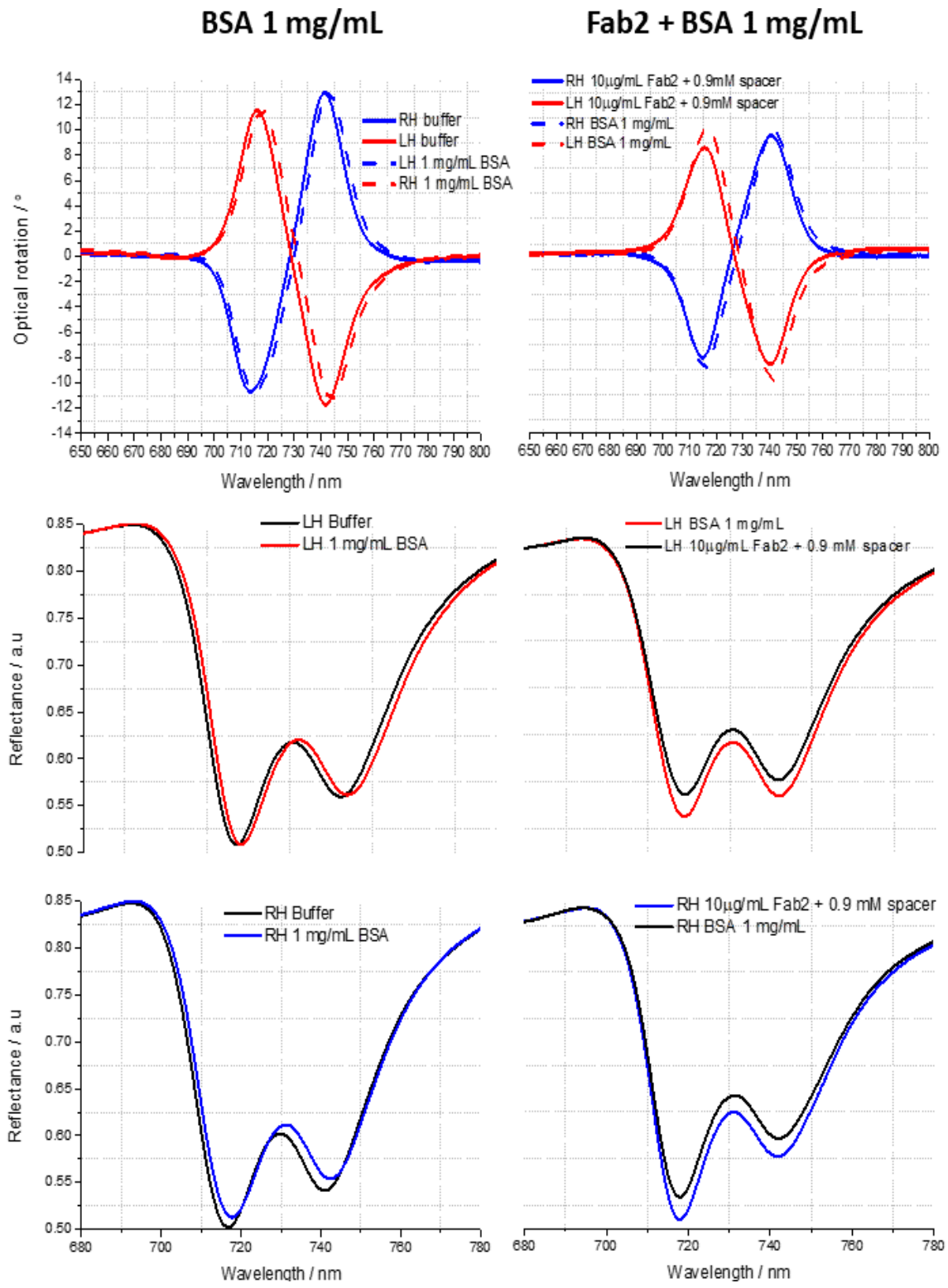

Figure 5 - 10: ORD and reflectivity spectra of BSA on gold thin film and BSA on functionalised surface. The left side of the figure shows the optical spectra for BSA used as a reference (on a gold slide). The right side of the figure shows the optical spectra for BSA on a functionalised surface with BSA at 1 mg/mL. The black lines are optical measurements in buffer. The coloured lines correspond to BSA measurements. Blue represents the RH data and red the LH data.

5.4.3.2 BSA-specifc F(ab')$_2$ with OVA:

The same experiment was carried out using OVA and BSA-specific F(ab')$_2$. OVA is a protein found in egg white, which is non toxic, and widely used in scientific research[38]. Its isoelectric point is 5.2. OVA has 385 amino acid residues and a Serpin fold consisting of a mix of α – helix and β – sheets taking the structure of a dimer in solution. We used this protein because like BSA, it belongs to the albumin family (group of globular proteins). The F(ab')$_2$ fragments are not specific for OVA proteins. This experiment was preformed to test the BSA-specific F(ab')$_2$ used with BSA to determine the error of the measurements taken (amount of protein binding to F(ab')$_2$). The experiment was carried out using the same conditions as with BSA + F(ab')$_2$. The ORD and reflectivity graphs are displayed in figure 5 - 11. The average shift for F(ab')$_2$ is 4.7, which means that there is a good coverage of fragments of the antibody on the surface. We show that the phase change in the ORD is not as significant as the one seen with BSA. The reflectivity data show no change in the damping of the signal meaning that the phase is most likely not affected.

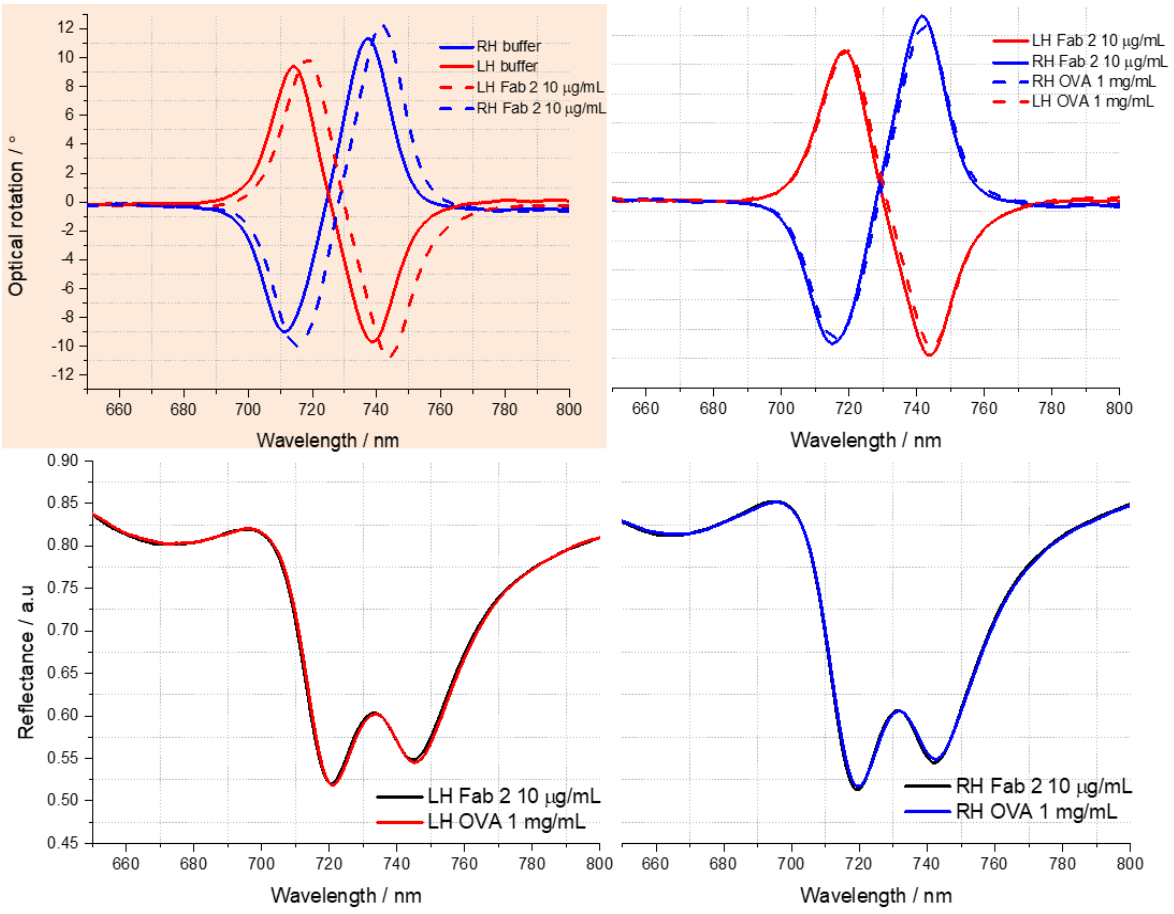

Figure 5 - 11: ORD and reflectivity spectra of OVA proteins carried out with BSA-specific F(ab')$_2$ coated slides. The top left ORD spectrum shows the amount of F(ab')$_2$ coverage of the slide.

5.4.3 Discussion:

To demonstrate the ability of chiral plasmonic fields to discriminate between specific and nonspecific PPIs, we compared the behaviour of polyclonal Fab' with the antigen BSA and nonantigen OVA. To discuss more precisely the difference and emphasize the enhancement of the asymmetry induced by BSA-F(ab')$_2$ complex, we have extracted the asymmetry parameter from the graph as shown in table 5 - 2. Here, we also display the matching parameters (the matching graphs are shown in the appendix).

	F(ab')$_2$		Gold
Protein	BSA	OVA	BSA
Concentration / mg/mL	1	1	1
Optical parameters			
Average shift	1.00 ± 0.20	0.60 ± 0.20	1.80 ± 0.20
A	0.92 ± 0.02	0.98 ± 0.02	1.03 ± 0.02
Matching parameters			
	RH-LH 1 mg/mL BSA	RH-LH 1 mg/mL OVA	RH-LH 1mg/mL BSA
ΔΔφ	-2.20 ± 0.20	-0.10 ± 0.20	-0.20 ± 0.20

Table 5 - 2: Optical and matching parameters extracted from the ORD and the reflectivity spectra for BSA (1 mg/mL) + F(ab')$_2$, OVA (1 mg/mL) + F(ab')$_2$ and BSA (1 mg/mL) on plain gold.

The protein coverage is quantified by the average shift and display differences. We noticed that, as expected, in the presence of the biorepellent spacer layer, less BSA adsorbs about 55 %, onto the mixed layer compared to the bare gold surface. The average shift between BSA-specific F(ab')$_2$ with BSA or OVA measurements is also rather similar taking the error into account. In fact, the result we get for this number is fairly accurate, the ratio between the average shift at the concentration of 1 mg/mL being:

$$\frac{average\ shift\ OVA}{average\ shift\ BSA} = \frac{0.6}{1} = 0.6 \quad (4)$$

And the ratio between the molecular masses:

$$\frac{M_w OVA}{M_w BSA} = \frac{42.7}{69.3} = 0.6 \quad (5)$$

The data clearly show that both BSA and OVA bind to the mixed Fab' layer. The average shift values of 1.0 nm and 0.6 nm scale with the molecular mass of the BSA (69.3 kDa) and OVA (42.7 kDa) monomers (equation 5); the ratios of the average shifts and monomers

molecular mass are both equal 0.6. Consequently, an equal amount of the two proteins are adsorbed. The data clearly demonstrate that both BSA and OVA bind strongly to the anti-BSA $F(ab')_2$ because they are retained on the surface even after being rinsed with phosphate buffer saline (PBS). Although similar quantities of BSA and OVA adsorb, different levels of asymmetry are observed for each, with significant asymmetry observed for BSA but not OVA. As explained in the introduction of this chapter, non-specific binding leads to a complex with no specific geometry. Thus, the chiroptical signal is weaker because all the complex conformations formed are averaged out. For the BSA-$F(ab')_2$ complex the asymmetry parameter A is around 0.9. The asymmetry parameter A for BSA on plain gold is 1, there is no phase change in the signal and thus no asymmetry detected. This is caused by the fact that BSA is randomly orientated at the surface and the chiroptical signal is averaged out. The difference in A is stronger for BSA- $F(ab')_2$ complex, indicating that there is a larger phase change for the left-handed ORD (figure 5 - 10). Although OVA is bound to $F(ab')_2$ the RH/LH ratio is also about 1, therefore, we conclude that OVA must be randomly orientated.

This suggests that while BSA binds specifically to the ensemble of anti BSA $F(ab')_2$ molecules on the surface producing a significant change in the asymmetry, OVA binds non-specifically to the same ensemble, producing almost no asymmetry (figure 5 - 12). The $F(ab')_2$ used were tested with an enzyme-linked immunosorbent assay (ELISA) and were confirmed to be only BSA specific, meaning that OVA cannot complex with them. Therefore, despite the precaution taken to minimize structural distortions, the selectivity of the Fab' proteins has in part been affected by immobilisation directly onto the gold surface of the polycarbonate slide, thus enabling OVA to bind. This kind of structural degradation of the selectivity has been seen before in SPR measurement. The loss of selectivity can be attributed to a structural distortion of the $F(ab')_2$ fragment, which generates protein surfaces that result in non-specific binding of OVA. Because no specific epitopes on the surface of the OVA are involved in binding, random $F(ab')_2$-OVA aggregates are formed, which on average for the ensemble have an isotropic chiral dielectric response.

We can conclude that the asymmetry parameter A is a good indicator of the order of chiral material on the surface. Since non-specific PPI interaction results in an isotropic chiral dielectric response, we can discriminate between specific and non-specific binding partners. When we do not see any asymmetry (A=1) the material is randomly orientated at the surface. But if A is not equal to 1 then there is order at the surface and the asymmetry is enhanced. The second part of table 5 - 2 shows the matching parameters. The BSA-$F(ab')_2$ complex exhibits a larger change in $\Delta\Delta\varphi$. Non-specific BSA-BSA protein interactions are less likely to occur with BSA-specific $F(ab')_2$ coated slides, and this will increase the

asymmetry. As for the experimental parameters, we have similar numbers between OVA-F(ab')$_2$ complex and BSA alone on gold. The change in ΔΔφ translates in the ORD spectra by a change in the peak-to-peak height of the signal (chapter 3). If BSA is ordered at the surface, then we see a phase change (in ΔΔφ) and A is different from 1; but if it is disordered then there is no asymmetry in the phase of the dark mode.

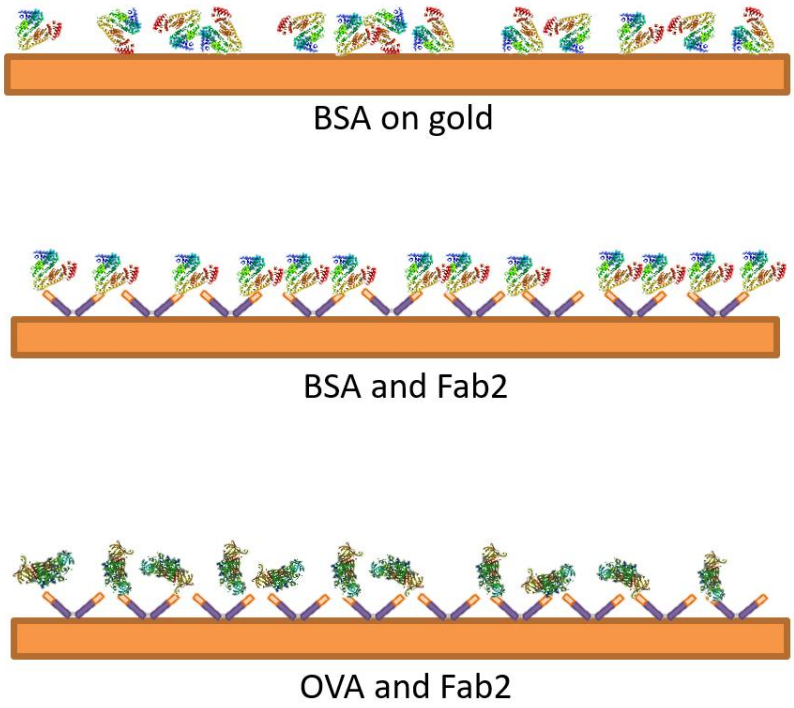

Figure 5 - 12: Summary of the different orientations of material at the surface. BSA on gold is randomly orientated, but when the antibody is added the BSA is ordered at the surface. OVA randomly binds to BSA-specific F(ab')$_2$.

To sum up, from the asymmetry parameters we see that OVA-F(ab')2 complex behaves in the same way as BSA without F(ab')$_2$ and does not show a significant asymmetry. This is proof that BSA interacts with F(ab')$_2$ fragments and gets ordered on the surface leading to enhancement of the chirality in the optical signal. As said in the introduction a protein antibody complex with a specific geometry (anisotropic) is an indicator of specific PPI.

5.5 Conclusion:

In this chapter, we have studied the protein-protein interactions with chiral fields, focusing on the antibody-antigen interactions. We showed that spectroscopic measurements using chiral plasmonic nanostructures provide a description of the specificity of a PPI based on the level of structural anisotropy of the complex. Linear optical measurements such as ORD and reflectivity were used to probe the specificity of this bond. Studying the interaction

between an antibody and an antigen is of great importance to understand the mechanism behind this bond.

Here, we used F(ab')2 fragments from polyclonal rabbit IgG to study the interaction between BSA and antibody. We created a monolayer of $F(ab')_2$ on our substrate. We showed that we could detect the presence of $F(ab')_2$ on the surface, those being made of amino acids, they exhibit asymmetry in the signal. The asymmetry parameters extracted from the graphs show that without a spacer there is less order on the surface, the asymmetry parameters are smaller. We added EG-thiol as a spacer, and we could see that the asymmetry was increasing. This was particularly true for A, the parameter quantifying the phase of the ORD signal. More order on the surface makes it easier for $F(ab')_2$ to react with BSA. The asymmetry in the phase φ of the dark mode is increased (three times larger) once EG-thiol is added.

We investigated the behaviour of BSA on a plain gold surface and on a surface coated with $F(ab')_2$. OVA was used as a control to show that $F(ab')_2$ was indeed specific for BSA. Distinction between BSA with and without $F(ab')_2$ could be made in the ORD of the signal. The BSA-F(ab')2 complex induced changes in the peak-to-peak height of the ORD signal. The asymmetry parameter A exhibits no asymmetry for BSA on plain gold but displays an asymmetry for BSA attached to gold with $F(ab')_2$, even at low concentration. This is explained by the fact that all the BSAs specifically bind to $F(ab')_2$ and all the proteins have the same orientation leading to the change in the LH signal. BSA on plain gold is randomly orientated and thus the chiroptical signal decreases. However, structural distortion of the F(ab') occurs when immobilised on the gold making them less specific thus able to complex with OVA. OVA is shown to bind to $F(ab')_2$, but because these $F(ab')_2$ fragments are not specific for OVA the OVA is disordered at the surface and small aggregates are formed. This is confirmed by the asymmetry parameters A not showing chirality. When modelling the data, we realised that the asymmetry in BSA-$F(ab')_2$ complex measurement arises from the phase change in the dark mode (φ). This chapter emphasizes the importance of protein orientation at the surface for biosensing. The strategy used in this chapter, is unique in that it is rapid and provides a structure-based measure of specificity. It contrasts with established state-of-art strategies based on measuring the strength of binding affinities, which monitor selectivity in binding rather than the specificity of the PPI. This new approach provides a mechanism for rapid screening of PPIs, a capability ideal for medical diagnostic or proteomic applications where high-throughput methods are a prerequisite.

5.6 References:

(1) Montgomery, C. R. (Ed.) Protein-Protein Interactions (PPIs): Types, Methods for Detection and Analysis. Nova (2016).

(2) Jones, S.; Thornton, J. M. Principles of Protein-Protein Interactions. Proc Natl Acad Sci USA (1996), 93 (1), 13–20.

(3) Kobe, B.; Guncar, G.; Buchholz, R.; Huber, T.; Maco, B.; Cowieson, N.; Martin, J. L.; Marfori, M.; Forwood, J. K. Crystallography and Protein-Protein Interactions: Biological Interfaces and Crystal Contacts. Biochem. Soc. Trans. (2008), 36 (6), 1438–1441.

(4) Kelly, S. M.; Price, N. C. The Use of Circular Dichroism in the Investigation of Protein Structure and Function. Curr. Protein Pept. Sci. (2000), 1 (4), 349–384.

(5) Pierce, M. M.; Raman, C. S.; Nall, B. T. Isothermal Titration Calorimetry of Protein-Protein Interactions. Methods (1999), 19 (2), 213–221.

(6) Berggård, T.; Linse, S.; James, P. Methods for the Detection and Analysis of Protein-Protein Interactions. Proteomics (2007), 7 (16), 2833–2842.

(7) Davies, D. R.; Cohen, G. H. Interactions of Protein Antigens with Antibodies. Proc Natl Acad Sci USA (1996), 93 (1), 7–12.

(8) Ehler, T. T.; Malmberg, N.; Noe, L. J. Characterization of Self-Assembled Alkanethiol Monolayers on Silver and Gold Using Surface Plasmon Spectroscopy. J. Phys. Chem. (1997), 101 (8), 1268–1272.

(9) Scarano, S.; Mascini, M.; Turner A.P.F.; Minunni, M. Surface Plasmon Resonance Imaging for Affinity-Based Biosensors. Biosens Bioelectron, (2010), 25 (5), 957-966.

(10) Anker, J. N.; Hall, W. P.; Lyandres, O.; Shah, N. C.; Zhao, J.; Van Duyne, R. P. Biosensing with Plasmonic Nanosensors. Nat. Mater. (2008), 7 (6), 442–453.

(11) Tullius, R.; Karimullah, A. S.; Rodier, M.; Fitzpatrick, B.; Gadegaard, N.; Barron, L. D.; Rotello, V. M.; Cooke, G.; Lapthorn, A.; Kadodwala, M. “Superchiral” Spectroscopy: Detection of Protein Higher Order Hierarchical Structure with Chiral Plasmonic Nanostructures. J. Am. Chem. Soc. (2015), 137 (26), 8380–8383.

(12) Liu, Y.; Liu, Y.; Mernaugh, R. L.; Zeng, X. Single Chain Fragment Variable Recombinant Antibody Functionalized Gold Nanoparticles for a Highly Sensitive Colorimetric Immunoassay. Biosens. Bioelectron. (2009), 24 (9), 2853–2857.

(13) Špringer, T.; Ermini, M. L.; Špačková, B.; Jabloňků, J.; Homola, J. Enhancing Sensitivity of Surface Plasmon Resonance Biosensors by Functionalized Gold Nanoparticles: Size Matters. Anal. Chem. (2014), 86 (20), 10350–10356.

(14) Prime, K. L.; Whitesides, G. M. Self-Assembled Organic Monolayers : Model Systems for Studying Adsorption of Proteins at Surfaces. Science (1991), 252 (5009), 1164–1167.

(15) Ostuni, E.; Yan, L.; Whitesides, G. M. The Interaction of Proteins and Cells with Self-Assembled Monolayers of Alkanethiolates on Gold and Silver. Colloids Surf B Biointerfaces (1999), 15 (1), 3–30.

(16) Häkkinen, H. The Gold–Sulfur Interface at the Nanoscale. Nat. Chem. (2012), 4 (6), 443–455.

(17) Lipman, N. S.; Jackson, L. R.; Trudel, L. J.; Weis-Garcia, F. Monoclonal Versus Polyclonal Antibodies: Distinguishing Characteristics, Applications, and Information Resources. ILAR J. (2005), 46 (3), 258-268.

(18) Flaherty, D. K. Immunology for Pharmacy. Elsevier (2012).

(19) Trilling, A. K.; Beekwilder, J.; Zuilhof, H. Antibody Orientation on Biosensor Surfaces: A Minireview. Analyst (2013), 138 (6), 1619–1627.

(20) Albers, W. M.; Auer, S.; Helle, H.; Munter, T.; Vikholm-Lundin, I. Functional Characterisation of Fab′-Fragments Self-Assembled onto Hydrophilic Gold Surfaces. Colloids Surf B Biointerfaces (2009), 68 (2), 193–199.

(21) Brogan, K. L.; Wolfe, K. N.; Jones, P. A.; Schoenfisch, M. H. Direct Oriented Immobilization of F(Ab′) Antibody Fragments on Gold. Anal. Chim. Acta (2003), 496 (1–2), 73–80.

(22) Klein, J. S.; Gnanapragasam, P. N. P.; Galimidi, R. P.; Foglesong, C. P.; West, A. P.; Bjorkman, P. J. Examination of the Contributions of Size and Avidity to the Neutralization Mechanisms of the Anti-HIV Antibodies B12 and 4E10. Proc. Natl. Acad. Sci. USA (2009), 106 (18), 7385–7390.

(23) Carter, D. P.; Staehelin, L. A. Evaluation of IgG Molecules, Fab' Fragments and IgG-horseradish Peroxidase Conjugates as Surface Labels for Freeze-Etched Membranes. J. Microsc. (1979), 117 (3), 363–373.

(24) Vikholm-Lundin, I. Immunosensing Based on Site-Directed Immobilization of Antibody Fragments and Polymers That Reduce Nonspecific Binding. Langmuir (2005), 21 (14), 6473–6477.

(25) Crivianu-Gaita, V.; Thompson, M. Immobilization of Fab' Fragments onto Substrate Surfaces: A Survey of Methods and Applications. Biosens. Bioelectron. (2015), 70, 167–180.

(26) Yu, S.; Perálvarez-Marín, A.; Minelli, C.; Faraudo, J.; Roig, A.; Laromaine, A. Albumin-Coated SPIONs: An Experimental and Theoretical Evaluation of Protein Conformation, Binding Affinity and Competition with Serum Proteins. Nanoscale (2016), 8 (30).

(27) Bain, C. D.; Biebuyck, H. A.; Whitesides, M. G. Comparison of Self -Assembled Monolayers on Gold: Coadsorption of Thiols and Disulfides. Langmuir (1989), 5 (3), 723–727.

(28) Yoshimoto, K.; Nishio, M.; Sugasawa, H.; Nagasaki, Y. Direct Observation of Adsorption-Induced Inactivation of Antibody Fragments Surrounded by Mixed-PEG Layer on a Gold Surface. J. Am. Chem. Soc. (2010), 132 (23), 7982–7989.

(29) Prime, K. L.; Whitesides, G. M. Adsorption of Proteins onto Surfaces Containing End-Attached Oligo(Ethylene Oxide): A Model System Using Self-Assembled Monolayers. J. Am. Chem. Soc. (1993), 115 (23), 10714–10721.

(30) Xi, E.; Venkateshwaran, V.; Li, L.; Rego, N.; Patel, A. J.; Garde, S. Hydrophobicity of Proteins and Nanostructured Solutes Is Governed by Topographical and Chemical Context. Proc Natl Acad Sci USA (2017), 114 (51), 13345–13350.

(31) Jack, C.; Karimullah, A. S.; Tullius, R.; Khorashad, L. K.; Rodier, M.; Fitzpatrick, B.; Barron, L. D.; Gadegaard, N.; Lapthorn, A. J.; Rotello, V. M.; Cooke, G.; Govorov, A. O.; Kadodwala, M. Spatial Control of Chemical Processes on Nanostructures through Nano-Localized Water Heating. Nat. Commun. (2016), 7, 10946.

(32) Hermanson, G. T. PEGylation and Synthetic Polymer Modification. Bioconjugate Techniques (2013); 787–838.

(33) Bürck, J.; Wadhwani, P.; Fanghänel, S.; Ulrich, A. S. Oriented Circular Dichroism: A Method to Characterize Membrane-Active Peptides in Oriented Lipid Bilayers. Acc. Chem. Res. (2016), 49 (2), 184–192.

(34) Sigal, G. B.; Bamdad, C.; Barberis, A.; Strominger, J.; Whitesides, G. M. A Self-Assembled Monolayer for the Binding and Study of Histidine-Tagged Proteins by Surface Plasmon Resonance. Anal. Chem. (1996), 68 (3), 490–497.

(35) Tullius, R.; Platt, G. W.; Khorashad, L. K.; Gadegaard, N.; Lapthorn, A. J.; Rotello, V. M.; Cooke, G.; Barron, L. D.; Govorov, A. O.; Karimullah, A. S.; Kadodwala, M. Superchiral Plasmonic Phase Sensitivity for Fingerprinting of Protein Interface Structure. ACS Nano (2017), 11 (12), 12049–12056.

(36) Tassin, P.; Zhang, L.; Zhao, R.; Jain, A.; Koschny, T.; Soukoulis, C. M. Electromagnetically Induced Transparency and Absorption in Metamaterials: The Radiating Two-Oscillator Model and Its Experimental Confirmation. Phys. Rev. Lett. (2012), 109 (18), 187401.

(37) Murayama, K.; Tomida, M. Heat-Induced Secondary Structure and Conformation Change of Bovine Serum Albumin Investigated by Fourier Transform Infrared Spectroscopy. Biochemistry (2004), 43 (36), 11526–11532.

(38) Huntington, J. A.; Stein, P. E. Structure and Properties of Ovalbumin. J. Chromatogr. B Biomed. Sci. Appl. (2001), 756 (1–2), 189–198.

5.7 Appendix:

	RH-LH $F(ab')_2$ 10 µg/mL	RH-LH $F(ab')_2$ 100 µg/mL	RH-LH $F(ab')_2$ 10 µg/mL + spacer
$\Delta\Delta\omega_r$	-0.50 ± 0.20	-1.10 ± 0.20	0.10 ± 0.20
$\Delta\Delta\omega_d$	-0.50 ± 0.20	-1.10 ± 0.20	0.10 ± 0.20
$\Delta\Delta k$	0.00 ± 2.10^{-4}	2.00 ± 2.10^{-4}	11.00 ± 2.10^{-4}
$\Delta\Delta\gamma_r$	-10.0 ± 3.10^{-4}	-10.0 ± 3.10^{-4}	0.00 ± 3.10^{-4}
$\Delta\Delta\gamma_d$	-2.00 ± 2.10^{-4}	4.00± 2.10^{-4}	12.0± 2.10^{-4}
$\Delta\Delta\theta$	0.00 ± 0.20	0.00 ± 0.20	0.00 ± 0.20
$\Delta\Delta\varphi$	-0.70 ± 0.20	-0.60 ± 0.20	-3.00 ± 0.20

Table 5 - 3: Asymmetry in the matching parameters for the reflectivity signal of slides coated with $F(ab')_2$. Buffer is used as a reference.

	$F(ab')_2$		Gold
Matching parameters	RH-LH 1 mg/mL BSA	RH-LH OVA (1 mg/mL)	RH-LH 1 mg/mL BSA
$\Delta\Delta\omega_r$	-0.10 ± 0.20	-0.20 ± 0.20	0.00 ± 0.20
$\Delta\Delta\omega_d$	-0.10 ± 0.20	-0.20 ± 0.20	0.00 ± 0.20
$\Delta\Delta k$	8.00 ± 2.10^{-4}	0.00 ± 2.10^{-4}	0.00 ± 2.10^{-4}
$\Delta\Delta\gamma_r$	-5.00 ± 3.10^{-4}	0.00 ± 3.10^{-4}	0.00 ± 3.10^{-4}
$\Delta\Delta\gamma_d$	18.00 ± 2.10^{-4}	6.00 ± 2.10^{-4}	7.00 ± 2.10^{-4}
$\Delta\Delta\varphi$	-2.20 ± 0.20	-0.10 ± 0.20	-0.20 ± 0.20
$\Delta\Delta\theta$	0.00 ± 0.20	0.00 ± 0.20	0.00 ± 0.20

Table 5 - 4: Asymmetry parameters extracted from the ORD and the reflectivity spectra for BSA (1 mg/mL) + $F(ab')_2$, OVA (1 mg/mL) + $F(ab')_2$ and BSA (1 mg/mL) on plain gold.

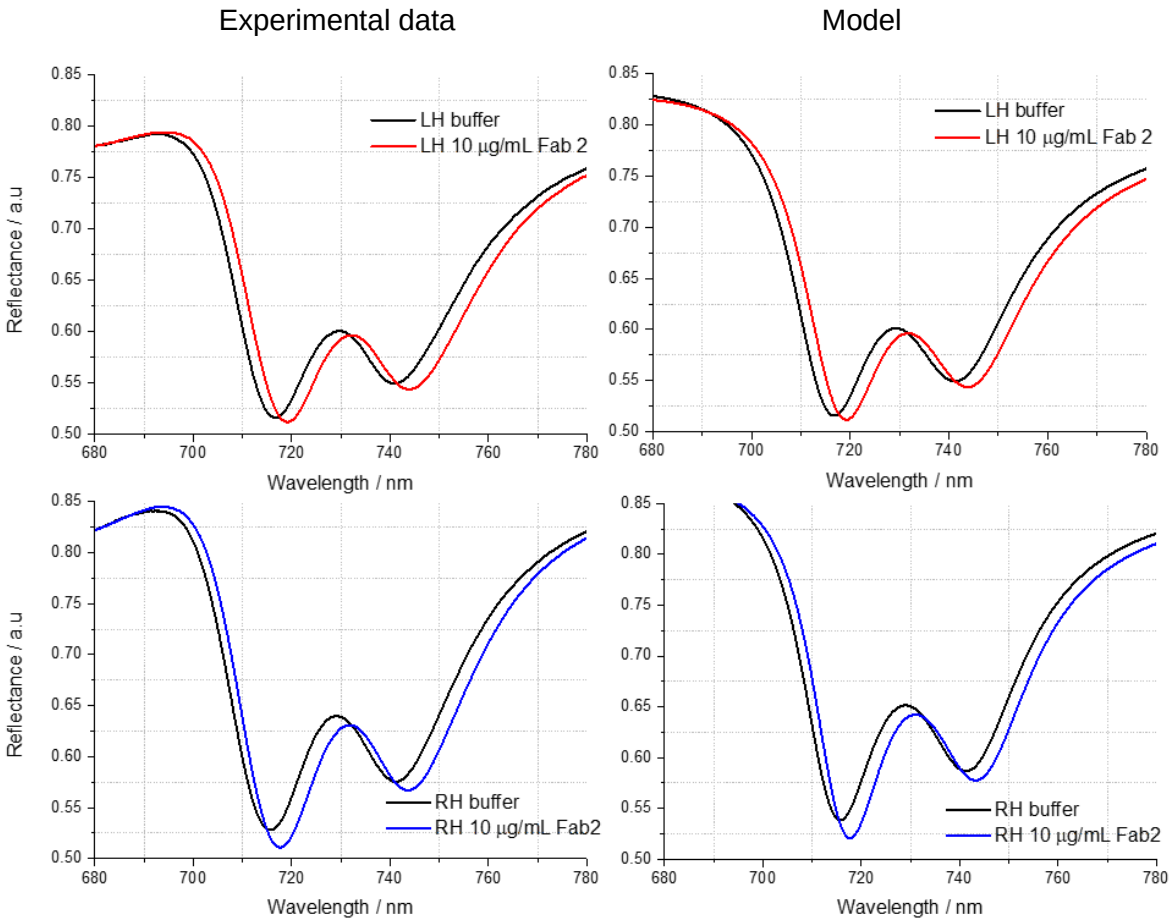
Experimental data
Model
Reflectance / a.u
Wavelength / nm
LH buffer
LH 10 µg/mL Fab 2
RH buffer
RH 10 µg/mL Fab2
0.85
0.80
0.75
0.70
0.65
0.60
0.55
0.50
680
700
720
740
760
780

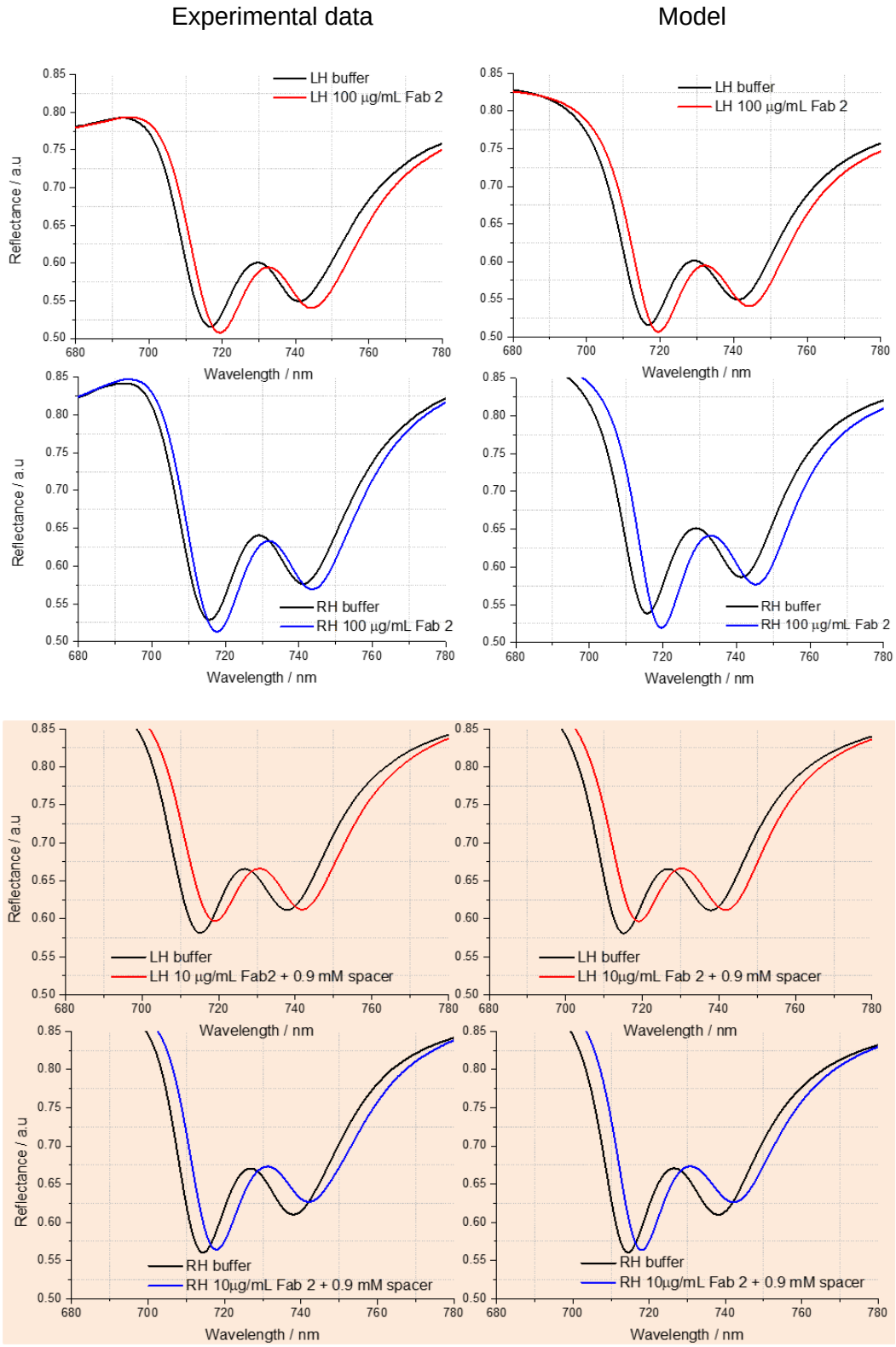

Figure 5 - 13: Experimental and matched reflectivity spectra of a functionalised gold slide. The experimental data is shown in the left part of the figure and the matched data on the right. The reflectivity spectra are plotted for each structure, the black solid line are measurements done in buffer. The coloured lines are the $F(ab')_2$ measurement data with the red line representing LH and blue RH.

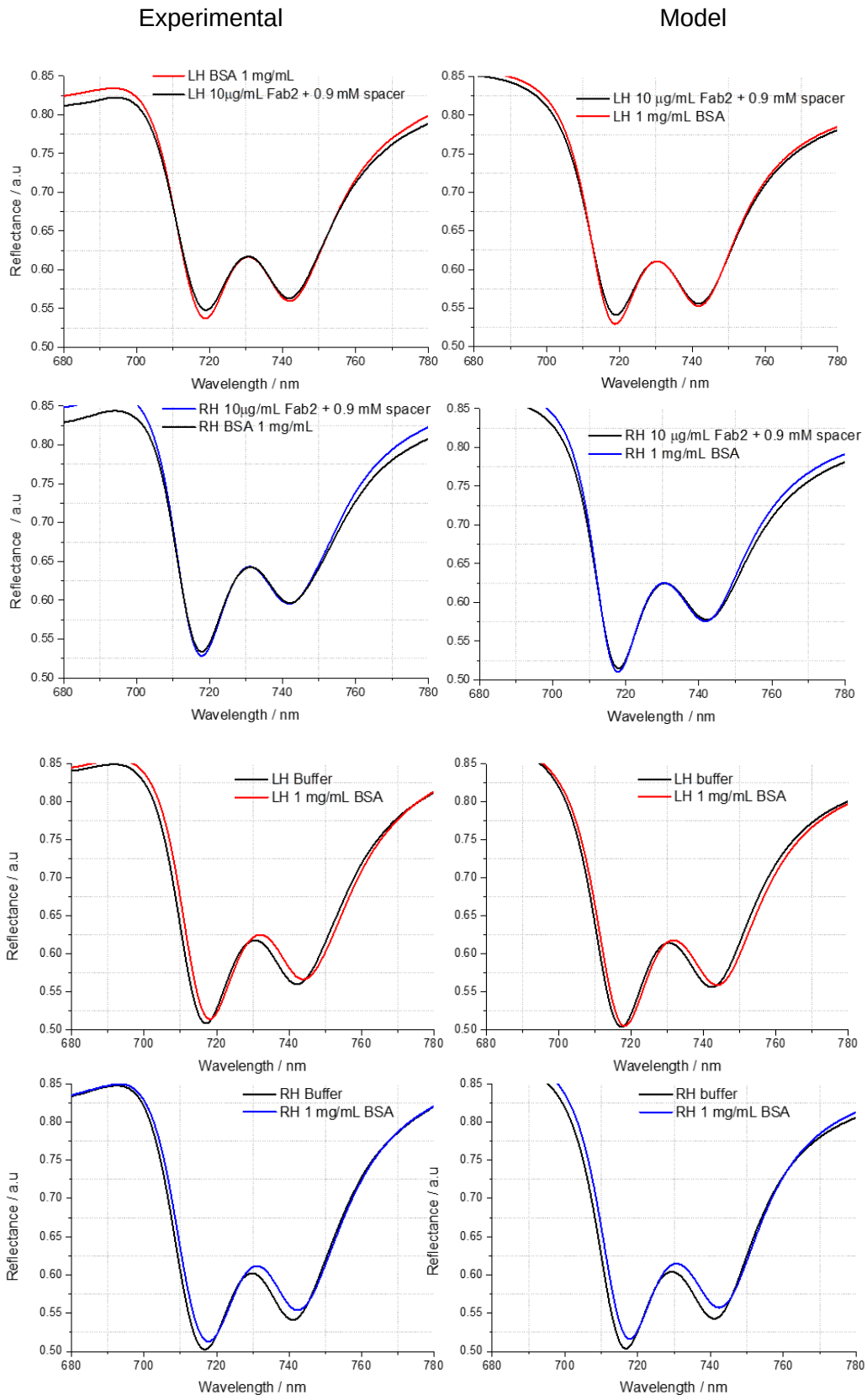

Figure 5 - 14: Reflectivity graphs of BSA on a functionalised surface and a non-functionalised one. The left column shows the experimental data and the right the graphs from the model data with PIT modelling (chapter 2).

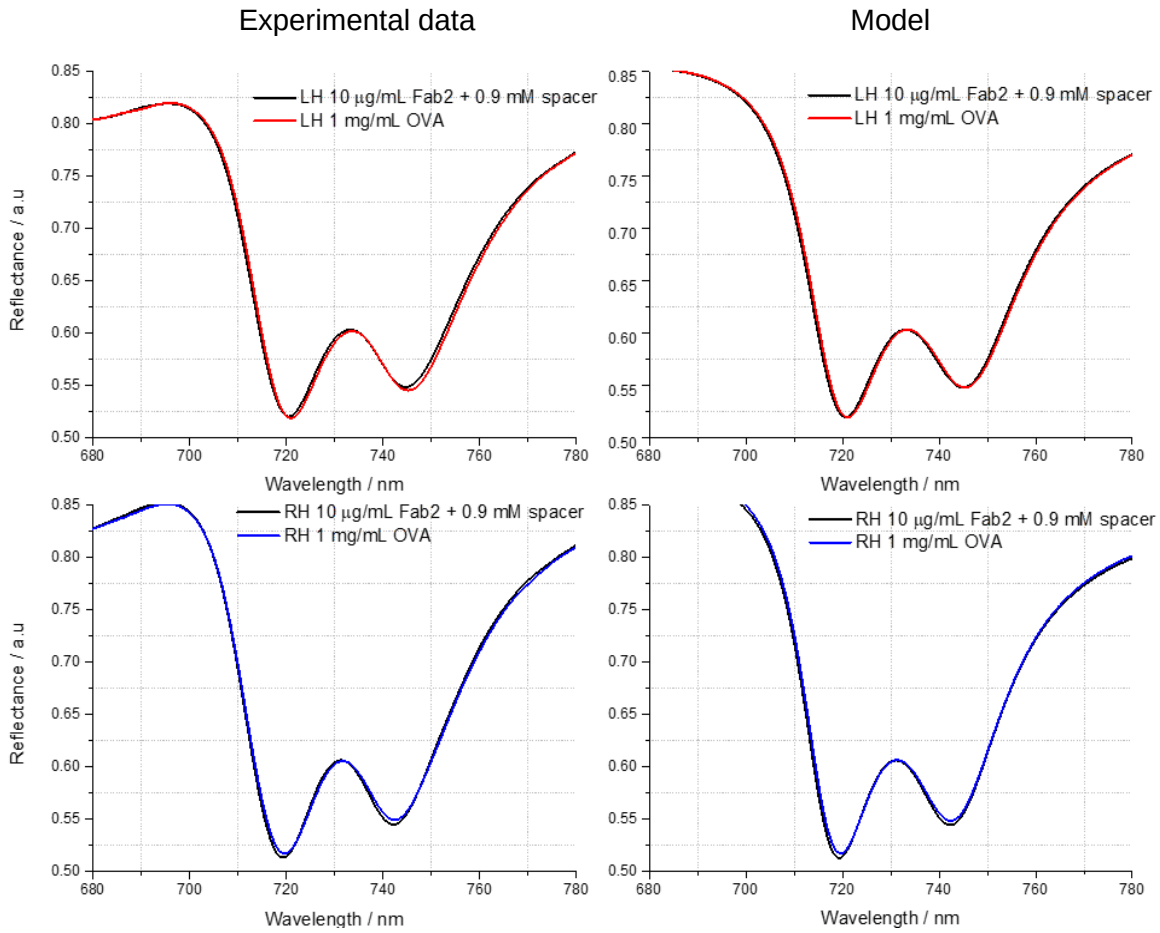

Figure 5 - 15: Reflectivity graphs of OVA on a functionalised surface. The left column shows the experimental data and the right column the graphs from the data modelled with PIT modelling.

Chapter 6: Distinction between icosahedral plant viruses with chiral plasmonic fields

In this chapter, we will use chiral plasmonic fields to study plant viruses. Plant viruses have different sizes, shapes and symmetries that permit the investigation of chirality on the nano-meso scale[1]. Viruses are highly symmetric, but they are made of L-amino acids and have chiral secondary structure elements[2], so they can induce a change in the chiroptical signal. In addition to the different shapes and symmetries of viruses, they contain nucleic acids packaged within the outer shell of the protein, in a semi-ordered structure. We will investigate the difference of whole viruses containing both proteins and RNA, with RNA-free particles. A new route to distinguish quickly between pathogen and non-pathogen particles will be explored by looking at the behaviour of these viruses, when exposed to the plasmonic fields.

6.1 Introduction:

Viruses come in different sizes and shapes and are known to infect every form of life. At the most basic level viruses contain genetic material (RNA or DNA); which is packaged into protein capsids[2] to facilitate delivery into suitable host cells where the genetic material can be copied, and new viruses produced. This ability of the capsid proteins to act as a delivery vehicle has attracted a lot of interest[3,4]. These virus-like particles (VLP) are non-infectious because they contain no viral genetic material[5]. They can be produced naturally and are candidate delivery system for genes or other therapeutics[6] (virus member of Papillomaviridae and Polyomaviridae families). In this chapter we will be looking at plant viruses. These particles are well characterised and relatively easy to produce[7]. A lot of research effort is focused on the plant virus field because of the financial aspect of the loss those viruses involve, especially for the food supply[8,9]. Most plant viruses come in two shapes: helical and icosahedral[9]. In this chapter we will focus on viruses of icosahedral shape.

The analysis, structural characterisation and reproduction of viruses are essential to understand virus epidemiology. Studying plant viruses is easier and safer than studying pathogenic human specific viruses. Indeed, plant viruses work in a similar way to those of mammals; any information collected about the way they function is invaluable for immunology purpose[7].

The analytical techniques nowadays require high resolution size detection and compatibility with specific buffer. It also requires detection to be carried out under precise biologically

relevant conditions[10]. Several techniques must be used to characterise one virus. The techniques available today for virus characterisation are atomic force microscopy (AFM), mass spectroscopy, electron microscopy (EM), fluorescence microscopy, size exclusion chromatography and light scattering technique[11]. Moreover, the analytical techniques available today are optimised for protein detection making them not trivial to use for particles with a much larger size and mass. Most of these techniques require materials of high purity and are time consuming to perform.

In this chapter, we will show primarily results on how chiral plasmonic fields, generated with a nanopatterned surface, can be used to characterise plant viruses. We will compare viruses with a similar structure but different sizes. Specifically, we will be looking at the following viruses: turnip yellow mosaic virus (TYMV), cowpea mosaic virus (CpMV), cucumber mosaic virus (CMV) and cauliflower mosaic virus (CaMV). These viruses are all icosahedral. They are all RNA containing particles except for CaMV which contains DNA[12]. For the same viruses we will be looking at the empty capsids and the intact virus particles containing RNA. We will show how these different particles affect the ORD and the reflectivity of light, and how we can use these different behaviours to differentiate them. Optical measurements with particles tagged with a gold binding domain will be also carried out. We will show here that we can identify differences in viruses of similar symmetry and between particles containing genetic material and empty capsids. Viruses with a gold binding domain will be studied under chiral plasmonic fields. Thiol tagged TYMV will be shown to display a higher asymmetry because of their orientation at the surface. It will be shown that the immobilisation method is changing the surface charge distribution of the virus and thus gives another type of asymmetry.

6.2 Structures and functions of plant viruses:

Viruses can be classified in groups according to their type of genetic material, symmetry, size and shape, and their mode of replication[13]. A virus carries genetic material used to replicate itself in a host[14]. The viral genome is contained in a capsid made of assembled protomer and coated with the coat protein[15]. On top of that, there are glycoproteins involved in the infectious process of cells (figure 6 - 1). A virus replicates itself by infecting a cell. When the replication is done the cell lyses and the virions are released in the body[16]. The capsid of the virus displays a quasi-symmetry, interchangeable hexamer or pentamer created by an assembly of the same protein[17].

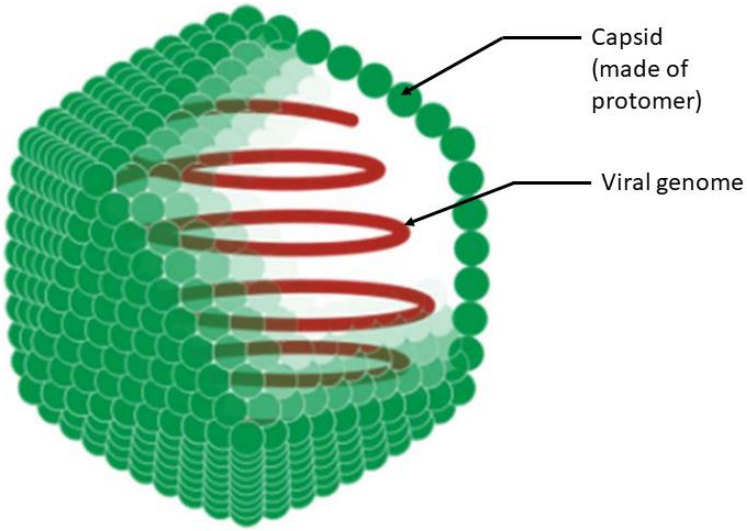

Figure 6 - 1: Simple representation of the structure of a plant virus.

The size of virus particles can range from 10 nm to 400 nm[7]. Their capsids are made of an assembly of proteins called coat-proteins. Even though viruses are rather symmetrical they are made of proteins which are known to be chiral thanks to several features (chapter 2) and because they are made of amino acids (all L).

A virus must infect a cell in order to duplicate itself[16]. On its own, a virus cannot replicate because it lacks the protein synthesis facilities and borrows it from the host. The capsid of a virus is the first part of the virus that interacts with the cell. It is also crucial for the survival of the virus in a host. Plant viruses can contain RNA or DNA, 75 % of plant viruses contain single stranded RNA. They can encode in a range of 1 to 12 proteins, while human viruses can encode a range of 100 to 200 proteins for the most complex viruses[18].

Icosahedral symmetry has 60 rotational symmetries which are either 5-fold, 3-fold or 2-fold, and a symmetry order of 120 including transformations that combine a reflection and a rotation. A football is a common object that has icosahedral symmetry. This shape is optimum to form a closed spherical shell made of a repeating pattern of protein subunit, which is why most of plant viruses are of icosahedral shape[19]. According to the quasi-symmetry principle, the capsid can be described by a sheet of hexamers, some of them being replaced by pentamers following selection rules given by the T number[19]. Viruses differ in symmetry because of their triangulation numbers (T) which vary according to the type of virus. This specific number characterises the number of asymmetric subunits but does not give information on the size of the particle. The triangulation number can be calculated, with the assignment of an origin, according to the following formula[20]:

$$T = h^2 + hk + k^2 \quad (1)$$

Where h and k are whole numbers, h is the number of units in line toward the same pentagon and k is the number of units on either side of the pentagon. Some viruses have different values for T but a similar diameter. Figure 6 - 2 shows three types of icosahedral geometry for viruses with different T numbers.

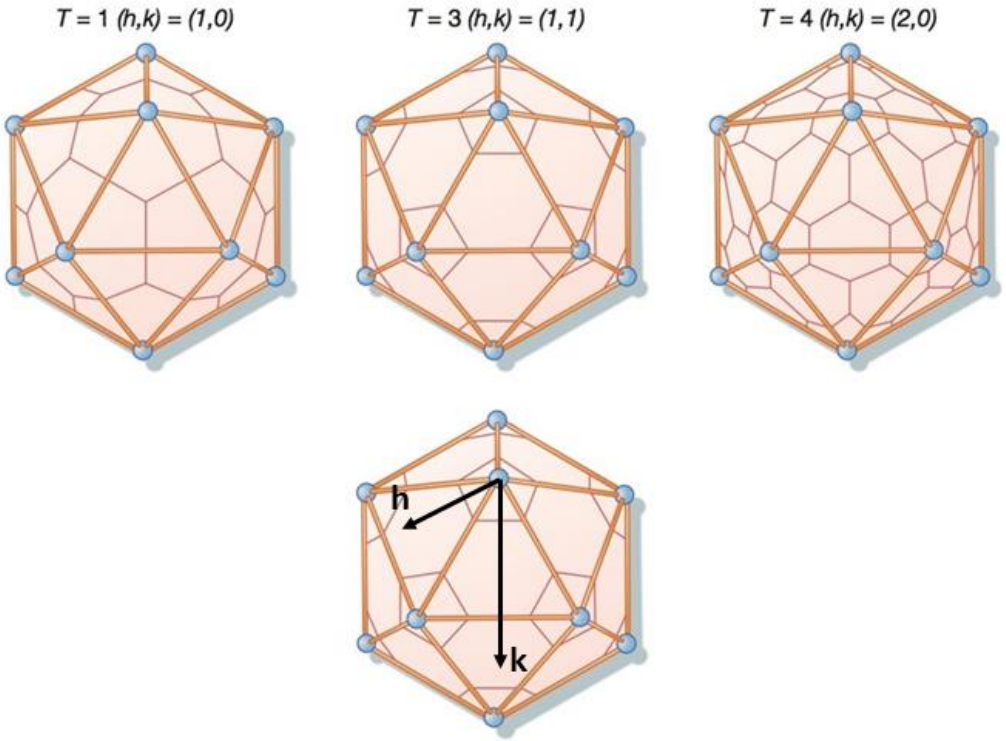

Figure 6 - 2: Picture of three possible symmetries of icosahedral viruses with different triangulation numbers and the axis to calculate it.

The structural properties of the viruses studied in this chapter are detailed in the table 6 - 1.

	CpMV	TYMV	CaMV
T number	1	3	7
Diameters / nm	28-30	30	50
isoelectric point	5.5	3.6	7.02
genetic material	RNA	RNA	DNA

Table 6 - 1: Properties of the plant viruses used in this chapter.

The cowpea mosaic virus (CpMV) is from the family Comoviruses, Secoviridae. The genome of the virus consists of two encapsidated positive strain RNAs[21,22]. The capsid of the virus is made of two coat proteins, a small one and a larger one, respectively 20 kDa and 40 kDa; 60 copies of each[23]. Its contamination vector is the chrysomelid beetle. Turnip yellow mosaic virus (TYMV) belongs to the family of tymoviruses. The capsid is made of 180 units of a coat-protein of 25kDA. The contamination vector is here again an insect: the beetle. Cauliflower mosaic virus (CaMV) is one of the few plant viruses that contain circular double strained DNA. The DNA is encapsulated in a spherical capsid. Transmission of

viruses between plants is done by aphid (insects) vectors. The virus we used came from the family of Caulimoviruses, Caulimoviridae. Its capsid is a multilayer structure with 420 subunits and it is made of two coat-proteins of 37 kDa and 42 kDa[12].

6.3 Results and discussion:

The initial viruses studied here are of icosahedral shapes, but they differ in their T numbers. First, we attempted to show that these viruses of the same shapes, but different sizes give different results when exposed to chiral plasmonic fields. In a second part, we then compared results given by TYMV RNA containing / empty capsids to CpMV RNA containing / viruses like particles (VLP - empty capsid).

6.3.1 Icosahedral virus:

Virus particles, of three different sizes and T numbers (table 6 - 1), were all run at three different concentrations: 0.01 mg/mL, 0.1 mg/mL and 1 mg/mL. The viruses bound non-specifically to the gold surface. They did not have a gold binding domain and thus were randomly orientated on the gold surface. ORD and reflectance spectra were recorded for all of them.

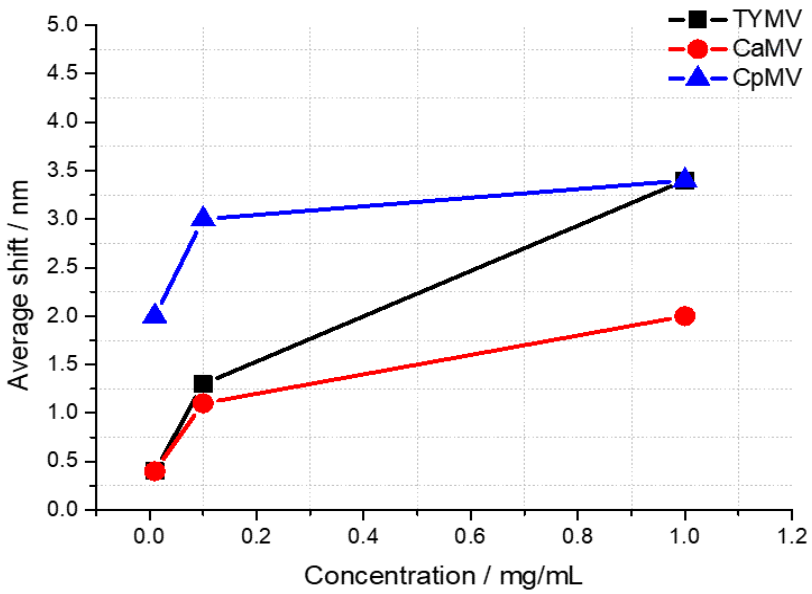

Figure 6 - 3: Average shift value versus the viruses for the three icosahedral viruses, CaMV (red), TYMV (black) and CpMV (blue).

The graph on figure 6 - 3 shows that the average shift of the particles is not simply related to the sizes of the particles. Indeed at 0.01 mg/mL TYMV and CaMV have the same average shift, when there are respectively 30 nm and 50 nm. The results presented in this chapter were recorded with the concentration 0.1 mg/mL. At 0.1 mg/mL the asymmetry is the highest. We can see on figure 6 - 3 that the saturation of the substrate is reached at 1 mg/mL for CaMV and CpMV, because the average shift value does not increase anymore (asymptote on the graph). It is at this concentration that the chiroptical signal is the

strongest. Virus particles being significantly larger than proteins, saturation of the substrate can be reached at lower concentration.

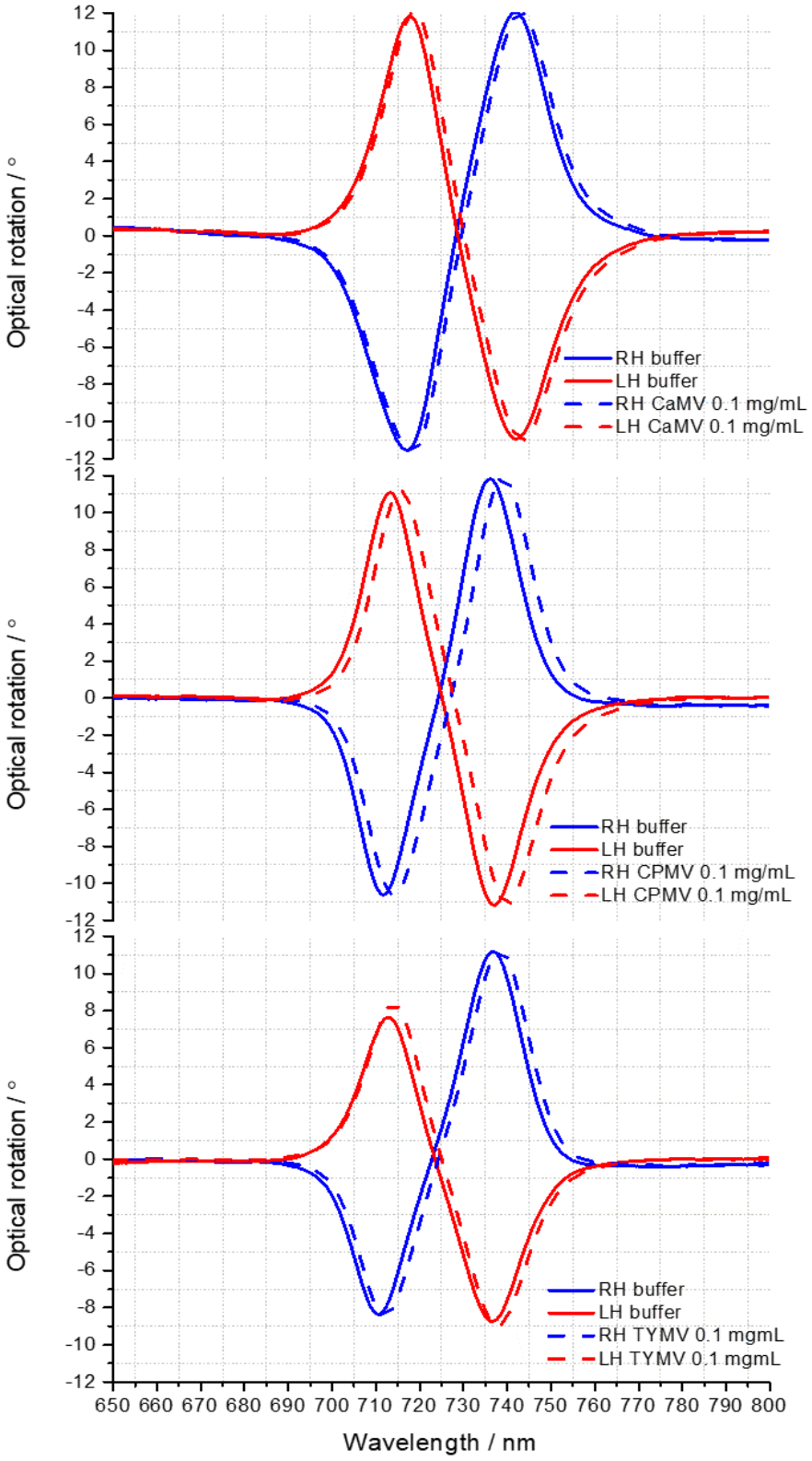

Figure 6 - 4: ORD of icosahedral viruses at the concentration of 0.1 mg/mL. From top to bottom the spectra are for CaMV, CpMV and TYMV.

The ORD spectra for the three viruses are presented in figure 6 - 4. We observe several differences between the viruses in the ORD and reflectivity spectra. We notice a difference in the ratio of the height of the TYMV ORD data. This does not happen in the ORD spectra of CpMV and CaMV. Only the LH signal is affected by the change, which gives us an asymmetry in A.

The change in the height ratio we see is the same effect as seen with the protein DHQ (chapter 4). It is important to note that CpMV and TYMV have the same size (diameter between 28-30nm) but different T numbers. The ORDs show that these two viruses behave differently when exposed to polarised light, with one of them (CpMV) showing no asymmetry and TYMV displaying an asymmetry in the ORD amplitudes.

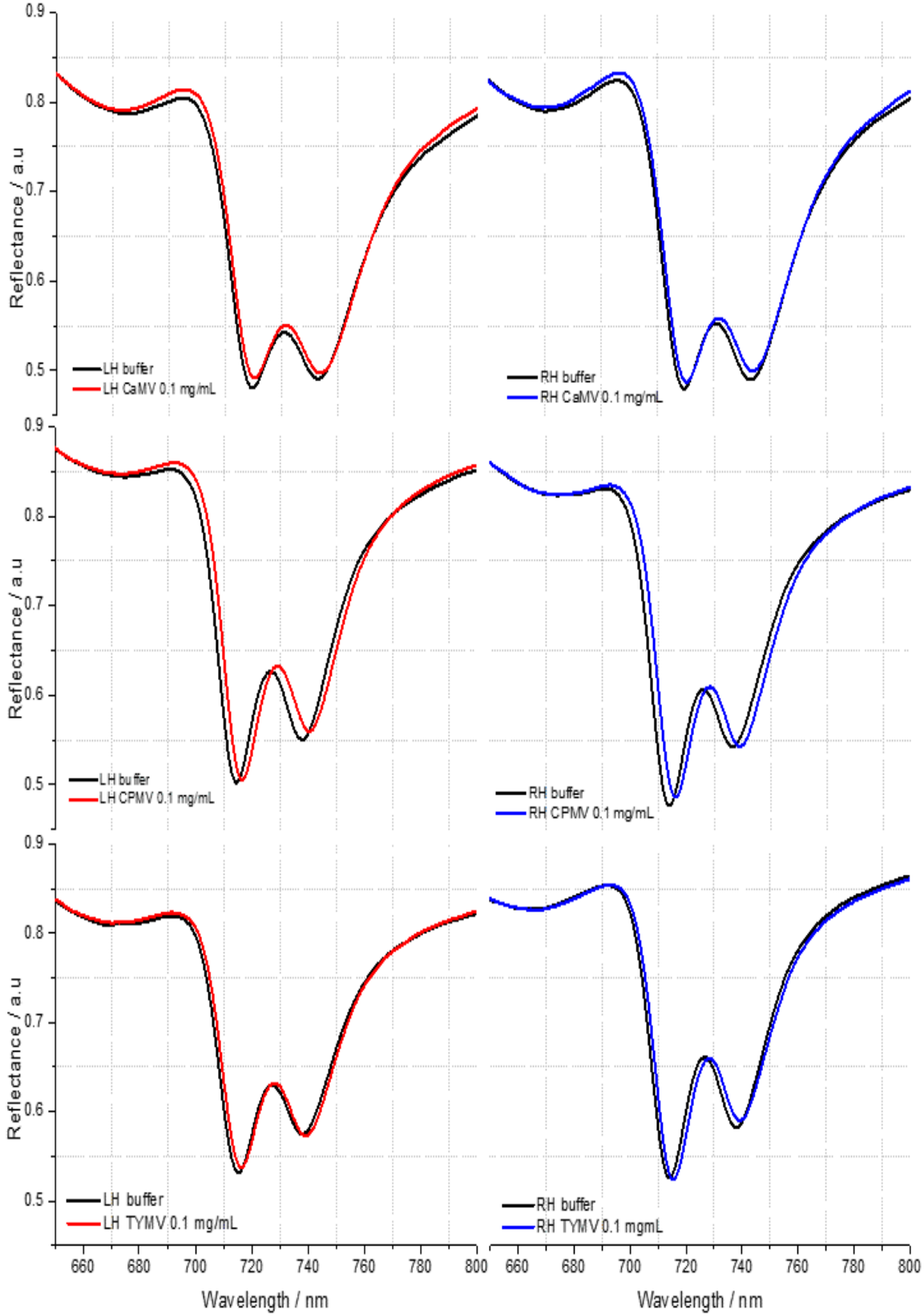

Figure 6 - 5: Reflectivity spectra of icosahedral viruses at the concentration of 0.1 mg/mL. From top to bottom the spectra are for CaMV, CpMV and TYMV. The black lines are produced from buffer measurements and the coloured lines are the spectra from virus measurements. Red and blue being respectively LH and RH signals.

The latest conclusions are supported by the reflectivity data in figure 6 – 5 (matching graphs in appendix 6 – 10). From the reflectivity we have extracted the optical parameters displayed in table 6 – 2 (all matching parameters are in table 6 – 6 in the appendix). Here again the only parameter exhibiting a change is the phase of the signal produced with TYMV particles, ΔΔφ. There is also a change in the phase for CpMV but the effect is less intense.

	CpMV	TYMV	CaMV
pI	5.5	3.6	7.02
optical parameters			
average shift	3.00 ± 0.20	1.30 ± 0.20	1.10 ± 0.20
ΔΔλ	-0.10 ± 0.20	-0.30 ± 0.20	-0.40 ± 0.20
ΔΔS	0.10 ± 0.20	-0.60 ± 0.20	-0.30 ± 0.20
A	1.00 ± 0.02	0.91 ± 0.02	0.99 ± 0.02
matching parameters			
ΔΔ ϕ	1.20± 0.20	-2.10 ± 0.20	-0.80 ± 0.20

Table 6 - 2: Optical and matching parameters for CpMV, TYMV and CaMV at 0.1 mg/mL.

The values for the ΔΔλ and ΔΔS asymmetry in the shift and separation in the reflectivity peaks, are similar with an error between all the viruses, thus these parameters cannot be used to distinguish them one from another. The parameter A shows a clearer difference between TYMV behaviour and CaMV, CpMV. The parameter A for both CaMV and CpMV is, with an error, equal to 1. When TYMV one is 0.91, exhibiting a clear asymmetry in the signal.

TYMV, CpMV and CaMV have isoelectric points (pI) of respectively 3.6, 5.5 and 7.02[24,25,22]. The buffers used for the experiment all had a pH between 7 and 7.5. We explained in chapter 4 the chiral plasmonic fields are sensitive to the surface charges of the particles. The pI of TYMV is much lower than the pI of the other two viruses, reason why it displays more asymmetry than the other two viruses. We introduced in chapter 4 the parameter A which is sensitive to the charge repartition of the surface of a particle. Because the pI of TYMV is much lower, its surface charge is predominantly positive and thus will have a greater impact on the phase change of the signal. This is confirmed by the matching parameters because TYMV displays the largest asymmetry. CpMV does not display an asymmetry for A because the pH at the gold surface is lower than the one in solution. Ions are attracted to the gold surface, thus the concentration H^+ increases and the pH decreases (here the pH is likely to be close to 6). CaMV and CpMV, having both pI with 1 point away from the pH value, are in a pseudo-zwitterion form. In chapter 4 a scale of A values compared to 1 in function of pH was given. The value here agrees with that scale. According to table 6 – 2, A and the parameter ΔΔϕ qualify the state of surface charge, but ΔΔϕ is more sensitive so we assume that it also qualifies the structure of the virus. Indeed, viruses being made of different coat proteins, they will give different kinds of asymmetry.

In terms of size CpMV and TYMV have effectively the same diameter (28 nm) while CaMV is significantly wider (50 nm). None of the changes seen here seems to be related to the size of the particle. A reason why CaMV does not change the amplitude of the ORD signal could be that the particle is large (nearly a sphere of 50 nm diameter) and is probably too large for the length of the decay of the evanescent field in the z direction.

6.3.2 Discrimination between full and empty particles:

We looked at the empty capsid particles of viruses and at intact virions at the same time to see whether there were distinct signatures for these two forms. We recorded ORDs and reflectivity spectra from the empty capsid of the virus at the same time. This was done only with TYMV and CpMV because the genetic material in CaMV is DNA and is known to be more difficult to remove. Here again we concentrated on the asymmetry parameter A because it is the one consistently showing the largest asymmetry.

6.3.2.1 Cowpea mosaic virus virions/capsid comparison:

The two particles, TYMV and CpMV exhibit different behaviours. This is shown in the reflectivity and the ORD (figure 6 – 6, reflectance are in the appendix figure 6 - 11). We first display CpMV results. The ORD does not display an asymmetry in A for both virions and VLP. We can state from the average shift being almost equal for virions and capsids, that there is about the same number of particles at the surface.

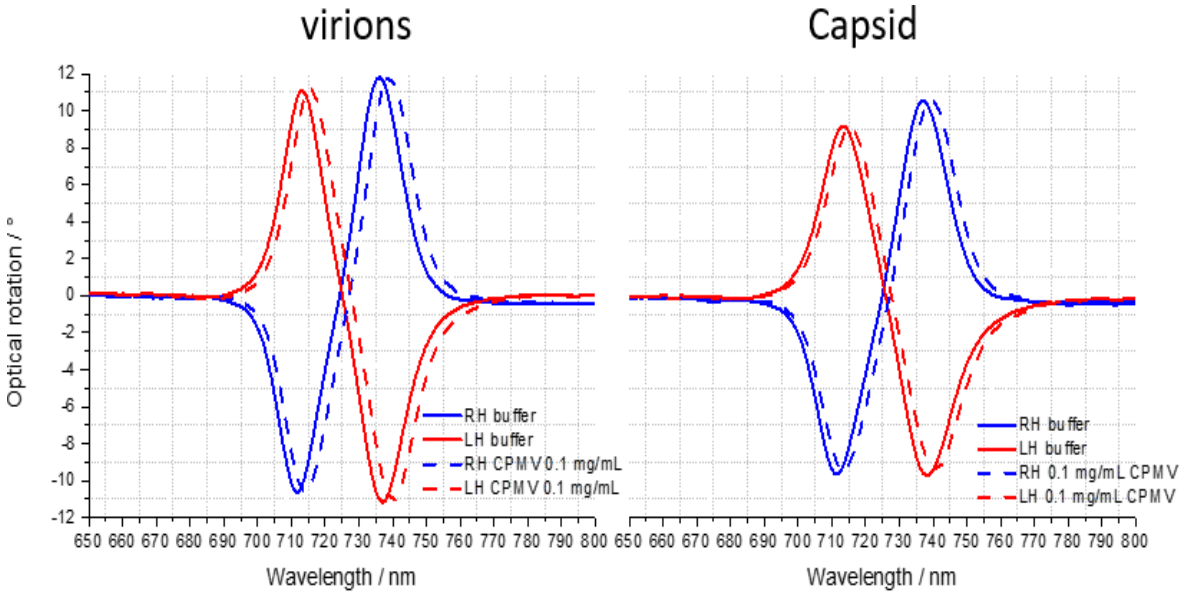

Figure 6 - 6: ORD spectra of CpMV particles at the concentration of 0.1 mg/mL. The left spectrum was taken with RNA containing particles (virion). The right spectrum was taken with empty particles (capsid).

	virions	capsid
pI	5.5	-
optical parameters		
average shift	3.00 ± 0.20	2.50 ± 0.20
A	1.00 ± 0.02	1.02 ± 0.02
matching parameters		
ΔΔ ϕ	1.20 ± 0.20	2.20 ± 0.20

Table 6 - 3: Asymmetry parameters and matching parameters extracted from the ORD and the reflectance spectra of CpMV for virions and capsids.

Table 6 - 3 contains the asymmetry parameters extracted from the reflectance data. Here we notice that the asymmetry increases in ΔΔφ for the VLP (full table and matching spectra in the appendix table 6 – 7 and figure 6 - 12). We said, in chapter 4, that the phase of the signal is actually sensitive to the particle surface charge. It is safe to assume that, in order to be stable without genetic material inside, the capsid has to slightly change its chemistry. This results in the movements of charges at the surface of the capsid. This theory is verified by the fact that the pIs for the virions and the capsid are different. Hence here the asymmetry in φ increases, because the net charges of the particles have changed.

Another theory is with the parameter of the chiroptical signal ξ (chapter 2). According to the CD spectra this value will be reversed for proteins and monosaccharide. When the RNA is removed from the capsid only one ξ value remains for the proteins. Therefore, the phase of the asymmetry is rising.

6.3.2.2 Turnip Yellow mosaic virus virions/capsid comparison:

The TYMV displays a similar kind of behaviour. First, we have shown that there is some asymmetry in the virions data, especially for A. Here looking at the reflectivity and the ORD we notice that the empty particles do not exhibit the same asymmetry as the virions (figure 6 – 7 reflectance in the appendix figure 6 - 13). It can be explained by the fact that the pI of the empty particles is higher than the pI of the virions. Thus, the distribution of charge at the surface of the capsid is more even and will interact less with the chiral field and thus does not affect the phase of the signal.

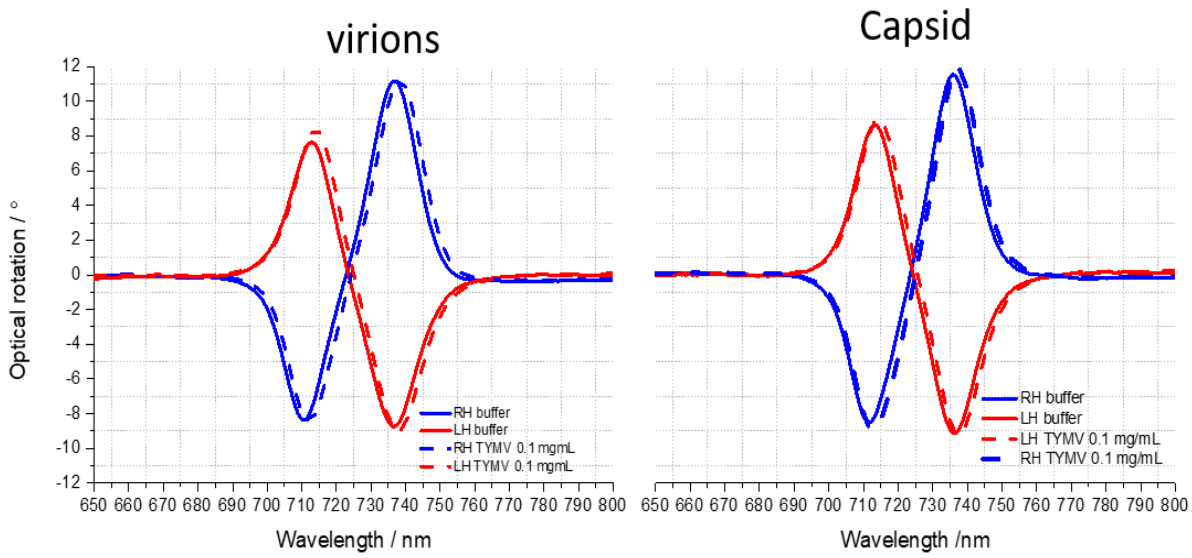

Figure 6 - 7: ORD spectra of TYMV particles at the concentration of 0.1 mg/mL. The left spectrum was taken with RNA containing particles (virion). The right spectrum was taken with empty particles (capsid).

This is confirmed by the reflectivity data. The asymmetry parameters are displayed in table 6 - 4 with the matching parameters (full table and matching spectra in the appendix table 6 - 8 and figure 6 - 14).

	virions	capsid
PI	3.6	6
optical parameters		
average shift	1.30 ± 0.20	1.30 ± 0.20
A	0.91 ± 0.02	1.00 ± 0.02
matching parameters		
ΔΔ ϕ	-2.10 ± 0.20	1.60 ± 0.20

Table 6 - 4: Asymmetry parameters and matching parameters extracted from the ORD and the reflectance spectra of TYMV empty particles and virions.

From the data in table 6 - 4 we can see that A is 0.91 for the virions and 1 for the capsid. The parameter A equals to 1 when the analyte is an achiral material. The virions can display some chirality because the particles are highly acidic and thus strongly positively charged. But the pI of the capsid is twice the pI of the virion. The sign of the asymmetry for ΔΔφ is reversed between the virions and the capsid. This supports the theory about ξ reversing its sign. TYMV being slightly wider than CpMV there might be more genetic material inside. Thus, the chiroptical signal will be dominated by the RNA signal, explaining the larger asymmetry with the virions. Unlike CpMV where the chiroptical signal of the virions is dominated by the coat protein (the capsid of CpMV being slightly smaller than TYMV, it contains less genetic material). When the genetic material is removed from the TYMV

capsid, the chiroptical signal becomes dominated by the coat protein of the capsid explaining the change of sign in the ΔΔϕ value.

6.3.3 Thiol based immobilisation of TYMV:

The aim here was to enhance the chiroptical signal coming from TYMV particles by means of tagging the virus particles. We showed in the previous chapter that ordering proteins at the surface of the gold, meaning binding them in a specific orientation leads to chiral signal enhancement. We thus tried the same approach here with viruses. One of the most common techniques to bind a particle to a gold nanoparticle or on gold thin film is to use a thiol. It is possible to put thiols on viruses and on TYMVs as well. We did not know which amount of thiol was needed to saturate the capsid of the virus. We thus tried two concentrations of thiol 5 mM and 10 mM. It is important to note here that the two different concentrations of thiol were used to coat the virus, but it does not mean that each particle had respectively 5 mM or 10 mM of thiol on its capsid. We did not know how many thiols were on the capsids. The thiol groups were attached to the lysines at the virus surface by means of N-Hydroxysuccinimide (NHS) ester chemistry also called amine-reactive cross linker chemistry. At physiological pH the amines of a protein are positively charged and therefore sit at the protein surface. These amines then become available for conjugation reagent. A fluorometric thiol assay was used to confirm the virus thiolation (figure 6 - 8). In this figure we see that thiol saturation on the virus is reached with 5 mM, as the two particles exhibit the same amount of fluorescence. In this figure we can also see that the level of fluorescence increases with the concentration of virus meaning that the virus has been successfully coated with thiolate. The control TYMV without thiol shows only a small increase in fluorescence.

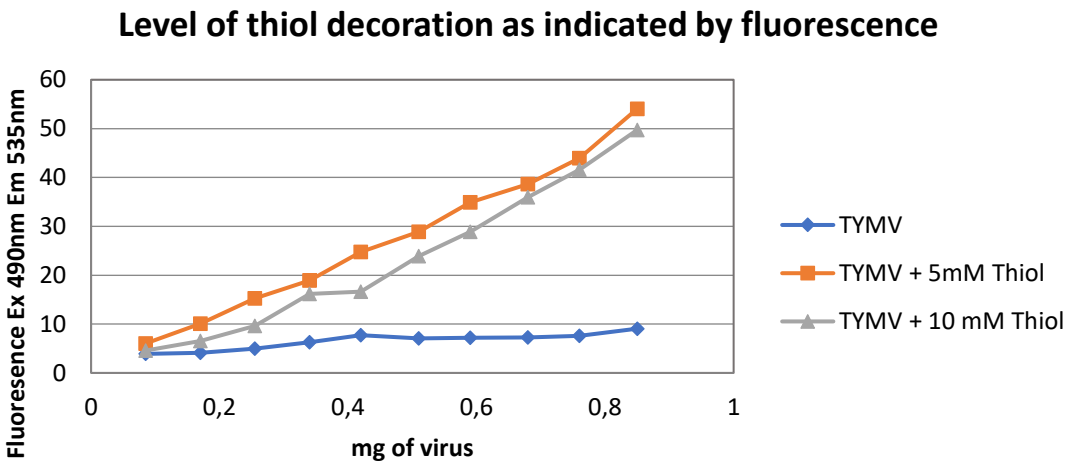

Figure 6 - 8: Result of the fluorometric thiol assays.

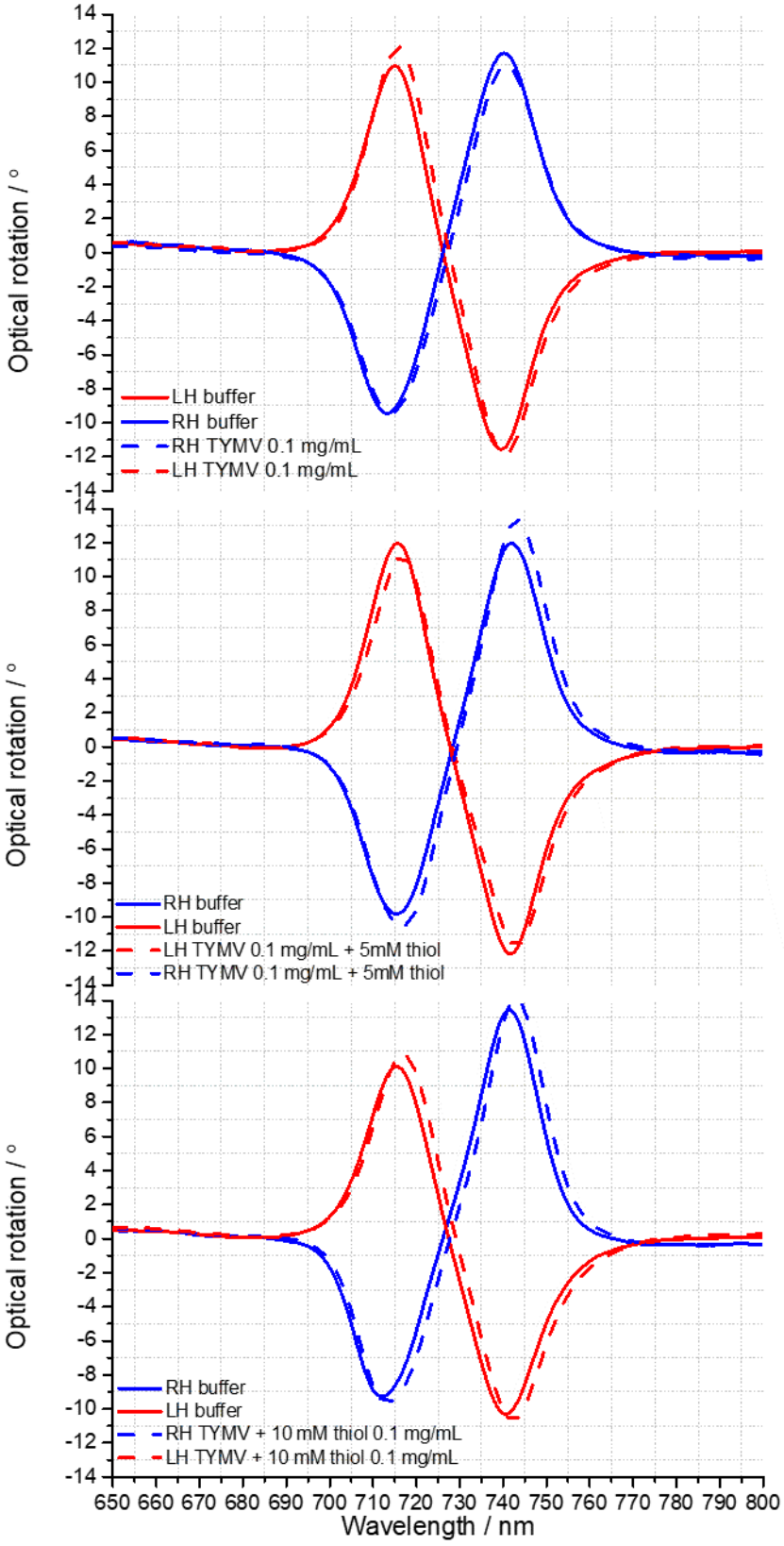

Figure 6 - 9: ORD data of TYMV with different amounts of gold binding domain attached at the surface. The first graph is the ORD of non-tagged particles, the second graph is the ORD of particles tagged with 5 mM thiol. The third graph is the ORD of particles tagged with 10 mM thiol.

The ORDs for those particles are shown in figure 6 - 9. We see that the particles behave differently according to the amount of thiol they have been coated with.

In all the ORD spectra we notice that the amplitude of the signal changes. The effect of the change is in the same direction for the virions with no thiol and for those with 10 mM thiol. But the ORD changes in the opposite direction for TYMVs tagged with 5 mM thiol. For the particles tagged with 5 mM the asymmetry in A increases.

For the particles tagged with 10mM thiol the asymmetry is even smaller than the one displayed by the non-tagged particles. Indeed, the amplitudes of the signal in both LH and RH increase in the ORD of the thiol-tagged particles, when it is mainly the LH signal that gets affected in the ORD of non-tagged particles. The asymmetry parameters extracted from the ORD and reflectivity data are shown in table 6 – 5 (full table in the appendix table 6 – 9).

	no thiol	5 mM thiol	10 mM thiol
optical parameters			
average shift	1.30 ± 0.20	1.40 ± 0.20	1.60 ± 0.20
A	0.91 ± 0.02	1.16 ± 0.02	1.00 ± 0.02
matching parameters			
ΔΔϕ	-2.10 ± 0.20	3.40 ± 0.20	1.10 ± 0.20

Table 6 - 5: Asymmetry parameters extracted from reflectance and ORD spectra for thiol tagged virus at different concentrations of thiol.

The asymmetry is displayed once more in ΔΔφ. However, the signs of the parameters are reversed for both viruses with different thiol concentrations. The changes induced to the phase of the signal are different. When a protein is thiol-tagged, its pKa decreases. Meaning that the positive surface charge becomes neutral or slightly more negative. This explains the change of sign in ΔΔϕ and the fact that A is above one. The insertion of a thiol has a significant impact on the charge distribution (lysine having a positively charged primary amine) as an R-group which is converted to an uncharged amide by the addition of the NHS bound thiol. The viruses tagged with 5 mM thiol are those that show the larger asymmetry. The TYMV tagged with 10 mM thiol has more orientations available to bind the gold, while with 5 mM thiol the virus is tagged at discrete points. The chiroptical signal from these different orientations cancels out, decreasing the asymmetry of the optical signal. This also means that 10 mM thiol saturates the virus particles.

6.4 Conclusion:

In this chapter we showed that plasmonic chiral fields give promising results to differenciate viruses of the same shape. We compared three different icosahedral viruses with dissimilar sizes and diverse compositions. The particles we studied do not display the same types of asymmetry in the signal. We showed that the asymmetry they display could be linked to the

charge distribution on the surface of the virus. Indeed, despite the fact that the viruses have the same structure (icosahedral) they do not exhibit the same type of asymmetry. CaMVs and CpMVs do not display any changes in the ORD signal, while TYMVs and CpMVs show a change in the phase of the reflectance signal. We hypothesised that these differences are not due to the sizes of the particles because CpMVs and TYMVs are of similar sizes. But the TYMV has a pI much lower than the other viruses meaning that the distribution of charge on the particles is drastically different from CaMV and CpMV. This supports the theory that the phase parameter is an indicator of the particle net charges. We then used this parameter to distinguish between intact virions and empty viral capsids. Indeed, the particles with viral genomes inside had a distribution of charges significantly different from the empty capsids, most likely to preserve the integrity of the capsids. Due to this property, if the virions of the virus (TYMV) display some asymmetry then the capsids which have a higher pI, and thus a more even distribution of charges, do not induce a change in the chiroptical signal. This could be verified in the ORD of only one of the viruses tested. Further work needs to be done for the other two. The parameters, given by the EIT modelling, show that the phase of the reflectance signal appears to be sensitive to the structure differences between the virions and the capsids. Both the RNA and the coat protein of the virus exhibit ξ value of opposite signs. The VLP will thus display a different kind of asymmetry from the virions because the asymmetry is induced only by the coat protein.

We then used chemical immobilisation of TYMV tagged with lysine specific thiol compound to enhance the optical signal. We saw indeed an enhancement of the asymmetry in A. This is likely due to the orientation of the particles on the surface impacting the phase of the signal. The surface charge distribution is altered by tagged thiols; thus A is different from non-tagged particles. It was also showed that there is a saturation limit for tagging the virus because the particles tagged with the highest concentration of thiol show a decrease in the chiroptical signal. The phase φ in the parameters for the tagged TYMV exhibits an asymmetry but it is reverse compared to the non-tagged virus. This could be due to the thiol eliminating the positive charge of the lysine amino acid residue thus inducing a change in the charge distribution. The particles with new net charges will interact differently with the chiral field. This is corroborated by the data extracted from the particles saturated with thiol. The φ for these particles is of the same sign as the 5 mM thiol particles but the asymmetry is different.

To sum up this chapter we can say that A could be used to distinguish between virus particles thanks to the repartition of charges at their surface. This property can also be used to discriminate between virions and capsids to some extent, depending on what dominates the chiroptical signal (genetic material or proteins from the capsids). We also show that

viruses with domain specific immobilisation chemistry can enhance the chiroptical signal of the virus particles. Further research in this domain could lead to the detection of asymmetries in virus particles that do not show any asymmetry on their own.

6.5 References:

(1) Roossinck, M. J. Mechanisms of Plant Virus Evolution. Annu. Rev. Phytopathol. (1997), 35, 191–209.

(2) Zlotnick, A.; Huiskonen, J. Editorial Overview: Virus Structure and Assembly: Virions — from Structure and Physics to Design Principles. Curr. Opin. Virol. (2016), 18, vii–viii.

(3) Czapar, A. E.; Steinmetz, N. F. Plant Viruses and Bacteriophages for Drug Delivery in Medicine and Biotechnology. Curr. Opin. Chem. Biol. (2017), 38, 108–116.

(4) Wen, A. M.; Steinmetz, N. F. Design of Virus-Based Nanomaterials for Medicine, Biotechnology, and Energy. Chem. Soc. Rev. (2016), 45 (15), 4074–4126.

(5) Yildiz, I.; Shukla, S.; Steinmetz, N. F. Applications of Viral Nanoparticles in Medicine. Curr. Opin. Biotechnol. (2011), 22 (6), 901–908.

(6) Prasad, B.V.V.; Schmid, M. F. (2012) Principles of Virus Structural Organization. (2013). In: Rossmann M., Rao V. (Eds.) Viral Molecular Machines. Advances in Experimental Medicine and Biology, vol 726. Springer, Boston, MA.

(7) Roossinck, M. J. (Ed.) Plant Virus Evolution. Springer (2008).

(8) Hull, R. Plant Virology. Academic Press (2013).

(9) Scholthof, K-B. G.; Adkins, S.; Czosnek, H.; Palukaitis, P.; Jacquot, E.; Hohn, T.; Hohn, B.; Saunders, K.; Candresse, T.; Ahlquist, P.; Hemenway, C.; Foster, G. D. Top 10 Plant Viruses in Molecular Plant Pathology. Mol. Plant Pathol. (2011), 12 (9), 938–954.

(10) Kondylis, P.; Schlicksup, C. J.; Zlotnick, A.; Jacobson, S. C. Analytical Techniques to Characterize the Structure, Properties, and Assembly of Virus Capsids. Anal. Chem. (2019), 91, 1, 622–636.

(11) Mateu, M. G. Structure and Physics of Viruses; Springer, 2013.

(12) Foster, G. D., Taylor, S. C. (Eds.) Plant Virology Protocols-From Virus Isolation to Transgenic Resistance. (1998). MIMB, vol 81.

(13) Hull, R. Plant Virology. Academic Press (2014).

(14) Moorefield, B. From Chemistry and Physics to Biology. Nature (2014), 511 (S7509), 16–17.

(15) Salthouse, D. G.; Indelicato, G.; Cermelli, P.; Keef, T.; Twarock, R. Approximation of Virus Structure by Icosahedral Tilings. Acta Cryst. (2015), A 71, 410–422.

(16) Cohen, F. S. How Viruses Invade Cells. Biophys. J. (2016), 110 (5), 1028–1032.

(17) Johnson, J. E.; Speir, J. A. Quasi-Equivalent Viruses : A Paradigm for Protein Assemblies. J. Mol. Biol. (1997), 269 (5), 665–675.

(18) Heinlein, M. Plant Virus Replication and Movement. Virology 2015, 479–480.

(19) Zandi, R.; Reguera, D.; Bruinsma, R. F.; Gelbart, W. M.; Rudnick, J. Origin of Icosahedral Symmetry in Viruses. Proc. Natl. Acad. Sci. U. S. A. (2004), 101 (44), 15556–15560.

(20) Rossmann, M. G.; Johnson, J. E. Icosahedral RNA Virus Structure. Annu. Rev. Biochem (1989), 58 : 533–573.

(21) Sainsbury, F.; Cañizares, M. C.; Lomonossoff G. P. Cowpea Mosaic Virus : The Plant Virus – Based Biotechnology Workhorse. Annu. Rev. Phytopathol. (2010), 48 (1), 437–457.

(22) Montague, N. P.; Thuenemann, E.; Saxena, P.; Saunders, K.; Lenzi, P.; Lomonossoff, G. P. Recent Advances of Cowpea Mosaic Virus-Based Particle Technology. Human Vaccines (2011), 7(3), 383-90 .

(23) Lin, Y.; Su, Z.; Niu, Z.; Li, S.; Kaur, G.; Lee, L. A.; Wang, Q. Layer-by-Layer Assembly of Viral Capsid for Cell Adhesion. Acta Biomaterialia (2008), 4(4), 838–843.

(24) Aljabali, A. A. A.; Barclay, J. E.; Céspedes, O.; Rashid, A.; Staniland, S. S.; Lomonossoff, G. P.; Evans, D. J. Charge Modified Cowpea Mosaic Virus Particles for Templated Mineralization. Advanced Functional Materials (2011), 21(21), 4137–4142.

(25) Michen, B.; Graule, T. Isoelectric Points of Viruses. J. Appl. Microbiol. (2010), 109 (2), 388–397.

6.6 Appendix:

	TYMV	CaMV	CpMV
$\Delta\Delta\ \omega_r$	0.60 ± 0.20	0.40 ± 0.20	0.00 ± 0.20
$\Delta\Delta\ \omega_d$	0.40 ± 0.20	0.40 ± 0.20	0.00 ± 0.20
$\Delta\Delta\ k$	2.00 ± 2.10^{-4}	0.00 ± 2.10^{-4}	-2.00 ± 2.10^{-4}
$\Delta\Delta\ \gamma_r$	$0.00 \pm \pm 3.10^{-4}$	0.00 ± 3.10^{-4}	4.00 ± 3.10^{-4}
$\Delta\Delta\ \gamma_d$	10.0 ± 2.10^{-4}	2.00 ± 2.10^{-4}	-2.00 ± 2.10^{-4}
$\Delta\Delta\ \theta$	0.00 ± 0.20	0.00 ± 0.20	-0.10 ± 0.20
$\Delta\Delta\ \phi$	-2.10 ± 0.20	-0.80 ± 0.20	1.15 ± 0.20

Table 6 - 6: Matching parameters extracted from the reflectivity data for the three icosahedral viruses.

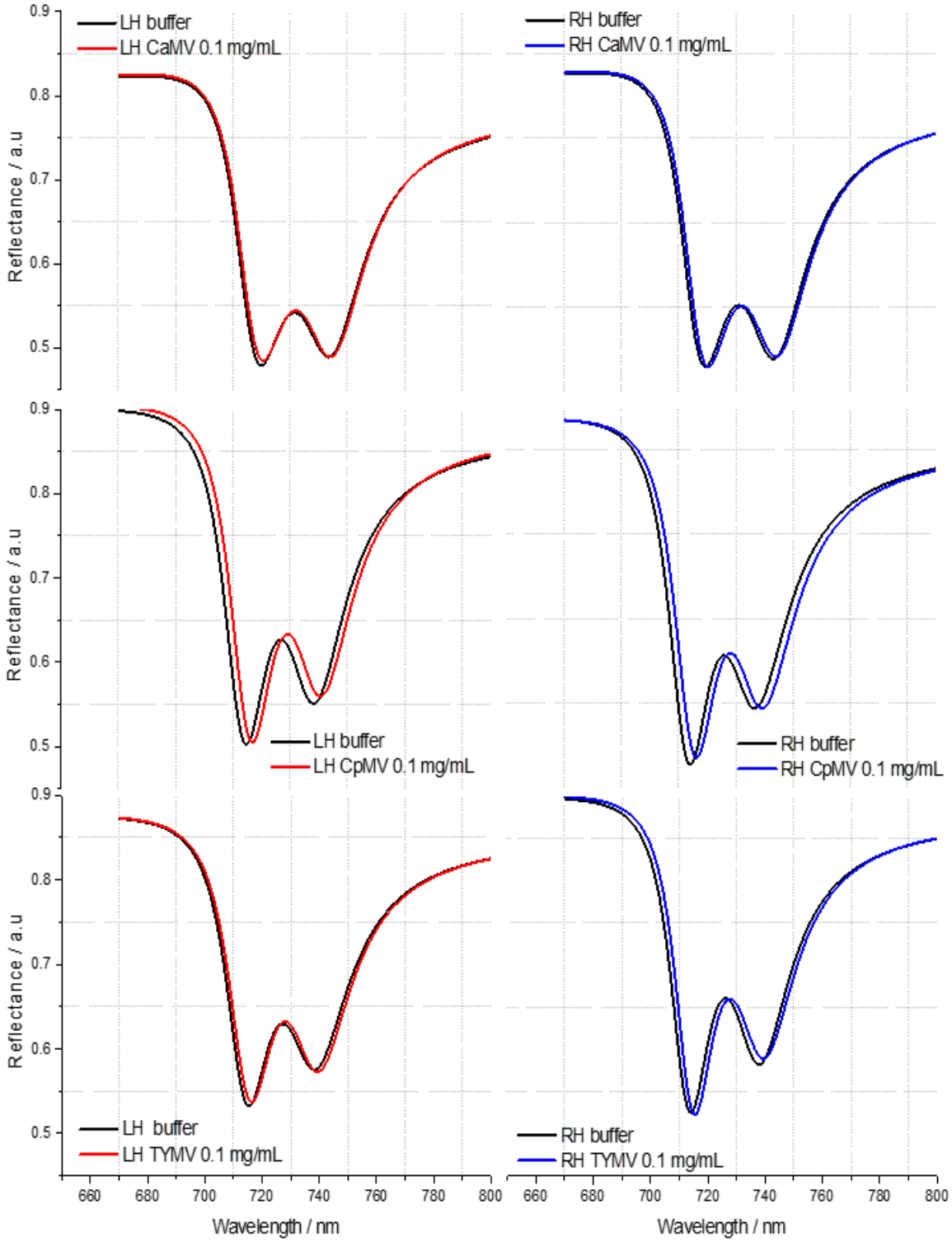

Figure 6 - 10: Model spectra of icosahedral viruses at the concentration of 0.1 mg/mL. From top to bottom the spectra are for CaMV, CpMV and TYMV. The black lines are produced from buffer measurement and the coloured lines are the spectra from viruses measurement. Red and blue being respectively LH and RH signals.

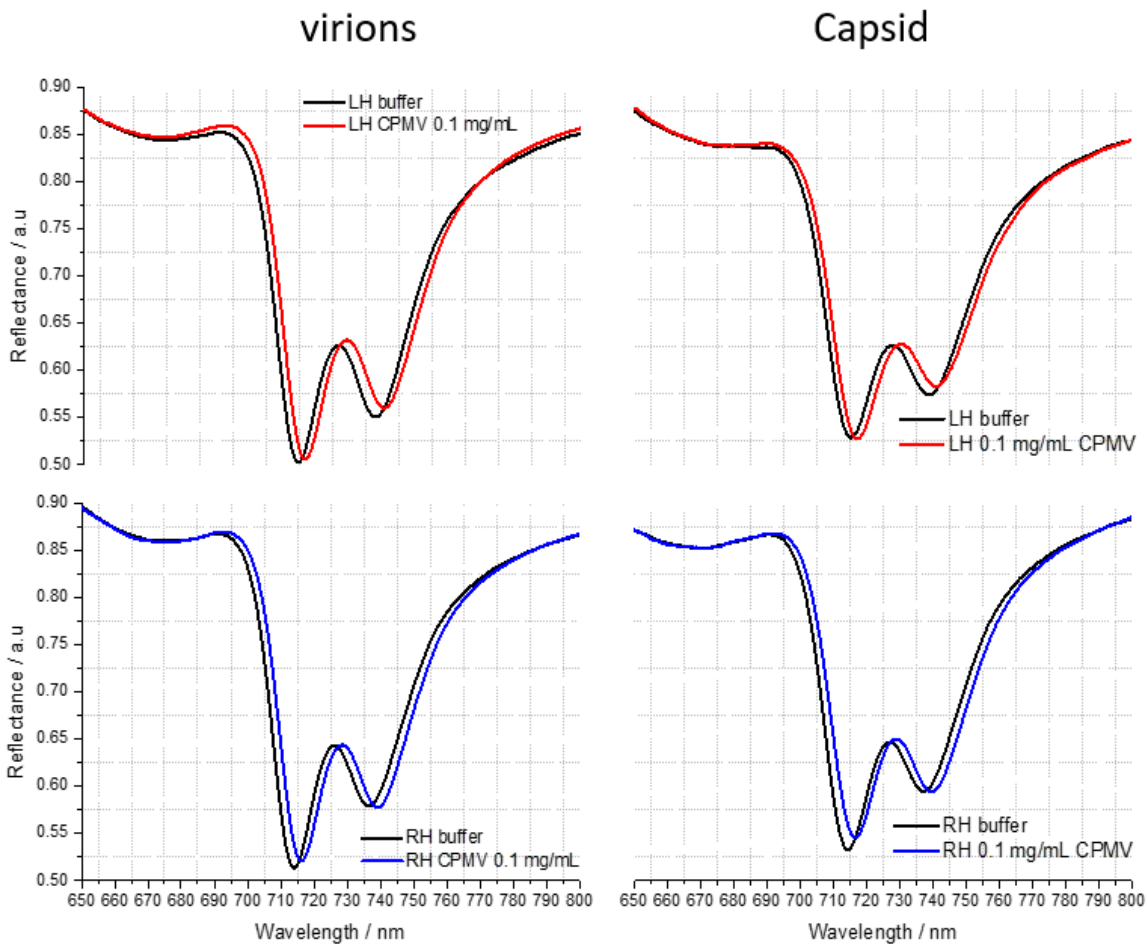

Figure 6 - 11: Reflectance of CpMV. The left side shows LH and RH reflectance from the RNA containing particles (virions). The right side of the figure shows the reflectance from the empty particles (capsids).

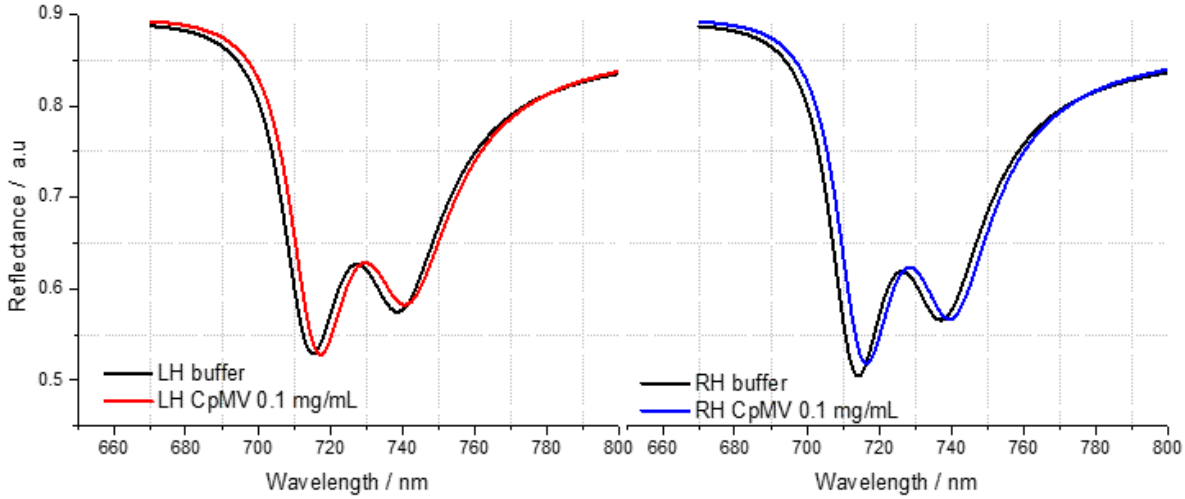

Figure 6 - 12: Model spectra of CpMV VLP at 0.1 mg/mL. The left graph is the modelled LH reflectance and the graph at the right is the modelled RH reflectance.

optical parameters		
	virions	capsid
average shift	3.00 ± 0.20	2.50 ± 0.20
ΔΔλ	-0.10 ± 0.20	0.10 ± 0.20
ΔΔS	0.10 ± 0.20	-0.10 ± 0.20
A	1.00 ± 0.02	1.02 ± 0.02
matching parameters		
ΔΔ wr	0 ± 0.20	0.2 ± 0.20
ΔΔ wd	0 ± 0.20	0.2 ± 0.20
ΔΔ k	-2.00 ± 2.10^{-4}	0.00 ± 2.10^{-4}
ΔΔ gr	4.00 ± 3.10^{-4}	0.00 ± 3.10^{-4}
ΔΔ gd	-2.00 ± 2.10^{-4}	-3.00 ± 2.10^{-4}
ΔΔ θ	-0.1 ± 0.20	0.00 ± 0.20
ΔΔ ϕ	1.15 ± 0.20	2.2 ± 0.20

Table 6 - 7: Asymmetry parameters and matching parameters extracted from the ORD and the reflectance spectra of CpMV for virions and capsid.

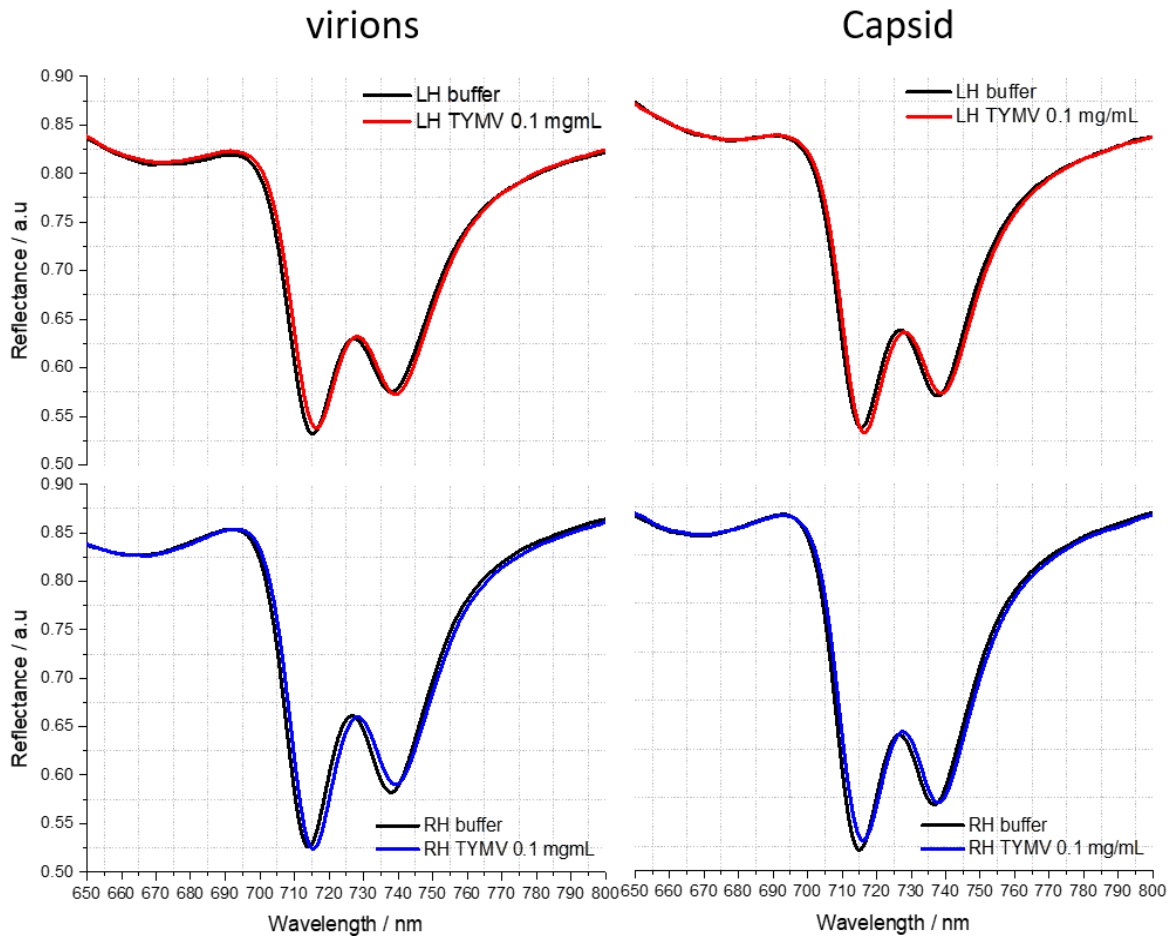

Figure 6 - 13: Reflectance of TYMV. The left side shows LH and RH reflectance from the RNA containing particles (virions). The right side of the figure shows the reflectance from the empty particles (capsids).

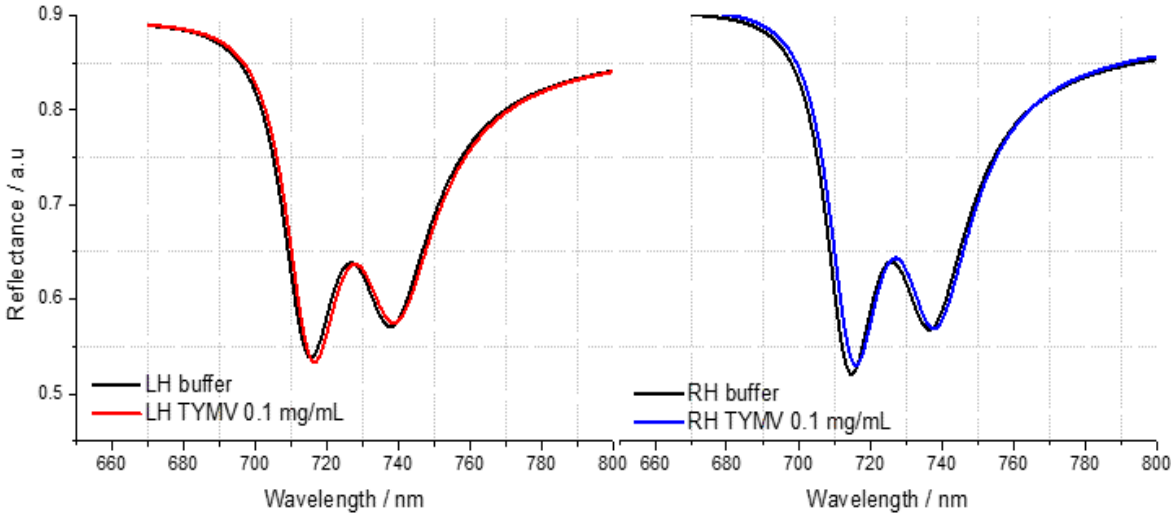

Figure 6 - 14: Model spectra of TYMV VLP at 0.1 mg/mL. The left graph is the modelled LH reflectance and the graph at the right is the modelled RH reflectance.

optical parameters		
	virions	capsid
average shift	1.30 ± 0.20	1.30 ± 0.20
ΔΔλ	-0.30 ± 0.20	0.10 ± 0.20
ΔΔS	-0.20 ± 0.2	-0.30 ± 0.20
A	0.91 ± 0.02	1.00 ± 0.02
matching parameters		
ΔΔ wr	0.60 ± 0.20	0.20 ± 0.20
ΔΔ wd	0.40 ± 0.20	0.20 ± 0.20
ΔΔ k	2.00 ± 2.10^{-4}	0.00 ± 2.10^{-4}
ΔΔ gr	0.00 ± 3.10^{-4}	0.00 ± 3.10^{-4}
ΔΔ gd	10.0 ± 2.10^{-4}	0.00 ± 2.10^{-4}
ΔΔ θ	0.00 ± 0.20	0.00 ± 0.20
ΔΔ ϕ	-2.10 ± 0.20	1.60 ± 0.20

Table 6- 8: Asymmetry parameters and matching parameters extracted from the ORD and the reflectance spectra of TYMV empty particles and virions.

optical parameters			
	no thiol	5 mM thiol	10 mM thiol
average shift	1.30 ± 0.20	1.40 ± 0.20	1.60 ± 0.20
ΔΔλ	-0.30 ± 0.20	-0.10 ± 0.20	-0.20 ± 0.20
ΔΔS	-0.50 ± 0.20	0.00 ± 0.20	-0.20 ± 0.20
A	0.91 ± 0.02	1.16 ± 0.02	1.00 ± 0.02
matching parameters			
$\Delta\Delta\omega_r$	-0.20 ± 0.20	0.20 ± 0.20	0.00 ± 0.20
$\Delta\Delta\omega_d$	-0.20 ± 0.20	0.20 ± 0.20	0.00 ± 0.20
ΔΔk	-2.00 ± 2.10^{-4}	-2.00 ± 2.10^{-4}	0.00 ± 2.10^{-4}
ΔΔγr	0.00 ± 3.10^{-4}	0.00 ± 3.10^{-4}	0.00 ± 3.10^{-4}
ΔΔγd	1.00 ± 2.10^{-4}	-9.00 ± 2.10^{-4}	-4.00 ± 2.10^{-4}
ΔΔθ	0.00 ± 0.20	0.00 ± 0.20	0.00 ± 0.20
ΔΔϕ	-0.90 ± 0.20	3.40 ± 0.20	1.10 ± 0.20

Table 6 - 9: Asymmetry parameters extracted from reflectance and ORD spectra for thiol-tagged viruses at different concentrations of thiol.

Chapter 7: Effect of the mesoscale structure on the chiroptical signal of rod-shaped viruses

In this chapter, rod-shaped tobacco mosaic viruses (TMV) a plant virus and M13 filamentous bacteriophages (M13) are studied with plasmonic chiral fields. TMVs and M13 were chosen because they slightly differ in structure and interact differentially with the gold surface. Here, we will show that for rod-shaped viruses the chiroptical response highly depends on the orientation of the virus at the surface. In more detail, we will explain how the ξ value of the chirality tensor (chapter 2) behaves according to the space orientation of the rod-shaped particles. In addition, we will show that we can distinguish between TMV virions and TMV virus-like particles (VLP) using plasmonic chiral fields, by applying asymmetry parameters.

7.1 Introduction:

In this chapter plasmonic chiral fields were used to study rod-shaped viruses (TMVs) and M13 bacteriophages. Plant viruses are of great interest for nanoscience because of their size range from 10nm to 1µm and their rather homogeneous structures[1,2]. They are stable in a wide range of pH, salt and temperature. In chapter 4, we showed that the biomolecules print a “reverse” image of their surface charges onto the gold. Here, we applied this theory to particles with drastic structural differences compared to the DHQases. Because of the change in shape and structure the “reverse” image printed onto the metafilm surface is completely different, the charges are not positioned in the same way, and thus must interact in a different manner with the chiral fields.

Here, we studied TMV plant viruses and M13 bacteriophages which were loaded onto the metafilm gold surface. Because of the difference in structure compared to icosahedral viruses (chapter 6) we hypothesised that the interaction with the plasmonic fields would be different. Approximately 10% of plant viruses are rod-shaped with the most common virus being TMV[3]. TMV has been intensively studied and the virus has a well-known rigid structure and is easily crystallized. Alongside TMV we studied M13 filamentous bacteriophage which has a similar structure to rod-shaped viruses apart from being more flexible[4].

TMV and M13 do not have the same shape thus they differentially bind onto the gold surface. Their position onto the gold determines how their surface charges are exposed to the chiral fields, and this was shown to be a completely different orientation than seen with the icosahedral viruses discussed previously in chapter 6. The aim of this study was to investigate if differences in surface charge orientation can induce changes in the interaction

with the plasmonic fields. In chapter 6, we showed that discrimination between different icosahedral viruses was possible thanks to differences in isoelectric point (pI). Here, we show that the method cannot be applied to discriminate between the structure of rod-shaped viruses and the structure of filamentous bacteriophages. However, we speculate that the distribution of charge at the surface of the virus interferes with the chiral fields. We demonstrate that the excess of charge at the molecule surface does not alter the optical signal because the shape of the biomolecule is drastically different (not spherical) compared to other biomolecules exposed to plasmonic fields studied in this thesis. We demonstrate that the geometry of the charge distribution at the surface plays a pivotal role in the outcome when particles are exposed to plasmonic chiral fields. As described in chapter 5, the asymmetry parameters can be applied to qualify the change in the ORD peak height and serves as an indicator of the order of the analyte at the gold surface. It was confirmed by the use of TMV virus-like particles (VLP) that do not contain genetic material compared to TMV virions. VLP particles have a different surface charge density than the virions and thus do not exhibit the same kind of asymmetry.

The theory tested is that the change in the optical signal depends on the direction of the perturbation, here the surface charges of viruses. It is shown that the detection of the surface charge is effective in the z direction but not in x and y because they average out, and not because the reverse image effect does not take place. This can be explained with the diagonal element of the optical chirality tensor. This chapter emphasizes the limit of this spectroscopy technique.

7.2 Virus structures and properties:

7.2.1 TMV virions, TMV-VLPs and helical viruses:

Helical viruses are one of two shapes: filamentous or rod-shaped. Their capsids can be as long as needed to enclose the virus genome[5]. In theory, there is no limit to the amount of genetic material the capsid can store. But unlike for icosahedral viruses, this kind of structure is limited by the biological and physical environment, explaining why rod-shaped viruses are so rare[6].

TMVs belong to the block of helical viruses. All filamentous viruses have a similar helical structure, consisting of a capsid made up of protein arranged in a circular fashion and a central cavity in the shape of a tube[7]. TMV is a positive-sense single-stranded RNA virus in genus Tobamovirus that infects a wide range of plants and is so far known non-pathogenic to mammals. The pI of TMV is described in literature to lie around pH4[8]. The size of TMV virions used in this study is 300 x 180nm, the pitch of the helix is 2.3 nm and the particle

consists of 95% protein and 5% RNA[9,10], and the TMV-VLPs are helical structures which variable length x 18nm (figure 7 – 1). The secondary structure of the TMV coat protein consists of 40-50% of α-helix, 40-50% irregular structure and 0-20% of β-sheets[11]. Unlike the icosahedral virus, the size of the helical virus depends on the genetic material that is encapsidaded. Indeed, if genetic material is added to TMV particles the capsid will extend. In addition, we will compare spectra obtained with TMV virions to TMV-VLPs, both rod-shaped structures similar in size.

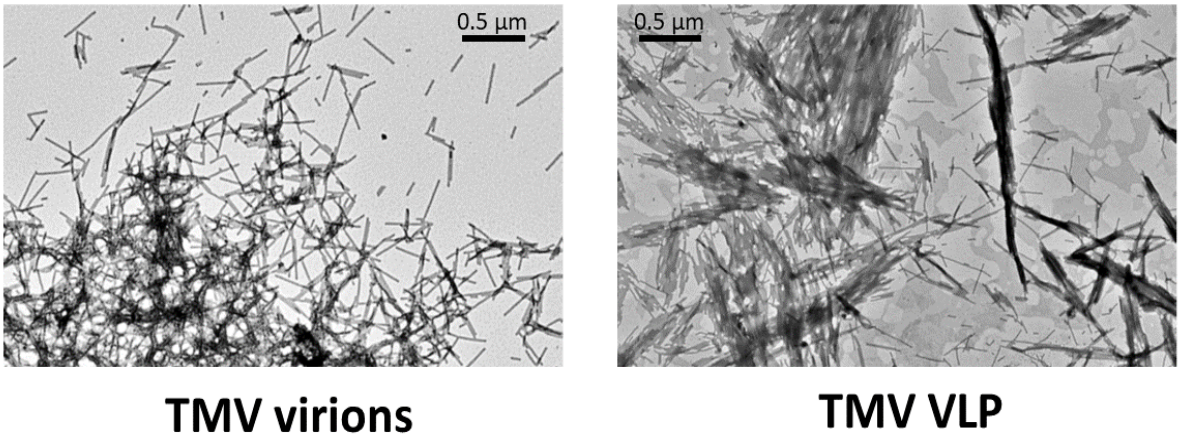

Figure 7 - 1: Shows the TEM images of TMV virions (left) and TMV-VLPs (right). The VLPs are genome-free TMV particles produced in bacteria, more specifically there are the protein shell of the virus. Those particles are non-infectious and are slightly less stable than the RNA containing particles.

7.2.2 M13 filamentous bacteriophages:

M13 filamentous bacteriophage (M13) is a phage which infects the bacterium *Escherichia coli.* M13 is often used in nanotechnology for nanoarchitecture entity[12]. The capsid is made of five different coat proteins, the main one is p8 with the minor coat proteins sitting at the phage extremity and these are: p3, p6, p7 and p9. M13 is composed of a single-stranded DNA molecule[13], enclosed in a cylindrical capsid. It is approximately 6.5 nm wide and 880 nm long (figure 7 – 2). The capsid is made up of two major coat proteins: approximately 2700 copies of P8 and 5 copies of P3 at one end[14–17]. This virus is less rigid than TMV and much more flexible and has a pI that lies around pH4.2. These particles can be tagged with a gold binding domain at the end of the particles[18]. However, the particles used here had no gold-binding domain.

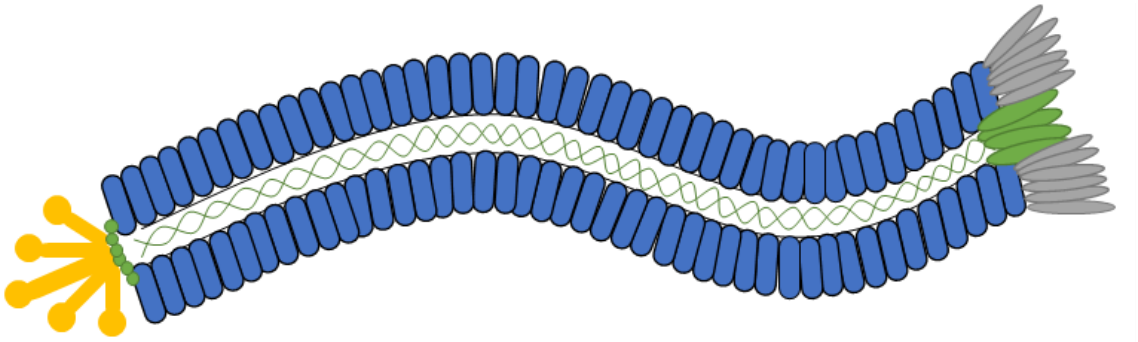

Figure 7 - 2: Representation of M13 filamentous bacteriophage.

7.2.3 Orientation of the virus on the surface:

Due to their differences in shape, TMV and M13 are not exposed to the chiral fields in the same way (figure 7 - 3). Icosahedral viruses are symmetric therefore their orientation onto the gold surface does not affect the spectra. Helical viruses bind to the gold surface on their side and thus appear like rods, the viruses are mainly exposed to the field in the x and y directions. With the field being circular, any change in x will be compensated in y, thereby any effect will be averaged out. M13 on the other hand, can either be orientated straight in the field or on the side on the surface. M13 is symmetric in the xy plane, but not in the z direction and thus this should change the optical signal in the z direction. However, M13 can have different orientations compared to the rod-shaped virus and is unlike rod-shaped viruses more flexible. Even if M13 is bound to the gold straight, there is no guarantee that it is straight in the z direction. None of the virus particles used here had a gold binding domain, therefore, they appear in a random orientation on the gold surface.

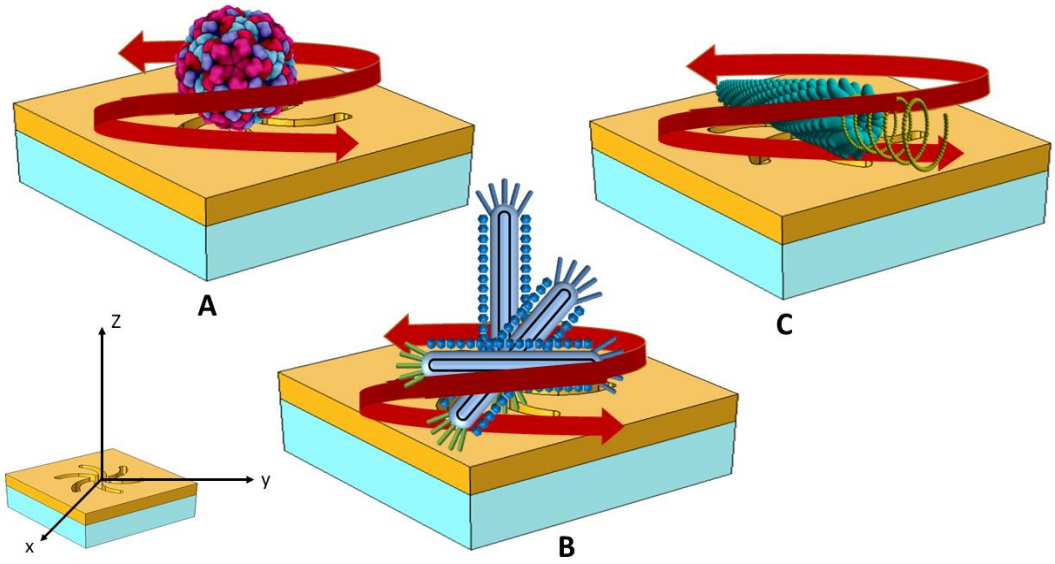

Figure 7 - 3: Icosahedral (A), M13 bacteriophage (B) and helical shaped (C) viruses exposed to the chiral plasmonic field.

7.3 Results and discussion:

7.3.1 M13:

First M13 was loaded onto a gold surface at a final concentration of 0.1 mg/mL, dissolved in water. Figure 7 - 4 displays the ORD and the reflectance spectra.

The ORD for M13 does not display any asymmetry (in the shift ΔΔλ, or in the ratio of the height) in both the LH and RH signals. A small change can be detected in the phase of the reflectivity for both the LH and RH signals, with RH being more obvious. Table 7 - 1 contain the asymmetry parameters and the matching parameters (the matching graphs are shown in the appendix figure 7 - 9).

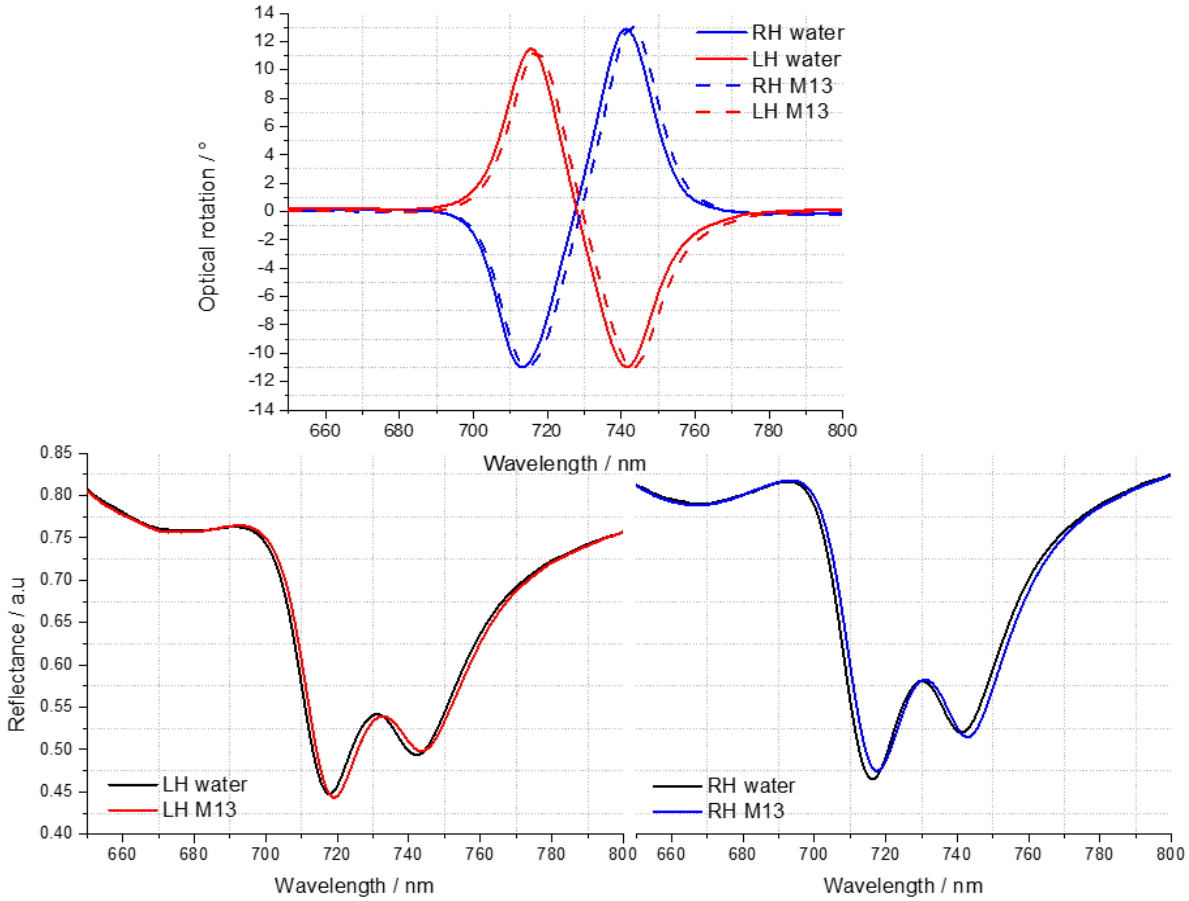

Figure 7 - 4: ORD and LH, RH reflectance spectra of M13 at 0.1 mg/mL.

	M13
Optical parameters	
Concentration mg/mL	0.1
average shift	1.70 ± 0.20
A	1.00 ± 0.02
matching parameters	
ΔΔϕ	2.20 ± 0.20

Table 7 - 1: Asymmetry parameters and matching parameters for M13 at 0.1 mg/mL.

A is equal to 1. Given that the pI is pH4.2 for M13 and the virions were dissolved in water (pH 7) the virus should be negatively charged. The overall charge of M13 is rather low, it goes from +2 to -2 at acidic and basic pH, respectively[19]. But in chapter 4, we showed that molecules with an overall net charge of +4 could alter the height of the ORD signal. As explained in chapter 5, A is also an indicator of order at the surface. Thus an explanation for the achiral value of A could be that M13 is randomly orientated in all possible directions creating an isotropic environment. Most of the particles are lying in the xy plane. The particles are flexible thus, even if the virions sit straight on the surface, nothing guaranties that it is straight in the z direction. However, based on the parameter ΔΔφ, we can see a significant asymmetry (table 7 - 1). Indeed, in figure 7 - 4 we can detect an opposite change in the reflectivity phase. We speculate that the charge affects the phase of the signal, but that the effect is too small to be seen in the ORD. From this we make the hypothesis that there is a preferential orientation for surface charges to interact with the plasmonic fields, and it is in the z direction.

7.3.2 TMV:

We ran TMV at 1 mg/mL. Figure 7 - 5 shows the ORD and the reflectance spectra. The ORD and reflectivity data show that the average shift is quite small (table 7 - 2). Due to the lack of symmetry and preferential orientation it is more difficult for this virus to bind to the gold. The average shift confirms that the virus hardly sticks to the gold surface. The ORD from TMV does not display any asymmetry. There is no difference in the shift (ΔΔλ) or in the height of the signal (A). This could be due to the orientation of TMV on the surface (figure 7 - 5). Because the virus is orientated on its side, the surface charges are not located in the same way as they are in spherical molecules. Thus, the interaction between the field and the surface charges cannot be observed.

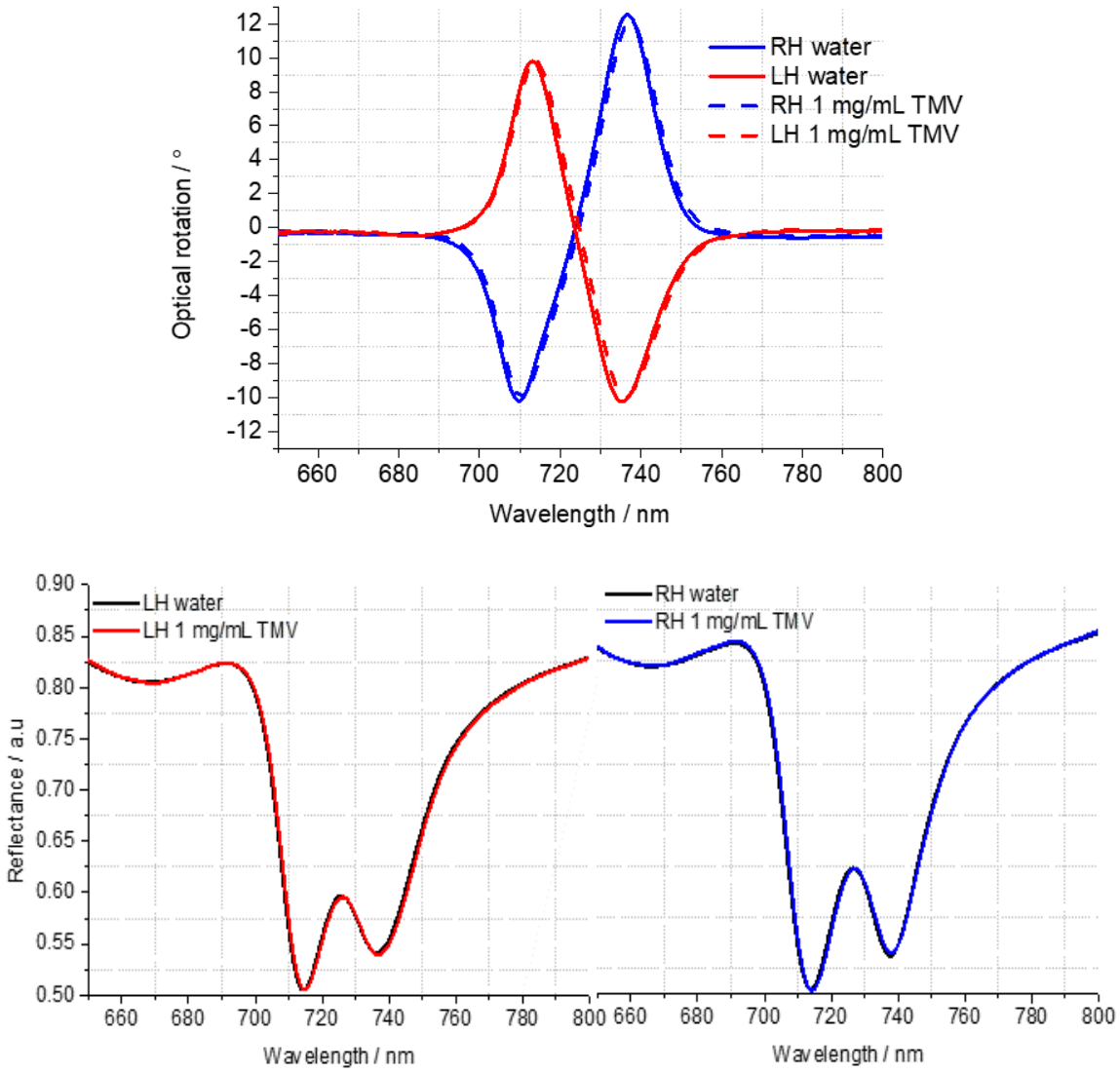

Figure 7 - 5: ORD and LH and RH reflectance data of TMV at 1 mg/mL.

The reflectance data show no change in the phase of the signal and this is confirmed by the matching parameters (table 7 – 2 matching graphs in the appendix figure 7 - 12), which display no asymmetry. Given that TMV has a pI that lies around pH 4[8] the ratio should not be equal to one, because the virus has an excess of negative charges at its surface.

	TMV
Optical parameters	
Concentration mg/mL	1
average shift	0.80 ± 0.20
A	0.98 ± 0.02
matching parameters	
ΔΔϕ	-0.30 ± 0.20

Table 7 - 2: Asymmetry parameters from the experimental and the matched data for TMV at 1mg/mL.

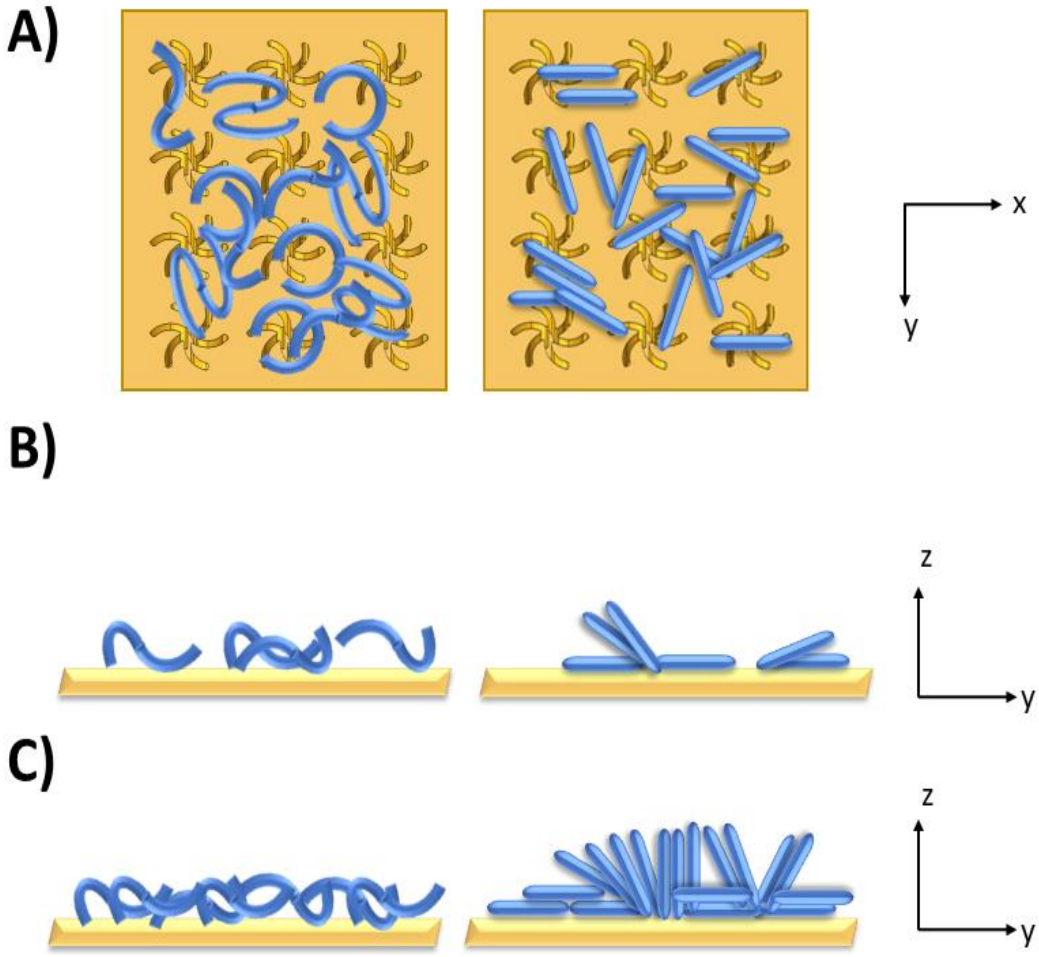

Figure 7 - 6: Representation of the orientation of M13 and TMV on the slide. A) top view of metamaterial and B) side view of the metamaterial with pictures on the left showing M13 and pictures on the right showing TMV. C) Side view of the metamaterial saturated with viruses.

At a concentration of 1 mg/mL, ΔΔφ is small because the surface is saturated with the virus and so it results in a variety of orientations causing averaging in the signal. Hence the

environment becomes more isotropic. Due to its shape and the way it binds to gold, the rod-shaped virus will saturate the surface at lower concentration compared to the icosahedral virus (figure 7 – 6); in the xy plane rod-shaped viruses are much bigger. The reflectance can be more sensitive than the ORD. The surface charges do interact with the chiral fields, otherwise there would be no change in the phase of the reflectance signal. We assume that because of the virus orientation the change in the optical signal is too elusive to be seen.

The same phenomenon happens with the two viruses. We recall here that the tensor of optical activity is[20–22]:

$$\xi^{\mathrm{iso}} = \begin{vmatrix} \xi_{xx}^{\mathrm{iso}} & 0 & 0 \\ 0 & \xi_{yy}^{\mathrm{iso}} & 0 \\ 0 & 0 & \xi_{zz}^{\mathrm{iso}} \end{vmatrix}, \quad (1)$$

When the viruses do not saturate the surface, the particles are mainly in the xy plane so the diagonal elements of the tensor are as follows: $\xi_{xx}^{\mathrm{iso}} = \xi_{yy}^{\mathrm{iso}} \gg \xi_{zz}^{\mathrm{iso}}$.

For TMV, as the concentration of viruses increases at the surface, the particles pile up at the surface (figure 7 – 6C) and the zz component of the tensor increase is to be of almost equal value as ξ_{xx}^{iso} and thus ξ_{yy}^{iso}. The diagonal component of the tensor becomes equal and the asymmetry decreases. This is possible only for TMVs because the rods are rigid. M13 displays an asymmetry at a high concentration on the phase of the signal ($\Delta\Delta\phi$) because it is flexible. Thus, the particles do not extend in the z direction but spread on the xy plane and end up forming multiple layers on this plane. Consequently, ξ_{zz}^{iso} stays rather small compared to ξ_{xx}^{iso} and ξ_{yy}^{iso}.

7.3.3 TMV VLP:

Chiral plasmonic fields were used to look at the VLPs of TMVs. In chapter 6, it was shown that VLPs give a weaker chiroptical signal, however, these particles were spherical. Those particles sit on the gold in the same way as the corresponding virions because it is only the outer shell that interacts with the metafilm.

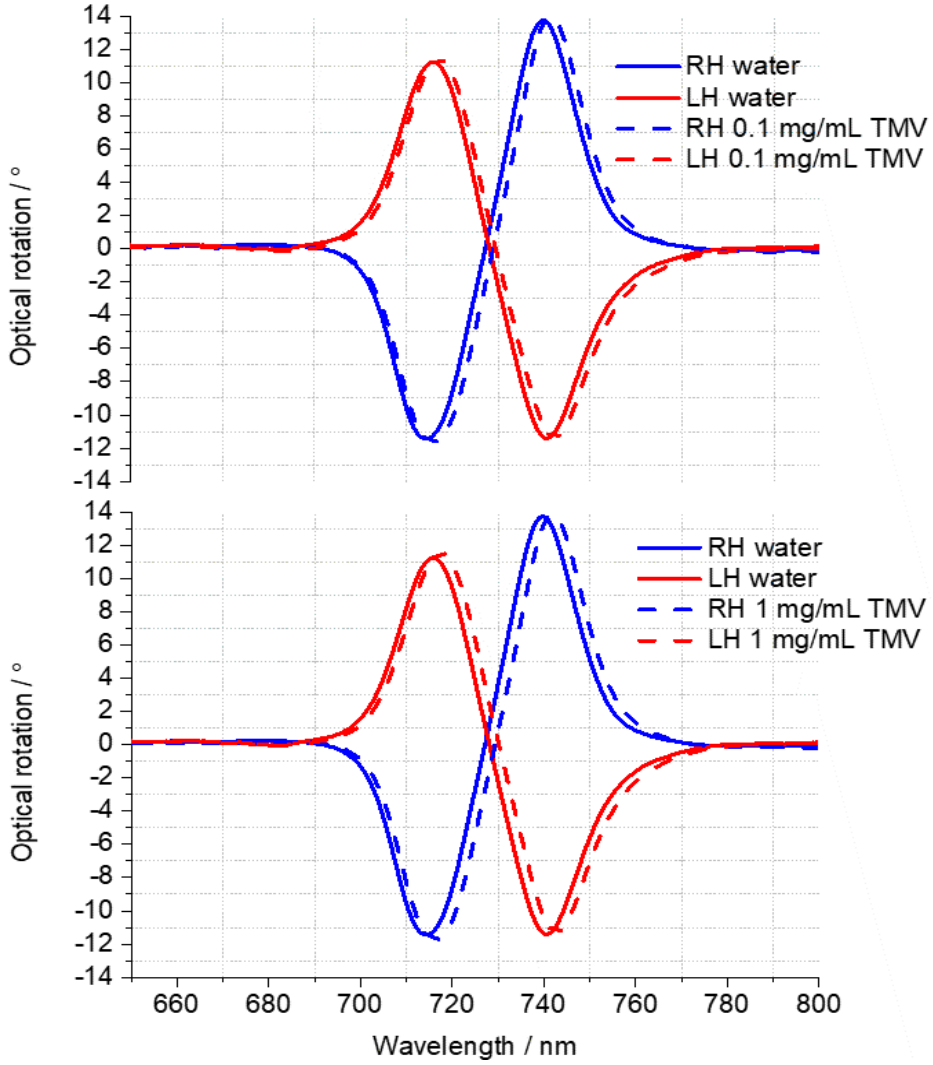

Figure 7 - 7: ORD of TMV VLP at three different concentrations from top to bottom: 0.1 mg/mL and 1 mg/mL.

The rod-shaped VLPs of TMV do not have the same length. Because they do not contain genetic material, their pI is higher than the pI of the virions[23]. Thus, we expected less interaction with the chiral fields due to the more even distribution of charges at the surface of the rods. We notice in figure 7 - 7 that the average shift (table 7 - 3) was larger with the VLPs than with the virions at all concentrations tested. The ORD does not display any asymmetry, neither in the shift nor in the height of the LH and RH signals.

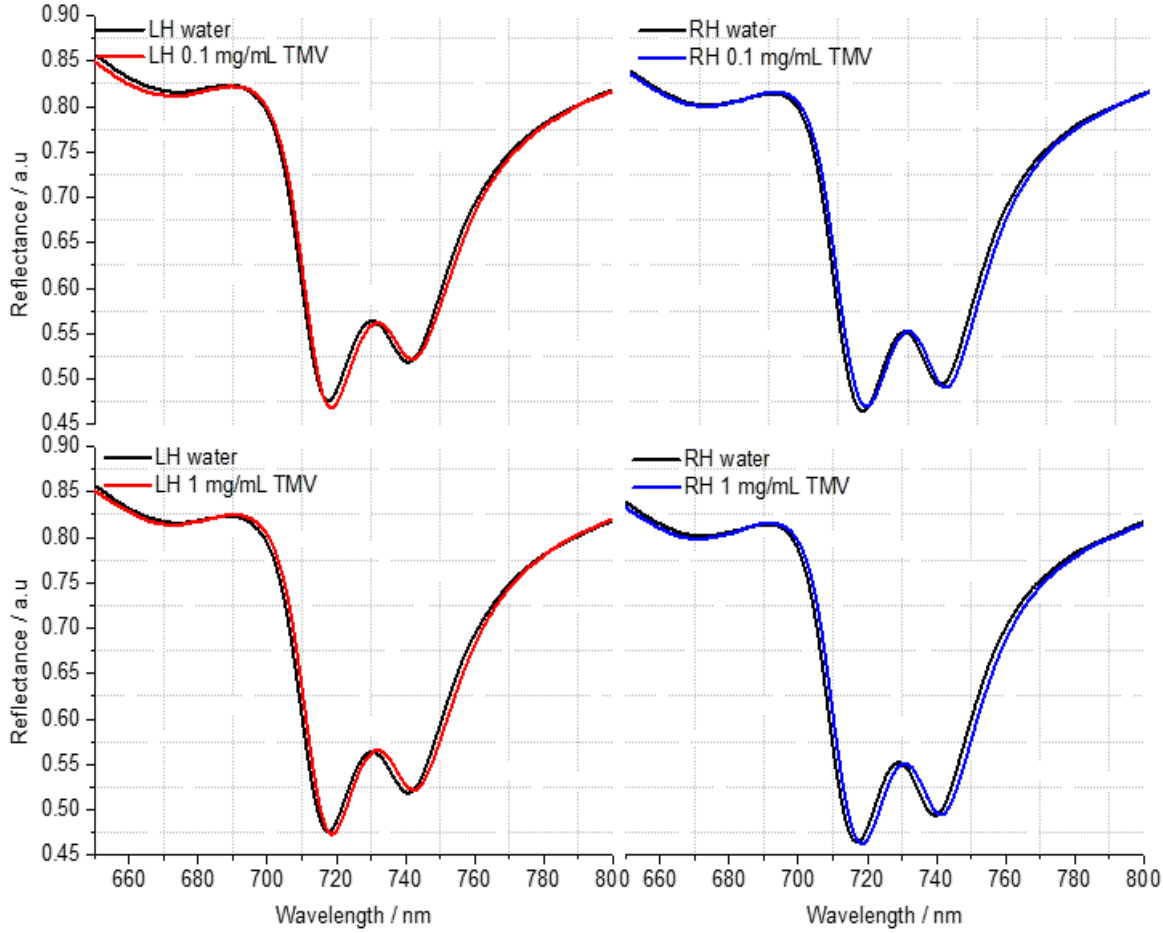

Figure 7 - 8: Reflectance of TMV VLP at two different concentrations from top to bottom: 0.1 mg/mL and 1 mg/mL.

Optical parameters		
concentration mg/mL	0.1	1
average shift	1.60 ± 0.20	2.20 ± 0.20
A	1.00 ± 0.02	1.00 ± 0.02
matching parameters		
ΔΔϕ	1.70 ± 0. 20	0.30 ± 0. 20

Table 7 - 3: Asymmetry parameters from the experimental and the data, modelled with PIT modelling (chapter 2) for TMV VLP at final concentrations of 0.1 mg/mL and 1mg/mL.

Table 7 - 3 shows similar results to table 7 - 2 showing that there is no asymmetry in A. However, there is an asymmetry in ΔΔϕ which is decreasing with increasing concentrations, due to saturation of the surface. The explanation is the same as for the virions meaning that the value of ξ_{zz}^{iso} increase. The environment becomes more isotropic. The asymmetry in the phase is larger with the virions at 0.1 mg/mL. The spectra at this concentration show an opposite phase change (Top figure 7 - 8), in both LH and RH signals (matching graphs in

the appendix figure 7 - 11). The average shift is much higher than with the virions. Given that VLPs are lighter particles, more are needed to saturate the surface.

7.4 Conclusion:

Previously (in chapter 4) we showed that detection of surface charges with plasmonic fields was possible using biomolecules with a spherical or pseudo-spherical shape. We applied this method to icosahedral viruses, and we saw promising results for surface charge determination. In this study, M13 filamentous bacteriophages and rod-shaped viruses were exposed to plasmonic chiral fields. These rod-shaped viruses do not exhibit the same asymmetry in the optical signal as icosahedral viruses, even though those particles have a low pI and thus have an uneven distribution of charges at the surface. It was shown that the phase of the dark mode ΔΔφ displayed a small asymmetry but not the ORD. Accordingly, we assume that the overall net charge of the virus still interferes with the dark mode resonator of the structures but, because most of the interaction happens in the xy plane it is averaged out and will not show in the ORD. Thus, there is a component equal to 0, the one for the z direction, in the optical chirality tensor. The rod-shaped virus and M13 have a different structure, with M13 being more flexible. They do not sit on the surface gold in the same way, TMV has more particles in the z direction, making the environment isotropic and the asymmetry very weak. M13 exhibits an asymmetry in ΔΔφ only. We speculated that according to the virus particles orientation, the diagonal elements of the tensor of optical activity would behave differently, especially the zz component leading to more or less asymmetry in the signal.

However, TMV VLPs exhibit an asymmetry in the phase of the reflectivity, the ΔΔφ parameter. We hypothesised that due to their size and the way they bind to the gold, they saturate the surface at a low concentration, which does not make it ideal for chiroptical measurements. We observed a similar behaviour with the icosahedral VLPs, meaning that removing genetic material leads to more asymmetry since the saccharide of the RNA cancels out the CD rising from the coat protein.

The hypothesis we made could be strengthened by increasing the chiroptical signal of the viruses. Further work would be to bind a gold binding domain to M13 bacteriophages, making them able to sit straight onto the gold surface[17]. This would lead to order on the surface and a different orientation of the virus surface charges. The orientation of surface charges would be in the z direction and thus could lead to stronger interactions with the chiral fields. Adding a gold binding domain to TMVs in order to have the particles straight in the chiral field could show interesting results. Indeed, the charges being orientated in a

completely different way, the interference with the fields could be stronger. However, TMVs are long particles and the evanescent fields in gold metafilm are around 50 nm height.

7.5 References:

(1) Gaur, R. K.; Petrov, N. M.; Patil, B. L.; Stoyanova, M.I. Plant Viruses: Evolution and Management. Springer (2016).

(2) Hull, R. Plant Virology. Academic Press. (2014).

(3) Scholthof, K-B. G.; Adkins, S.; Czosnek, H.; Palukaitis, P.; Jacquot, E.; Hohn, T.; Hohn, B.; Saunders, K.; Candresse, T.; Ahlquist, P.; et al. Top 10 Plant Viruses in Molecular Plant Pathology. Mol. Plant Pathol. (2011), 12 (9), 938–954.

(4) Makowski, L. Phage Display : Structure, Assembly and Engineering of Filamentous Bacteriophage M13. Struc. Bio. (1994), 4 (2), 225–230.

(5) Mateu, M. G. (Ed.) Structure and Physics of Viruses; Springer, (2013).

(6) Narayanan, K. B.; Han, S. S. Helical Plant Viral Nanoparticles — Bioinspired Synthesis of Nanomaterials and Nanostructures. Bioinspiration & Biomimetics. (2017), 12 (3).

(7) Klug, A. The Tobacco Mosaic Virus Particle : Structure and Assembly. R. Soc. (1999), 354 (1383), 531–535.

(8) Oster G. The Isoelectric Points of Some Strains of Tobacco Mosaic Virus. J. Biol. Chem. (1951), 190, 55–60.

(9) Foster, G. D.; Taylor, S. C. (Eds). Plant Virology Protocols. From Virus Isolation to Transgenic Resistance. Humana Press (1998).

(10) Larkin, E. J.; Brown, A. D.; Culver, J. N. Fabrication of Tobacco Mosaic Virus-Like Nanorods for Peptide Display. Methods Mol Biol. (2018), 1776, 51-60.

(11) Fish, S. R.; Hartman, K. A.; Stubbs, G. J.; Thomas, G. J. Jr. Structural Studies of Tobacco Mosaic Virus and Its Components by Laser Raman Spectroscopy. Biochemistry (1981), 20 (26), 7449–7457.

(12) Marvin, D. A. Filamentous Phage Structure, Infection and Assembly. Struc. Bio. (1998), 8 (2), 150–158.

(13) Henry, T. J.; Pratt, D. The Proteins of Bacteriophage M13. Proc Natl Acad Sci U S A. (1969), 62(3), 800–807

(14) Liu, A.; Abbineni, G.; Mao, C. Nanocomposite Films Assembled from Genetically Engineered Filamentous Viruses and Gold Nanoparticles : Nanoarchitecture- and Humidity- Tunable Surface Plasmon Resonance Spectra. Adv. Mater. (2009), 21 (9), 1001–1005.

(15) Li, K.; Chen, Y.; Li, S.; Nguyen, H. G.; Niu, Z.; You, S.; Mello, C. M.; Lu, X.; Wang, Q. Chemical Modification of M13 Bacteriophage and Its Application in Cancer Cell Imaging. Bioconjugate chem. (2010), 21 (7), 1369–1377.

(16) Dong, D.; Sutaria, S.; Hwangbo, J. Y.; Chen, P. A Simple and Rapid Method to Isolate Purer M13 Phage by Isoelectric Precipitation. Appl Microbiol Biotechnol (2013), 97 (18), 8023–8029.

(17) Causa, F.; Moglie, R. D.; Iaccino, E.; Mimmi, S.; Marasco, D.; Scognamiglio, P. L.; Battista, E.; Palmieri, C.; Cosenza, C.; Sanguigno, L.; et al. Evolutionary Screening and Adsorption Behavior of Engineered M13 Bacteriophage and Derived Dodecapeptide for Selective Decoration of Gold Interfaces. J. Colloid Interface Sci. (2013), 389 (1), 220–229.

(18) Blaik, R. A.; Lan, E.; Huang, Y.; Dunn, B. Gold-Coated M13 Bacteriophage as a Template for Glucose Oxidase Biofuel Cells with Direct Electron Transfer. ACS Nano (2016), 10 (1), 324–332.

(19) Bhattacharjee, S.; Glucksman, M. J.; Makowski, L. Structural Polymorphism Correlated to Surface Charge in Filamentous Bacteriophages. Biophys. J. (1992), 61 (3), 725–735.

(20) Govorov, A. O.; Fan, Z. Theory of Chiral Plasmonic Nanostructures Comprising Metal Nanocrystals and Chiral Molecular Media. ChemPhysChem (2012), 13 (10), 2551–2560.

(21) Theron, I. P.; Cloete, J. H. The Electric Quadrupole Contribution to the Circular Birefringence of Nonmagnetic Anisotropie Chiral Media: A Circular Waveguide Experiment. IEEE, (1996), 44 (8), 1451–1459.

(22) Kelly, C.; Tullius, R.; Lapthorn, A. J.; Gadegaard, N.; Cooke, G.; Barron, L. D.; Karimullah, A. S.; Rotello, V. M.; Kadodwala, M. Chiral Plasmonic Fields Probe Structural Order of Biointerfaces. JACS (2018), 140, 8509–8517.

(23) Tiu, B. D. B.; Kernan, D. L.; Tiu, S. B.; Wen, A. M.; Zheng, Y.; Pokorski, J. K.; Advincula, R. C.; Steinmetz, N. F. Electrostatic Layer-by-Layer Construction of Fibrous TMV Biofilms. Nanoscale (2017), 9, 1580–1590.

7.6 Appendix:

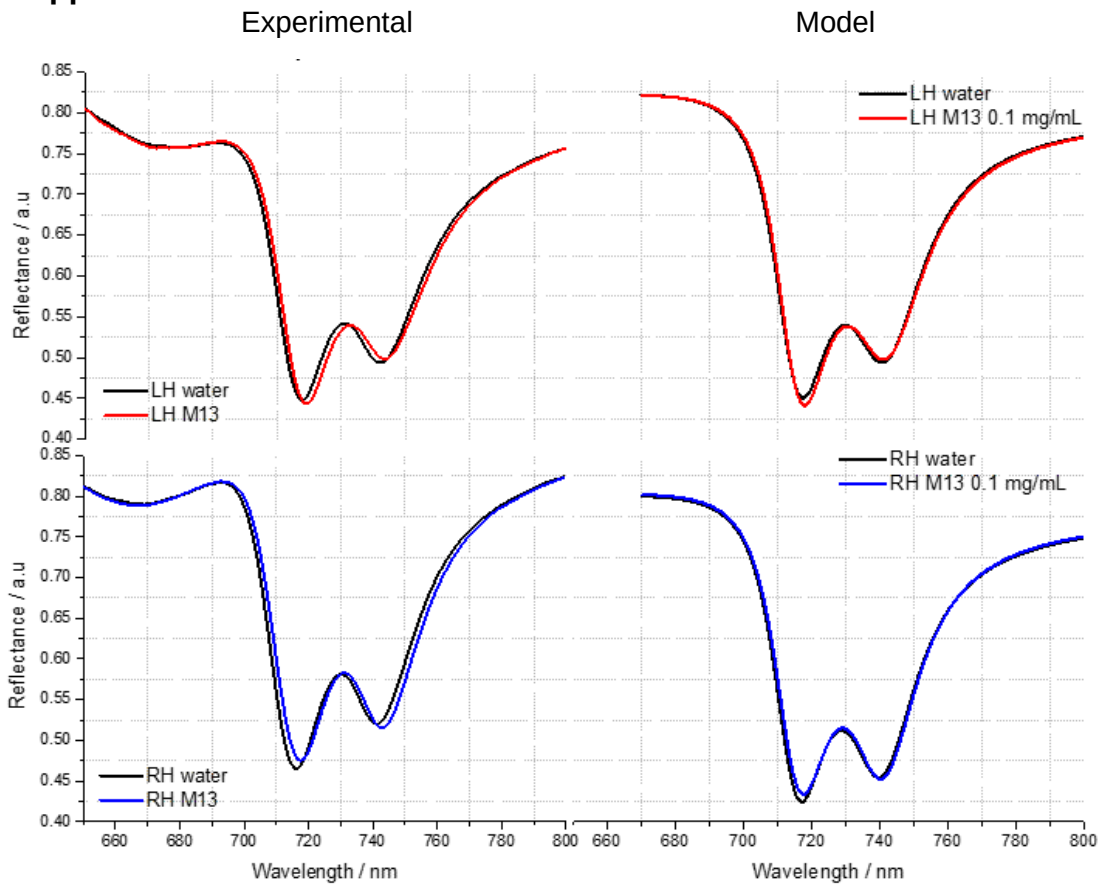

Figure 7 - 9: M13 matching graphs at the concentration of 0.1 mg/mL on the left part of the figure is the experimental data and the matching data is shown on the right part of the figure. The top part of the figure displays the LH data and the bottom part displays the RH data.

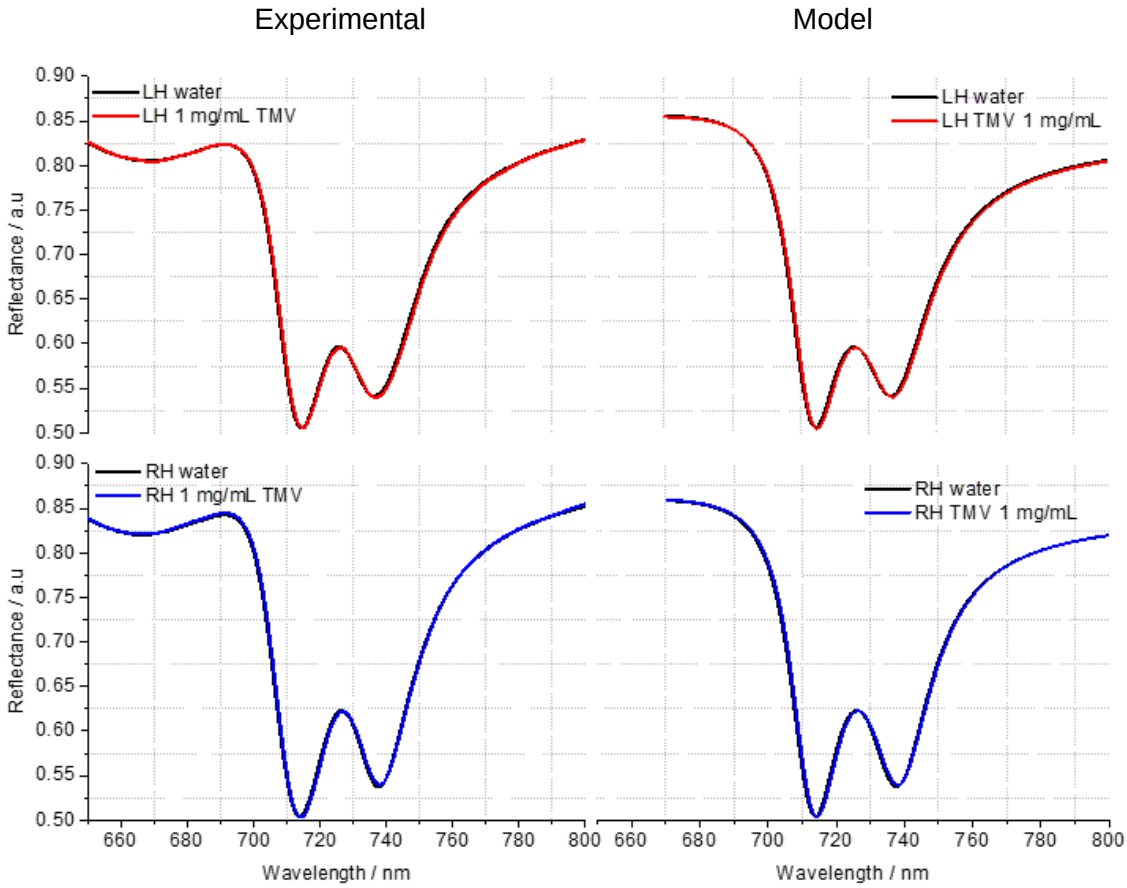

Figure 7 - 10: TMV virions matching graphs at the concentration of 1 mg/mL/ The left part of the figure is the experimental data and the matching data is shown on the right part of the figure. The top part of the figure displays the LH data and the bottom part displays the RH data.

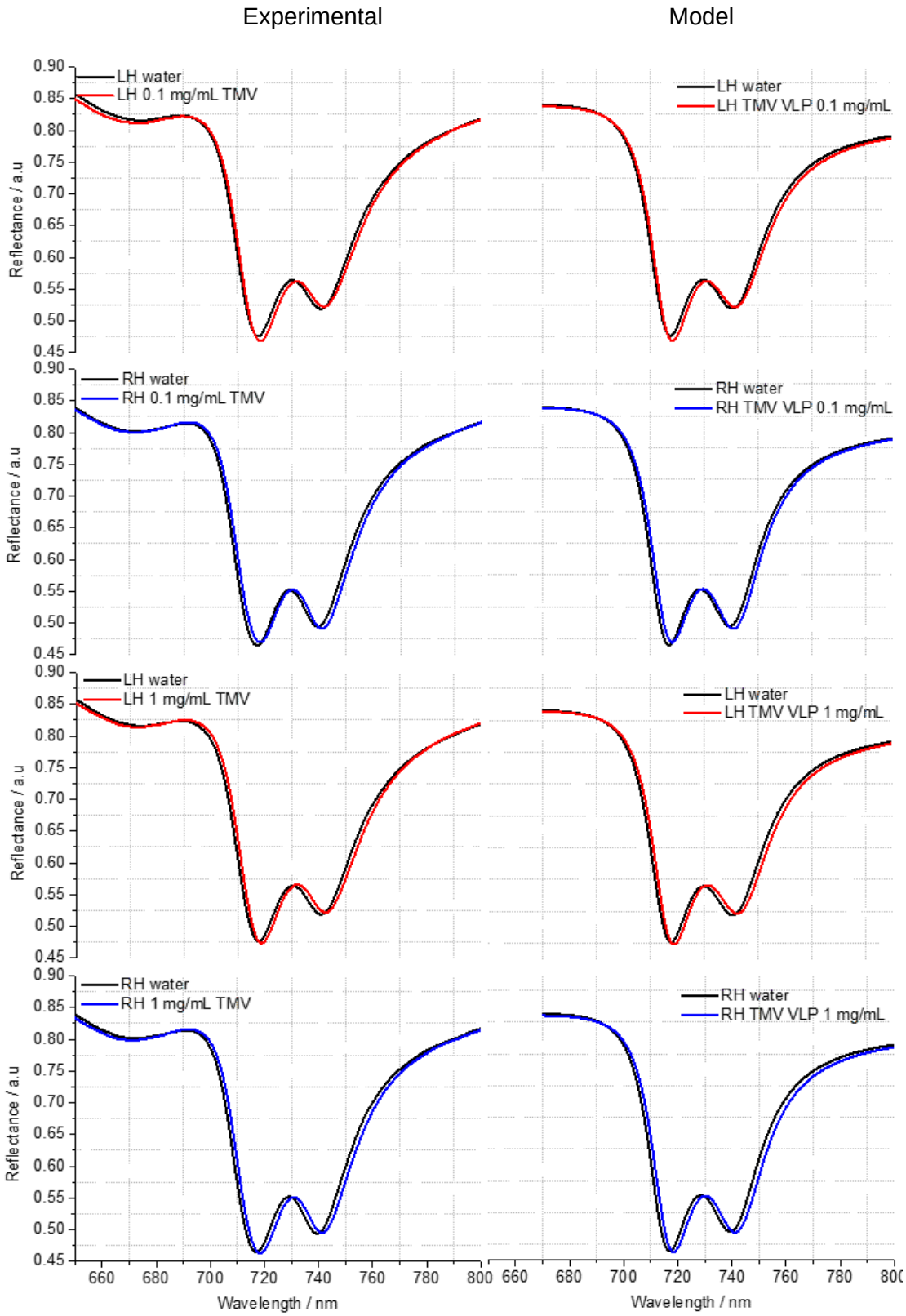

Figure 7 - 11: TMV VLP matching graphs at two concentrations 0.1 mg/mL and 1 mg/mL. The experimental data is displayed on the left part of the figure and the modelled data is shown on the right side of the figure.

Conclusion and future outlook

The sensitivity of chiral plasmonic fields to the surface charge density of biomolecules has been explored in this thesis. The enhancing or diminishing effect of the charges on the plasmonic fields was demonstrated by the ORD and reflectance spectra. An explanation of the physical effect was given, and several applications were presented for the phenomenon. In this section we will summarise the results chapters (4-7) and explore further applications or improvements of the methods.

In chapter 4 we showed how the effect of surface charges on plasmonic fields was discovered. Proteins with a different primary sequence but similar higher order structure were exposed to chiral fields. Since their primary sequence was dissimilar, a way to differentiate these proteins was via the overall surface charges, indeed as the amino acids have different pKa, they do not exhibit the same charges in the same environment (pH). Thus, the surface charge density of the DHQase were controlled by changing the pH of the solution they were dissolved in. Electrostatic calculations of the surface charges were performed, and from these simulations we could draw a map of the DHQase density of charges at several pH values from acidic to basic. We managed to link these maps to the ORD signals. When the surface charge of the protein was predominantly positive, the ORD LH signal height reduced greatly, and the RH signal was enhanced slightly. The opposite effect took place for a predominantly negatively charged protein; the ORD LH signal height showed a great enhancement while the RH signal slightly reduced. The difference in the strength of the effect according to the handedness was explained to be because of the chirality of the DHQ itself. The theory arising from the experimental data was that the charges at the surface of the nanostructure were interacting with the protein surface charges. Metaphorically, the protein imprinted an image of itself at the surface, inside the chiral fields. Because the distribution of charges is changed, and the evanescent fields arise from the movement of the charges at the surface of the gold, if these charges are altered then the fields can be enhanced or reduced. It was shown that the phenomenon happens only with an analyte on the surface and not in plain pH solution. A parameter was extracted from the height of the ORD to quantify the effect. A scale of the value of this parameter according to the state of charge of the biomolecule was given. Owing to this effect we can now find out the protein charge density at a given pH without knowing its primary sequence, and so the isoelectric point can be determined fairly accurately: the ratio of the ORD height will be 1 at the isoelectric point (pI). This latest statement was not tested. Further improvement of this work would be to expose a protein with an unknown sequence to plasmonic fields and predict its surface charge density and its pI. The method established

in this chapter shows promising results for a quick determination of the pIs of biomolecules and thus their electrostatic behaviour, that is to say the interaction with other proteins, the folding, the solubility and the ability to be crystallised.

In chapter 5, we showed a new property of the disposable plasmonic nanostructure, which is the determination of the specificity, or lack thereof, of an interaction between biomolecules. It was first shown that the surface of the plasmonic substrate could be coated with fragment antigen binding (Fab)2. It was shown that this fragment which retains the properties of the whole antibody can be attached onto the gold metafilm, via a gold-thiol bond, without losing its function even though it was slightly distorted on the surface. Two proteins from the albumin group were loaded on the coated surface, one with specific affinity with the antibody and the other one without. It was shown that, depending on the specificity of the complex (antigen-antibody) created, there would be an asymmetry in the ORD (specific interaction) or not (non-specific interaction). The explanation for the phenomenon is rather straightforward. It is due to the spatial geometry of the complex. A specific interaction leads to a complex with an established spatial orientation and thus an anisotropic environment; a non-specific complex leads to a more random spatial orientation and an isotropic environment. The order of the material at the surface could thus be linked to the asymmetry in the ORD. This work is a step further on previous work done by our group with Affimers. This work is also a step further in the functionalisation of our polycarbonate substrate. Indeed, it was already shown that self-assembled monolayer processes were efficient with our substrates, now we can say that functionalisation with (Fab)2 is a viable method for these substrates as well. In this chapter only one type of interaction was studied but there are many involved in biological processes. Further work would involve testing these other types of interaction and coming up with a fingerprint of the asymmetry arising from the specificity of the interaction according to its type. An alternative is to use this new type of functionalisation to enhance the biosensing signal. In fact, this was also tested for virus particles and showed promising results, but the method needs improvement, which is why the results are not shown in this thesis.

Chapter 6 explores the possibility of virus detection. Plant viruses were used here to show that polycarbonate structures were viable for detection of biomolecules much larger than proteins. This work was done in collaboration with biologists from the University of Glasgow and the James Hutton Institute. This chapter focuses on three viruses: turnip yellow mosaic virus (TYMV), cowpea mosaic virus (CpMV) and cauliflower mosaic virus (CaMV). This chapter follows the work shown in chapter 4, as the surface charges of viruses influence the ORD signal. The capsid of a virus (the shell that protects the genetic material) is made of an assembly of proteins and thus can display charges. This chapter focuses on

icosahedral viruses and shows that even though it is harder to distinguish between viruses than between proteins (the particles being much more symmetrical – the asymmetry is thus much weaker) it is still possible to do so, and the asymmetry arises due to charge density of the particles. The virus with the lower pI gives the highest asymmetry. It is shown that the phase of the reflectance signal also displays asymmetry and is more sensitive than the ORD signal. Indeed, the viruses with a pI close to the pH of the solution do not display an asymmetry in the ORD but have a significant asymmetry in the reflectance phase. Virus-like particles, meaning non-pathogen viruses (these particles do not contain genetic material), were also exposed to the plasmonic fields. It was shown that the particles do not display the same asymmetry, either the particle virion or the VLP has a stronger asymmetry. This effect came from the fact that the pI changes when the genetic material is removed from the capsid. This offers a route towards a fast method for the discrimination of pathogen and non-pathogen viruses.

Meanwhile a method to improve the chiroptical effect of the virus on the signal was explored. TYMV particles were tagged with a gold binding domain. The asymmetry was indeed enhanced but changed its sign. This confirmed that the asymmetry we saw was arising from the surface charges of the virus. Indeed, the thiol tag changed the pI of the virus and thus the sign of the asymmetry, because instead of having overall negative charges at a given pH it had a surface charge dominated by positive charges. Even if this method shows a great signal enhancement and can be used on other viruses, exploring a way to bind particles onto gold without changing the surface charge would be interesting.

In the final chapter, we determined the limit of our experimental technique using rod-shaped virus particles. The work was done here with Tabaco mosaic virus (TMV) and M13 bacteriophage. It was shown in this chapter that sensing rod-shaped viruses with our technique gives only weak asymmetry in the reflectance signal. It was suspected that it is because the interaction between the plasmonic fields and the surface charge takes place in the xy plane, whilst it can only be detected in the z direction. We pointed out that this was true even with the bacteriophage even though its structure is more flexible. However, there was a small asymmetry in the $\Delta\Delta\varphi$ parameter, meaning that the net charges still interact with the chiral fields. The problem was elucidated with the help of the chirality tensor diagonal components. The zz component of the tensor is very small compared to the xx and yy components giving rise to some asymmetry. But when the surface is saturated, all the components are equal and thus cancel out. The work done in this chapter is preliminary and does not mean that improvements cannot be made for rod-shaped viruses. Moreover, we showed that it was difficult to bind the TMV to the surface probably because of its shape as the virus saturates the surface at low concentration. VLP showed a bigger asymmetry.

Further work for this chapter would involve finding a way to tag viruses and bacteriophages in a way that orients them in the z direction. The literature is full of examples of tagged particles for both TMVs and M13. Another problem needs to be solved here: the length of this virus in the z direction once it is bound on the gold could be greater than the decay of the evanescent fields and so we would not able to detect any asymmetry due to chirality. Hence, another type of nanostructure would be needed.